Mono-X searches for simplified models of dark matter

Amelia Jean Brennan

ORCID: 0000-0002-8250-3351

Doctor of Philosophy
July 2016

School of Physics
The University of Melbourne

Submitted in Total Fulfilment of the
Requirements of the Degree of Doctor of Philosophy

Printed on archival quality paper

Abstract

The identity of dark matter remains one of the big open questions in particle physics; while much is known about its distribution throughout the Universe, very little is understood about its particle nature. In particular, a small but non-zero coupling to the Standard Model (SM) sector has not yet been ruled out. WIMP-type dark matter (DM), with weak-scale mass and couplings, may therefore be produced in proton collisions with the Large Hadron Collider (LHC), and detected by the ATLAS experiment.

Several collider searches are presented, which utilise the mono-X+$E_{\mathrm{T}}^{\mathrm{miss}}$ topology, wherein DM (the presence of which is inferred through the observation of missing transverse energy) is produced in association with some object X. The mono-jet process has the largest cross section, however mono-boson analyses, the focus of this thesis, have other advantages. The mono-$Z(\ell^+\ell^-)$ channel benefits from the straightforward identification of charged leptons within the detector and removal of the multi-jet background, while the mono-$W/Z(jj)$ channel is able to utilise the growing collection of electroweak boson identification techniques which exploit the two-prong substructure of a large-radius jet.

This thesis describes two ATLAS analyses that seek to constrain both Effective Field Theory (EFT) models and simplified models of DM. The ATLAS mono-$Z(\ell\ell)$ analysis uses 20.3 fb^{-1} of data produced at $\sqrt{s}$ = 8 TeV and selects events with a leptonically-decaying Z boson produced back-to-back with a large amount of $E_{\mathrm{T}}^{\mathrm{miss}}$. A count-and-count method finds that no excess above the SM prediction is observed, and so constraints are calculated for the suppression scale Λ of the EFTs, and for the quark-DM-mediator coupling of a simplified model with a scalar mediator exchanged in the t-channel. The ATLAS mono-$W/Z(jj)$ analysis uses the first 3.2 fb^{-1} of data produced at $\sqrt{s}$ = 13 TeV, and selects events with a single large-radius jet produced in association with $E_{\mathrm{T}}^{\mathrm{miss}}$. A profile likelihood fit of the SM background estimation and data is used to extract a limit on the signal strength for a vector mediator s-channel simplified model, and converted to

a limit on the suppression scale Λ for a $ZZ\chi\bar{\chi}$ contact operator.

A reinterpretation of Run I results from ATLAS for three common simplified models is also presented, including a comparison of the results from the mono-jet, mono-$Z(\ell^+\ell^-)$ and mono-$W/Z(jj)$ channels. Limits on the model coupling strengths are discussed. The strongest constraints are obtained with the mono-jet channel, however the leptonic mono-Z channel is able to remove the large multi-jet background to attain limits that are weaker by only a factor of a few.

It is essential that the reconstruction of objects within the ATLAS detector, along with their energy measurement and calibration, is well understood and that the performance is optimised. Along with a general discussion of the relevant objects in the detector (leptons, jets and $E_{\mathrm{T}}^{\mathrm{miss}}$), the *in situ* measurement of corrections to the energy scale of hadronically-decaying tau leptons is described.

Declaration

This is to certify that:

i This thesis, entitled 'Mono-X searches for simplified models of dark matter', comprises only my original work towards the PhD, except where indicated otherwise;

ii Due acknowledgement has been made in the text to all other material used;

iii This thesis has fewer than 100 000 words, exclusive of tables, bibliographies and appendices.

.....

Amelia Jean Brennan

Preface

This preface contains a summary for each chapter in this thesis including details of the resulting publications, and detailing the contributions from collaborators and supervisors.

- Chapter 1 is a general introduction. Chapters 2 and 3 are a review of the SM of Particle Physics and the evidence for DM, and of the EFT and simplified models of DM studied in this thesis. Chapter 4 is a description of the ATLAS detector and the reconstruction of physics objects.

- Chapter 5 describes work performed by the author in collaboration with F. Nuti and supervised by Prof. E. Barberio. The chapter includes a short description of the Tau Energy Scale (TES) as calculated by other members of the Tau Working Group within ATLAS, to provide context for the work done by the author. The author contributed to all aspects of the TES *in situ* correction derivation as described in the chapter. This work was included in the published paper of ref. [1].

- Chapter 6 is a description of the ATLAS mono-$Z(\ell\ell)$ analysis, where the author was one of several analysers contributing to the work, and is based on ref. [2] (an ATLAS-internal note) and the published paper ref. [3]. The author's contribution was in the simplified model interpretation: preliminary studies of the t-channel DM model, the generation of signal samples, the calculation of coupling constraints, the extension of the parameter space and developing the presentation of the results. The author also contributed to the development of the event selection software. Other analysis details are provided to give a full overview of the analysis.

- Chapter 7 describes the reinterpretation of Run I ATLAS mono-X constraints in a simplified model context, and presents constraints on three models obtained with three alternative channels. The work was published in ref. [4], on which this chapter is heavily based. The author of this thesis was the lead

author of that work, and developed the main concepts presented, as well as all the coded software used for signal sample generation, event selection and calculating constraints. Co-authors M. McDonald, J. Gramling and T. Jacques developed the mono-jet and mono-$W/Z(jj)$ reinterpretations and comparison with direct detection and relic density constraints, while the author was responsible for the mono-$Z(\ell\ell)$ reinterpretation, and provided input on all channels. All authors contributed to the writing and editing of the paper.

- Chapter 8 is a description of the ATLAS mono-$W/Z(jj)$ analysis, where the author was one of several analysers, and is based on refs. [5, 6]. The author contributed to the early testing and development of the analysis and the software framework, preparing SM background samples, and (most significantly) in the study and development of the 1-lepton control regions. In addition, the author provided feedback during all stages of the analysis. Details of the analysis performed by other collaborators are included in the chapter for context.

- Chapter 9 contains a summary of the thesis and concluding remarks.

Where work described in the thesis has been performed by other people, this is also acknowledged in each chapter.

Acknowledgements

I must begin by thanking my supervisors, Elisabetta and Nicole, for taking me on as a student and providing many opportunities over the past four years. You provided valuable guidance and were always available, particularly at awkward times of night when I was in Geneva. It has been wonderful to have two female supervisors who are so successful in their fields. Thanks also to Brian for offering technical support and advice at CERN.

I am grateful to the ARC Centre of Excellence for Particle Physics at the Terascale (CoEPP) for affording us so many opportunities and financial support, and particularly so many great Workshops. Special thanks are due to Sean for his computing support, willingness to help and for biting his tongue when I invariably said a stupid thing. CoEPP supports a really fantastic group of people and it has been exciting to be at the forefront of particle physics in Australia. I have also benefited greatly from the support of the Swiss Government, which allowed me to live in Geneva for a year and study at Université de Genève.

I couldn't have made it through this PhD without the other students in my (approximate) cohort, who have always celerated each other's achievements and offered encouragement in the tough times. Special thanks to Jackson, Pete and Rebecca for our Traditional Wedneday Coffees and keeping my cactus alive (just), and to Millie for enduring our never-ending paper and for constantly providing some much-needed emotional intelligence. Thanks also to Francesco, for guiding me with unending patience through the baptism of fire that was the TES and my introduction to ATLAS.

A big thankyou to Woody for invariably being up for a flat white and some fruit toast, or a beer (that inevitably became two), and always with a laugh. Thanks also to everyone on level 7 for some fascinating discussions and hilarious quiz responses.

Bec, it has meant a lot to me that we have been through our doctorates together, even if you did have to move interstate to pursue yours! I very much

admire your resilience and your loyalty, and am so grateful for your faith in me. We may both end up with PhDs but no doubt we shall share many more Malibu-and-Cokes and dance to Diplo together.

To Mum and Dad, thank you both so much for your unwavering support and regard over my entire academic career! You (unsurprisingly) encouraged my interest in maths and science from a young age, but you've also given me the other tools necessary to survive the past four years. Being able to show you around CERN and take you hiking in the Swiss Alps has been a real highlight—it makes me happy to make you proud. Thanks also to Mel, you've always reminded me to keep my head out of the clouds and pay attention for god's sake.

And finally, to Andy, I honestly couldn't have done this without you. I have so appreciated your knowledge and experience within the microcosm of physics academia, in combination with your perspective and your sense of the wider world. I am also grateful for all your efforts to ensure I've lived as well as worked during these past few years, particularly in planning so many trips and documenting our experiences together. You have supported me in all senses of the word, and your sense of humour, your drive and your willingness to let me do what I needed to do have all been invaluable. Thanks for following me back to Melbourne, and I am looking forward to our next adventures together.

For my parents and grandparents,
to whom education was so important.

Contents

List of Figures

List of Tables

Chapter 1

Introduction

The Standard Model (SM) of Particle Physics describes the known fundamental particles and the strong, weak and electromagnetic forces that mediate their interactions — the melding of theoretical ideas and experimental measurements by many physicists over many years has created one of the most comprehensive high-precision and highly-tested theories in existence. However, despite the discovery of the Higgs boson in 2012 [7, 8], it is also known to be incomplete. In addition to the missing description of the gravitational force, several important questions within the field of particle physics remain unanswered. One of the most significant of these is the existence of dark matter (DM), an unknown material that permeates our Universe with five times the abundance of well-understood matter, and which does not exist within the SM theory.

While examining the Coma cluster in 1933, Fritz Zwicky was one of the first to use the virial theorem to infer the existence of unseen matter, which he referred to as *dunkle Materie* [9]. Much evidence exists to indicate the presence of DM and its gravitational interactions, however it has not yet been observed in any purpose-built detector, suggesting it may not have any further interactions with the matter of the SM. Nonetheless, a small but non-zero coupling to SM particles has not yet been ruled out; interestingly, if such a coupling has a weak scale strength and the DM mass is in the GeV–TeV range, the resulting DM (known as a Weakly Interacting Massive Particle (WIMP)) has a calculated relic abundance which approximately matches that observed in the Universe today — an intriguing hint at DM's true nature, perhaps?

Myriad theoretical models of DM exist in the literature, and in an attempt to constrain as many of them as possible with generic experimental analyses, the Effective Field Theory (EFT) framework is commonly utilised. Models of this type include a single WIMP and hide the underlying physics of its interaction with the SM behind a suppression scale (see refs. [10–13] for some examples). While this framework is appropriate for low-energy interactions in DM-nucleon

scattering experiments, its validity has been called into question in the context of high-energy collider experiments such as those at the Large Hadron Collider (LHC) at CERN, Switzerland (see ref. [14] and others). As a result, simplified models, which explicitly include a single mediating particle that couples to the dark and SM sectors, have emerged as a powerful tool for the interpretation of collider, direct and indirect detection signals of DM. The increased parameter space that results from the additional degree of freedom makes it challenging to scan as wide a range of models as can be done with EFT models. However, constraints calculated within the context of a simplified model are valid across a comparatively broader energy range. A benchmark set of simplified models, with a mediator exchanged in either the s- or t-channels, have been identified by the experimental DM community for inclusion in collider searches [15].

The ATLAS detector, one of the four main experiments collecting data from the proton-proton collisions performed at the LHC, is able to search for DM hypothesised to couple to the SM (and quarks in particular), wherein a particle-antiparticle pair of DM particles may be produced from the collision of a pair of protons. However, as DM particles are expected to escape the detector without being observed, an additional object produced in the interaction is required to act as a probe; missing transverse momentum (denoted $E_{\mathrm{T}}^{\mathrm{miss}}$), a result of invisible particles and conserved momentum in the transverse plane, is the observable attributed to the DM. This topology gives rise to the mono-X + $E_{\mathrm{T}}^{\mathrm{miss}}$ signal, where X is commonly a quark or gluon (which hadronise to produce a jet as described later in this thesis), a photon or a W or Z boson. These channels form the basis of the generic mono-X DM searches at ATLAS and CMS, in the context of both EFT and, more recently, simplified model frameworks.

To reach the high-precision measurements required for these mono-X analyses, along with the many others which make up the scientific program of the ATLAS Collaboration, all aspects of the working detector must be well understood, and studies of performance carried out regularly to ensure the detection and reconstruction of particles is accomplished as effectively and efficiently as possible. This is particularly important in the context of the the high-energy and high-rate proton-proton collisions provided by the LHC. Most particles only deposit a certain percentage of their energy in the detector, and so an important step is calibration of the measured energy so that the true energy is recovered. Participation in such studies is required by all members of the ATLAS Collaboration.

Of course, not all analyses with ATLAS data are necessarily performed within the Collaboration, and model-independent limits are commonly released with mono-X results. These limits can then be reinterpreted by theorists (see refs. [16–44] for some of the available examples) with the DM model of their choice, to

further constrain the enormous parameter space available within the plethora of DM models.

This thesis describes a set of simplified models and constraints on their couplings to the SM obtained with the mono-boson search channels. Within the ATLAS Collaborations, the author was the first to include a t-channel simplified model in an exotics mono-X analysis, was at the forefront of the push for both s- and t-channel models to be a standard inclusion in addition to EFT models, and advocated for Run I EFT results to be recast as simplified model constraints. The author helped publish several documents promoting and describing simplified models for the ATLAS and CMS Collaborations [15, 45, 46], which includes a report proposing the benchmark set of simplified models since included in Run II studies.

This thesis begins with a general introduction to the relevant particles and forces of the SM, and a summary of the astrophysical evidence for DM, in chapter 2. Chapter 3 provides an overview of the EFT and simplified models of DM studied in the thesis. Chapter 4 introduces the ATLAS detector and the reconstruction of detected particles and their energies, while chapter 5 provides detail on the calibration of hadronically-decaying taus and an *in situ* correction to the resulting Tau Energy Scale. The Run I ATLAS mono-$Z(\rightarrow \ell^+\ell^-)$ analysis is described in chapter 6, while an external reinterpretation of a collection of Run I ATLAS mono-X analyses in the simplified model framework is the subject of chapter 7. Chapter 8 describes one of the first public ATLAS mono-X analyses of Run II, using hadronically-decaying W and Z bosons, and the thesis is concluded in chapter 9.

Chapter 2

The Standard Model and evidence for dark matter

The Standard Model (SM) of Particle Physics is one of the most robust and rigorously tested theories in physics. However, despite its success in describing the most fundamental particles and forces that we understand, we know that as a fully comprehensive description of all phenomena in our Universe, it remains incomplete. One significant gap is an explanation of dark matter (DM); although there is an abundance of astrophysical evidence for DM, the SM provides no suitable candidate.

This chapter shall proceed as follows. Section 2.1 will briefly describe the particles and forces of the SM, and comment on the not-yet understood aspects of particle physics that are missing. Section 2.2 will describe the evidence for DM, introduce the Weakly Interacting Massive Particle (WIMP) model of DM and discuss the various methods employed in attempts to uncover its nature.

2.1 The Standard Model

The SM is a gauge theory and can be expressed as a combination of its symmetry groups: $SU(3)_c \times SU(2)_L \times U(1)_Y$. $SU(3)_c$ is the gauge group of quantum chromodynamics (QCD), the theory of the strong interactions, and has eight generators leading to the eight massless gluons descibed below. $SU(2)_L \times U(1)_Y$ is the electroweak (EW) sector, which unifies the weak and electromagnetic (EM) forces, and has four generators leading to the bosons $W^{\pm}$, Z and γ. However, spontaneous electroweak symmetry breaking (EWSB) is needed to give mass to the (previously massless) W and Z bosons without violating local gauge invariance.

The forces can be described by bosons coupling to charges that must be conserved in an interaction, these are the colour charge (of strong interactions), the

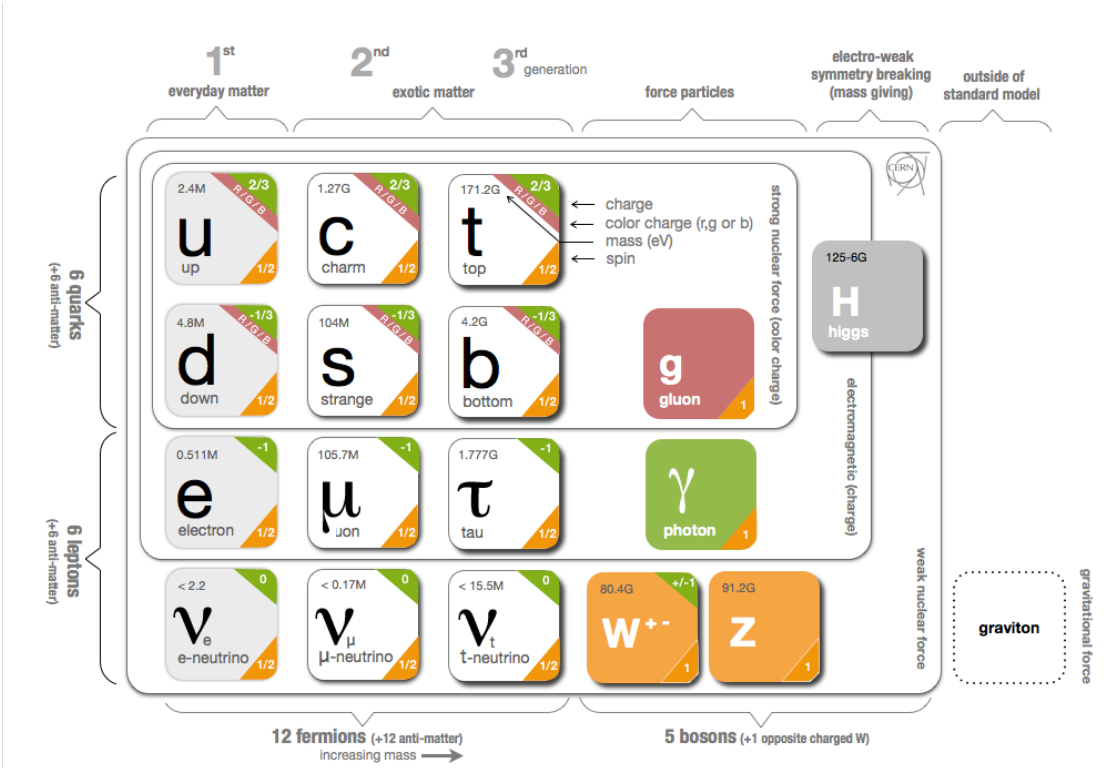

Figure 2.1: The fermions and bosons that make up the Standard Model of Particle Physics. Taken from ref. [47].

electric charge Q (of EM interactions), and the third component of weak isospin[1] I_3 (of weak interactions). The EW unification leads to an additional quantum number which is always conserved, known as weak hypercharge and defined by

$$Y_W = 2(Q - I_3) \ . \tag{2.1}$$

The particles of the SM are often described by three of their quantum numbers, the number of colour states under QCD, whether it transforms as a doublet or singlet under $SU(2)$, and the weak hypercharge.

2.1.1 Particles and Forces

The particles of the SM are considered to be either fermions (*matter* particles) or bosons (the carriers of force that mediate the interactions between them), and are listed in fig. 2.1, which shows their mass, spin and electric and colour charges. A very brief overview is provided below; all quoted masses are taken from ref. [48]. Note that unless otherwise stated, each particle has its own distinct antiparticle

[1] Weak isospin is the gauge symmetry of the weak interaction which connects quark and lepton doublets of left-handed particles in all generations.

under charge conjugation (changing the sign of all quantum numbers such as electric charge, lepton and baryon numbers).

Fermions

The fermions, displayed on the left-hand side of fig. 2.1, all have spin-$^1/_2$ and are divided into quarks and leptons. They are further split into three generations with similar properties but of increasing mass.

The quarks are classified as being *up*-type (with electric charge of $+^2/_3$) or *down*-type (with charge of $-^1/_3$). They all carry colour charge, so are considered 'red', 'green' or 'blue'. The three *up*-type quarks are called *up*, *charm* and *top*, with masses of $2.3^{+0.7}_{-0.5}$ MeV, 1.275 ± 0.025 GeV and $173.21 \pm 0.51(\text{stat}) \pm 0.71(\text{syst})$ GeV respectively. The three *down*-type quarks are called *down*, *strange* and *bottom*, and have masses $4.8^{+0.5}_{-0.3}$ MeV, 95 ± 5 MeV and 4.18 ± 0.03 GeV respectively. The left-handed quarks[2] are grouped as doublets of *up*- and *down*-type with I_3 equal to $\pm\frac{1}{2}$ respectively; the right-handed quarks remain as singlets with zero I_3. The first-generation quarks and their quantum numbers are therefore

$$Q_L = \begin{pmatrix} u \\ d' \end{pmatrix}_L \sim (3, 2, \frac{1}{3}), \quad u_R \sim (3, 1, \frac{4}{3}), \quad d_R \sim (3, 1, -\frac{2}{3}) \tag{2.2}$$

The second- and third-generation quarks have identical forms. Note that the *down*-type quarks in this representation are weak eigenstates rather than mass eigenstates, where the Cabibbo-Kobayashi-Maskawa (CKM) matrix parametrizes the rotation. Due to the confining nature of QCD interactions, quarks exist only in colour-singlet hadrons, as either a colour-anticolour pair (a *meson*) or as a red+blue+green quark triplet (a *baryon*).

The leptons are classified as either electrically charged or neutral. The charged leptons are the *electron* (e), the *muon* (μ), and the *tau* (τ), and have masses of $0.510998928 \pm 0.000000011$ MeV, $105.6583715 \pm 0.0000035$ MeV, and 1776.82 ± 0.16 MeV respectively. They have an electric charge of -1, and a corresponding anti-particle with positive charge. The neutral leptons are the *neutrinos* and there exists one corresponding to each charged lepton, known as the *electron neutrino* (ν_e), *muon neutrino* (ν_μ) and *tau neutrino* (ν_τ). In the SM the neutrinos are massless, however the observation of neutrino oscillations indicates that at least two do have mass, and so upper bounds on the mass are generally given instead. It is not yet clear whether neutrinos have distinct antiparticles.

The left-handed leptons are grouped as doublets of a neutrino and a charged

[2]The spinor representation ψ of a fermion can be decomposed into left- and right-handed components according to $\psi = \psi_L + \psi_R = P_L\psi + P_R\psi$, where $P_{L/R} = \frac{1}{2}(\mathbb{1} \mp \gamma^5)$ are the chirality projection operators and $\mathbb{1}$ is the 4×4 unitary matrix.

lepton, with $I_3 = \pm 1/2$ respectively. Right-handed charged leptons have $I_3 = 0$; right-handed neutrinos do not exist in the SM. The first-generation leptons and their quantum numbers are written below, the heavier generations take the same form.

$$E_L = \begin{pmatrix} \nu_e \\ e \end{pmatrix}_L \sim (1, 2, -1), \quad e_R \sim (1, 1, -2) \tag{2.3}$$

The 'normal' matter that we are familiar with (protons, neutrons and electrons) is constituted from the first generation of quarks and leptons, as the later, heavier generations will always decay to the lighter generations. Notably, the tau lepton is heavy enough to decay not just to lighter leptons, but also to hadrons.

Bosons

The bosons of the SM carry the known forces, and are all of integer spin; they are displayed on the right-hand side of fig. 2.1.

The photon γ is the mediator of the EM force, and couples to the fermions with non-zero electric charge, but carries no charge itself. It is spin-1, massless, and is its own antiparticle.

The $W^{\pm}$ and Z^0 bosons mediate the weak force and couple to all fermions, they are also spin-1 bosons. W^+ and W^- are a particle-antiparticle pair with electric charge ± 1, and $I_3 = \pm 1$, respectively. As a result, they can change fermion flavour (and generation, though this is relatively suppressed) through their absorption or emission. The W-boson mass is 80.385 ± 0.015 GeV. The Z^0 has a mass of 91.1876 ± 0.0021 GeV, and is its own antiparticle, carries no electric charge, and has $I_3 = 0$; it therefore couples via the weak force to all fermions (including the neutrinos) without altering their value of I_3.

The gluon is the mediator of the strong force and couples to fermions carrying colour charge. It also carries a $c - \bar{c}'$ charge (such as red-antigreen; there are eight such combinations), and thus can interact with itself through three-gluon and four-gluon vertices. The strong force is restricted to very short short-distance scales. The gluon is massless, spin-1, and electrically neutral.

The Higgs boson is the most recently discovered boson (announced by the ATLAS and CMS Collaborations in 2012) and is the first observed scalar (spin-0) boson. It is the boson of the Brout-Englert-Higgs mechanism, and transmits mass to the weak bosons via spontaneous EWSB. The fermion masses are generated by Yukawa couplings to the Higgs field. The Higgs boson carries no electric or colour charge, and has a mass of 125.7 ± 0.4 GeV.

2.1.2 Phenomena unexplained by the Standard Model

As extensive and comprehensive as the SM has proved itself to be, it does not yet explain all observed phenomena of the world around us. Some (but not all) of the most significant gaps are listed below.

- The confirmed observation of neutrino oscillations, in which neutrinos known to be of one flavour (say, a ν_μ) are later measured to be of a different flavour (say, a ν_τ), indicates that neutrino flavours are a superposition of mass eigenstates, which become out of phase as they propagate [49]. These eigenstates are related through the Pontecorvo-Maki-Nakagawa-Sakata (PMNS) matrix (analogous to the CKM matrix for quarks), and imply that at least two of the three known neutrinos must be massive. This is in stark contradiction to the SM, in which all neutrinos are massless.

- Inflation is expected to have erased any pre-existing matter-antimatter asymmetry, but today we observe an abundance of matter and almost no antimatter in our Universe. For this to have arisen, CP (*charge-parity*) violation is required to a degree that cannot be explained by the SM.

- While general relativity provides a unified description of gravity as a geometric property of spacetime, there is no quantum theory of gravity, and it is not yet known how to unify gravity with the three other fundamental forces into a single framework. Additionally, the question of why gravity is $\mathcal{O}(10^{32})$ times weaker than the weak force is unexplained by the SM. This is sometimes known as the *hierarchy problem* in particle physics, and can also be formulated as our lack of understanding for why the important scales of particle physics, namely the EW scale ($\sim$246 GeV), the scale where the weak and strong forces become equally strong ($\sim 10^{16}$ GeV), and where gravity joins them ($\sim 10^{19}$ GeV, also known as the Planck scale), span such an enormous range.

- Finally, the SM does not provide an adequate explanation for the bulk of matter that makes up our Universe, known as *dark matter* (DM). The only viable candidate, the neutrino, as an electrically neutral, weakly-interacting and massive particle, has been shown to provide only a small fraction of what is required by our current understanding of the distribution of DM in the Universe.[3] Baryonic matter, that described by the SM, is dominated by the mysterious DM, which is approximately five times more abundant.

[3] Additionally, SM neutrinos would be *hot* DM (moving at relativistic speeds), which we know to be inconsistent with cosmological observations which suggest that DM is *cold*.

Moreover, the energy-density of the Universe is dominated by dark energy ($\sim$70%), which is also completely unexplained by the SM.

It is clear that the SM, while an extremely comprehensive and well-described theory of the known particles and forces, does not fully describe our Universe, and so there is on-going work in many areas. The open question that is studied in later chapters is that of the nature of DM, and what we can discover or rule out of its properties through the use of high-energy collider physics.

First, however, we describe in the next section some of the experimental evidence for DM.

2.2 Evidence for Dark Matter

This section outlines some of the more compelling pieces of astrophysical evidence for the existence of DM, discusses the favoured possibility of a *weakly interacting massive particle*, and provides short summaries of the three main experimental methods we use to search for a DM candidate.

2.2.1 Astrophysical evidence for dark matter

Galaxy rotation curves The angular velocity of material orbiting a galaxy can be predicted by the amount of mass contained within. If the galaxy consists just of baryonic matter (that is, the visible stars and gas), the brightness of that galaxy would indicate its total mass, and therefore the angular velocity of an orbiting star could be predicted. However, the observed velocities for objects more than a few kpc[4] from the galactic centre are usually much greater than those predicted from just the visible, luminous matter, indicating the presence of an enormous halo of invisible, or 'dark', matter. An example of this is displayed in fig. 2.2 for the galaxy NGC 6503, showing the circular velocities of observed stars as a function of radius from the galactic centre; the contributions from the disk and gas are shown in dashed and dotted lines respectively, but an additional contribution from a DM halo, shown as the dot-dashed line, is required to match the observed data.

Gravitational lensing The presence of DM and its distribution in the Universe can be inferred by its effect on gravitational lensing, the observed bending of light from distant galaxies or clusters by mass which serves to distort the images of those sources. In particular, we can observe lensing effects where no baryonic matter is present, or stronger lensing than the visible matter would predict,

[4]One kpc is equal to 3.086×10^{19} metres.

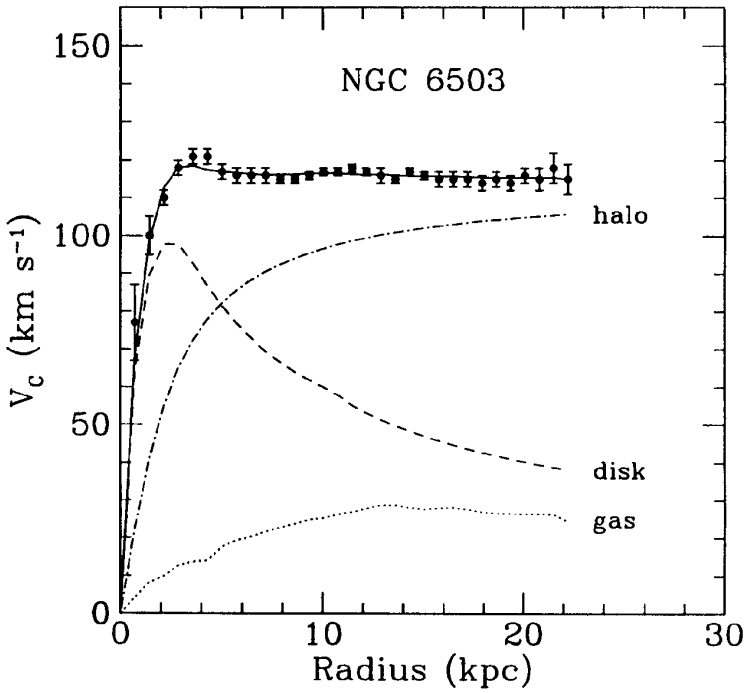

Figure 2.2: The rotational velocities of stars in galaxy NGC 6503, indicating the presence of a large DM halo. Taken from ref. [50].

leading us to conclude there must be present an additional amount of massive, invisible matter. Examples are displayed in fig. 2.3, showing the distorted images of far-away galaxies lensed by the Abell 2218 galaxy cluster (a), and the almost complete Einstein Ring formed by a distant blue galaxy strongly lensed by a closer galaxy LRD 3-757, a result of their alignment with respect to Earth (b). DM distributions can be partially mapped by studying their gravitational lensing effects; as a result of these efforts, DM is believed to extend out to 200 kpc from galaxy centres, considerably further than can be observed with rotation curves.

The Bullet Cluster The galaxy cluster 1E 0657-56, also known as the Bullet Cluster, was formed following the collision of two large galaxy clusters, and is shown in fig. 2.4. This image, from the Chandra X-ray observatory, shows the stellar matter in white/orange and the hot gas (which makes up the bulk of baryonic matter in the cluster) in pink; the overall mass distribution, obtained through analysis of gravitational lensing, is shown in blue. The centres of mass of the colliding galaxy clusters are clearly offset from the baryonic matter, indicating a large amount of invisible matter is present that is separate from the stellar or gaseous components. From this, the DM distributions are inferred.

The baryonic matter of the clusters was able to interact during the collision and slowed down as a result. On the other hand, the DM distributions are still reasonably spherical and appear to have passed right through each other, sug-

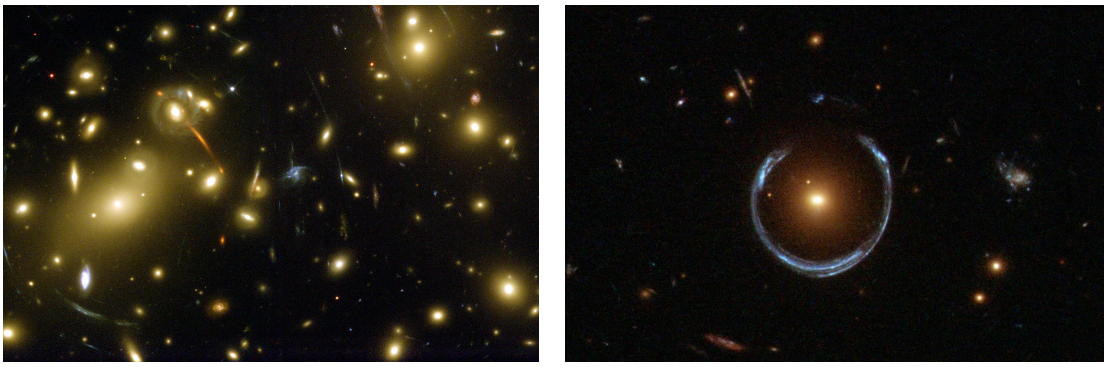

(a) (b)

Figure 2.3: (a) The galaxy cluster Abell 2218 acting as a gravitational lens for more distant galaxies, distorting and multiply-imaging them, as photographed by the Hubble Space Telescope in 1999. Image credit: NASA/ESA. (b) Luminous red galaxy LRD 3-757 strongly lensing a distant blue galaxy to create an almost complete Einstein Ring, as observed by the Hubble Space Telescope's Wide Field Camera 3. Image credit: ESA/Hubble.

gesting the DM doesn't interact significantly with either itself or baryonic matter, other than gravitationally. This is in contrast to what is predicted by theories of modified gravity that have been proposed as an alternative to DM, in which the apparent additional 'mass' in the galaxies would interact, rather than pass unimpeded. Observations of the Bullet Cluster are therefore considered as evidence not just the presence of DM, but of its particle nature.

Structure formation Large-scale simulations of gravitationally-interacting systems, known as N-body simulations, can be used to study the possible processes by which formation of structures occured in the Universe. These simulations tend to see agreement with observations only when DM is included in the modeling, providing further evidence for DM. In addition, whether or not the DM was relativistic at the time of structure formation (the point where the energy density of matter overtook that of radiation) greatly affects the way in which the formation proceeds in the simulation, as either a 'top-down' or 'bottom-up' process. The best agreement between simulation and observation of large-scale structures is obtained with non-relativistic DM (referred to as *Cold Dark Matter* (CDM)). This model, coupled with the assumption that the energy-density of our Universe is dominated by dark energy in the form of a cosmological constant Λ, gives the standard model of cosmology, known as the ΛCDM model.

Cosmic Microwave Background While previous examples demonstrate convincing evidence for the existence of DM, we need to look to the Cosmic Microwave Background (CMB) for precision information about its relative abundance. The CMB is thermal radiation from the early Universe, produced approx-

Figure 2.4: A composite image of the Bullet Cluster, from the Chandra X-ray observatory, showing the Hubble optical observation of the galaxies in white/orange, the X-ray observation of the hot gas in pink, and the dark matter distribution in blue as inferred by gravitational lens mapping. Image credit: NASA/CXC/SAO.

imately 380,000 years after the Big Bang, when electrons and protons combined to form hydrogen atoms and the Universe became electrically neutral (known as *recombination*). The photons were then able to propagate freely, carrying information about the state of matter at that time. The CMB, shown in fig. 2.7 as measured by the Planck collaboration in 2013, displays the spectrum of a black body with a temperature of ∼2.7255K, with deviations from local isotropy at a level of 10^{-4}K and globally at 10^{-5}K, matching the prediction of a thermal distribution resulting from quantum fluctuations before the period of inflation. The temperature fluctuations can be parameterised in terms of spherical harmonics,

$$\frac{\delta T}{T}(\theta,\phi) = \sum_{\ell=2}^{+\infty} \sum_{m=-\ell}^{\ell} a_{\ell m} Y_{\ell m}(\theta\phi) \tag{2.4}$$

where $Y_{\ell m}$ are the spherical harmonics for multipole moments ℓ. The power spectrum is written as a function of the complex harmonic coefficients [51]:

$$\mathcal{C}_\ell = \frac{1}{2\ell+1} \sum_{m=-\ell}^{\ell} \langle |a_{\ell m}|^2 \rangle \ . \tag{2.5}$$

The theory of inflation says that the fluctuations in temperature are Gaussian, meaning that the coefficients also have Gaussian distributions with a mean of zero and a variance given by $\mathcal{C}_\ell$. In this case, the power spectrum fully characterises the statistics of the CMB. A more meaningful quantity is the total power in multipole ℓ, given by $\ell(\ell+1)\mathcal{C}_\ell/2\pi$; this leads to the power spectrum plotted in fig. 2.6, showing the temperature fluctuations at different angular scales, with large scales on the left of the spectrum and small scales on the right. A cosmo-

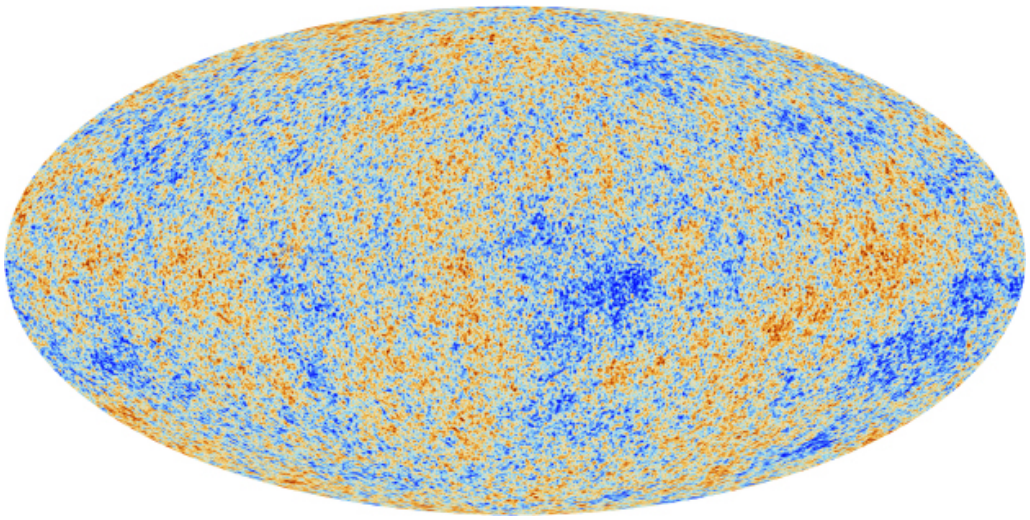

Figure 2.5: The anisotropies of the CMB, measured by the Planck satellite. Temperature variations from -300μK (blue) to 300μK (red) are shown. Taken from ref. [54].

logical theory (the ΛCDM model) incorporating both baryonic and dark matter, dark energy and the curvature of the Universe, can be fitted to the data to extract six parameters of that theory, including information about the DM density. That density, as quoted in ref. [52], is measured to be

$$\Omega_{\mathrm{DM}}h^2 = 0.1196 \pm 0.0031 \tag{2.6}$$

at 68% confidence level (where h is the dimensionless Hubble parameter, $h = H_0/100\mathrm{km}^{-1}$ s Mpc). This is consistent within uncertainties with the value previously measured by WMAP, of $\Omega_{\mathrm{DM}}h^2 = 0.1120 \pm 0.0056$ [53]. Following this measurement, the current best estimates for contributions to the energy-density of the Universe are 68.3% dark energy, 26.7% DM and only 4.9% baryonic matter.

2.2.2 Relic density calculations

We pause here to mention *relic density*, and relate this to the observed abundance of DM in the Universe. We start with the assumption that DM and SM particles can interact according to $\chi\overset{(-)}{\chi} \leftrightarrow f\bar{f}$ (where χ here represents the DM particle and f represents a SM fermion) with some interaction strength, and proceed as follows. In the early Universe, DM particles were in thermal equilibrium, that is, pair-annihilation of DM particles was balanced by pair-production processes from the ambient energy of the system, meaning that the DM abundance was approximately constant. As the Universe expanded and cooled, the thermal bath became unable to replace the annihilating DM particles. The strength of the interaction then determines how much further annihilation occured before the par-

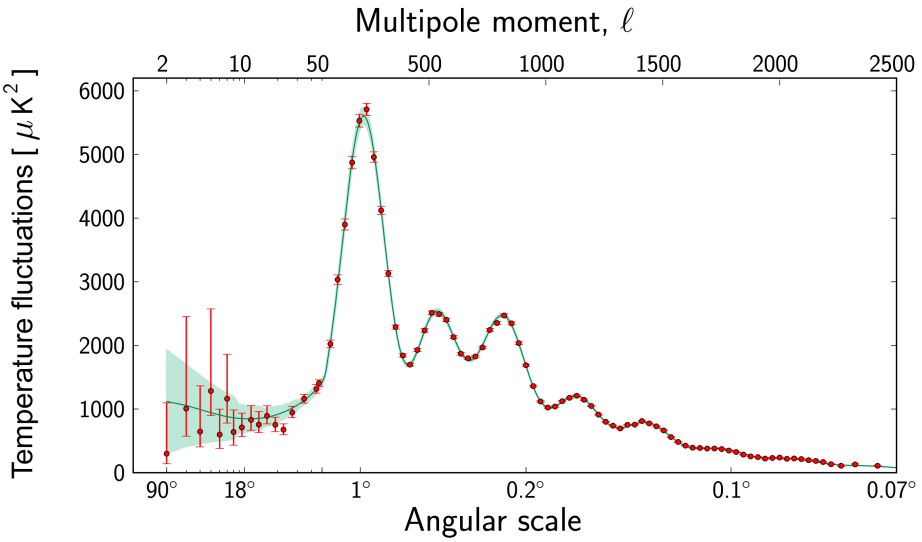

Figure 2.6: The power spectrum of the CMB, showing data measured by the Planck experiment (red) and the best-fit cosmological model (green), from which parameters including the DM density can be extracted. Taken from ref. [52, 54].

ticles could no longer interact, at which point the amount of DM was fixed. This remaining amount is known as the *relic density* or *relic abundance*, and the decoupling process is called *freeze-out*. Weaker interactions imply the freeze-out occured earlier, leading to a larger relic abundance. In the ΛCDM model of cosmology, the decoupling occured when DM was non-relativistic.

The relic density of some particle χ is given by [55]

$$\Omega_\chi h_0^2 \simeq \frac{1.07 \times 10^9 \text{GeV}^{-1}}{M_{\text{Pl}}} \cdot \frac{m_\chi}{T_F \sqrt{g_F^*}} \cdot \frac{1}{a + 3bT_F/m_\chi} \ , \tag{2.7}$$

where h_0 is the dimensionless Hubble parameter, M_{Pl} is the Planck mass, T_F is the freeze-out temperature, g_F^* is the number of relativistic degrees of freedom at freeze-out, and a and b are the first coefficients of the expansion in powers of v^2 of $\langle \sigma v \rangle$, the thermal average of annihilation cross section times particle velocity:

$$\langle \sigma v \rangle = a + b\langle v^2 \rangle + \mathcal{O}(\langle v^4 \rangle) \ . \tag{2.8}$$

It was demonstrated in ref. [56] that in the case of self-annihilating Majorana fermion DM with a mass >10 GeV, the density can be approximately fit with the function

$$\Omega_\chi h_0^2 = \frac{2.0 + 0.3 \log_{10}(10^{27} \langle \sigma \nu \rangle)}{10^{27} \langle \sigma \nu \rangle} \ , \tag{2.9}$$

leading to the following requirement for any model with Majorana fermion DM

that is desired to produce the correct relic abundance, and taking $\Omega_{\rm DM}h^2 \sim 0.11$:

$$\langle\sigma\nu\rangle \simeq 2.2 \times 10^{-26}\text{cm}^3\text{s}^{-1} \ . \tag{2.10}$$

For Dirac fermion DM, half the relic abundance of χ is replaced by $\bar{\chi}$, and so $\langle\sigma\nu\rangle$ is doubled. Note that for masses below 10 GeV there is a strong dependence of $\langle\sigma\nu\rangle$ on mass, reaching a maximum (in the Majorana case) of 5.2×10^{-26} cm^{3}s^{-1}.

This approximation becomes particularly significant in the next section, where we discuss one of the more popular types of DM particle.

2.3 The Weakly Interacting Massive Particle

In general, a candidate for DM should satisfy:

- stability on cosomological time scales (to ensure it hasn't decayed away by the present day),
- mass and abundance parameters (to give the observed relic density, see sec. 2.2.1),
- no EM interactions,
- no strong interactions, and
- weak interactions, if they exist, should be small.

Historically, the neutrino was the only SM candidate, however it is classed as *hot* dark matter (it would have been relativistic during structure formation), and has been shown to be able to contribute only a very small amount to the observed relic density. A more interesting candidate is a sterile neutrino, such as the right-handed neutrino, that has some small mixing with the SM neutrino, and has been proposed as a possible explanation for the flux of 3.5 keV X-rays observed in galaxy clusters (see refs. [57–62] and others). The Search for Hidden Particles (SHiP) experiment to search for sterile neutrinos of mass $<$2 GeV with the Super Proton Synchrotron (SPS) at CERN has recently been approved [63].

The axion, originally proposed as a solution to the strong CP problem, is a third candidate with a mass restricted to below 0.01 eV (see for e.g. ref. [64] for a review). This may be detected through its conversion to a photon in a strong magnetic field; constraints on the axio-photon coupling have been derived with Axion Dark Matter eXperiment (ADMX), CERN Axion Solar Telescope (CAST) and other experiments [65–68].

If we make the assumption that a DM candidate can interact with the SM through the weak force, several experimental strategies to search for such a candidate then open up. A DM particle of this type is known as a *Weakly Interacting Massive Particle* (WIMP), and is the candidate of interest to us for the remainder of this thesis. The assumption of some kind of interaction between the dark and SM sectors is not completely unfounded; the relative amounts of baryonic matter and DM are surprisingly similar in our Universe (DM is approximately 5 times more abundant), which would be very unlikely if the two types of matter were produced entirely independently, whereas a weak interaction could allow some kind of common production mechanism.

WIMP candidates tend to have masses around the weak scale ($\mathcal{O}$(GeV) to $\mathcal{O}$(TeV)), and cross sections at the EW scale. It can be shown that freeze-out for such a candidate occurs at $T_F \sim m_\chi/20$, meaning the WIMP is non-relativisitic at this time, consistent with the ΛCDM model of cosmology. In addition, the calculated relic density of a WIMP, via eq. 2.9, naturally matches the observed relic density—a phenomenon referred to as the *WIMP miracle*. This is considered as further motivation for allowing DM to interact weakly in our models.

2.3.1 Searching for WIMPs

Popular Beyond the Standard Model (BSM) theories already produce one or more WIMP-like DM candidates, such as the Lightest Supersymmetric Particle (LSP) in Supersymmetry (SUSY) (often the neutralino), or the Lightest Kaluza-Klein Particle (LKP) in models of extra dimensions. These BSM theories are generally fully-realised and complete, addressing not just the problem of DM but many of the other open questions in fundamental physics, some of which are listed in sec. 2.1.2 earlier. They have many new particles and a rich phenomenology, but also many free parameters, making it unfeasible to comprehensively search all of the possible available phase space. Nonetheless, searches for SUSY comprise a significant portion of the BSM searches in the ATLAS and CMS collaborations (see refs. [69–75] for example).

An alternative to these *top-down* models is to build instead from the bottom up, by adding just one or two new particles or interactions to build a minimal extension to the SM, with the aim of addressing only the DM question. We establish the generic properties common to a range of minimal models, and attempt to search for new physics within this structure. Such an approach is not usually intended to stand alone, but instead is considered a *toy model*; it is anticipated that a more comprehensive BSM model will include the physics of this toy model, and that such new physics is able to be studied in isolation from the other phe-

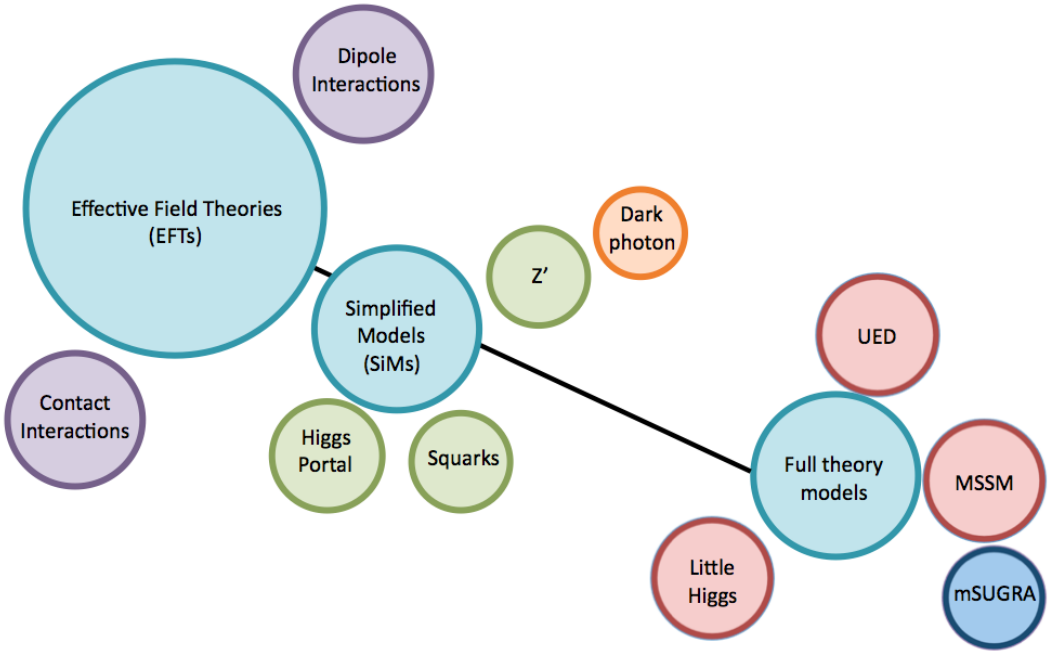

Figure 2.7: Some models of new physics with a DM candidate. Adapted from T. Tait, Lepton Photon 2013 [76].

nomenology of the broader model. In such a way, the observations and limits one can study and obtain with the toy model would be transferrable either directly, or with minor, easily understood variations, to the more comprehensive model.

Fig. 2.7, adapted from T. Tait, attempts to demonstrate the two opposite approaches. Minimally-extended models are in the top left corner (an Effective Field Theory (EFT), to be discussed in chapter 3, adds a single DM particle and a new-physics scale to the SM), and comprehensive BSM models such as the Minimal Supersymmetric Simplified Model (MSSM) are in the lower right corner. Toy models with increasing degrees of complexity are shown in between. Simplified models, which add a second additional particle to the SM, will be discussed in much more detail in the next chapter.

Simple interactions between a WIMP and the SM sector can proceed in three complementary ways, shown in fig. 2.8. Explicitly this figure shows an EFT coupling, however the central interaction can also be interpreted as encompassing all possible resolved interactions. The three processes are DM annihilation (left to right), scattering off a SM particle (bottom to top), and DM pair-production (right to left). These lead to three independent classes of experiments: indirect detection (looking for SM products of the DM annihilation), direct detection (looking for the recoil of a nucleus), and collider production (where the presence of dark matter can be inferred from missing energy). Ideally, constraints from one process can be translated into constraints on the other two. The three classes of experi-

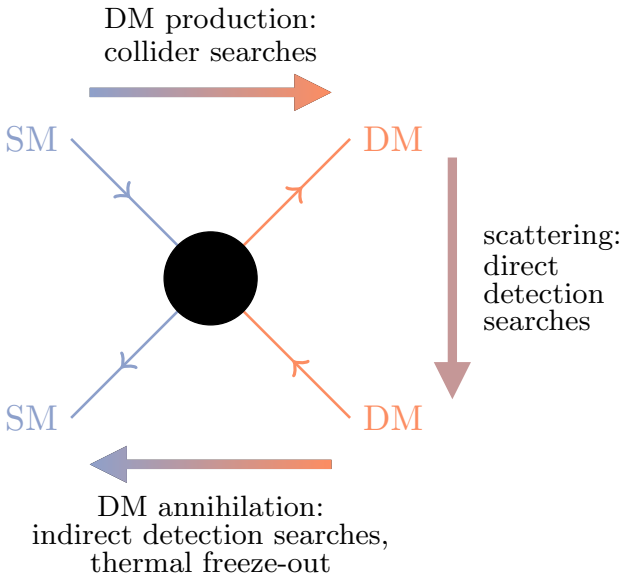

Figure 2.8: Three independent classes of experiment that look for the same underlying interaction in three possible processes. Based on ref. [77].

ment are discussed in further detail below.

2.3.2 Experimental approaches

Direct detection

If DM and SM fermions can interact, $\chi f \to \chi f$ scattering processes are expected to occur, which we constrain (given some further assumptions) by searching for small nuclear recoils within a large-volume detector. These interactions are commonly treated in the EFT regime (that is, as an effective 4-Fermi interaction), as the energy transfer involved for WIMP masses at the GeV scale is generally within an order of magnitude of 10 keV; for the underlying physics to be important, it would need to be at a scale smaller than this. Once standard assumptions are made about the expected WIMP flux (such as the DM local density, the circular velocity and the escape velocity [78]), the calculated scattering rate depends main on just the WIMP mass and the scattering cross section with nucleons. The interactions can be separated into two classes: spin-dependent and spin-independent. Spin-dependent interactions get their name because the DM couples to the nucleon spin, J, and so only valence nucleons will contribute to the scattering. An example is the axial-vector coupling to quarks, which in an EFT context (described further in chapter 3) is written as

$$\mathcal{L}_{\text{int}} = \frac{1}{\Lambda}(\bar{\chi}\gamma_5\gamma^\mu\chi)(\bar{q}\gamma_5\gamma_\mu q) \ , \tag{2.11}$$

where Λ is the scale at which the EFT breaks down. The differential DM-nucleus cross section is then

$$\frac{d\sigma}{d|\vec{q}|^2} = \frac{8G_F^2}{(2J+1)v^2} S(|\vec{q}|, \Delta q^{(p)}, \Delta q^{(n)}) \ , \tag{2.12}$$

where J is nuclear spin, v is the DM velocity, the $\Delta q^{(p/n)}$ are experimentally-determined constants relating to couplings to protons and neutrons, S is a nuclear-dependent form factor and G_F is the Fermi coupling constant. Fig. 2.9(a) shows an upper limit on the spin-dependent WIMP-proton scattering cross section, assuming that WIMPs couple only to protons. An equivalent plot exists for the WIMP-neutron cross section, but is not shown here.

Since only the valence nucleons are relevant to these interactions, there is no significant experimental gain from using a heavier target marterial. This is in contrast to the second class of spin-independent scattering, which can arise from scalar, vector and tensor EFT operators. We use the scalar interaction as an example, where the interaction Lagrangian and differential scattering cross section are

$$\mathcal{L}_{\text{int}} = \frac{1}{\Lambda}(\bar{\chi}\chi)(\bar{q}q) \ , \tag{2.13}$$

and

$$\frac{d\sigma}{d|\vec{q}|^2} = \frac{G_F^2}{v^2} C_{scal} F(E_r)^2 \tag{2.14}$$

respectively. $F(E_r)$ is a nuclear form factor and C_{scal} is a constant given by

$$C_{scal} = \frac{1}{\pi G_F^2}[Z f_p + (A-Z) f_n]^2 \ . \tag{2.15}$$

Here Z is the atomic number, A is the mass number and $f_{p/n}$ are the effective couplings to protons and neutrons. In this case, there are coherent contributions from all nucleons, giving a clear dependence on nuclear mass. The upper limits on the spin-independent scattering cross section are shown in fig. 2.9(b), taken from ref. [79] and adapted from ref. [80]. Interestingly, there have been on-going claims of a signal in the region $m_\chi < 100$ GeV by the DAMA/LIBRA [81], CoGeNT [82], CRESST-II [83] and CDMS-II [84] experiments. This is in conflict with exclusion limits from the XENON100 [85], LUX [86] and SuperCDMS [87] experiments, and is yet to be resolved.

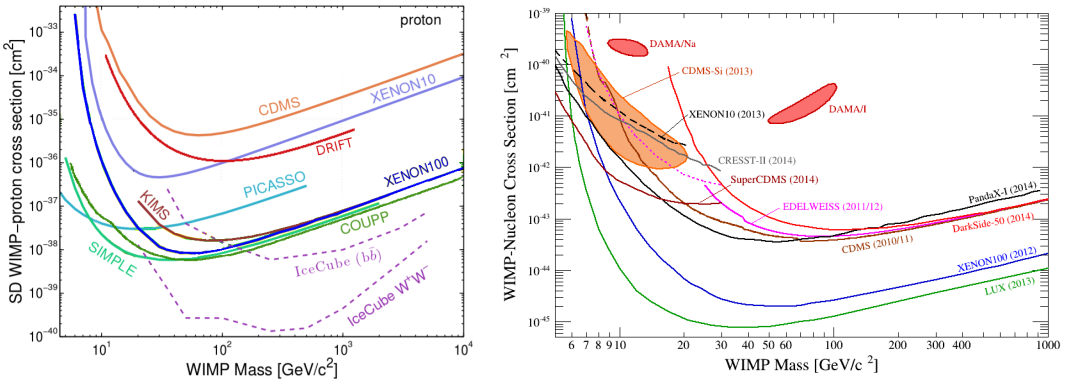

(a) (b)

Figure 2.9: Upper limits on spin-dependent (left) and spin-independent (right) scattering cross sections of DM and nucleons, from direct detection experiments. Note the additional limits from the IceCube neutrino detector, based on indirect detection observations. Taken from ref. [79] (fig. (b) adapted from ref. [80]).

Indirect detection

As described above, indirect detection searches are based on the idea that DM may be able to annihilate to SM particles, such as photons (gamma-rays), neutrinos or positrons (to name but a few). These resultant particles could then be observed, either here on Earth (at the IceCube neutrino detector in Antarctica [88], Super-Kamiokande [89] in Japan, or the Fermi-LAT gamma-ray observatory in orbit [90], for example) or in space (perhaps by the Alpha Magnetic Spectrometer (AMS) on the International Space Station [91]). Pair-annihilation would be more likely where there is a higher density of DM, which occurs when the DM clump together gravitationally, in the centre of our galaxy, in other galaxy clusters, or even in our own Sun or in the Earth. Observations are enormously complicated by the fact that there are many varied astrophysical backgrounds, some of which we understand and can model well, but many of which we do not. However, some signatures are particularly indicative of DM annihilation; one of these *smoking gun* signatures is the observation of a mono-energetic line in the photon spectrum in a certain direction in the sky, expected to arise from the annihilation process $\chi\bar{\chi} \rightarrow \gamma\gamma$. The non-observation of such predicted signatures would of course lead to constraints on models of DM, such as those shown in fig. 2.10, from the Fermi-LAT analysis of 25 dwarf spheroidal galaxies [92], depicting upper limits on the WIMP annihilation cross section assuming different SM final states. A similar logic can also constrain alternative models of unstable or meta-stable DM, that decay partially or in full to SM final states. Interestingly, as the DM is expected to accumulate in locations like the Sun through interactions with normal matter within the Sun as it passes through the DM halo, thus

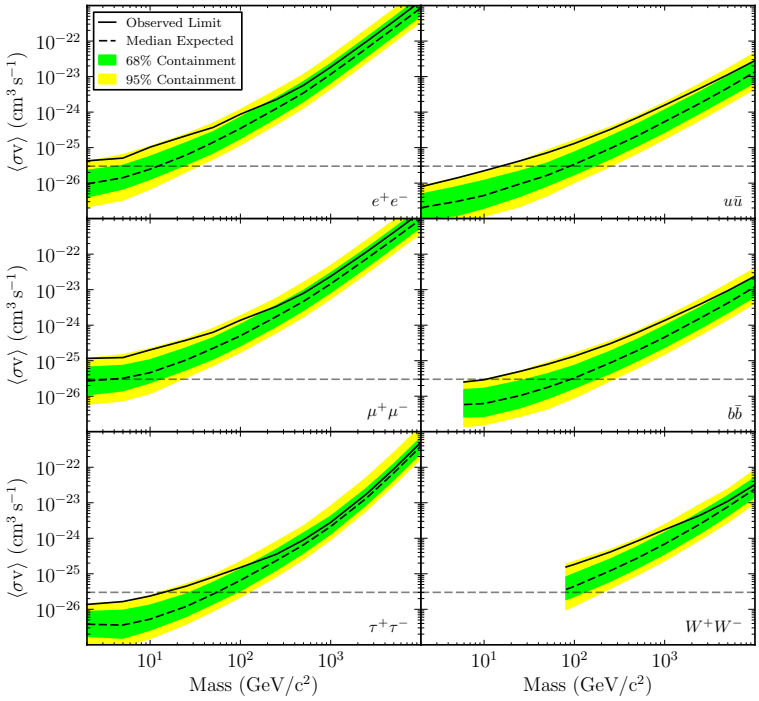

Figure 2.10: 95% C.L. upper limits on the WIMP annihilation cross section, assuming annihilation to different final states. Take. from Fermi-LAT, ref. [92].

losing energy and becoming trapped in the gravitational well, indirect detection limits can also be converted into limits on the DM-SM scattering cross section. An example of such limits from the IceCube neutrino detector are also included in fig. 2.9(a). A few intriguing hints have been observed in recent years, such as the excess in γ-rays at 1–10 GeV energies coming from the galactic centre and observed by Fermi-LAT (see refs. [93–99] for example), speculated to be the possible result of DM self-annihilating to a mixture of $b\bar{b}$ and $\ell^+\ell^-$ final states, but which may still be explained by astrophysical sources [100–103].

Collider searches

The pair-annihilation process described earlier can be reversed to represent the conversion of colliding SM particles, such as two quarks within colliding protons, into a pair of DM particles. However, these resulting particles would escape any apparatus designed to detect the products of such collisions, due to their extremely-weakly interacting nature. Hence, the $q\bar{q} \rightarrow \chi\bar{\chi}$ process is basically unobservable, unless there is at least one additional visible particle in the final state. Then, assuming the geometry of the collision is known, and following the law of conservation of momentum, the presence of DM can be inferred from the missing energy of the collision. (Of course, neutrinos are also generally invisible to detectors, and these purely SM processes comprise a significant back-

ground to the DM-production process.) This idea forms the basis of the several mono-X searches at the Large Hadron Collider (LHC), and is the focus of later chapters.

The next chapter delves further into the models of DM that we consider in detail in this thesis.

Chapter 3

Contact operators and simplified models

As has been noted, there are a plethora of possibilities for dark matter (DM) and its interactions with the Standard Model (SM). To be able to make a meaningful statement about DM, an analysis needs to choose a particular model, or class of models with similar behaviour, and be able to constrain that model. Several different models of DM will be considered in the searches discussed in this thesis, and these are introduced and discussed in this chapter.

Each model contains a DM particle which is assumed to be a Weakly Interacting Massive Particle (WIMP), as introduced in sec. 2.3.1. So as to narrow the scope of this work, the particle is chosen to be a fermion (most commonly a Dirac fermion), and is denoted χ.

This chapter will proceed as follows. Section 3.1 will describe the Effective Field Theory (EFT) class of DM models, as well as the associated problems with their implementation at high-energy colliders such as the Large Hadron Collider (LHC). Section 3.2 will introduce an alternative type of EFT in which the DM couples directly to a SM boson, and section 3.3 will describe the class of simplified models that are the focus of much of this thesis.

3.1 Contact operators for $f\bar{f}\chi\bar{\chi}$ interactions

This section reviews the use of EFT operators to build a minimal model of DM coupled to SM fermions; such models are studied and have limits placed upon them by the ATLAS analyses descibed in later chapters. The simplest EFT model of $f\bar{f}\chi\bar{\chi}$ interactions is determined by just the DM particle type (whether it is a scalar, or a fermion, and so on), its mass, and the nature (scalar, vector, etc) and scale of the underlying interaction—all other physics is assumed to be hidden at

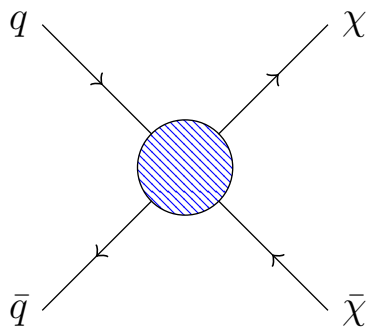

Figure 3.1: An EFT, or contact operator, that couples quarks to DM particles where the underlying interaction is assumed to be inaccessible at collider energies.

higher, inaccessible, energies. An example is depicted in fig. 3.1, it shows a pair of quarks coupled to a pair of DM particles, with a hidden underlying interaction.

This approach to EFT models is explored in detail in ref. [10], and a comprehensive list of operators can be found there. Originally, predominantly theorists were analysing these models using model-independent results from the collider experiments [10, 104–107]; the experimentalists have since begun constraining these models as well (see refs. [108–110] for some early examples).

The following subsections describe the EFT models relevant to the analyses included in this thesis, the issues of validity that have arisen in recent years, and the current iteration technique used by some analyses to recover a valid result.

3.1.1 Free parameters

The simple EFT model is based on some assumptions [10]:

- that the DM particle is the only new particle accessible at the relevant energy scale (here, this is the collider energy scale), and any other new particles are far too heavy to be produced on-shell in an interaction, so that the interaction can be treated as a contact interaction,
- that the DM particle is a singlet under the SM, therefore there can be no tree-level couplings to SM bosons, and
- that the DM is odd under some Z_2 symmetry, so it must be produced in pairs; this is also desirable since if a single DM particle could couple to the SM, it could then plausibly decay and would no longer be stable.

While not one of the original assumptions made in ref. [10], as noted in the introduction to this chapter we shall only consider the case of Dirac fermion DM.

Name	Operator
D1	$\frac{m_q}{\Lambda^3}\bar{\chi}\chi\bar{q}q$
D2	$\frac{im_q}{\Lambda^3}\bar{\chi}\gamma^5\chi\bar{q}q$
D3	$\frac{im_q}{\Lambda^3}\bar{\chi}\chi\bar{q}\gamma^5q$
D4	$\frac{m_q}{\Lambda^3}\bar{\chi}\gamma^5\chi\bar{q}\gamma^5q$
D5	$\frac{1}{\Lambda^2}\bar{\chi}\gamma^\mu\chi\bar{q}\gamma_\mu q$
D6	$\frac{1}{\Lambda^2}\bar{\chi}\gamma^\mu\gamma^5\chi\bar{q}\gamma_\mu q$
D7	$\frac{1}{\Lambda^2}\bar{\chi}\gamma^\mu\chi\bar{q}\gamma_\mu\gamma^5q$
D8	$\frac{1}{\Lambda^2}\bar{\chi}\gamma^\mu\gamma^5\chi\bar{q}\gamma_\mu\gamma^5q$

Name	Operator
D9	$\frac{1}{\Lambda^2}\bar{\chi}\sigma^{\mu\nu}\chi\bar{q}\sigma_{\mu\nu}q$
D10	$\frac{i}{\Lambda^2}\epsilon^{\alpha\beta}_{\mu\nu}\bar{\chi}\sigma^{\mu\nu}\chi\bar{q}\sigma_{\alpha\beta}q$
D11	$\frac{\alpha_s}{4\Lambda^4}\bar{\chi}\chi G_{\mu\nu}G^{\mu\nu}$
D12	$\frac{i\alpha_s}{4\Lambda^4}\bar{\chi}\gamma^5\chi G_{\mu\nu}G^{\mu\nu}$
D13	$\frac{i\alpha_s}{4\Lambda^4}\bar{\chi}\chi G_{\mu\nu}\tilde{G}^{\mu\nu}$
D14	$\frac{\alpha_s}{4\Lambda^4}\bar{\chi}\gamma^5\chi G_{\mu\nu}\tilde{G}^{\mu\nu}$

Table 3.1: The set of EFT operators coupling a DM bilinear to the SM. Based on [10].

The lowest dimensional operator coupling DM to the SM actually couples to the Higgs bilinear $|H|^2$, and induces a $\chi-\chi-h^0$ interaction following electroweak symmetry breaking (EWSB). While this is studied in refs. [111–113], it is not considered further here.

The next simplest set of operators couple a fermion bilinear of the form $f\Gamma\bar{f}$, where $\Gamma \in \{1, \gamma^5, \gamma^\mu, \gamma^\mu\gamma^5, \sigma^{\mu\nu}\}$, to a DM bilinear $\chi\Gamma'\bar{\chi}$. Both quarks and leptons are valid alternatives, however the lepton case is less relevant to the pp collider physics of interest here. These are listed in the first ten rows of table 3.1; also shown are the operators coupling to a pair of colour field strengths $G_{\mu\nu}G^{\mu\nu}$, included for completeness but not a focus of this thesis.

In the case of Majorana DM, the vector and tensor bilinears vanish (see ref. [114] for the equivalent list of operators); the remaining operators are directly related to the Dirac cases for the purposes of study at a collider, as there is no kinematic variation and the cross section simply undergoes a rescaling. If, instead, DM is a scalar particle (either real or complex), an equivalent list to table 3.1 is also found in ref. [10]. Such models have been studied elsewhere (see ref. [115] for a recent example) and will not be discussed further here.

It is possible to group the 14 Dirac EFT operators listed in table 3.1 further in the context of mono-X collider searches, as demonstrated by fig. 3.2, taken from ref. [116], showing the $E_{\mathrm{T}}^{\mathrm{miss}}$ and leading jet p_{T} of mono-jet events for each of the operators and a single DM mass. The first four operators demonstrate similar kinematic behaviours after cross section normalisation, as do the next four, and so on.[1] Note that this is not true generally, and in fact certain variables, such

[1]Ref. [117] points out that the jet p_{T} spectra for the D5 and D8 operators are the same within uncertainties at next-to-leading-order (NLO) + parton-shower level.

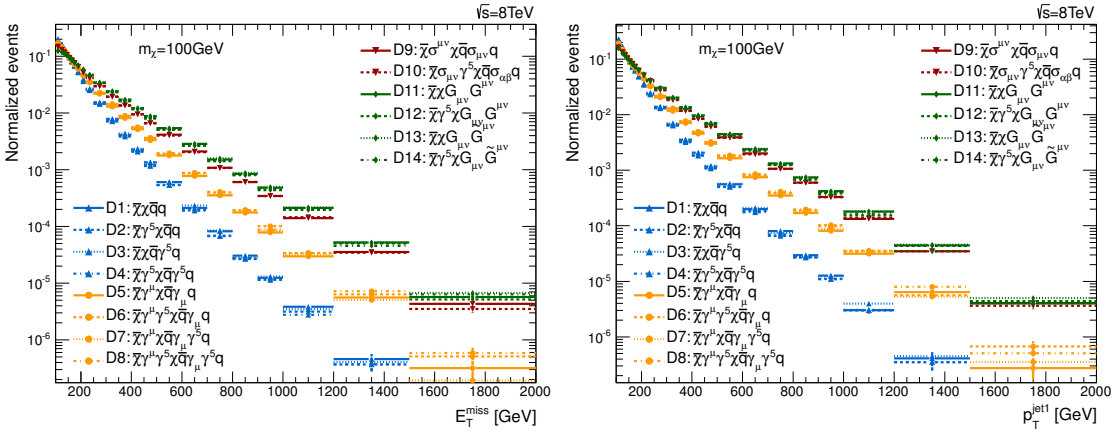

Figure 3.2: Kinematic distributions of the 14 EFT operators in a mono-jet study. Taken from ref. [116].

as the azimuthal angle difference in $2j$+$E_{\mathrm{T}}^{\mathrm{miss}}$ events, may be used to determine the underlying structure of the interaction (see, for e.g., ref. [117]). However, for the mono-X analyses discussed in this thesis, it is generally assumed that a set of representative operators can be chosen, where the remaining operators demonstrate the same kinematic behaviour and are related simply by a scaling of the cross section. The representative set of operators commonly chosen are the D1, D5, D9 and D11 operators. Thus, the first degree of freedom of an EFT mode studied in the mono-X collider context is the choice between these four operators.

The second degree of freedom is the mass of the DM particle. In the context of a collider search, we want this to be light enough such that it can be pair-produced—at the LHC, this means not more than $\mathcal{O}$(TeV). Below this mass, for a given choice of operator, the mass of the DM, m_χ, is the main determinant of the kinematics of the interaction. It can also be shown that for $m_\chi \lesssim \mathcal{O}(1$ GeV), the DM particle is effectively massless relative to the scale of the interaction and so the kinematic behaviour ceases to vary as the mass decreases (while, of course, the cross section continues to change). As a result, collider searches can be sensitive down to masses one or two orders of magnitude lower, that is, down to the MeV scale.[2] This leads us to one of the advantages of collider searches over direct detection experiments—while the latter become considerably less sensitive to masses $\lesssim$ 1–10 GeV (see the sharp upturn in the curves in fig. 2.9) due to the smaller momentum transfer, collider searches don't vary much in sensitivity in

[2]DM masses below this range stop being classed as a WIMP, marking a very loosely-defined cut-off for WIMP seaches. Collider searches also lose sensitivity for low mass DM, as large low-momentum backgrounds dominate and a smaller amount of $E_{\mathrm{T}}^{\mathrm{miss}}$ is less useful as a handle to select interesting events. However, see ref. [118] for an example of using lower energy colliders to probe low-mass WIMP DM.

this mass range.

The final degree of freedom in the EFT model is the suppression scale, denoted Λ. Because this is just a scaling of the cross section, it doesn't change the kinematic behaviour of the model, and therefore a scan over this parameter is not generally necessary. Instead, common practice in an analysis is to constrain this parameter as a function of the DM mass and operator type. In the simple case where the underlying physics 'hidden' by the contact interaction is the s-channel exchange of a heavy mediating particle (explored further in sec. 3.3 on simplified models), where that mediator has a mass of M_{med} and couples to quarks and the DM pair with strengths of g_q and g_χ respectively, the suppression scale can be directly related to these parameters according to $\Lambda \equiv M_{\text{med}}/\sqrt{g_q g_\chi}$.

Use in collider mono-X studies

As described in chapter 1, the search method at a collider that is the focus of this thesis is based on a mono-X + $E_{\text{T}}^{\text{miss}}$ topology, where the invisible DM particles are balanced against some visible object X in the transverse plane. Since the underlying physics of the contact interaction is too heavy to appear at collider energies, processes where the visible object is produced through this hidden physics are greatly suppressed, and we only need consider emission of the visible object from one of the initial state partons, as once the DM particles are produced they are assumed to be stable.

Fig. 3.3 shows the tree-level Feynman diagrams of the relevant processes. The upper diagram shows emission of a SM gauge boson; the photon can be detected while the electroweak (EW) bosons decay either hadronically or leptonically, leading to different final states, and the gluon produces a jet[3] visible in the detector. The lower diagrams indicate processes which are only relevant to the mono-jet search channel, where one of the incoming partons is a gluon.

These mono-X + $E_{\text{T}}^{\text{miss}}$ topologies will be discussed in further detail in later chapters.

Relation to direct and indirect detection

As noted previously, EFT models of DM are useful for comparing limits directly across experimental search channels; see the discussion in sec. 2.3.1 and fig. 2.8. The relevant expressions for converting a collider limit on the suppression scale to an equivalent limit on the DM-nucleon scattering cross section (studied in direct detection experiments) are taken from refs. [10, 109]:

[3]The details of a hadronic jet within a detector will be discussed in greater detail in chapter 4.

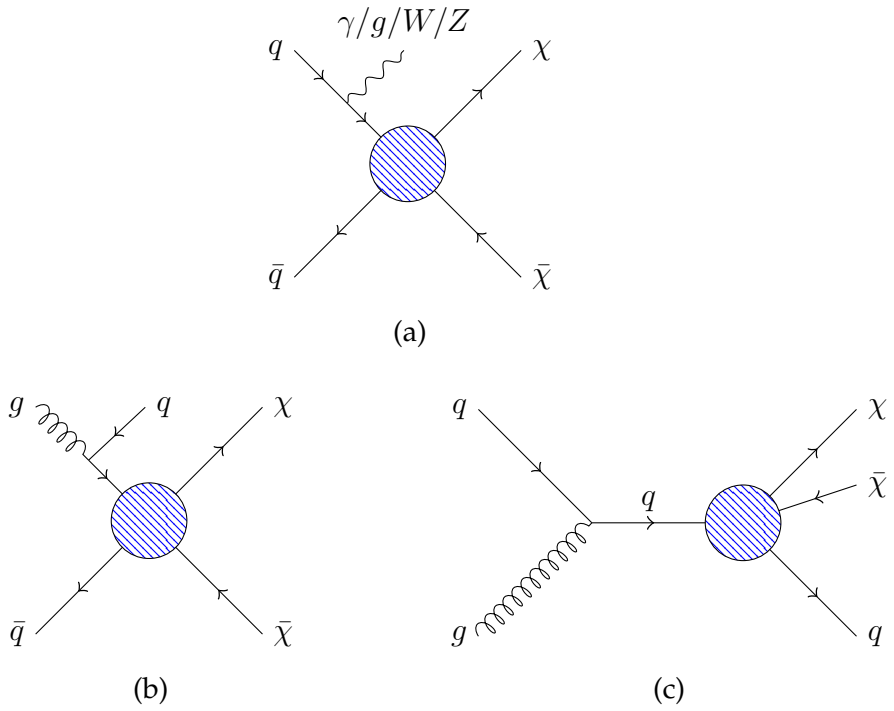

Figure 3.3: The possible tree-level processes producing a mono-X + $E_{\mathrm{T}}^{\mathrm{miss}}$ topology at a hadron collider. Diagrams (b) and (c) are only relevant for the mono-jet channel.

$$\begin{aligned}
\sigma_{\chi N}^{D1} &= 1.60 \times 10^{-37}\mathrm{cm}^2 \left(\frac{\mu_\chi}{1\mathrm{GeV}}\right)^2 \left(\frac{20\mathrm{GeV}}{\Lambda}\right)^6 \\
\sigma_{\chi N}^{D5} &= 1.38 \times 10^{-37}\mathrm{cm}^2 \left(\frac{\mu_\chi}{1\mathrm{GeV}}\right)^2 \left(\frac{300\mathrm{GeV}}{\Lambda}\right)^4 \\
\sigma_{\chi N}^{D8,D9} &= 4.7 \times 10^{-39}\mathrm{cm}^2 \left(\frac{\mu_\chi}{1\mathrm{GeV}}\right)^2 \left(\frac{300\mathrm{GeV}}{\Lambda}\right)^4 \\
\sigma_{\chi N}^{D11} &= 3.83 \times 10^{-41}\mathrm{cm}^2 \left(\frac{\mu_\chi}{1\mathrm{GeV}}\right)^2 \left(\frac{100\mathrm{GeV}}{\Lambda}\right)^6
\end{aligned} \tag{3.1}$$

where μ_χ is the reduced mass of the DM-nucleon system. Here, D1, D5 and D9 are spin-independent operators in the language of direct detection, while D8 and D9 are spin-dependent.

Similarly, we can convert suppression scale limits to limits on the $\chi\bar{\chi}$ annihilation cross section that is relevant to indirect detection experiments [105]:

$$\begin{aligned}
\sigma_{D5} v_{\mathrm{rel}} &= \frac{1}{16\pi\Lambda^4} \sum_q \sqrt{1-\frac{m_q^2}{m_\chi^2}} \left(24(2m_\chi^2+m_q^2) + \frac{8m_\chi^4 - 4m_\chi^2 m_q^2 + 5m_q^4}{m_\chi^2 - m_q^2} v_{\mathrm{rel}}^2\right) \\
\sigma_{D8} v_{\mathrm{rel}} &= \frac{1}{16\pi\Lambda^4} \sum_q \sqrt{1-\frac{m_q^2}{m_\chi^2}} \left(24m_q^2 + \frac{8m_\chi^4 - 22m_\chi^2 m_q^2 + 17m_q^4}{m_\chi^2 - m_q^2} v_{\mathrm{rel}}^2\right)
\end{aligned} \tag{3.2}$$

where v_{rel} is the relative velocity of the annihilating WIMPs.

3.1.2 Question of validity

The validity of EFT use in collider studies has recently been subject to considerable scrutiny. This is because, while the required assumption of small momentum transfer (such that any underlying physics is far out of the realm of accessibility) is reasonable in direct detection experiments, the much larger momentum transfers now being obtained at the LHC mean it is necessary to test whether that assumption also holds true in such circumstances. In particular, the reporting of a limit on the suppression scale Λ that is well *below* the transferred momentum of some portion of LHC events (even if the scale used to generate events for the studied model is large) has been called into question. This question was the focus of refs. [14, 119, 120], and we follow below a quantitative example taken from ref. [119] to demonstrate the problem and one solution proposed therein.

To proceed, a choice needs to be made about the underlying model, since whether or not there is a problem can depend on such hidden physics. Unfortunately, this of course negates the use of an EFT in the first place, however it is necessary to demonstrate the dangers of the EFT approach which—if used unthinkingly—can lead to invalid limits when reinterpreted in the context of a more complex model where the underlying physics is now accessible. (Sec. 3.3.4 will discuss this in further detail.) In this example, the interaction is assumed to proceed through the s-channel, via a mediator of mass M_{med}, with couplings to quarks and DM of g_q and g_χ respectively. Matching of the high-energy and low-energy models implies that

$$\Lambda = \frac{M_{\text{med}}}{\sqrt{g_q g_\chi}} \ . \tag{3.3}$$

The low-energy treatment is valid provided that the transferred momentum, Q_{tr}, is less than M_{med}, leading to

$$\Lambda > \frac{Q_{\text{tr}}}{\sqrt{g_q g_\chi}} \ . \tag{3.4}$$

Commonly it is assumed that the couplings g_q and g_χ will have a strength of $\mathcal{O}(1)$, however a hard upper limit of g_q, $g_\chi < 4\pi$ exists due to the requirement that the theory remain perturbative. These two possible cases give the following requirement for Q_{tr}:

$$Q_{\text{tr}} \lesssim \begin{cases} \Lambda & (g_q, g_\chi \sim 1) \\ 4\pi\Lambda & (g_q, g_\chi \sim 4\pi) \end{cases} \tag{3.5}$$

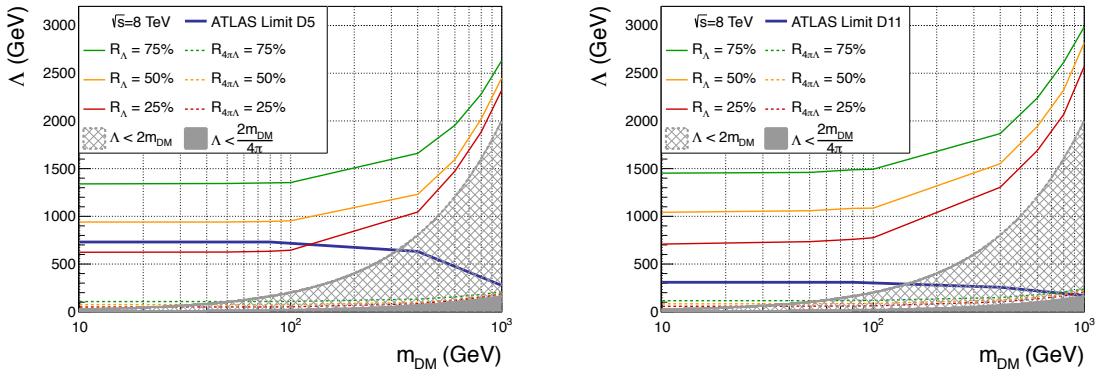

Figure 3.4: The lower limit from the 8 TeV mono-jet analysis on the EFT suppression scale Λ for the D5 operator (left) and D11 operator (right), shown in blue, and compared with lines of constant R_Λ^{tot}, defined in eq. 3.6. Taken from ref. [119].

The work of ref. [119] tests this criterion on an event-by-event basis to see how many events used in a toy analysis (which approximates the ATLAS mono-jet analysis) satisfy the validity constraint. The authors measure the ratio of

$$R_\Lambda^{\text{tot}} \equiv \frac{\sigma|_{Q_{\text{tr}}<\Lambda}}{\sigma} \,, \tag{3.6}$$

where the condition of eq. 3.5 is satisfied.

For a full description of this work (including the analytical and numerical methods and comparison), see ref. [119]. Fig. 3.4, taken from that work, demonstrates how validity is affected for the D5 and D11 operators: the plots show lines of constant R_Λ^{tot} (at 25%, 50% and 75%) as a function of m_χ and Λ, and compare these with the limits on Λ from the ATLAS analysis [11]; note that the ATLAS limits are independent of assumptions about the underlying physics, but *could* be interpreted in the context of a s-channel mediator. Notably, the ATLAS limit on the D5 operator lies in a region where less than 50% of events used to obtain that limit (within the toy analysis) are actually valid under the assumption of an s-channel mediator with couplings of $\mathcal{O}(1)$. In the D11 case it is considerably worse, with about 10% of events satisfying validity constraints. In both cases, the validity can be rescued by relaxing the assumption on the coupling strengths; the extreme case of g_q, $g_\chi < 4\pi$ is shown as the dashed lines in the plots, and all events are valid in this case for both the D5 and D11 operators, up to $m_\chi \sim \mathcal{O}$(TeV).

These examples serve to demonstrate that the EFT model of DM should not be used unquestioningly, but that the assumption of validity should always be checked. Unfortunately, doing so in a meaningful way will generally require making assumptions about the underlying physics. Two alternative directions can be taken from here:

- a rescaling of the limit on Λ that takes into account the fraction of valid events, as described below, or
- moving instead toward simplified models of DM, where the underlying physics is made explicit, thereby increasing the number of degrees of freedom of the model, but also ensuring its validity.

A fuller description of simplified models will be given in sec. 3.3.

Rescaling procedure

The rescaling method proposed by refs. [119, 121] is based on the idea that if a certain percentage of events used to obtain a limit on the suppression scale Λ of an EFT are invalid, we can remove those events and recalculate a limit on Λ. Of course, removing events will then serve to weaken the limit, and so an iterative procedure is required.

A new limit, Λ^i, is calculated from the initial limit Λ^{init} by including only the fraction R_v^i of valid events, according to

$$\Lambda^i = [R_v^i]^{1/(2(d-4))}\Lambda^{\text{init}} \tag{3.7}$$

where d is the operator dimension, equal to 7 for D1 and D11, and 6 for D5 and D9. Eq. 3.4 is then retested, yielding a new value of R_v^i, and eq. 3.7 is reprocessed with Λ^i as the new Λ^{init}. This process is repeated until there is no change—either the fraction of valid events has stabilised to $R_v^i = 1$, or no events are left and $R_v^i = 0$. In this latter case there is no meaningful limit on Λ.

The next section describes an alternative type of EFT, in which the contact interaction couples DM particles directly to SM gauge bosons.

3.2 Contact operators coupling to bosons

An alternative and less-commonly studied EFT is one that couples DM to SM bosons rather than fermions. Such an operator is depicted in fig. 3.5, where a contact interaction couples a DM pair to a Z boson. These EFTs are interesting when they couple to an EW boson as they are then best studied in mono-boson channels, rather than the standard mono-jet channel.

This section briefly describes the derivation of such models, closely following the description in ref. [122].

Since χ is a SM singlet, the coupling to a SM boson must be a higher-dimensional operator, beginning at dimension-7. However, EWSB implies that dimension-5 descendent operators must also arise; these originate from

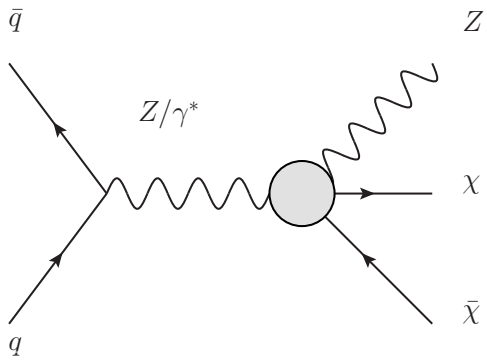

Figure 3.5: The $ZZ\chi\bar{\chi}$ EFT operator, which couples the DM directly to a Z boson. Taken from ref. [122].

$$\frac{1}{\Lambda_5^3}\chi\bar{\chi}(D_\mu H)^\dagger(D^\mu H) \tag{3.8}$$

where Λ_5 is the suppression scale for this dimension-5 operator, and $D_\mu H$ is the covariant derivative acting on the SM Higgs doublet. When this is expanded, and H replaced by its vacuum expectation value, the operator becomes

$$\frac{m_W^2}{\Lambda_5^3}\bar{\chi}\chi W^{+\mu}W_\mu^- + \frac{m_Z^2}{2\Lambda_5^3}\bar{\chi}\chi Z^\mu Z_\mu \ . \tag{3.9}$$

Such an expression implies that the ratio of couplings to W and Z is fixed.

At dimension-7, coupling to the kinetic terms of the EW bosons is given by

$$\frac{1}{\Lambda_7^3}\bar{\chi}\chi \sum_{i=1,2,3} k_i F_i^{\mu\nu}F^i_{\mu\nu} \tag{3.10}$$

where Λ_7 is the suppression scale for the dimension-7 operator and the F_i are the field strengths for the SM gauge groups ($U(1)$, $SU(2)$ and $SU(3)$). The couplings of $\bar{\chi}\chi$ to SM gauge bosons are

$$\begin{aligned}
g_{gg} &= \frac{k_3}{\Lambda_7^3} \\
g_{WW} &= \frac{2k_2}{\sin^2\theta_w\Lambda_7^3} \\
g_{ZZ} &= \frac{1}{4\sin^2\theta_w\Lambda_7^3}\left(\frac{k_1\sin^2\theta_w}{\cos^2\theta_w} + \frac{k_2\cos^2\theta_w}{\sin^2\theta_w}\right) \\
g_{\gamma\gamma} &= \frac{1}{4\cos^2\theta_w}\frac{k_1+k_2}{\Lambda_7^3} \\
g_{Z\gamma} &= \frac{1}{2\sin\theta_w\cos\theta_w\Lambda_7^3}\left(\frac{k_2}{\sin^2\theta_w} - \frac{k_1}{\cos^2\theta_w}\right)
\end{aligned} \tag{3.11}$$

The relative contributions from each coupling type is adjusted by tuning k_1/k_2.

As the mono-Z channel will feature heavily in later chapters of this thesis,

we emphasise the case with a Z boson in the final state, referred to as the $ZZ\chi\bar{\chi}$ operator. As well as the dimension-5 operator in eq. 3.9, both the ZZ and $Z\gamma$ dimension-7 operators contribute, and these can mix to a degree that is one of the free parameters of the model. Cases of maximal and minimal mixing are defined by requiring either $k_1 = k_2$, or $k_1 = \cos^2\theta_w / \sin^2\theta_w k_2$ (where the exchange of a γ becomes negligible).

3.3 Simplified models of dark matter

Simplified models of DM can be thought of as the step above EFT models in complexity. They include one or more additional degrees of freedom by *opening up* the EFT operators, generally in quite simple ways, with the inclusion of at least one mediating particle. While the advantage of this procedure is that the validity problems associated with EFTs may disappear since the the new model is often renormalisable, the disadvantage is that the theory has lost some of the model-independence that was so attractive about the EFT formalism. Thus, while it may be preferable to use simplified models in circumstances where the validity of an EFT model is questionable, they should by no means be considered a replacement of the EFTs, which are good at hiding considerably more complex physics (such as multiple renormalisable interactions at higher energy scales) that should not be discounted. Additionally, the simplified models do not *necessarily* satisfy renormalisability or unitarity [37].

3.3.1 Free parameters

First, we discuss in more detail the free parameters of a basic simplified model (containing a single mediating particle), where we shall stick to the assumption of a Dirac fermion DM particle, denoted χ. While simplified models can of course be developed for DM of other natures (say, as a scalar or vector particle), that has been studied elsewhere; see refs. [123–126] for some examples.

The contact interaction shown in fig. 3.6(a) can be opened up in two ways, with exchange of a mediating particle in either the s- or t-channel, shown in figs. 3.6(b) and (c) respectively; both of these can be treated as a contact operator in the heavy-mediator limit. The choice of channel will partially restrict allowed aspects of the mediator, as it fixes the couplings of the mediator to either quark-quark-mediator and mediator-DM-DM, or to quark-mediator-DM. In the former case, the mediator is required to be a SM singlet, electrically neutral and uncoloured, while in the latter case, the t-channel mediator is necessarily electrically charged (+2/3 if coupling to u-type quarks, -1/3 if coupling to d-type

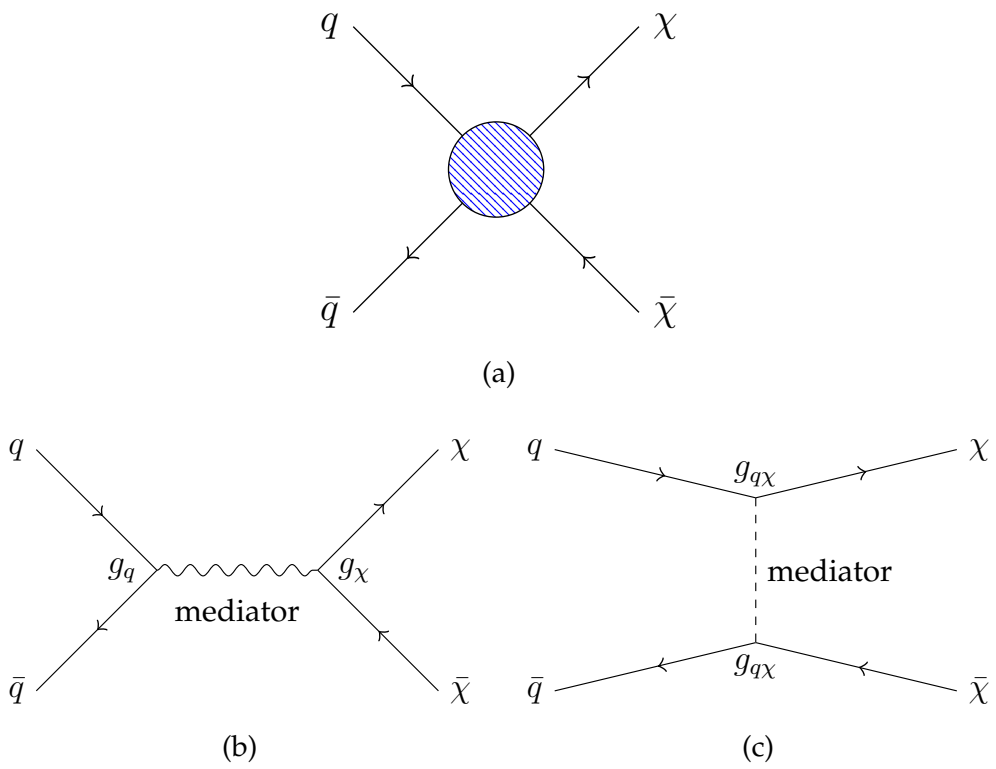

Figure 3.6: A contact interaction (a) can open up in the s-channel (b) or t-channel (c). A vector s-channel mediator and scalar t-channel mediator are shown here to reflect choices discussed in the text.

quarks) and must carry colour. Moreover, an additional choice can be made about whether the mediator couples to the left-handed (LH) quark $SU(2)$ doublet or the right-handed (RH) quark singlet (or both), as in each case, the $SU(2)$ gauge structure should be matched by the mediator. Both choices have appeared in the literature, see refs. [127] and [41] for examples. Importantly, the charge of the t-channel mediator under the SM gauge structures means that it is able to radiate SM bosons, which is significant for the mono-X + $E_{\mathrm{T}}^{\mathrm{miss}}$ topology.

The spin-structure of the mediator is also fixed by spin conservation; while it is angular momentum that is in reality being conserved, the parity of the number of half-integer spin particles on each side of the interaction must be maintained. In each three-particle interaction that has arisen thus far (quark-quark-mediator, mediator-DM-DM, quark-mediator-DM), the quark and DM are both spin-1/2 fermions, and so the mediator must have integer-spin. Commonly it is chosen to be scalar[4] (spin-0) or vector (spin-1), however other options (a spin-2 tensor, or something even more exotic) do exist in the literature.

The mass of the mediator is another free parameter, though this is also subject to some constraints. An s-channel vector mediator with axial couplings (de-

[4]A spin-0 mediator exchanged in the s-channel will undergo mixing with the other spin-0 particle of the SM, the Higgs boson. See for e.g. refs. [105, 128] for comments on this.

mediator channel	mediator type	couplings ($< 4\pi$)	mediator mass	DM mass
s-channel (SM singlet)	scalar	scalar	M_{med} (GeV)	m_χ (GeV)
		pseudo-scalar		
	vector	vector		
		axial-vector	$M_{\text{med}} > g_\chi m_\chi / \sqrt{4\pi}$	
	other		M_{med} (GeV)	
t-channel (charged, coloured, an $SU(2)$ doublet if coupled to LH quarks)	scalar	scalar	$M_{\text{med}} > m_\chi$	
		pseudo-scalar		
	vector	vector		
		axial-vector		
	other			

Table 3.2: The parameter space for the basic set of s- and t-channel simplified models.

scribed below) to quarks and DM should have a mass such that $M_{\text{med}} > g_\chi m_\chi / \sqrt{4\pi}$ to avoid violating unitarity [35–37]. A t-channel mediator should be heavier than the DM mass, to ensure that DM is the lightest stable particle and hence produces an appropriate relic density.

The next simplified model parameters are the couplings that govern the strength of the interactions. For the s-channel case, the mediator couplings to the quark-pair and the DM-pair are labeled g_q and g_χ respectively. The t-channel case has just a single coupling, labeled $g_{q\chi}$. The interactions may be chiral, leading us to distinguish between scalar ($\mathbb{1}$) and pseudo-scalar (γ^5) couplings, and vector (γ^μ) and axial-vector ($\gamma^\mu\gamma^5$) couplings. All couplings have a 'hard' upper limit of 4π to ensure the theory remains perturbative, though stronger limits may apply.

The final free parameter of each simplified model is, of course, the DM mass. Like the EFT case, this needs to be small enough to be pair-produced in a collider for a meaningful analysis, and once it drops below $\mathcal{O}$(1 GeV), it is effectively massless and the kinematic behaviour of the model stabilises.

A summary of the simplified model choices and parameters is shown in table 3.2.

There is clearly a large parameter space available within the simplified model framework, and such models have been prevalent within the theory community, who have been reinterpreting model-independent limits from collider-based experiments for some time [17–44]. Similarly to the case of EFT models, the experimental community has been a little slower in adopting this strategy, particularly due to the preferred use of the more generic EFT framework, before the EFTs were demonstrated to be of questionable validity in certain cases. As such, the use of simplified models within experimental analyses (such as the ATLAS and CMS mono-X groups) has only begun to occur recently—the inclusion of a version of the t-channel simplified model with a scalar mediator in the ATLAS Run I mono-$Z(\to \ell^+\ell^-)$ analysis, described in chapter 6 of this thesis, was one of the first instances, while the vector s-channel model was included as a reinterpretation of the ATLAS and CMS mono-jet Run I analyses [12, 115].

3.3.2 Recommended simplified models

In an attempt to standardise the approach across experimental analyses, and to facilitate cross-checking of models and comparison of results, a Dark Matter Forum was formed in 2014. This group was comprised of analysts from the ATLAS and CMS Exotics groups as well as DM theorists, and aimed to 'propose a prioritized, compact set of benchmark simplified models' for use by both ATLAS and CMS for Run II searches. The resulting report is found at ref. [15]; the author was responsible for the section within that work on the t-channel model with a scalar mediator.

The first half of the report is devoted to a set of five simplified models: the s-channel scalar, pseudo-scalar, vector and axial-vector mediator models, and the t-channel scalar mediator model. (Other models, such as two-Higgs-doublet models leading to a mono-Higgs signature, or EFT models coupling directly to SM EW bosons (such as that discussed in sec. 3.2), are also discussed in the report.) Currently, the sections on the s-channel scalar and pseudo-scalar mediator models acknowledge, but do not address, the implicit mixing with the Higgs boson required to remain $SU(2)$ gauge invariant, and as a result they are not considered further here. The remaining three models are the predominant simplified models studied in chapters 6, 7 and 8 of this thesis, and we discuss them in greater detail below.

The first model to be discussed in detail is the s-channel vector mediator model, denoted from hereon as sV. The interaction Lagrangian is given by

$$\mathcal{L}_{sV} = -\xi_\mu \left[\sum_q g_q \bar{q} \gamma^\mu q + g_\chi \bar{\chi} \gamma_\mu \chi \right] \tag{3.12}$$

where ξ_μ is the vector mediator and the sum is over all quarks. A simplifying assumption, that g_q is the same for all quarks, is made to ensure maximal flavour symmetry. A similar model with axial-vector couplings to the SM and dark sectors is denoted the sA model, with an interaction Lagrangian given by

$$\mathcal{L}_{sA} = -\xi_\mu \left[\sum_q g_q \bar{q} \gamma^\mu \gamma^5 q + g_\chi \bar{\chi} \gamma_\mu \gamma_5 \chi \right] \ . \tag{3.13}$$

As noted in sec. 3.3.1, this model has restrictions on the mediator mass to avoid violating perturbative unitarity.

The sV and sA models (described by eqs. 3.12 and 3.13) are studied in chapter 7; the sV model is included in the analysis of chapter 8.

The final simplified model that is studied in this thesis is the t-channel scalar mediator model, denoted tS, with interaction Lagrangian

$$\mathcal{L}_{tS} = \sum_i \left(g^L_{q\chi} \phi^i_L \bar{Q}^i_L + g^{u,R}_{q\chi} \phi^i_{u,R} \bar{u}^i_R + g^{d,R}_{q\chi} \phi^i_{d,R} \bar{d}^i_R \right) \chi + \text{h.c.} \ , \tag{3.14}$$

where ϕ^i_L are the mediator doublets under $SU(2)$ that couple to the LH quark doublets, the $\phi^i_{u,R}$ and $\phi^i_{d,R}$ are singlets that couple to the RH quarks, and the sum is over the three generations. The mediators have the same quantum numbers as the quarks, that is,

$$\phi^i_L = \begin{pmatrix} \phi^i_{u,L} \\ \phi^i_{d,L} \end{pmatrix} \sim (3, 2, \frac{1}{3}) \, , \quad \phi_{u,R} \sim (3, 1, \frac{4}{3}) \, , \quad \phi_{d,R} \sim (3, 1, -\frac{2}{3}) \, , \tag{3.15}$$

and are all set to have equal mass. The couplings $g^L_{q\chi}$, $g^{u,R}_{q\chi}$ and $g^{d,R}_{q\chi}$ can be used to turn on and off the different couplings, though generally the couplings are assumed to be equal across quark generations. Several versions of this model are common in the literature, examples are seen in refs. [41] (where either all couplings are allowed, or $g^L_{q\chi}$, $g^{u,R}_{q\chi}$ = 0, within i = 1,2) and [127] (where $g^{u,R}_{q\chi}$, $g^{d,R}_{q\chi}$ = 0). The latter reference also sets χ to be Majorana, a decision motivated by the emergence of this simplified model within Supersymmetry (SUSY), where the DM fermion is a neutralino, the scalar mediator is a squark doublet, and the necessary gluino is heavy and therefore decoupled. This model, with a single mediator doublet, is included as the work of the author in the Run I ATLAS mono-$Z(\to \ell^+\ell^-)$ analysis, the focus of chapter 6. The model as written in eq. 3.14, with $g^{u,R}_{q\chi}$, $g^{d,R}_{q\chi}$ = 0, is one of the models studied in chapter 7. In all variants, the

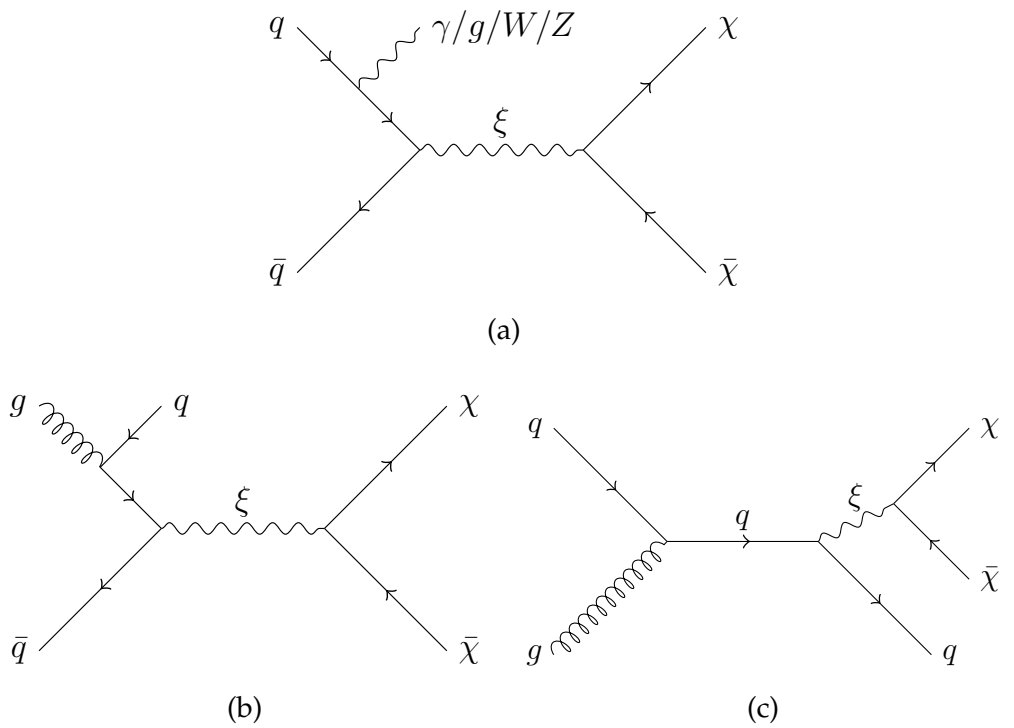

Figure 3.7: The possible tree-level processes producing a mono-X + $E_{\mathrm{T}}^{\mathrm{miss}}$ topology at a hadron collider, for an s-channel simplified model. The lower diagrams are only relevant for the mono-jet channel.

collider phenomenology is the same (excepting the inclusion of additional production modes if, say, third generation quarks are coupled or not), and only a cross section rescaling is required.

Use in collider mono-X studies

Similarly to the EFT case described in sec. 3.1.1, in both s and t-channel models an initial state parton can produce the visible object X necessary to mono-X + $E_{\mathrm{T}}^{\mathrm{miss}}$ collider searches. Additional mono-jet processes, with a gluon in the initial state, are also present in both simplified model types. However, as noted above, the t-channel mediator is also able to radiate a visible particle, leading to additional diagrams in this case.

Figs. 3.7 and 3.8 show the available tree-level processes; in both cases, the lower diagrams are relevant only to the mono-jet channel.

3.3.3 The mediator width

In each of the models described above, the width of the mediator is important, as it can lead to a resonant enhancement in the cross section in the case where it is small, and can impact the kinematic behaviour of the decay products. While

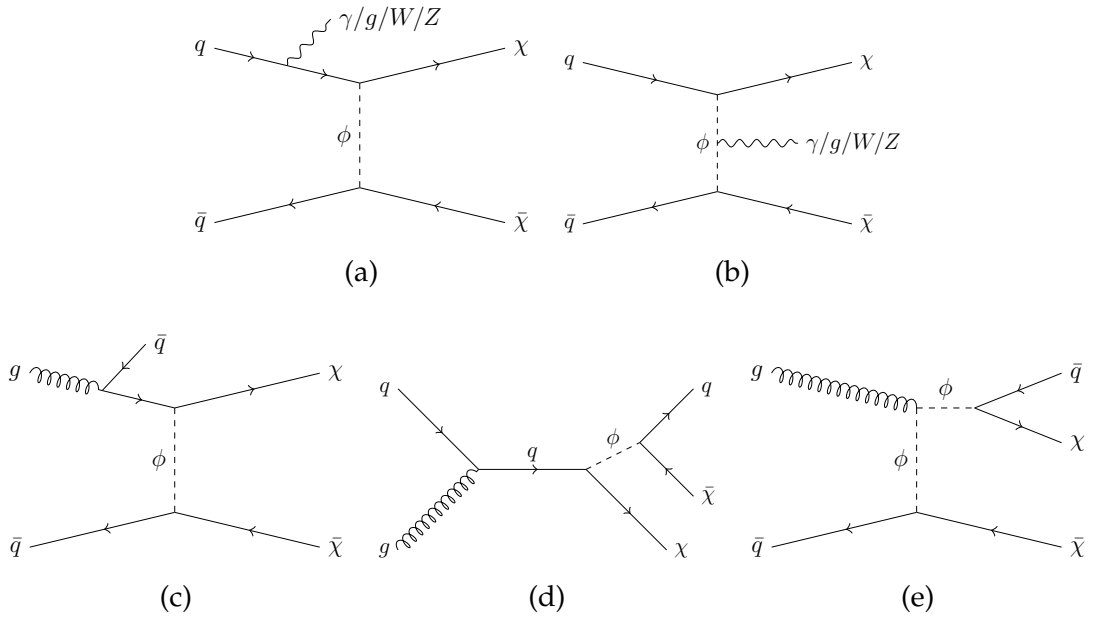

Figure 3.8: The possible tree-level processes producing a mono-X + $E_{\mathrm{T}}^{\mathrm{miss}}$ topology at a hadron collider, for an t-channel simplified model. The lower diagrams are only relevant for the mono-jet channel.

the *minimum* natural width of a mediating particle is determined by its mass and couplings to all possible decay products[5], models with a fixed width have also been used in some analyses. Common choices are $\Gamma = M_{\mathrm{med}}/8\pi$, which would arise when a single quark couples to a mediator with a strength of g_q = 1, and $M_{\mathrm{med}}/3$, chosen to ensure the mediator remains a *narrow* resonance [105, 129].

The natural width of the s-channel vector mediator model is given by

$$\begin{aligned}\Gamma_{sV} = & \frac{g_\chi^2 M_{\mathrm{med}}}{12\pi}\left(1+\frac{2m_\chi^2}{M_{\mathrm{med}}^2}\right)\left(1-\frac{4m_\chi^2}{M_{\mathrm{med}}^2}\right)^{\frac{1}{2}}\Theta(M_{\mathrm{med}}-2m_\chi) \\ & + \sum_q \frac{g_q^2 M_{\mathrm{med}}}{4\pi}\left(1+\frac{2m_q^2}{M_{\mathrm{med}}^2}\right)\left(1\frac{4m_q^2}{M_{\mathrm{med}}^2}\right)^{\frac{1}{2}}\Theta(M_{\mathrm{med}}-2m_q)\ ,\end{aligned} \tag{3.16}$$

while the width for the axial-vector model is

[5]Note that 'minimum' here refers to the fact that if a toy model is embedded within a more complex theory, the mediator may have couplings to further particles, thereby increasing its width.

$$\Gamma_{sA} = \frac{g_\chi^2 M_{\text{med}}}{12\pi}\left(1-\frac{4m_\chi^2}{M_{\text{med}}^2}\right)^{\frac{3}{2}}\Theta(M_{\text{med}}-2m_\chi) + \sum_q \frac{g_q^2 M_{\text{med}}}{4\pi}\left(1-\frac{4m_q^2}{M_{\text{med}}^2}\right)^{\frac{3}{2}}\Theta(M_{\text{med}}-2m_q)\ . \tag{3.17}$$

The width of the t-channel scalar mediator model, with couplings to LH quarks, is given by

$$\Gamma_{tS} = \sum_q \frac{g_{q\chi}^2 M_{\text{med}}}{16\pi}\left(1-\frac{m_q^2}{M_{\text{med}}^2}-\frac{m_\chi^2}{M_{\text{med}}^2}\right) \times\sqrt{\left(1-\frac{m_q^2}{M_{\text{med}}^2}+\frac{m_\chi^2}{M_{\text{med}}^2}\right)^2-4\frac{m_\chi^2}{M_{\text{med}}^2}}\ \Theta(M_{\text{med}}-m_q-m_\chi)\ . \tag{3.18}$$

The quadratic dependence of the width on the couplings g_q, g_χ and $g_{q\chi}$ is evident, and makes clear that large couplings, while they may be smaller than the perturbative limit of 4π, can lead to a width of comparable or even larger magnitude to the mediator mass, begging the question of how meaningful the modeling of such a resonance as a particle can be. In later chapters, we will restrict ourselves to widths that satisfy $\Gamma < M_{\text{med}}$.

The cross section of the collider production process $pp \to \bar{\chi}\chi + X$, through mediator exchange in the s-channel, is related to the simplified model parameters through a Breit-Wigner propagator term [105]:

$$\sigma(pp \to \bar{\chi}\chi + X) \sim \frac{g_q^2 g_\chi^2}{(Q_{\text{tr}}^2 - M_{\text{med}}^2)^2 + \Gamma^2/4} E^2\ , \tag{3.19}$$

where E is of order the partonic centre-of-mass energy and Q_{tr} is the transferred momentum. When M_{med} and Q_{tr} are of the same order, a resonance effect is observed in the cross section, and the mediator width (as well as the mass) is important in determining the broadness of this resonance. The width can also affect the kinematic behaviour of the process.

In the case of a very light mediator mass (i.e. $M_{\text{med}} \ll Q_{\text{tr}}$), eq. 3.19 simplifies to

$$\sigma \sim \frac{g_q^2 g_\chi^2}{Q_{\text{tr}}^4}\ . \tag{3.20}$$

In this case, the mediator will always be off-shell, and its mass and width do not

have a significant impact on the interaction. The DM mass determines a lower bound on Q_{tr} (by requiring that there is enough energy to pair-produce the DM pair); the couplings limit the strength of the interaction, but do not affect the kinematic behaviour. The fact that the cross section, and hence the limits one might obtain on the couplings, are reasonably independent of the mediator mass can be contrasted to the case of direct detection searches, where the scattering cross section goes like [105]

$$\sigma(\chi N \to \chi N) \sim \frac{g_q^2 g_\chi^2}{M_{\text{med}}^4} \mu_{\chi N}^2 \ , \tag{3.21}$$

indicating the limits will strengthen as M_{med} get smaller.

Alternatively, in the case of a heavy mediator (i.e. $M_{\text{med}} \gg Q_{\text{tr}}$), eq. 3.19 simplifies to

$$\sigma \sim \frac{g_q^2 g_\chi^2}{M_{\text{med}}^4} \sim \frac{1}{\Lambda^4} \ . \tag{3.22}$$

Here, there is no longer a dependence on Q_{tr} and the cross section falls off as the mediator mass increases. Again, the mediator is far off-shell in such interactions, and neither its mass nor width will affect the kinematics. In this heavy mediator limit, the limits should match those obtained by the EFT approximation; comparing the two model types is explored further in the following subsection.

3.3.4 Comparison with EFT models

As eq. 3.19 shows, the simplified model cross section can undergo resonant enhancement when the mediator goes on-shell, which the EFT regime does not allow. This is demonstrated by fig. 3.9(a), taken from ref. [129], that plots a limit on $\Lambda \equiv M_{\text{med}}/\sqrt{g_q g_\chi}$ for the axial-vector mediator model by recasting limits from the CMS mono-jet analysis [12], and shows three distinct regions. Region II is where the resonant enhancement, and its dependence on mediator width, can be seen. In this region, the EFT limit is too conservative relative to the true obtainable upper limit on Λ. Far more problematic is region III, where the simplified model cross section is smaller than that in the EFT model, leading to a weaker limit than that resulting from the EFT implementation and again demonstrating the danger of using an EFT to approximate a simplified model.

In region I, the simplified model enters the heavy-mediator limit, where the limit on Λ is independent of M_{med}, and is expected to align with the limit obtained within an EFT framework. This is explicitly demonstrated by fig. 3.9(b), taken from ref. [115], which shows the lower limit on Λ (here labeled $M_\star$) as a function of mediator mass for two DM masses of 50 and 400 GeV in blue and orange

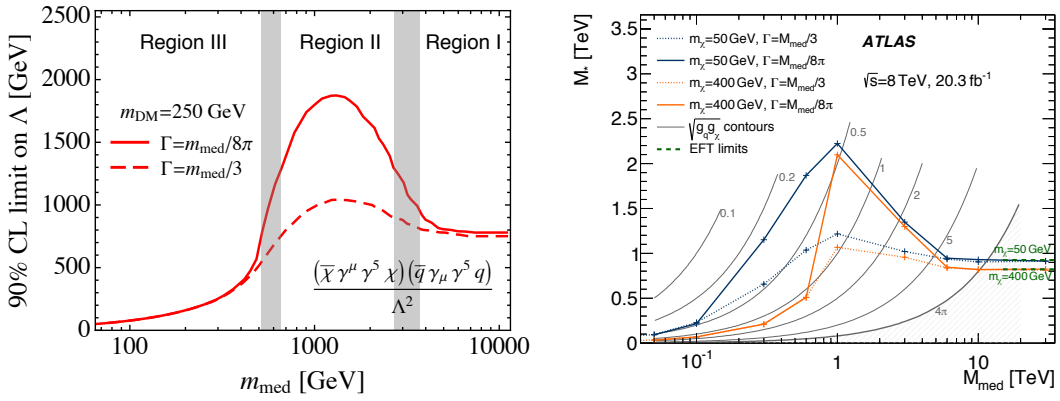

(a) (b)

Figure 3.9: The resonant mediator effect in the s-channel mediator model. Taken from refs. [129] (left) and [115] (right).

respectively. The green dashed lines show the EFT model limits, which precisely match the simplified model limits.

The relationship between the EFT and simplified model formalisms of DM are made clear by eq. 3.22 in the heavy mediator limit, and in fact it can be shown that the s-channel vector and axial-vector mediator models contract to become the D5 and D8 models respectively (refer to table 3.1). The t-channel scalar mediator model contracts to an effective operator of the form $(q\chi)(\bar{q}\bar{\chi})$, however this can be Fierz transformed to the form $(\bar{q}\Gamma q)(\bar{\chi}\Gamma\chi)$, where Γ is a combination of γ^μ and $\gamma^\mu\gamma^5$; that is, it becomes a combination of the D5 and D8 operators. We therefore expect that in the heavy mediator limit, all three simplified models will behave very similarly to the D5 representative operator.

A further point of difference, and another advantage of the simplified model approach, is that alternative search channels become available. A di-jet search for the s-channel mediator is such an example, since if the mediator is produced through quark pair-annihilation, it should also decay back to a quark pair, manifesting in the detector as two jets. Experimental limits on the coupling of quarks to the hypothetical Z' (a new vector particle) can therefore be reinterpreted as a limit on g_q. Fig. 3.10, taken from ref. [130], shows these limits as a function of mediator mass. We note that the large di-jet cross section might indicate that the di-jet channel is the better approach for searching for the s-channel simplified models; however, in the case where g_q is smaller than g_χ, the di-jet analysis limits can be evaded, and the mono-X searches for $pp \to \chi\bar{\chi} + X$ events will provide stronger limits. The multiple search channels are therefore complementary, and address different regions of phase space.

The models discussed in this chapter are all included in the mono-X + $E_{\mathrm{T}}^{\mathrm{miss}}$

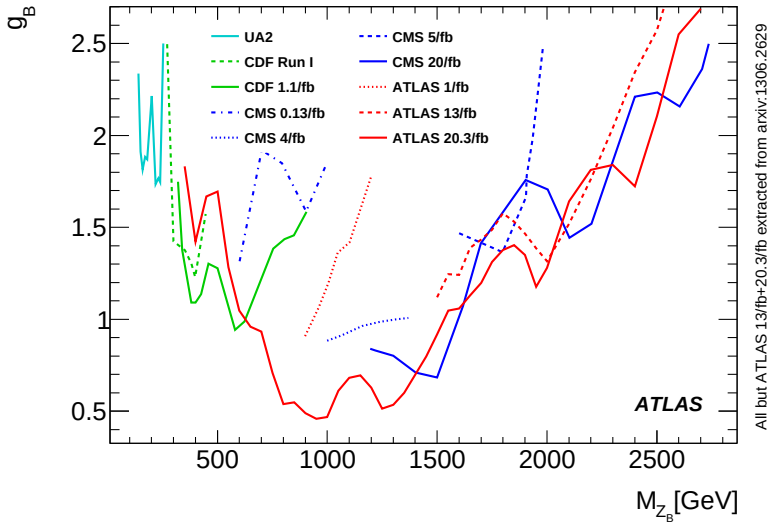

Figure 3.10: Upper limits on the coupling g_q from multiple di-jet searches for a Z' particle. Taken from ref. [130].

analyses discussed in later chapters of this thesis. However, the experiment that can collect the data to perform such studies has not yet been introduced, and is the subject of the next chapter.

Chapter 4

Detection and reconstruction

This section will briefly describe the operation of the Large Hadron Collider (LHC), the main components of the ATLAS detector, and the reconstruction of physics objects relevant to analyses, namely, electrons, photons, muons, taus, jets and missing transverse energy.

4.1 The Large Hadron Collider

The LHC, situated at CERN in Geneva, Switzerland, is the largest and most powerful particle accelerator in the world. It is a circular collider 27km around, running as deep as 175m underground under the border between Switzerland and France. It is designed to collide bunches of protons or lead (Pb) ions at interaction points within the four main experiments (ATLAS, CMS, LHCb and ALICE) situated around the ring.

The LHC began operating in November of 2009 (following a delay in 2008 caused by a damaging magnet quench), colliding proton bunches at a centre-of-mass energy of 7 TeV (3.5 TeV for each proton beam) and increasing to 8 TeV in 2012. Most of the analysis described in this thesis is performed with 8 TeV data from Run I, which ended in January 2013. Following two years of upgrades to the LHC and detectors (the *long shutdown*), the LHC begin delivering physics data in mid-2015 at a centre-of-mass energy of 13 TeV. The final analysis within this thesis was performed using the preliminary data obtained during the first six months of Run II. The LHC has not yet reached its design energy of 14 TeV.

The LHC can be divided into eight octants, four of these are used for acceleration of the protons and ions (through use of radiofrequency (RF) cavities), beam cleaning and the beam dump, while the others are the locations for the beam collisions and the four main experiments[1]: *A Large Ion Collider Experiment* (AL-

[1] In addition to the four experiments described in the text, the TOTEM (*TOTal Elastic and diffrac-*

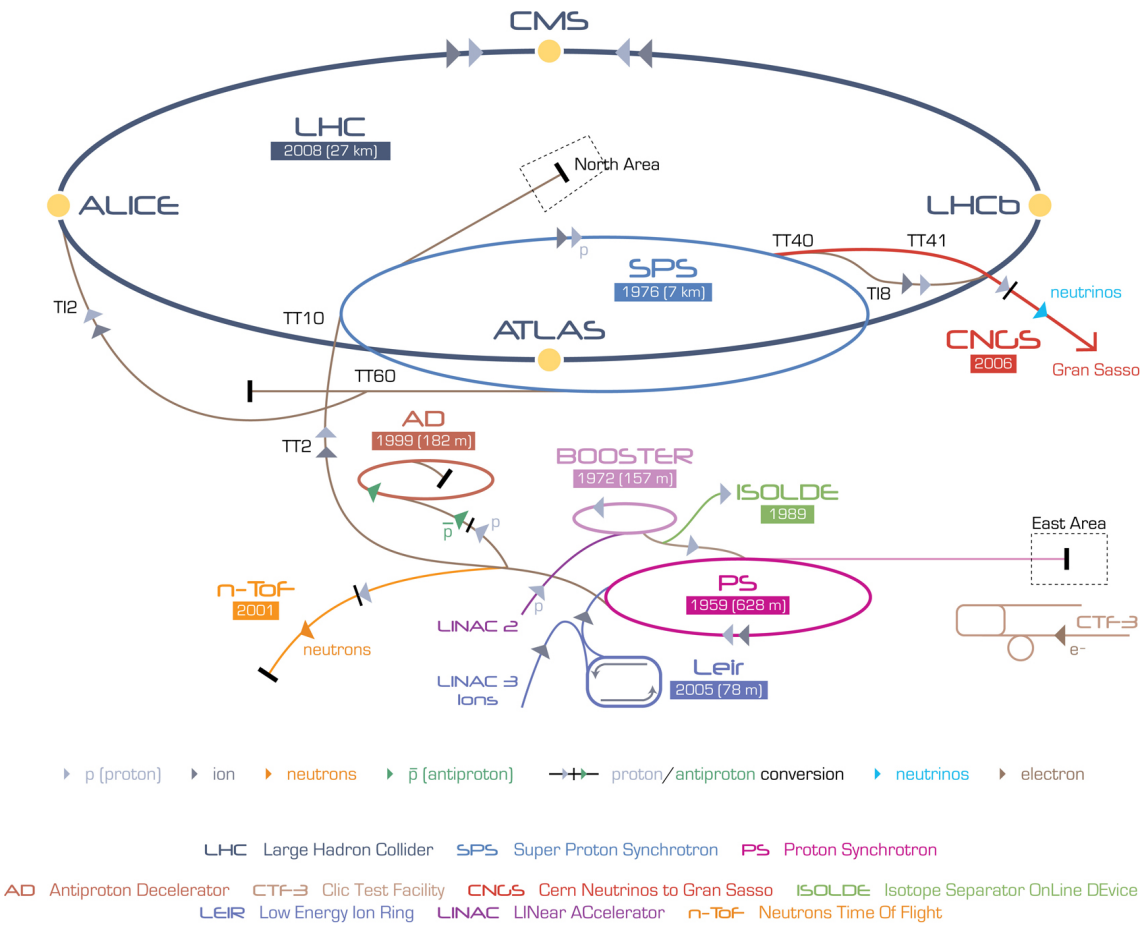

Figure 4.1: The CERN accelerator complex. Taken from ref. [131].

ICE) studies the heavy ion collisions, the LHC*b* experiment specialises in *b*-quark physics, and *A Toroidal LHC ApparatuS* (ATLAS) and the *Compact Muon Solenoid* (CMS) experiments are general-purpose detectors, which together provided evidence for the detection of the Higgs boson in 2012. The ATLAS detector shall be described in further detail in sec. 4.2.

The LHC complex is shown in fig. 4.1. Proton bunches begin in the linear accelerator (LINAC) where they reach energies up to 50 MeV, then are injected into the Proton Synchrotron (PS) booster followed by the Super Proton Synchrotron (SPS), reaching energies of 25 GeV and 450 GeV respectively. The final step is into the LHC ring, where the protons are accelerated by RF cavities up to the desired energy (4 TeV in Run I, 6.5 TeV in Run II).

While the high energy of colliding protons is extremely important in studying potential new physics, also important, and necessary for the statistical approach each analysis must take, is the luminosity provided by the collider: a higher luminosity means more events and a greater statistical power. The luminosity, L, is

tive cross section Measurement), LHCf (*LHC forward*) and MoEDAL (*Monopole and Exotics Detector at the LHC*) experiments are also located around the LHC ring.

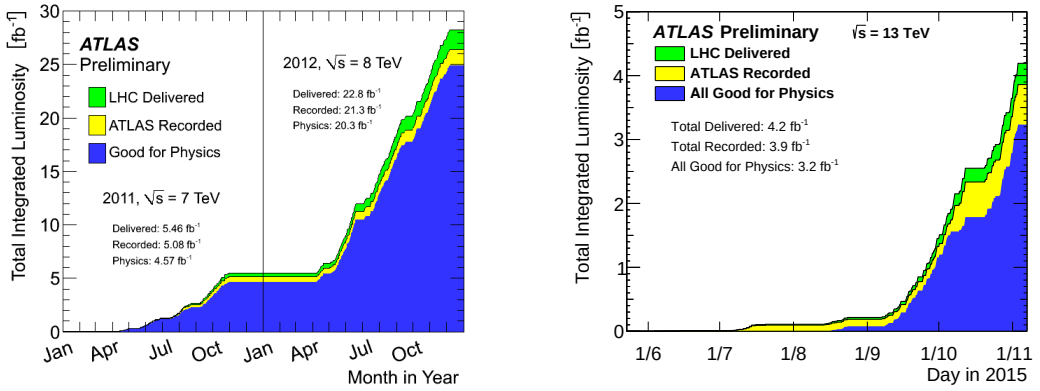

(a) (b)

Figure 4.2: The total integrated luminosity recorded by the ATLAS detector in Runs I (left) and II (right). Taken from refs. [132] and [133].

related to the bunch parameters by

$$\mathrm{L} = \frac{f_{\text{crossing}} N_{\text{bunch 1}} N_{\text{bunch 2}}}{\mathcal{A}} \tag{4.1}$$

where f_{crossing} is the frequency of bunch crossings, the Ns are bunch sizes and $\mathcal{A}$ is the cross sectional area of the beam overlap.

The number of protons per bunch (N_{bunch} in eq. 4.1) was increased during Run I from 1.2×10^{11} in 2010 to 1.7×10^{11} in 2012, while the bunch spacing ($1/f_{\text{crossing}}$) has been reduced from 50ns to 25ns in Run II. Fig. 4.2 shows the total integrated luminosity ($\mathcal{L} = \int \mathrm{L}\ \mathrm{dt}$) collected by the ATLAS detector for the 7 and 8 TeV runs in 2011/2012 (left) and the 13 TeV run in 2015 (right).

Unfortunately, while more protons per bunch will increase the likelihood of a hard collision between two protons, it also increases the likelihood of multiple interactions between protons in the two crossing bunches, meaning that a detector will record data from multiple interaction points in each event. The number of interactions per bunch crossing is known as *in-time pileup*, and is shown in fig. 4.3 for Run I (left) and Run II (right), as measured by the ATLAS detector. *Out-of-time pileup* is similarly problematic, and arises when signals from previous bunch crossings remain in the detector; for example, the liquid argon (LAr) calorimeters (described in sec. 4.2.2) are sensitive to signals from the preceding 12 bunch crossings during 50ns bunch spacing operation, which increases to 24 during 25ns operation [134, 135].

The ATLAS detector is described in the next section.

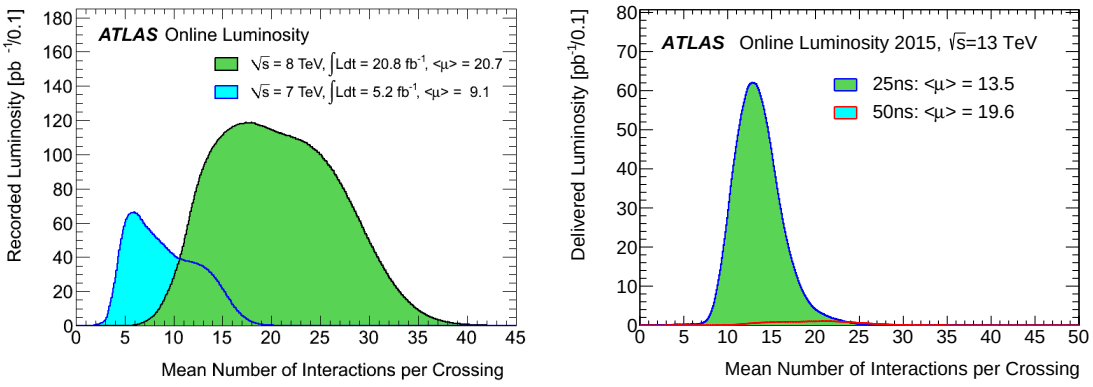

(a) (b)

Figure 4.3: The in-time pileup measured by the ATLAS detector in Runs I (left) and II (right). Taken from refs. [132] and [133].

4.2 The ATLAS detector

At 46m long, 25m in diameter and weighing close to 7000 tonnes, the cylindrically-shaped ATLAS detector is the largest detector on the LHC ring. This section provides a brief description of the main components of the ATLAS detector, and is heavily based on refs. [134, 136].

ATLAS uses a right-handed coordinate system with its origin at the nominal interaction point (IP) in the centre of the detector and the z-axis along the beam pipe. The x-axis points from the IP to the centre of the LHC ring, and the y-axis points upward. Cylindrical coordinates (r, ϕ) are used in the transverse plane, ϕ being the azimuthal angle around the beam pipe. The polar angle θ is measured with respect to the LHC beam-line. The pseudorapidity η is an approximation for rapidity y in the high energy limit, and is defined in terms of the polar angle θ by $\eta = -\ln\tan(\theta/2)$. Transverse momentum and energy are defined as $p_{\mathrm{T}} = p \times \sin(\theta)$ and $E_{\mathrm{T}} = E \times \sin(\theta)$, respectively.

The entire ATLAS detector is shown in fig. 4.4, and can be broken down into three main detectors: the *inner detector* (used for particle identification and tracking), the *calorimeters* (used for energy measurement) and the *muon spectrometer* (for identification and energy measurement of muons). All components are approximately symmetric about the IP. Specific details for each of the main detector components are given below.

4.2.1 The Inner Detector

The inner detector (ID) is the innermost detector within ATLAS, and is depicted in fig. 4.5. It is 7.024m long and 2.3m in diameter, and sits within a 2T magnetic field provided by a solenoid surrounding the detector. As noted above, it is used

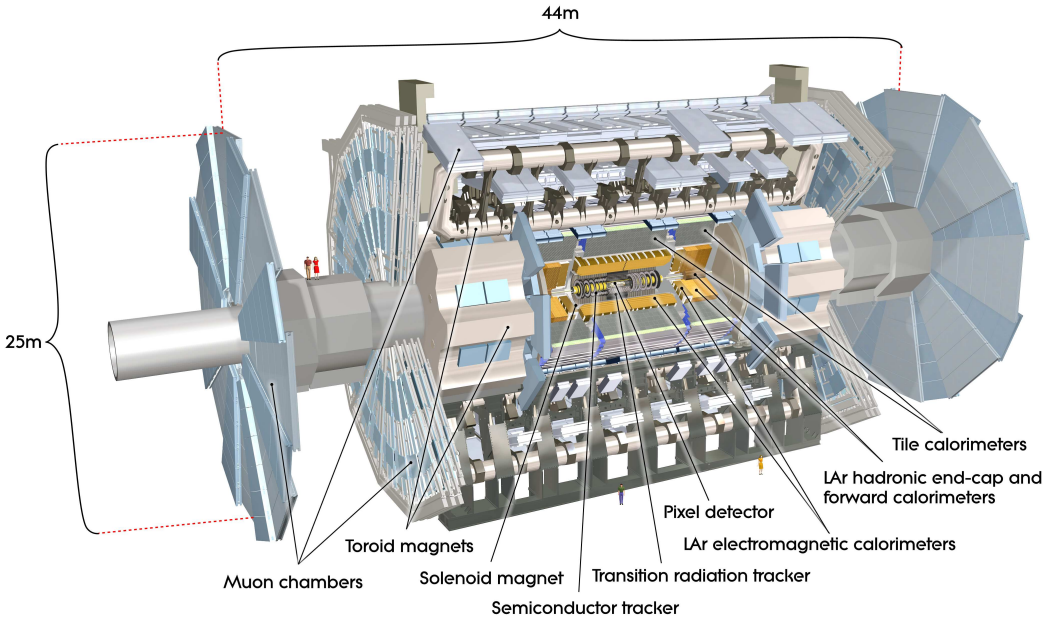

Figure 4.4: The ATLAS detector. Taken from ref. [134].

predominantly for the tracking of particles out to a pseudorapidity, $|\eta|$, of 2.5, and is designed to reconstruct particle tracks and vertices with good momentum resolution. Additionally, the ID can also be used to identify electrons with $p_{\mathrm{T}} \in$ [500 MeV, 150 GeV] with $|\eta| < 2.0$.

The ID has three layers, the *pixel detector*, *semiconductor tracker* and *transition radiation tracker*.

The pixel detector contains three layers of high-precision, high-granularity semiconductor modules (1744 in total), which each contain close to 50,000 pixels, with 46,080 independent read-out channels per module, and 80.4 million channels in total. It provides excellent resolution in each layer, 10μm in the transverse plane and 115μm in the axial (barrel) or radial (endcaps) plane.

Between Runs I and II, a significant upgrade to the pixel detector was made, with the installation of the Insertable B-Layer (IBL) [137, 138]. This was inserted within the innermost layer (the B-layer) of the original pixel detector, following the resizing of the beam pipe, and was designed to handle the planned increase in instantaneous luminosity of the LHC after Run II, which is expected to reach more than twice the peak luminosity of 1×10^{34} cm^{-2} s^{-1} for which the pixel detector was designed. The IBL is a hybrid silicon pixel detector constructed of 14 tilted, overlapping staves at $\langle r \rangle$ = 3.3cm from the centre of the beam pipe, and extends out to $|\eta|$ = 3.0. Its 12 million pixels are ∼60% of the size of those in the original pixel detector, providing improved resolution. As a result of the IBL, the tracking capability of the ID is signficantly improved, particularly for vertex

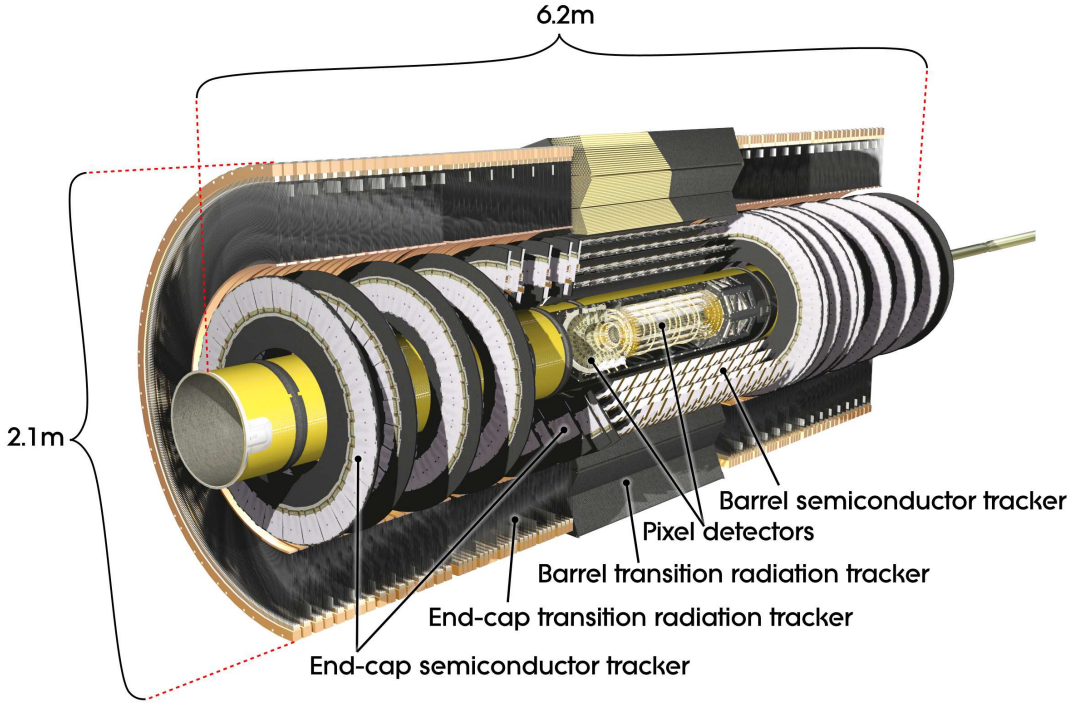

Figure 4.5: The inner detector of ATLAS. Taken from ref. [134].

reconstruction and tagging of b-hadrons.

The semiconductor tracker (SCT) contains layers of silicon microstrips, arranged such that any particle will travel through at least four layers in either the barrel or the endcap. It provides a per-layer resolution of 17μm in the transverse plane, and 580μm in the axial and radial planes.

The transition radiation tracker (TRT) is made up of polyimide straw tubes, 4mm in diameter, that each contain a gas mixture of Xe, CO_2 and O_2. The gas is ionised as charged particles pass through, and the resulting electrons then move toward a central, positively charged anode wire. The time taken to reach the anode is used to determine the radial distance to the ionisation point within the straw. Electrons can also emit X-rays as they transition between the gas mixture and the straw, produce ionising photons which show as larger signal amplitudes than the minimum-ionising charged particles. Electrons with $p_{\mathrm{T}} < 150$ GeV can be identified this way, however other particles with $p_{\mathrm{T}} > 150$ GeV can also produce this signal and so the identification ability is lost. All charged tracks satisfying $|\eta| < 2.0$ and $p_{\mathrm{T}} >$ MeV cross at least 36 straws, except in the transition region between the barrel and endcap ($0.8 < |\eta| < 1.0$), where they cross at least 22.

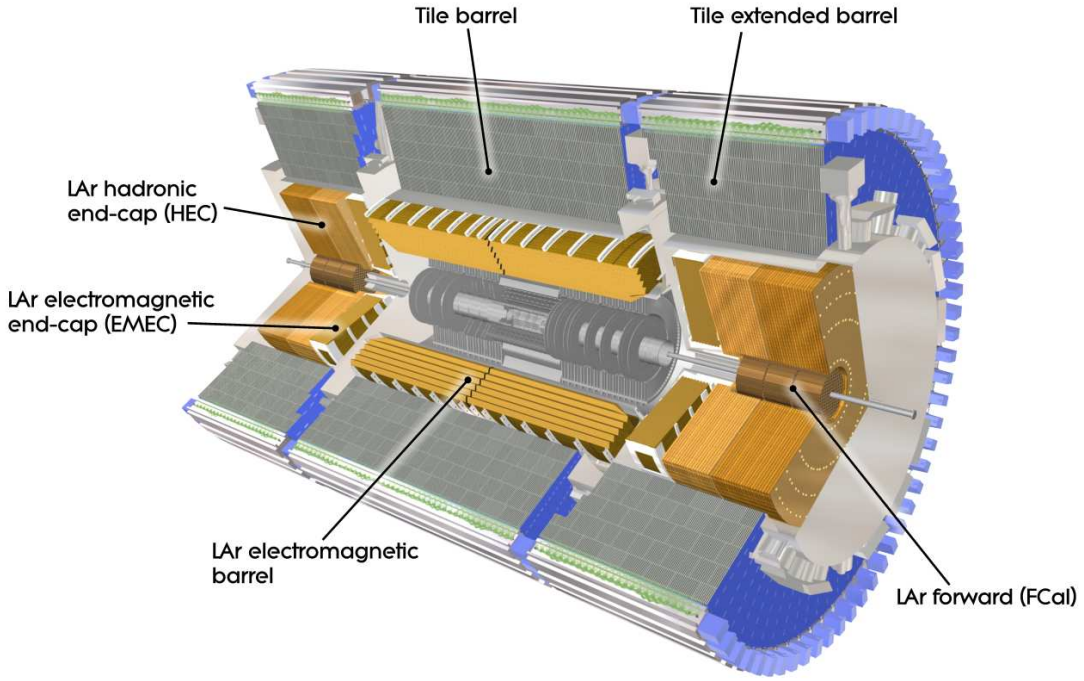

Figure 4.6: The calorimeter system of ATLAS. Taken from ref. [134].

4.2.2 The Calorimeter

The calorimeter system of ATLAS, shown in fig. 4.6, is designed to measure the energy of particles as they pass into the detector and are stopped. Only neutrinos and muons are able to pass through relatively unaffected, these are known as minimally ionising particles (MIPs). The calorimeter system extends out to $|\eta|$ = 4.9, and is separated into the inner electromagnetic (EM) calorimeter (for EM showers seeded by electrons or photons) and the outer hadronic calorimeter (for showers seeded by hadrons). In both systems, sampling calorimetry is used, in which particles pass through alternate layers of absorbing and active material; the former layers are designed to force an interaction in order to produce a shower, while the latter layers measure the amount of energy in the shower. While some energy is generally lost in the absorbing layers, this can be quantified and calibrated for.

The EM calorimeter, as noted above, measures the energy of electrons and photons, which cannot be treated independently; electrons can radiate photons, while photons can produce electron-positron pairs, undergo Compton scattering with electrons, and be converted to electrons through the photoelectric effect. The low-energy electrons that are ultimately produced in an electron/photon shower will form ions and so are absorbed, ending the showering process. Given a sufficiently deep calorimeter, most of the energy of such a shower can be contained.

The radiation length of a material, denoted X_0, is the average distance an electron travels in the material to reduce its energy by a factor of e through EM interactions. Generally, more than 20 radiation lengths are needed to fully contain an EM shower. The absorbing material in the EM calorimeter is lead, which has a relatively short radiation length of X_0 = 0.561cm. The active material is liquid argon (LAr), chosen for its uniform nature, stability and radiation-hardness. The LAr is ionised as particles pass through, and the electrons drift to a set of copper electrodes. A signal shaper, optimised for the 25ns bunch spacing, is applied to shorten the readout time.

The absorbing and active layers are arranged in a distinct accordian geometry (seen in fig. 4.7(a)), which provides full coverage in the ϕ dimension. In the barrel region ($|\eta| < 1.475$), the ElectroMagnetic Barrel (EMB) has three layers: strip cells of size 0.0031 $\times$ 0.098 in $\eta \times \phi$-space (which is needed to discriminate photons from π^0 decays), a second layer of cells with size 0.025 $\times$ 0.0245 (where most of the energy is captured, and providing good resolution in both dimensions), and a third, coarser-granularity layer of 0.05 $\times$ 0.0245 cells (where less precision is needed). In the endcap region ($1.375 < |\eta| < 3.2$), the ElectroMagnetic EndCap (EMEC) is constructed from two coaxial wheels with a similar structure to the EMB. The region between the barrel and endcap ($1.375 < |\eta| < 1.52$), known as the crack region, contains a considerable amount of inactive material required for access to the ID, leading to losses in energy and performance. This region is often removed in physics analyses.

The hadronic calorimeter is used to measure the decay of hadrons, however a hadronic shower is not strictly contained within the hadronic calorimeter; neutral pions, for example, which are produced in $\sim$30% of events, are most likely to decay to a pair of photons, which deposit their energy in the EM calorimeter. Hadronic jets in general are quite complicated objects, producing charged and neutral mesons and baryons, as well as invisible processes almost 30% of the time. As a result, a considerable amount of the hadronic energy is undetectable, and, to complicate matters further, the fraction of energy that is observed tends to depend on the energy of the process, requiring a significant calibration effort.

The nuclear interaction length of a material, λ_I (the hadronic equivalent to the EM radiation length), is the distance travelled by a particle before it undergoes a hadronic interaction, that is, a strong interaction with the nucleus. Due to the much smaller cross section of the nucleus compared to the surrounding electron cloud, λ_I tends to be much larger the X_0 (a factor of 5–30 times longer) for the same material. Calorimeters normally require about 10 nuclear interaction lengths to contain a hadronic shower, however it becomes impossible to fully

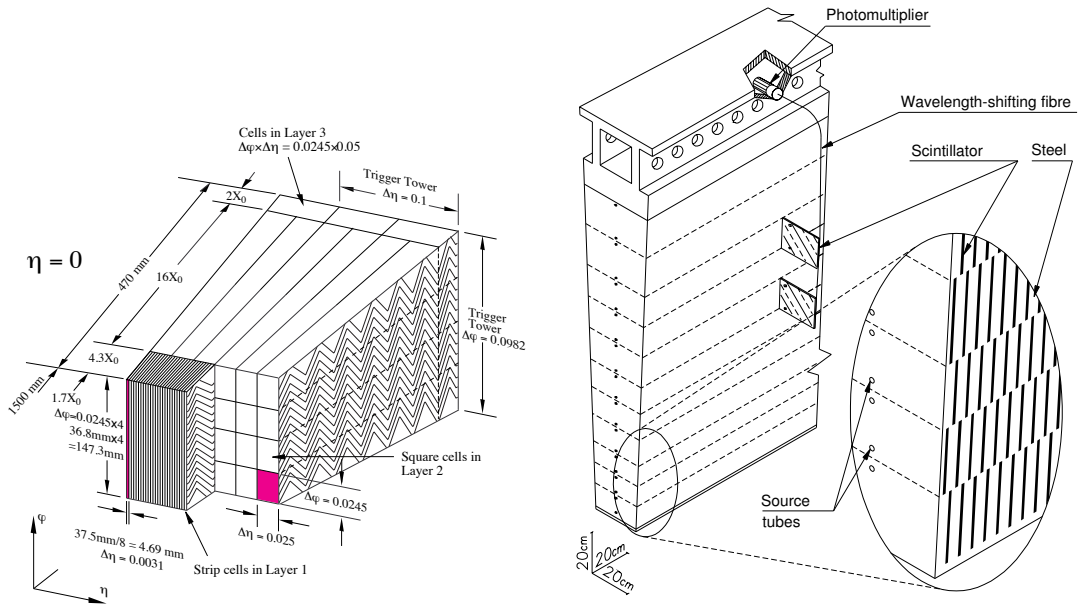

(a) (b)

Figure 4.7: The accordian geometry of the EM calorimeter system (left), and a tile calorimeter module (right) of the ATLAS detector. Taken from ref. [134].

contain very high-energy showers.

The active material in the barrel ($|\eta| < 0.9$) and extended barrel ($0.8 < |\eta| < 1.7$) of the ATLAS hadronic calorimeter is plastic scintillating tiles, while steel (λ_I = 16.8cm) is employed as the absorbing material. As a hadron interacts, photons are produced in the tiles at a rate proportional to the energy deposited, and collected with wavelength-shifting fibres in each cell. The cells are grouped together in η to form a module, and read out through photomultiplier tubes (PMTs)—see fig. 4.7(b). Similarly to the EM calorimeter, the tile calorimeter has three layers, but with a coarser granularity as hadronic showers are less compact than EM showers; the first layer has cells of $0.1 \times \pi/32$ in $\eta \times \phi$-space, for example.

The Hadronic EndCap (HEC) calorimeter uses LAr and copper as the active and absorbing materials, and is arranged in two wheels each of two layers; the first layer has 24 copper plates per module, while the second has just 16. The cells have size of $\sim 0.1 \times 0.1$ in $\eta \times \phi$-space in the range $1.5 < |\eta| < 2.5$, and 0.2×0.2 in $2.5 < |\eta| < 3.2$.

A special Forward Calorimeter (FCal) covers the region $3.1 < |\eta| < 4.9$. The extreme, high-energy particle flux in this region means the calorimeter needs to be radiation-hard, with a short radiation length so as to stop the high-energy particles. It consists of three layers; the first is an EM calorimeter, with LAr and copper (which has X_0 = 1.44cm and λ_I = 15.3cm, as well as the conductivity needed to effectively cool the material) as the active and absorbing materials. The two fol-

lowing layers are hadronic calorimeters, which employ LAr and tungsten (λ_I = 9.94cm) as the respective materials. In total, the FCal has 27.6 radiation lengths and 9.94 nuclear interaction lengths of calorimeter.

4.2.3 The Muon Spectrometer

The muon spectrometer (MS), which extends to $|\eta| < 2.7$, measures the momenta of muons by bending their trajectories through the use of a toroidal magnet system, and measuring the curvature. The magnetic field is produced by the large barrel toroid magnet ($|\eta| < 1.4$, ∼0.5 T) and smaller endcap magnets in the ends of the barrel toroid ($1.6 < |\eta| < 2.7$, ∼1.0 T); the magnetic field in the transition region ($1.4 < |\eta| < 1.6$) is a combination of the two fields.

There are two sub-detectors in each of the barrel and endcap, as shown in fig. 4.8. In both cases, one of the sub-detectors is used for fast, low-precision measurement (which can be employed by the trigger), and the other for slower but high-precision momentum measurement. The fast sub-detector uses Resistive Plate Chambers (RPCs) in the barrel ($|\eta| < 1.05$), with a resolution of 10mm × 10mm in $z \times \phi$-space, and Thin Gap Chambers (TGCs) in the endcap ($1.05 < |\eta| < 2.4$), with a resolution of 2–6mm×3–7mm in $r \times \phi$-space.The high-precision sub-detectors use Monitored Drift Tubes (MDTs) in both the barrel and endcap ($\eta < 2.7$) with a resolution of 35μm in the z or r dimensions.

The innermost module of the inner layer of the endcap has an additional set of Cathode Strip Chambers (CSCs), covering the smaller region of $2.0 < |\eta| < 2.7$ in which there is an increased particle flux. These provide a spatial resolution of 40μm but have a much shorter collection time than the MDTs, which would be overwhelmed if they were used in this high-flux region.

4.2.4 Trigger

The ATLAS trigger system has three levels, known as L1, L2 and Event Filter (EF), which are designed to reduce the event rate so as to record only interesting events. The frequency of collisions is 20 MHz, which needs to be reduced to nearer 200 Hz. While the trigger process is performed, a complete read-out of the detector is stored in a storage buffer, and discarded if it fails to pass the complete trigger chain.

The L1 trigger looks for high-p_{T} muons, electrons, photons, jets or hadronic taus, large missing transverse momentum ($E_{\mathrm{T}}^{\mathrm{miss}}$), or large total transverse energy. It takes data from the trigger chambers in the MS and reduced-granularity calorimeter information which is then compared by the central trigger processor against the trigger menu (a list of all desired combinations of triggers). Pre-

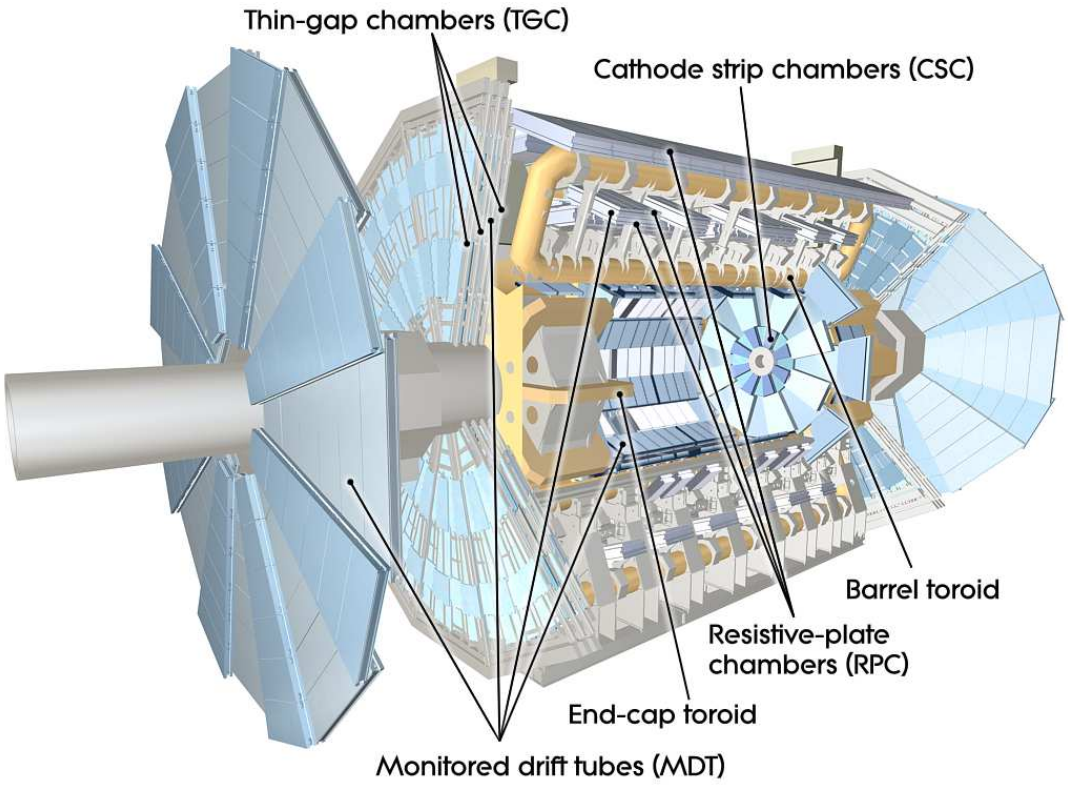

Figure 4.8: The muon system of the ATLAS detector. Taken from ref. [134].

scaling of menu items may be used at this point as it is useful for increasing sensitivity to low p_{T} events without being overwhelmed by di-jet events, however this is not often used in physics analyses where high-p_{T} objects are the most interesting. The L1 trigger takes $\sim$2.5μs to make a decision, thereby reducing the rate to 75kHz. It defines regions of interest (RoIs) (regions in (η, ϕ) that contain interesting features) and passes this information, along with the trigger menu option that was satisfied, to the L2 trigger.

The L2 trigger is seeded by the RoIs information, and matches the full granularity and precision data in each region ($\sim 2\%$ of the total event data) to information from the ID, before testing the event against a second trigger menu. It takes approximately 40ms to make a decision for each event, and reduces the rate to 3.5kHz. The EF uses an offline analysis procedure, including object calibrations, alignment corrections and so on, to make a final decision for each event. The processing time is much greater, at close to 4s, which reduces the rate to $\sim$200Hz.

The L2 and EF levels are referred to together as the High Level Trigger (HLT). Events passing the HLT are recorded to disk in RAW data format.

4.2.5 Event Simulation

The Monte Carlo (MC) *simulation* of events is an integral part of any analysis; it is used for generating possible new physics signals, checking our understanding of Standard Model (SM) processes, estimating the predicted background processes of an analysis, and estimating the calibration of various object parameters. To simulate such events, we need to generate the underlying, hard scattering process, propagate the resulting physical processes (decay, hadronisation, scattering and so on) to the final-state particles, and simulate the interaction of those particles with the materials of the detector to be able to compare the simulated events with the recorded data. A brief description of the simulation process is below, following closely the details in ref. [139].

The first step is to simulate the interaction of the two initial state partons, known as the *hard process*, calculated with a matrix element corresponding to one or more Feynman diagrams that describe the process. Spin interactions and interference effects are taken into account here, so the angular distributions of final state particles are affected by the number of partons specified in the hard process.

Higher-order quantum chromodynamics (QCD) effects are taking into account in the next stage, the *hadron shower*, where all partons (including those in the initial state) can split or radiate gluons, a process which may happen multiple times. This is followed by *hadronisation*, where coloured objects are combined into colourless hadrons, often producing short-lived resonances which then decay. Finally, the partons of the initial protons that were *not* involved in the hard process are allowed to interact, this is known as the *underlying event*.

The distribution of parton momenta within the proton is modeled with a Parton Distribution Function (PDF), the choice of which is a parameter of an analysis, and different PDFs are preferred for different processes. For example, the leading order (LO) PDFs CTEQ6L1 [140] and MSTW2008LO [141] are popular for the signal generation of new physics processes, while the next-to-leading-order (NLO) PDF CT10NLO [142] is more commonly used for SM background generation. In addition to the PDF, a specific tune (an adjustment of the underlying event model as well as the generator showering model) is often used to improve the agreement with data; a list of ATLAS tunes can be found at ref. [143].

Some generators, such as PYTHIA [144, 145], are able to perform all the generation steps listed above, however in the analyses described in this thesis, separate, specialist, generators are chosen to handle the matrix element calculation and parton showering separately. For example, the MADGRAPH generator [146] produces Feynman diagrams for a given process, as well as source code to compute

the corresponding matrix elements, and can do this to arbitrary orders of quantum electrodynamics (QED), QCD and new physics (NP) (although the number of diagrams increases rapidly with each increase in order, leading to a significant decrease in speed). The source code is then used to simulate events, where the parameters of SM and NP particles can be changed at will. Other generators used in this thesis include SHERPA [147], POWHEG [148–151], POWHEGBOX [152], ALPGEN [153], ACERMC [154, 155], MC@NLO [156, 157], HERWIG [158], JIMMY [159] and GG2WW [160]. QED radiative corrections are usually implemented using PHOTOS [161, 162], and tau decays with TAUOLA [163]. The output of event simulation is referred to as being at *truth-level* or *generator-level*, as it does not yet take into account the detector reconstruction of the events (and is in fact detector-independent).

All particles that are long-lived enough to reach the detector material before decaying (if they are not stable) are next propagated through a simulation of the ATLAS detector [164]. For full simulation of the detector, the GEANT4 [165] model is used, providing the best treatment of interactions by stepping the relativistic particles through the different materials in the detector and calculating all scattering, energy loss, charge deposition processes and so on. However, this method is computationally expensive, and often a faster, more approximate simulation is employed, known as Atlfast-II (AFII) [166], which simplifies the treatment of the ATLAS calorimeters.

To approximate the effect of pileup, a set of *minimum bias* events are overlaid, produced with a special PYTHIA8 LHC tune [164].

The final set of simulated events are recorded in Raw Digital Object (RDO) format, retaining the truth-level information.The RAW and RDO formats are very large and therefore not very user-friendly, so they are restricted to the first two tiers of the Worldwide LHC Computing Grid (WLCG) (known as 'the Grid' for short), Tier 0 and Tier 1. The information is instead converted to Event Summary Data (ESD) and Analysis Object Data (AOD) formats, where most of the information is discarded and only that needed to reconstruct interesting objects is retained. In Run I, the preferred format was known as Derived^3 Physics Data (D3PD), wherein some analysis selections were applied to reduce the dataset size, and the format was flattened from objects to types. In Run II, this was replaced with the xAOD format, similar to the AOD format but directly readable in ROOT [167].

4.3 Object reconstruction

The reconstruction of objects within the ATLAS detector will now be briefly described.

4.3.1 Electrons and photons

Electrons and photons are reconstructed from their tracks in the ID and the energy they deposit in the EM calorimeter. A cluster in the calorimeter is defined with a fixed size of 3×5 cells in the middle layer of the calorimeter, and the total energies of the three calorimeter layers in this window are summed. The window is then shifted until the total transverse energy is maximised; this is known as the *sliding-window* algorithm [168]. If the maximum E_{T} is greater than 2.5 GeV, the region is considered a seed, and is compared against tracks that have been reconstructed in the ID.

Electrons and photons can be distinguished by their signatures in the tracker, where a photon is neutral and so leaves no track, but the electron is charged and so is visible. If the cluster is matched to a track pointing to the IP, the cluster is tagged as an electron, while if there is no matching track in the detector, the cluster is tagged as an unconverted photon. If there is a matching track leading to a secondary vertex, rather than the IP, the cluster is tagged as a converted photon. Next, the clusters are rebuilt with 3×7 (5×5) central-layer cells in the barrel (endcap) for electrons and converted photons, and 3×5 (5×5) cells in the barrel (endcap) for unconverted photons.

While photons are relatively straightforward to identify, electrons have larger backgrounds (alternative particles which can mimic the electron signature of a collimated, contained signature in the EM calorimeter); in particular, jets will always be a non-negligible background to electrons as they have such a large cross section. For Run I data and simulation, three sets of criteria are available which balance the likelihood of including a fake electron coming from a jet against including as many real electrons as possible, labeled *loose*++, *medium*++ and *tight*++, with increasing purity and decreasing efficiency (see ref. [169, 170] for further details). The definitions are inclusive, so *medium*++ electrons satisfy all *loose*++ criteria, and *tight*++ electrons satisfy *medium*++ and *loose*++ definitions. All three electron identification definitions are used in the Run I analysis described later in this thesis.

The *loose*, *medium* and *tight* electron identification criteria were updated for Run II, using a likelihood-based method, and can be found in ref. [171]. Only *loose* electrons, which have an efficiency of $\sim$95% for electrons with $E_{\mathrm{T}} \simeq 40$ GeV [172],

are relevant for the Run II analysis described in this thesis.

Finally, once the electrons and photons have been reconstructed and identified, their energies are calibrated, and the electron cluster energy and track momentum measurements are combined, improving the resolution at low energies. Details of the calibration can be found in ref. [173].

4.3.2 Muons

The reconstruction of muons uses information from the ID and MS, and occasionally the calorimeter if the MS is not available. Hits in the layers of the MS are combined to create local track segments, which are combined in turn to build up a global MS track. A track in the ID is also constructed (satisfying certain quality constraints) which is then matched to a MS track.

Four types of muons are defined:

- **ComBined (CB) muons** result from a good match between tracks in the ID and MS, which are then combined to improve the resolution;
- **Segment Tagged (ST) muons** have a clear ID track that is matched only to track segments of the MS, and are useful for increasing the range of acceptance;
- **Stand Alone (SA) muons** can exist in the range $2.5 < |\eta| < 2.7$ where there is no ID coverage, they therefore have a track in the MS which is not matched to any in the ID; and
- **Calorimeter Tagged (CaloTag) muons** have an ID track matched to an energy deposit in the calorimeter but no MS track, and are used when there is a gap in the MS, such as for $|\eta| < 0.1$.

Different algorithms exist to combine the ID and MS information; so-called STAtistical COmbination (STACO) muons [174] are used in this thesis.

In Run II, inclusive *loose*, *medium* and *tight* identification criteria were defined for muons (see ref. [175]). *Loose* muons are used in this thesis, which include all the muon types described above, though CaloTag and ST muons are restricted to $|\eta| < 0.1$.

Once identified, the muon p_{T} scale and resolution are calibrated, by comparing di-muon invariant mass distributions against the well-understood J/ψ, Υ and Z peaks; see ref. [176] for further details.

4.3.3 Jets

Jets are reconstructed in the ATLAS detector predominantly using information from the calorimeters. Clustering in the calorimeter is based not on a sliding-window algorithm (as was used to identify electrons and photons in the EM calorimeter), but on topological clustering (creating so-called *topo-clusters*) which groups cells based on the significance of their neighbouring cells.[2] The topo-clusters are seeded by cells with a large signal-to-noise ratio $\Gamma \equiv |E_{\text{cell}}/\sigma_{\text{noise,cell}}| > 4$, where σ_{noise} is the width of noise and includes contributions from pileup. Neighbouring cells are then iteratively added to the cluster if they satisfy $\Gamma > 2$, and the first ring of cells with $2 > \Gamma > 0$ is included to define the edge of the cluster. Sub-clusters are split if there are local maximum cells with more than 500 MeV of energy, where cells belonging to more than one sub-cluster are weighted for each depending on their energy and distance to the local maxima. The topo-cluster energy is the sum of all the constituent cell energies, the mass is set to zero, and the position is obtained by weighting the η and ϕ of the contributing cells according to their (absolute) energies.

The sampling fraction of the calorimeter is used to estimate the actual energy of the particle shower, and the topo-clusters are then considered as reconstructed at the EM scale; these are sometimes known as *EM topo-clusters*, and can go straight into a jet-finding algorithm as described below. However, while this energy scale is appropriate for EM processes, hadronic processes require a further level of calibration to account for the high level of variability in the decay products they produce, and the energy they deposit in the calorimeter. The common scheme is called Local Hadronic Calibration (LC)[3], which classifies the topo-clusters as mainly electromagnetic or hadronic, and a calibration factor is applied to each cell depending on the cluster energy and the cell energy, where the factors are derived from single charged or neutral pion simulations. Specifically, weights are applied to correct for the non-compensation of the calorimeter material, and energy deposited outside the reconstructed clusters and in non-sensitive regions [177]. The resulting clusters are often called *LC topo-clusters*.

The calibrated topo-clusters are then used as inputs ('pseudoparticles') to the chosen jet-finding algorithm. A general sequential recombination algorithm uses distances d_{ij} between pseudoparticles i and j, where

$$d_{ij} = \min(k_{\text{T},i}^{2p}, k_{\text{T},j}^{2p}) \frac{\Delta_{ij}^2}{R^2} \ . \tag{4.2}$$

[2]This leads to clusters with variable numbers of cells, which is appropriate for jets since hadronic clusters have a more varied energy response compared to EM jets (formed by the energy deposits of electrons and photons).

[3]Note that this is also often written as *local cluster weighting* (LCW).

Here $k_{\mathrm{T},i}$ is the transverse momentum of object i, $\Delta_{ij} \equiv (y_i - y_j)^2 + (\phi_i - \phi_j)^2$, and R is a radius parameter. p is a parameter used to determine the relative power of the momentum and distance scales. An ordered list of all the distances d_{ij} and the adapted transverse momenta $k_{\mathrm{T},i}^{2p}$ is created; if the smallest element is one of the d_{ij}, the pseudoparticles i and j are added together to form a new pseudoparticle, and the process is repeated. If the smallest element is instead one of the $k_{\mathrm{T},i}^{2p}$, pseudoparticle i is removed, and considered a jet.

The jet algorithms used within this thesis are the anti-k_{T} algorithm [178], where p = -1, the Cambridge-Aachen (C/A) algorithm [179], where p = 0, and the inclusive k_{T} algorithm [180], where p = 1; each case produces an infra-red and collinear safe result. The radius parameter for narrow anti-k_{T} jets (generally arising from QCD processes) is commonly set to R = 0.4 or 0.6, while for large-radius jets (commonly used for identification of hadronically-decaying electroweak (EW) bosons, appearing in chapters 7 and 8 of this thesis) it is R = 1.0 or 1.2; the C/A algorithm is typically used for large-radius jets with R = 1.0 or 1.2.

The reconstructed jets are further calibrated with the Jet Energy Scale (JES), which is an extensive and constantly-evolving process, derived predominantly with simulation. The jet energy response $\mathcal{R}$ is defined by

$$\mathcal{R} = \left\langle \frac{E_{\text{reco}}}{E_{\text{truth}}} \right\rangle \ , \tag{4.3}$$

where E_{reco} is the energy of a jet reconstructed from calorimeter clusters and E_{truth} is the energy of a so-called *truth jet*, where the stable hadronised decay products are input as the jet constituents. Following corrections for pileup and jet origin (specifically, the jet should be pointing back to the IP), the inverse of the average response, as a function of energy and η, is applied as a correction factor. Following this step, jets are considered as EM+JES- or LC+JES-calibrated. To reduce the possible bias from a purely MC-derived JES, a residual correction has been obtained from *in situ* measurements, and is applied to jets in data. For further details, see for e.g. refs. [181–185].

Finally, the Jet Energy Resolution (JER) (the width of the response function of eq. 4.3) is given by

$$\frac{\sigma}{E} = \sqrt{\left\langle \left(\frac{E_{\text{reco}} - E_{\text{truth}}}{E_{\text{truth}}} \right)^2 \right\rangle - \left\langle \frac{E_{\text{reco}} - E_{\text{truth}}}{E_{\text{truth}}} \right\rangle^2} \tag{4.4}$$

Large-radius jets

Large-radius jets often undergo some form of grooming, designed to remove the soft components of a jet and thereby reducing the effects of pileup and the under-

lying event. There are three main categories [186]:

- **trimming:** the elements of a jet are reclustered (often with a different clustering algorithm) with a smaller radius parameter R_{subjet}, and the subjets are removed ('trimmed') if they carry less than some fraction f_{cut} of the original jet p_{T} [187];

- **pruning:** similar to trimming, the jet elements are reclustered, where the second element of each pair-wise clustering is discarded if the separation ΔR_{ij} is greater than $R_{\text{cut}} \times 2m_j/p_{\text{T},j}$, or if the p_{T} fraction of the softer subjet with respect to the p_{T} of the pair is smaller than a parameter Z_{cut} [188, 189];

- **split-filtering:** the last step of the C/A clustering of a large-R jets is reversed to produce two subjets, if these satisfy the momentum balance requirement $\sqrt{y_{12}} \equiv \min(p_{\text{T},1}, p_{\text{T},2})\Delta R_{12}/m_{12} > \sqrt{y_{\text{min}}}$ the jet proceeds to the filtering stage[4], otherwise the de-clustering process continues with the highest-mass subjet and iterates. To filter, the elements of the surviving jet are reclustered with R_{subjet} = min(0.3, ΔR_{12}), and any radiation outside the three hardest subjets is discarded [190].

Track jets

An alternative to calorimeter jets, track jets are reconstructed using charged-particle tracks left in the ID as input to the desired jet-finding algorithm. The tracks are required to satisfy $p_{\text{T}} > 500$ MeV and have at least one and six hits in the pixel and SCT sub-detectors respectively, while impact parameter requirements are imposed to ensure the tracks originate at the primary vertex so as to reduce the contribution from pileup.

b-jets

The identification of jets resulting from the decay of b-quarks, usually referred to as b-jets, is commonly used in ATLAS analyses, particularly for the identification of top-quarks which decay to a b-quark at least 90% of the time. The resulting b-quark itself decays via emission of a W boson to produce a lighter quark, most often a c-quark, with the decay of the W leading to a so-called *semi-leptonic* or *fully-hadronic* object. Compared to jets originating from light quarks or gluons,

[4]Note that a mass-drop requirement, $\mu_{12} \equiv \max(m_1, m_2)/m_{12} < \mu_{\text{frac}}$, is sometimes included to give the mass-drop filtering algorithm, and is used in the analysis of chapter 7. This was dropped for Run II analyses, and demonstrated in ref. [186] to be redundant.

b-jets produce a different shower profile, and their fast decay can lead to a secondary displaced vertex, meaning they can be identified with some degree of certainty (often with multivariate analysis (MVA) techniques).

In Run I, the most common *b-tagging* algorithm was the MV1 tagging algorithm [191, 192], performed on anti-k_{T}, R = 0.4, LC-topo jets. Working points defined by the b-tagging efficiency were defined, and calibrated in a di-lepton control region [192]. In early Run II, the preferred b-tagging algorithm was the MV2c20 tagger [191–193], performed on anti-k_{T}, R = 0.2, *track* jets rather than calorimeter jets, and taking advantage of improvements in track reconstruction [193–195].

4.3.4 Tau leptons

The tau is the heaviest of the leptons, and will decay before reaching the active parts of the ATLAS detector, meaning it can only be identified by its decay products. If it decays leptonically, we observe one of the lighter charged leptons, which cannot be distinguished from those produced directly via other processes. Leptonically-decaying tau leptons must therefore be included (usually as a background) in any analysis involving electrons or muons. The heavy mass of the tau (1.777 GeV [48]) means that it can also decay hadronically, which it does approximately 65% of the time. Taus usually decay to a particular mix of charged and neutral hadrons, and so methods have been developed to identify the hadronically-decaying tau. This identification, and in particular the calibration of the energy scale of hadronic taus, is the topic of chapter 5.

As with the other charged leptons described above, three working points for tau leptons are defined, labeled *loose*, *medium* and *tight*, based on a boosted decision tree (BDT) algorithm designed to reject electrons and jets. See ref. [1] for further details.

4.3.5 Missing transverse momentum

Missing transverse momentum, sometimes referred to as missing transverse energy and denoted $E_{\mathrm{T}}^{\mathrm{miss}}$, is a way to measure the balance of momentum of an event in the transverse plane (the $x-y$ plane), since the initial transverse momentum of the incoming protons is close to zero. If all products of the collision were observable, the $E_{\mathrm{T}}^{\mathrm{miss}}$ would also be close to zero, however 'true' $E_{\mathrm{T}}^{\mathrm{miss}}$ comes from invisible products (such as the SM neutrino, or more exotic new particles such as dark matter (DM)), and 'fake' $E_{\mathrm{T}}^{\mathrm{miss}}$ from mismeasured energies of other visible objects.

The following paragraphs describe the calorimeter-based $E_{\mathrm{T}}^{\mathrm{miss}}$ commonly used in Run I analyses (known as `RefFinal`), and are based on refs. [196, 197]. The minor changes implemented for $E_{\mathrm{T}}^{\mathrm{miss}}$ calculations in Run II are described at the end of this section, and are based on ref. [198].

Missing transverse momentum is defined as the negative vector sum of the $\vec{p}_{\mathrm{T}}$ of visible objects in the detector, and is denoted $\vec{E}_{\mathrm{T}}^{\mathrm{miss}}$, however it is common to refer to the magnitude, $E_{\mathrm{T}}^{\mathrm{miss}}$. The total $E_{\mathrm{T}}^{\mathrm{miss}}$ is a combination of the x- and y-components, according to

$$\begin{aligned} E_{\mathrm{T}}^{\mathrm{miss}} &= \sqrt{(E_x^{\mathrm{miss}})^2 + (E_y^{\mathrm{miss}})^2}\ , \\ \phi^{\mathrm{miss}} &= \arctan(E_y^{\mathrm{miss}}/E_x^{\mathrm{miss}})\ . \end{aligned} \tag{4.5}$$

Most objects deposit their energy in the ATLAS calorimeter, with the significant exception of muons (as they are MIPs), and so the $E_{\mathrm{T}}^{\mathrm{miss}}$ is calculated from a combination of the calorimeter and muon terms:

$$E_i^{\mathrm{miss}} = E_i^{\mathrm{miss,\,calo}} + E_i^{\mathrm{miss},\,\mu} \tag{4.6}$$

where $i = x, y$. The muon term is calculated from muons observed in the MS, according to

$$E_i^{\mathrm{miss},\,\mu} = -\sum_{\mathrm{muons}} p_i^{\mu} \tag{4.7}$$

where $i = x, y$, and the muons are required to be within $|\eta| < 2.7$. Only *combined* muons are considered in the region of tracker coverage ($|\eta| < 2.5$), to suppress contributions from fake muons.

The calorimeter term, $E_i^{\mathrm{miss,\,calo}}$, consists of contributions from reconstructed objects (described below), according to

$$E_i^{\mathrm{miss,\,calo}} = E_i^{\mathrm{miss},\,e} + E_i^{\mathrm{miss},\,\gamma} + E_i^{\mathrm{miss},\,\tau_{\mathrm{had}}} + E_i^{\mathrm{miss,\,jets}} + E_i^{\mathrm{miss},\,\mu,\,\mathrm{calo}} + E_i^{\mathrm{miss,\,SoftTerm}}\ , \tag{4.8}$$

where τ_{had} is a hadronically-decaying tau, and *SoftTerm* refers to topo-clusters not already associated to any reconstructed object. In the case of overlapping objects, the order of priority is left to right in eq. 4.8, meaning (for example) that a calorimeter cell which is associated to both an electron and a jet will only be considered as part of the electron. Each term is calculated from the negative sum of cell energies in the reconstructed objects, according to

$$E_x^{\text{miss, term}} = -\sum_{i=1}^{N_{\text{cell}}^{\text{term}}} E_i \sin(\theta_i)\cos(\phi_i)$$
$$E_y^{\text{miss, term}} = -\sum_{i=1}^{N_{\text{cell}}^{\text{term}}} E_i \sin(\theta_i)\sin(\phi_i) \tag{4.9}$$

where E_i, θ_i and ϕ_i are the energy, polar angle and azimuthal angle of each cell. Notably, the energies are *calibrated* according to the reconstructed object with which each cell is associated. See ref. [196] for details of the constituent objects.

$\boldsymbol{E}_{\mathbf{T}}^{\mathbf{miss}}$ in Run II

In Run II, the change in the $E_{\mathrm{T}}^{\mathrm{miss}}$ calculation that is relevant to this thesis is in the SoftTerm, which, rather than being measured in the calorimeter, is instead measured from tracks in the ID, and so is known as the track-based soft term (TST) [198]. Such a change is driven by the fact that tracks can be matched to the primary vertex, thus reducing the sensitivity of the SoftTerm to pileup.

Tracks in the ID are required to satisfy $p_{\mathrm{T}} > 0.4$ GeV, $|\eta| < 2.5$, and additional quality requirements [184]. They should pass requirements on the number of hits in the ID, and resulting vertices are required to pass cuts on the impact parameters ($|d_0|, |z_0| < 1.5$cm). The tracks that contribute to the SoftTerm must not already be matched to a reconstructed object, be matched to the primary vertex, and survive overlap removal cuts with calorimeter clusters: tracks are removed if they are within $\Delta R < 0.05$ of an e/γ cluster, or $\Delta R < 0.2$ of a tau, or ghost-associated to a jet [199, 200]; ID tracks associated to a combined or segment-tagged muon are replaced with the combined ID+MS fit. Additionally, tracks with a momentum uncertainty of greater than 40% are removed.

Removing the muon contribution

In some cases, the p_{T} of muons is summed back into the $E_{\mathrm{T}}^{\mathrm{miss}}$, effectively removing it from the calculation and making muons a source of missing transverse momentum. This type of $E_{\mathrm{T}}^{\mathrm{miss}}$ is denoted in this thesis as $E_{\mathrm{T,\,no}\,\mu}^{\mathrm{miss}}$, and is important to the analysis described in chapter 8.

Such an approach may be taken for a few reasons. The $E_{\mathrm{T}}^{\mathrm{miss}}$-based trigger is purely calorimeter-based and therefore does not include the contribution from muons, so analyses which use this trigger may set a cut on $E_{\mathrm{T,\,no}\,\mu}^{\mathrm{miss}}$ to ensure they define a signal region where the trigger is fully efficient. Additionally, data-driven background estimations in control regions refined by one or two muons

(such as $W \to \mu\nu$ and $Z \to \mu\mu$) become simpler when muons are no longer included in the $E_{\mathrm{T}}^{\mathrm{miss}}$ calculation; see sec. 8.4.

Track-based $\boldsymbol{E_{\mathrm{T}}^{\mathrm{miss}}}$

An alternative to the calorimeter-based $E_{\mathrm{T}}^{\mathrm{miss}}$ definition described above is the use of track-based $E_{\mathrm{T}}^{\mathrm{miss}}$, denoted $\vec{p}_{\mathrm{T}}^{\,\mathrm{miss}}$. This is calculated fully from tracks in the ID, which must satisfy constraints such as those for the TST. When large $E_{\mathrm{T}}^{\mathrm{miss}}$ is required in an analysis (such as the mono-X analyses which are the main topic of this thesis), track-based $E_{\mathrm{T}}^{\mathrm{miss}}$ is useful for reducing fake $E_{\mathrm{T}}^{\mathrm{miss}}$, particularly that which arises through mismeasurement of a jet in a di-jet event. Requiring that the track-based $E_{\mathrm{T}}^{\mathrm{miss}}$ is relatively large, aligned with the calorimeter-based $E_{\mathrm{T}}^{\mathrm{miss}}$, and not aligned with a jet, are all effective 'anti-QCD' selections.

Chapter 5

Corrections to the Tau Energy Scale

The tau lepton, denoted τ, is the heaviest lepton in the Standard Model (SM) with a mass of 1.777 GeV [48], and features in many ATLAS analyses, such as measurements of SM processes [201–205] and searches for the Higgs boson [206], or new physics searches including Supersymmetry [207–209], extended Higgs sectors [210–212], heavy bosons [213], leptoquarks [214], etc. Good performance of the ATLAS detector is required both to identify tau leptons and reduce the tau energy scale uncertainties and resolution, and to do this well over a large energy range ($p_{\mathrm{T}} \sim$ 15 GeV – few TeV). The tau has a relatively short decay length of 87μm, and therefore generally decays before reaching the active regions of the ATLAS detector. As a result, while the lighter charged leptons are observed directly within the detector, the tau is observed instead through its decay products; more specifically, the *visible* decay products, since at least one neutrino is always produced in tau decay but is invisible to the detector. The tau decays leptonically approximately 35% of the time (however the electron or muon cannot be distinguished from those arising in direct production processes), and to hadrons the rest of the time. Of the hadronic decays, 72% include a single charged pion (a *charged track*, from a *1-prong* tau), 22% contain three charged pions (from a *3-prong* tau), and the majority of the remaining decays produce charged kaons. Up to one additional neutral pion is produced in 78% of hadronic decays. The dominant decay modes are listed in table 5.1. The visible decay products of the hadronic tau decay are referred to as τ_{had}, and manifest in the detector as a jet.

Topoclusters that are reconstructed into hadronic taus are calibrated at the Local Hadronic Calibration (LC) scale, described in sec. 4.3.3. While this does a reasonable job for narrow jets produced by far more common quantum chromodynamics (QCD) processes (in conjunction with the Jet Energy Scale (JES)), it is not optimised or sufficient for the specific behaviour of hadronic taus: the particular mix of charged hadrons produced in the decay, and a more collimated decay requiring a narrower cone size (ΔR = 0.2). (It also does not correct for the under-

Type	Process	Branching fraction [%]
leptonic	$\tau^+ \to e^+\nu_e\bar{\nu}_\tau$	17.8
	$\tau^+ \to \mu^+\nu_\mu\bar{\nu}_\tau$	17.4
hadronic (1-prong)	$\tau^+ \to \pi^+\bar{\nu}$	10.8
	$\tau^+ \to \pi^+\pi^0\bar{\nu}$	25.5
	$\tau^+ \to \pi^+\pi^0\pi^0\bar{\nu}$	9.3
	$\tau^+ \to \pi^+\pi^0\pi^0\pi^0\bar{\nu}$	1.1
hadronic (3-prong)	$\tau^+ \to \pi^+\pi^+\pi^-\bar{\nu}$	9.0
	$\tau^+ \to \pi^+\pi^+\pi^-\pi^0\bar{\nu}$	2.7

Table 5.1: The dominant decay modes of the tau. Note that processes with opposite charge are implied. Rare decay modes (with five charged pions, or to kaons) are not shown. Adapted from ref. [48].

lying event or for pileup contributions.) A further calibration, known as the Tau Energy Scale (TES), is therefore desirable, which takes advantage of these aspects of hadronic taus. The TES is derived from simulation, and is designed to calibrate the energy of the reconstructed tau to within a few percent of the true energy scale (i.e. the energy of the tau at generator-level), and thereby also improve the energy resolution. To ensure there is no bias introduced from a purely simulation-based calibration, uncertainties on the modeling can be obtained by studying the difference between data and simulation using an *in situ* method with $Z \to \tau_{\text{lep}}\tau_{\text{had}}$ events. This method can also provide small data-driven corrections to the TES.

Work on the TES calibration was performed by other members of the ATLAS Tau Working Group, and is discussed in broad detail in sec. 5.1, to provide context for the work of the author on the *in situ* study of corrections to the TES, discussed in finer detail in sec. 5.2.

5.1 The Tau Energy Scale

This section describes work performed by other members of the ATLAS Tau Working Group, and is included to provide context for the following section on corrections to the TES. It follows closely the description given in ref. [1].

Calculation of the TES uses simulated events of $Z \to \tau\tau$, $W \to \tau\nu$ and $Z' \to \tau\tau$ processes simulated with PYTHIA8 [145]. Reconstructed τ_{had} candidates are required to satisfy $E_{\text{T}} > 15$ GeV and $|\eta| < 2.4$, ΔR(other jets) > 0.5, and be matched to a true τ_{had} with $E_{\text{T,vis}}^{\text{true}} > 10$ GeV. Additionally, they must meet *medium* tau iden-

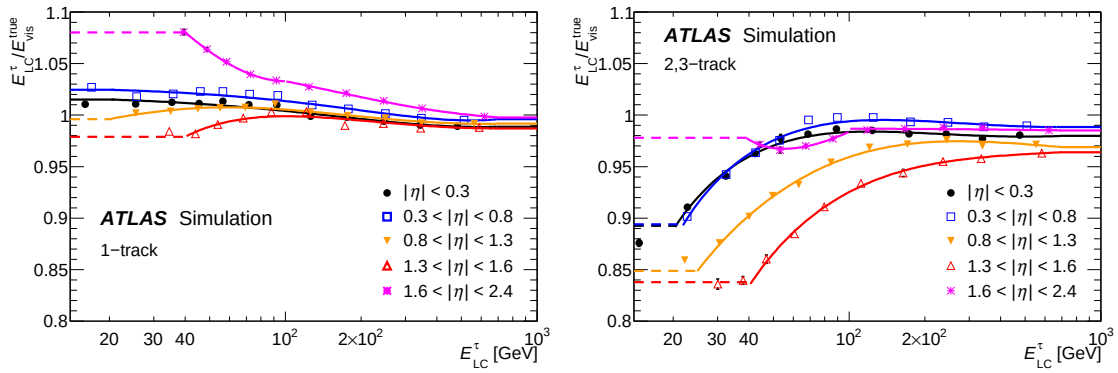

(a) (b)

Figure 5.1: τ_{had} energy response curves as a function of the reconstructed τ_{had} energy E^{τ}_{LC} for hadronic tau decays with (a) one and (b) more than one associated tracks. Each curve corresponds to a region of absolute pseudorapidity. The region where markers are shown corresponds approximately to a transverse energy $E^{\tau}_{\text{T,LC}} > 15$ GeV. For very low and very high energies, the response curves are assumed to be constant. Taken from ref. [1].

tification criteria.

For each reconstructed tau, the ratio of the reconstructed energy at the LC scale E^{τ}_{LC} to the true visible energy $E^{\text{true}}_{\text{vis}}$ is calculated. The reconstructed taus are then binned according to the number of charged tracks (1 or more than 1), intervals of pseudorapidity ($|\eta| < 0.3$, $0.3 < |\eta| < 0.8$, $0.8 < |\eta| < 1.3$, $1.3 < |\eta| < 1.6$, and $1.6 < |\eta| < 2.4$), and intervals of $E^{\text{true}}_{\text{vis}}$. In each bin, the distribution of the $E^{\tau}_{\text{LC}}/E^{\text{true}}_{\text{vis}}$ ratio is fitted with a Gaussian and the mean value is calculated from this. The mean values, as a function of the average E^{τ}_{LC} in each bin, are then fitted with an empirically-derived functional form; this is known as a response curve, and is a preliminary form of the TES calibration. These response curves are shown in fig. 5.1.

Further corrections are then calculated and applied. The first addresses a pseudorapidity bias, introduced by underestimated reconstructed cluster energies in poorly instrumented regions of the ATLAS detector. This bias is found to be non-negligible only in the transition region of the detector, where the correction is smaller than 0.01. The final pseudorapidity correction is implemented with $\eta^{\text{reco}} = \eta^{\text{LC}} - \eta^{\text{bias}}$. The second correction addresses the effect of pileup contributions to the reconstructed energy, which are not taken into account by the LC scale. In each event, the number of reconstructed proton-proton interaction vertices, n_{vtx}, is obtained, and a proportional amount of energy is subtracted; the energy subtracted per vertex is derived for different regions of $|\eta^{\text{reco}}|$ and number of associated tracks, and is within the range of 90–420 MeV (increasing with $|\eta|$). Overall, these additional pseudorapidity and pileup corrections adjust the TES

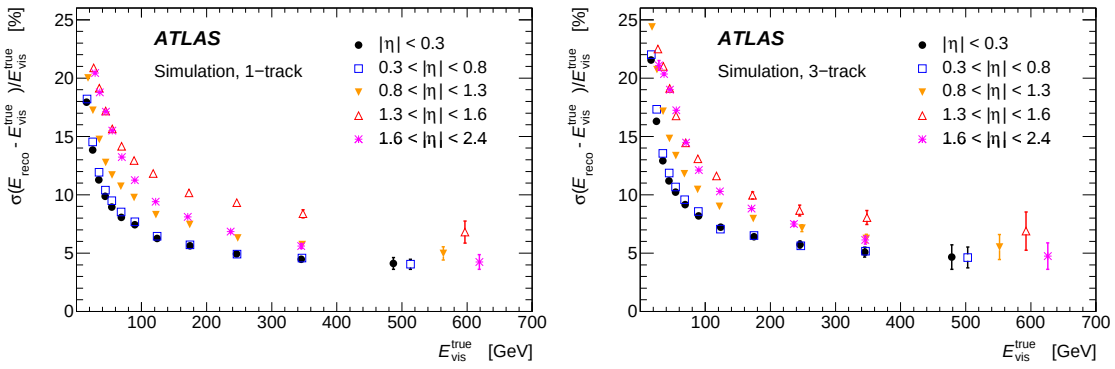

(a) (b)

Figure 5.2: Energy resolution for hadronically decaying tau leptons, separately for (a) one and (b) three associated tracks and for different pseudorapidity regions. The resolution shown is the standard deviation of a Gaussian function fit to the distribution of $(E_{\text{reco}} - E_{\text{vis}}^{\text{true}})/E_{\text{vis}}^{\text{true}}$ in a given range of $E_{\text{vis}}^{\text{true}}$ and $|\eta_{\text{vis}}^{\text{true}}|$. Taken from ref. [1].

by less than 2%.

Once the further corrections are applied, the energy resolution is determined, defined by $\sigma(E_{\text{reco}} - E_{\text{vis}}^{\text{true}})/E_{\text{vis}}^{\text{true}}$ (where σ is the standard deviation of a Gaussian fit to the variable in brackets), and again binned according to number of associated tracks and pseudorapidity. For true visible energies above a few hundred GeV the resolution is approximately 5%, and increases to 20–25% for very low $E_{\text{vis}}^{\text{true}}$. Plots of the resolution, as a function of $E_{\text{vis}}^{\text{true}}$, are shown in fig. 5.2.

5.2 Corrections to the Tau Energy Scale

As described above, the TES calibration is derived purely with simulation, to obtain agreement between the true energy scale (at generator-level) and the reconstructed energy. Therefore, in addition to uncertainties on the absolute TES, uncertainties on the modeling are also necessary, to check for any bias that may have been introduced in the simulation-based TES.

Systematic uncertainties on the TES are calculated with two methods. The deconvolution method, described briefly in ref. [1] and following an almost identical method to ref. [215], allows estimation of uncertainties on both the absolute TES by looking at differences between the true and reconstructed visible energies, as well as the modeling by comparing simulation directly with data. The *in situ* method, described in this section, looks just at the modeling, using a tag-and-probe study of a highly pure sample of hadronically-decaying taus in $Z \to \tau_{\text{lep}}\tau_{\text{had}}$ events. Both methods also provide small data-driven corrections to the TES.

The remainder of this chapter describes work performed by the author in col-

laboration with another student, unless otherwise stated.

The visible mass of a Z boson decaying to a leptonic tau (that is, a tau that decays to an electron or muon) and a hadronic tau (which produces a jet of hadrons) is given by

$$\begin{aligned} m_{\text{vis}} &= \sqrt{|p^{\text{lep}} + p^{\tau_{\text{had}}}|^2} \\ &\simeq \sqrt{2p_{\text{T}}^{\text{lep}} p_{\text{T}}^{\tau_{\text{had}}} (\cosh(\Delta\eta) - \cos(\Delta\phi)))} \end{aligned} \tag{5.1}$$

where p^{lep} is the momentum of the lepton from the decay of the leptonic tau, $p^{\tau_{\text{had}}}$ is the momentum of the visible decay products of the other hadronic tau, and $\Delta\eta$ and $\Delta\phi$ are the differences in pseudorapidity and azimuthal angle between them.

The *in situ* method of obtaining corrections to the TES is based on the idea that a small linear change in the p_{T} of the hadronic tau will shift the visible mass of the Z in a corresponding small linear fashion. That is, if we shift the p_{T} of all τ_{had} in a sample of $Z \to \tau_{\text{lep}}\tau_{\text{had}}$ events according to

$$p_{\text{T}}^{\tau\prime} = (1 + \alpha)p_{\text{T}}^{\tau}\,, \tag{5.2}$$

this leads to a change in the peak position of the distribution of the visible mass of the Z boson, as

$$\begin{aligned} m_{\text{vis}}{}' &\simeq \sqrt{2p_{\text{T}}^{\text{lep}}(1 + \alpha)p_{\text{T}}^{\tau\text{-had-vis}} (\cosh(\Delta\eta) - \cos(\Delta\phi)))} \\ &\simeq (1 + \frac{1}{2}\alpha)m_{\text{vis}} \end{aligned} \tag{5.3}$$

for small values of α. A comparison of the peak postion in data and in simulation is therefore a simple way to estimate what the small correction to the tau p_{T}, α, should be.

5.2.1 Data and simulation

The data used in this study were collected with the ATLAS detector during 2012. The total integrated luminosity during this time is equal to 20.3 fb^{-1}, collected at a centre-of-mass energy of the colliding protons of $\sqrt{s}$ = 8 TeV.

The simulation of the $Z \to \tau_{\text{lep}}\tau_{\text{had}}$ signal and expected SM backgrounds is performed in steps, from matrix element (ME) generation (using ALPGEN [153], HERWIG [216, 217], MC@NLO [156] or ACERMC [154, 155]), simulation of parton fragmentation and hadronisation (using PYTHIA6 [144] or HERWIG), underlying event (UE) modeling (using PYTHIA6 or JIMMY [159]), to simulation of the interaction of particles produced in the collisions with the detector material (using GEANT4 [165]). The Parton Distribution Function (PDF) used in the generation

comes from either CTEQ6L1 [140] or CT10 [142]. The UE simulation is tuned (using PERUGIA2011C [218], AUET2 [219] or AUET2B [143] tunes) based on studies of collision data. Recommendations from the ATLAS collaboration, based on specific performance studies for each process, are used to choose the best programs at each step of the generation. In each case, tau decays are modeled by TAUOLA [163, 220], and radiative corrections to particle decays are included by PHOTOS [221]. Corrections based on the pileup conditions (in-time and out-of-time) are implemented following minimum bias collision simulations performed with PYTHIA8 [222].

The details of simulation for each of the signal and background samples are listed in table 5.2. In each case, the simulation is scaled according to the total luminosity obtained in data, and the next-to-leading-order (NLO) cross section, to obtain the number of events expected in each process.

We note here that an alternative signal sample was tested, using an embedding method (see ref. [223] for details of the embedding procedure). This method takes $Z \to \mu\mu$ events from data, and creates a $Z \to \tau\tau$ sample by replacing the muons with simulated taus at the level of reconstructed tracks and calorimeter cells. However, the resulting systematic uncertainties from this procedure, particularly those arising from both the muon isolation and the removal of the muon energy in the calorimeter, were larger than those obtained through pure simulation of $Z \to \tau\tau$ events, and so this alternative signal sample is not used.

5.2.2 Object and event selection

First we describe the selection of physics objects and events, where the objective is to obtain a highly pure sample of signal events ($Z \to \tau_{\text{lep}}\tau_{\text{had}}$). While theoretically the leptonic tau is just as likely to decay to an electron as to a muon (a consequence of lepton universality), we include only events where the leptonic tau decays to a muon and muon neutrino, and veto events containing an electron. This is because electrons are more likely to be reconstructed as a τ_{had} than muons, and because the uncertainty on the electron energy reconstruction is larger than that of the muon.

Events are preselected with a single-muon trigger; at Event Filter (EF) level, events must contain an isolated muon with $p_{\text{T}}^{\mu} > 24$ GeV (which fires the so-called `EF_mu24i_tight` trigger) or a muon with $p_{\text{T}}^{\mu} > 36$ GeV with no isolation requirement (which fires the `EF_mu36_tight` trigger) [224, 225].

Offline, objects identified as muons are produced by the combined STACO reconstruction algorithm, see sec. 4.3.2. A muon candidate (the 'tag' of our tag-and-probe method) must satisfy $p_{\text{T}}^{\mu} >$26 GeV and $|\eta^{\mu}| < 2.5$, to ensure it lies in

Process	ME Generator	Parton shower, UE	PDF	Tune
Z	ALPGEN	PYTHIA6	CTEQ6L1	PERUGIA2011C
$\gamma^* \to \ell^+\ell^-$	ALPGEN	HERWIG + JIMMY	CTEQ6L1	AUET2
W	ALPGEN	PYTHIA6	CTEQ6L1	PERUGIA2011C
W^+W^-	ALPGEN	HERWIG + JIMMY	CTEQ6L1	AUET2
$W^\pm Z$	HERWIG	HERWIG	CTEQ6L1	AUET2
ZZ	HERWIG	HERWIG	CTEQ6L1	AUET2
$t\bar{t}$	MC@NLO	HERWIG + JIMMY	CT10	AUET2
single-top (s-channel)	MC@NLO	HERWIG + JIMMY	CT10	AUET2
single-top ($W^\pm$-channel)	MC@NLO	HERWIG + JIMMY	CT10	AUET2
single-top (t-channel)	ACERMC	PYTHIA6	CTEQ6L1	AUET2B

Table 5.2: The signal and background samples considered in this analysis, and the various programs and associated parameters used to simulate them at matrix element level and to model the parton showering and hadronisation and underlying event.

the plateau of the muon trigger efficiency curve. To satisfy track quality requirements, the muon track should have a minimum distance from the primary vertex in the z direction of less than 10 mm. Finally, the muon must be isolated as this is the strongest discriminator against QCD multijet events: the summed p_{T} and summed E_{T} of tracks in the EM and hadronic calorimeters within a cone of ΔR = 0.4 and 0.2 of the muon, but not associated to the muon, known as p_{T}Cone40 and E_{T}Cone20 respectively, must not be greater than 6% of p_{T}^{μ}.

Reconstructed hadronic taus (the 'probe') must satisfy $p_{\mathrm{T}}^{\tau_{\mathrm{had}}} > 20$ GeV and $|\eta^{\tau_{\mathrm{had}}}| < 2.5$. As the study is of minor corrections to the energy calibration, the TES should already have been applied to the energy of reconstructed hadronic taus. To reduce contamination from jets, the tau candidates should satisfy *medium* identification requirements, by passing the JetBDTSigMedium flag [1], have either one or three associated tracks, and have an electric charge of ± 1. If more than one hadronic tau candidate is identified, that with the largest p_{T} is selected. An event is vetoed if the tau candidate is also consistent with being a muon of $p_{\mathrm{T}} > 4$ GeV, or a *medium* electron with $p_{\mathrm{T}} > 15$ GeV.

Selected events require that the reconstructed primary vertex have at least four associated tracks. To reject events originating from cosmic ray backgrounds, non-collision backgrounds or calorimeter noise, events should satisfy data quality requirements which ensure that each sub-system of the ATLAS detector was working properly when the data were collected [226]. Each event should contain exactly one muon and at least one hadronically-decaying tau candidate; the muon and tau are required to have charges of opposite sign. The muon and tau are required to be relatively close in pseudorapidity, such that $|\eta_{\tau_{\mathrm{had}}} - \eta_{\mu}| < 1.5$.

The main background to the $Z \rightarrow \tau_{\mathrm{lep}}\tau_{\mathrm{had}}$ signal comes from $W(\rightarrow \mu\nu)$+jets events, where a jet is misidentified as a hadronic tau. We implement three additional selection criteria to reduce this background as much as possible. Firstly, we require that $p_{\mathrm{T}}^{\tau_{\mathrm{had}}} - p_{\mathrm{T}}^{\mu} >$ -15 GeV, motivated by the expectation that the visible hadronic tau (produced in association with a single neutrino) will have a larger transverse momentum than the muon (produced with two neutrinos); this serves to reduce the W+jets background, as the lepton from the W decay is often produced with a higher p_{T} than the misidentified jet. The transverse mass of a leptonically-decaying W boson is defined as

$$m_{\mathrm{T}} = \sqrt{2p_{\mathrm{T}}^{\mu} \cdot E_{\mathrm{T}}^{\mathrm{miss}}(1 - \cos\Delta\phi(\mu, E_{\mathrm{T}}^{\mathrm{miss}}))}\,, \tag{5.4}$$

this variable peaks at around 80 GeV for W+jets events. To further reduce this background, we require that $m_{\mathrm{T}} < 50$ GeV. Finally, we impose

$$\cos\Delta\phi(\tau_{\text{had}}, E_{\text{T}}^{\text{miss}}) + \cos\Delta\phi(\mu, E_{\text{T}}^{\text{miss}}) > -0.5\,. \tag{5.5}$$

This variable peaks at zero for signal events, as the neutrinos tend to point in the direction of the Z decay products, but is consistently less than zero for W+jets, where the neutrino instead points away from the lepton candidates. Studies showed that a cut tighter than -0.3 created an artificial shift in the visible mass peak towards a lower value.

The distributions of the latter four variables discussed above are shown in fig. 5.3. In each case, all selections except that affecting the variable shown are applied. The distributions of the visible mass m_{vis} following all selections are shown in figs. 5.4(a) and (b) for the 1-track and 3-track cases respectively.

5.2.3 Background estimation

The dominant backgrounds in this analysis are W+jets events and the multijet background from QCD processes, followed by Z+jets events, with minor contributions from $t\bar{t}$, single-top and diboson (W^+W^-, $W^\pm Z$, ZZ) events. With the exception of the diboson events, most background events contain at least one so-called *non-prompt* μ or τ_{had} (hereon referred to as *non-prompt backgrounds*), which is either a misidentified object, or produced through hadron decay or interaction with matter. While a non-prompt lepton is unlikely to be selected, the high production rate means non-prompt backgrounds are non-negligible. Non-prompt leptons are poorly modeled by simulation; background processes with one non-prompt lepton are therefore normalised with a data-driven scale factor (while keeping the distribution shape from simulation), while those with two non-prompt leptons (prevalent in the multijet background) are estimated with a purely data-driven method.

To estimate these backgrounds we use the $OS - SS$ method, which arises from the fact that there is no charge correlation between the μ and τ_{had} in the non-prompt backgrounds, whereas prompt backgrounds (where the μ and τ_{had} are produced directly in the primary interaction, or through the decay of a W, Z, H or τ) generally produce leptons of opposite-sign. We can therefore use the same-sign (SS) region to isolate the non-prompt backgrounds.

The $OS - SS$ method is based around a data-driven estimation of the multijet background. We begin with a SS control region (CR) which is defined with the same selection as the signal region (SR) except that the μ and τ_{had} are required to have charge of the same sign. We subtract the contribution from backgrounds containing at least one prompt lepton, where these are estimated from simulation but normalised with a data-driven scale factor (the derivation of which is

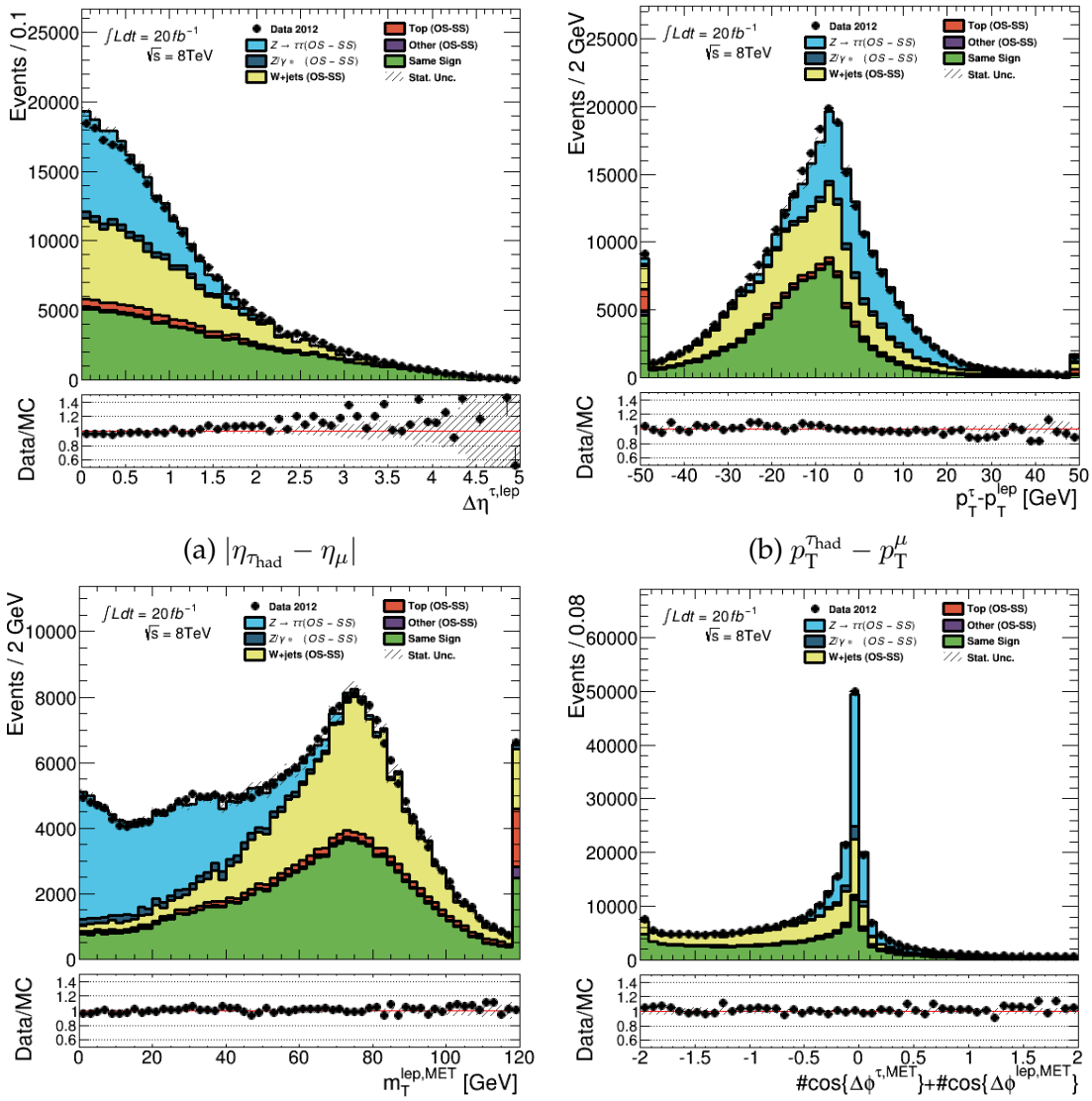

(a) $|\eta_{\tau_{\text{had}}} - \eta_{\mu}|$

(b) $p_{\text{T}}^{\tau_{\text{had}}} - p_{\text{T}}^{\mu}$

(c) m_{T}

(d) $\cos\Delta\phi(\tau_{\text{had}}, E_{\text{T}}^{\text{miss}}) + \cos\Delta\phi(\mu, E_{\text{T}}^{\text{miss}})$

Figure 5.3: The distributions of four variables used to select $Z \to \tau_{\text{lep}}\tau_{\text{had}}$ signal events and to reduce the main background $W(\to \mu\nu)$+jets. In each case, all cuts except that affecting the shown variable are applied.

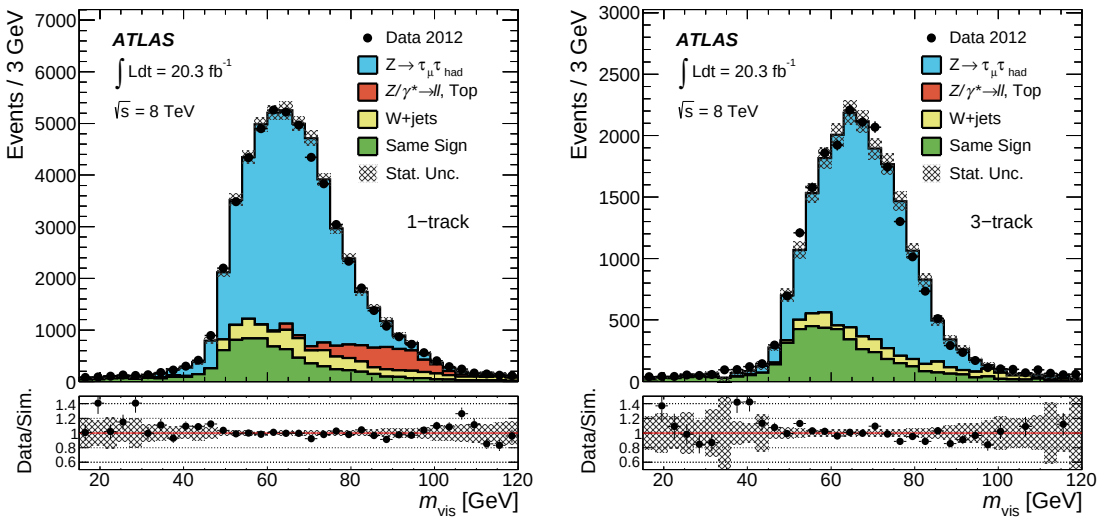

(a) 1 associated track (b) 3 associated tracks

Figure 5.4: The m_{vis} distributions, comparing simulation and data, for τ_{had} with (a) one and (b) three associated tracks.

described below), to leave the multijet contribution:

$$N_{SS}^{\text{multijet}} = N_{SS}^{\text{data}} - \sum_{i} k_{SS}^{i} \cdot N_{SS}^{i} \tag{5.6}$$

where the sum is over SS backgrounds with at least one prompt lepton, and k_{SS}^{i} is the SS scale factor for the appropriate background.

The multijet background is then estimated in the SR by multiplying N_{SS}^{multijet} by a scale factor r_{QCD}, designed to convert the number of events in the SS CR to events in the opposite-sign (OS) SR. This scale factor is not exactly 1, due to the different relative fractions in the OS and SS cases of $q\bar{q}$, $qq\prime$, $q\bar{q}\prime$, qg and gg in the final state—charge correlation in the resulting fake μ and τ_{had} is expected when they arise from jets in $q\bar{q}$, $qq\prime$ and $q\bar{q}\prime$ events. r_{QCD} is calculated in a CR defined with $E_{\text{T}}^{\text{miss}} > 20$ GeV, $m_{\text{T}} < 30$ GeV, one (non-isolated) muon, and one hadronic tau (satisfying a looser tau ID than in the SR). Background contributions from W+jets, Z+jets and top events make up about 25% of the distribution; these are estimated from simulation and subtracted. The ratio of OS to SS events is obtained for the case where the muon isolation matches what is required in the SR, this defines r_{QCD} and is measured to be 1.11 ± 0.08.

The total OS background is the sum of the multijet background (scaled from SS to OS) and the OS contribution from backgrounds with at least one prompt lepton; as noted above, the latter are estimated from simulation but normalised with a data-driven scale factor. That is,

$$\begin{aligned} N_{OS}^{\text{bkg}} &= r_{\text{QCD}} \cdot N_{SS}^{\text{multijet}} + \sum_i k_{OS}^i \cdot N_{OS}^i \\ &= r_{\text{QCD}} \cdot N_{SS}^{\text{data}} + \sum_i \left(k_{OS}^i \cdot N_{OS}^i - r_{\text{QCD}} \cdot k_{SS}^i \cdot N_{SS}^i \right) \end{aligned} \tag{5.7}$$

where the summed term is often shorted to N_{OS-SS}^i.

The scale factors in eq. 5.7, used to normalise the W+jets, Z+jets and top backgrounds, have been derived by other members of the ATLAS Collaboration, as follows:

- $\boldsymbol{W(\rightarrow \mu\nu)}$**+jets** A CR is defined by requiring $E_{\text{T}}^{\text{miss}} > 20$ GeV and $m_{\text{T}} > 70$ GeV as well as a muon and hadronic tau, to obtain a sample with high W+jets purity. Since the τ_{had} misidentification rate is different for jets from hadronisation of a quark (dominant in the OS final state) and gluon (dominant in the SS final state), the OS and SS scale factors are measured separately. These are displayed in table 5.3.

- $\boldsymbol{Z(\rightarrow \mu\mu)}$**+jets** This background contribution is split into two parts, depending on whether a muon or a jet is misreconstructed as a τ_{had}. In the former case, OS and SS CRs are defined by selecting events with an invariant mass of the muon and hadronic tau in the range $80 < m_{\text{inv}}^{\mu,\tau} < 100$ GeV; data and simulation are found to agree within statistical uncertainties in both regions and so the scale factors are set to 1. In the latter case, a CR is defined by the presence of two opposite-sign same-flavour leptons plus a hadronic tau. Since there is no charge correlation between the single reconstructed muon and the τ_{had}, no difference between the OS and SS cases is expected, so a single scale factor is derived, and is shown in table 5.3.

- **top** A CR is defined with $E_{\text{T}}^{\text{miss}} > 20$ GeV, $m_{\text{T}} > 50$ GeV, and at least two jets with $p_{\text{T}} > 30$ GeV where the highest-p_{T} jet is consistent with having come from a b-quark. The resulting OS and SS scale factors are listed in table 5.3.

Finally, diboson events make the smallest contribution to the total background, and consist of almost all prompt leptons. They are well-modeled by simulation, and therefore no scale factors are required.

The values of the scale factors are summarised in table 5.3.

5.2.4 Estimators of α

Once the selection is performed to obtain a highly-pure sample of the $Z \rightarrow \tau_{\text{lep}}\tau_{\text{had}}$ signal, and background contributions are estimated, we are able to compare the

Scale factor	Calculated value
r_{QCD}	1.11 ± 0.08
$k_{OS}^{W+\text{jets}}$	0.80 ± 0.05
$k_{SS}^{W+\text{jets}}$	0.93 ± 0.08
$k_{OS}^{Z\to\mu\mu}$	1
$k_{SS}^{Z\to\mu\mu}$	1
$k^{Z\to\mu\mu+\text{jets}}$	0.56 ± 0.03
k_{OS}^{top}	0.84 ± 0.16
k_{SS}^{top}	0.95 ± 0.22

Table 5.3: The scale factors for OS and SS non-prompt backgrounds.

simulation against data to determine if a further correction to the transverse momentum of the τ_{had} is required. We can shift the visible mass peak by shifting the p_{T} of the hadronic taus, and look for good agreement with the data, but first we need to define exactly what 'good agreement' means in this context. That is, we need to determine the best way to quantitatively compare the distributions in simulation and data.

Several methods are proposed, which can be roughly separated into 'statistical' and 'function-peak' categories. The 'statistical' options are to use either the median or mean of the visible mass distribution, over the range 45–90 GeV (the region where the $Z \to \tau^+\tau^-$ signal dominates over the background). A 'function-peak' option instead fits a function to the distribution in this same range and takes the position of the function's peak as the estimator. Ideally, assuming all $Z \to \tau^+\tau^-$ decay products and their energies were detected and measurable, the mass peak would have a Breit-Wigner form with a width equal to that of the Z. However, the undetectable neutrinos and the finite resolution of the lepton and tau energies serve to broaden the visible mass peak, while its shape is biased by the event selection criteria; therefore, no obvious parameterisable function exists to fit the asymmetric shape. We instead test the following set of fitting functions:

- **convolved Gaussian and Breit-Wigner:** a symmetric distribution used to model a resonance with a non-zero decay width and resolution uncertainty,
- **bifurcated Gaussian:** a Gaussian distribution with different widths on either side of the peak, used to model asymmetric distributions with a non-zero resolution uncertainty,
- **bifurcated Gaussian and Landau:** sums a bifurcated Gaussian with a Lan-

dau function which acts on one of the distribution tails,

- **Crystal Ball:** a Gaussian peak with a falling power-law tail on one side, used to model non-Gaussian detector responses,
- **bifurcated Crystal Ball:** a bifurcated Gaussian peak and power-law tails on both sides, similar to the Crystal Ball function but allowing for more asymmetry, and
- **5^{th} order polynomial:** not justified for any physical reason, however contains enough degrees of freedom to properly model the distribution without over-fitting.

Each function is fitted to the m_{vis} distribution using the RooFit package [227], and the position of the peak taken as the estimator in each case.

As noted above, the best estimator should be robust against changes in the background, and should certainly not depend on such changes. Since the contribution to the m_{vis} distribution from the background is not flat in the range 45–90 GeV, statistical estimators such as the mean and median will be more strongly affected as α is varied and the distribution shifts. One way to demonstrate the sensitivity to background is to vary the value of α only for the background simulated samples, and *not* for the $Z \to \tau_{\text{lep}}\tau_{\text{had}}$ signal, and to see how the estimator varies with respect to the baseline case where $\alpha = 0$. An example of this is shown in fig. 5.5. The mediator of the distribution is the most problematic estimator, showing a large dependence on the behaviour of the background, and the mean estimator also shows a strong sensitivity to background. The fitted functions shown perform better, which is expected as their position should be mostly determined by the dominant peak in the (unchanged) signal sample, however some small dependence still remains. Following this study, the mean and median are no longer considered as potential candidates for the estimator.

If we label the estimator in each method as *est* (i.e. the median, the mean or the peak position), we can compare simulation against data with a variable *diff*, according to

$$diff = est_{\text{data}} - est_{\text{sim}} \,. \tag{5.8}$$

Ideally, this variable should be robust against variations in the background estimation and not strongly affected by systematic variations. Additionally, it would be linear in α, so one could then take as the final TES correction the value of α where *diff* = 0. We find, however, that the peak position of the summed bifurcated Gaussian and Landau function does not scale linearly with α, as the shift is

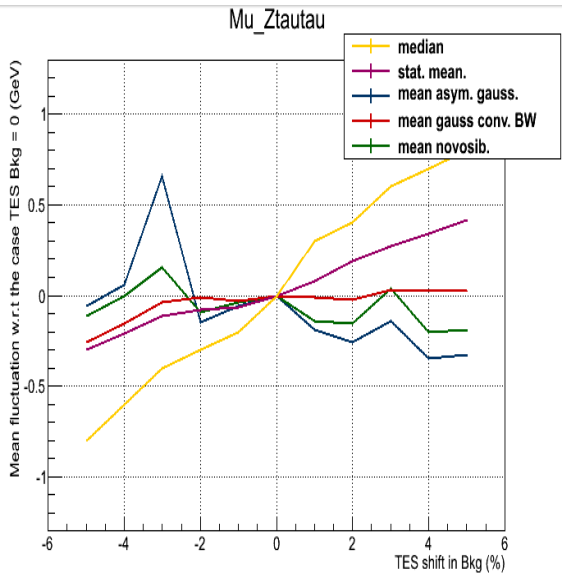

Figure 5.5: The variation of each estimator when only hadronic taus in the background samples have a TES correction applied, relative to the $\alpha = 0$ case.

absorbed into other fit parameters, and in fact this estimator gives two solutions for a match between simulation and data; it is therefore discarded as a candidate.

At this point we pause to consider an alternative to fitting the data and the total simulation (that is, the signal + background), the shape of which is a central asymmetric peak dominated by signal but visibly skewed by the presence of background processes (as clearly seen in fig. 5.4). As the $Z \to \tau_{\text{lep}}\tau_{\text{had}}$ process is most interesting to us, a better option may be to compare the $Z \to \tau_{\text{lep}}\tau_{\text{had}}$ signal against data with the background subtracted ('data - background').

To compare the two scenarios, we look at the *shape* of the distributions through use of the statistical higher moments, the standard deviation (the spread or width), the skewness (a measure of the asymmetry) and the kurtosis (the 'sharpness' of a distribution). These are plotted in fig. 5.6 as a function of α, where the red line corresponds to the unaltered data, the yellow line to the total simulation (signal + background), the green line to data - background, and the blue line to the simulated $Z \to \tau_{\text{lep}}\tau_{\text{had}}$ signal. Note that these plots are over the m_{vis} range 50–90 GeV, which is slightly reduced from the total studied range 45–90 GeV. We also studied the effect of extending this range to 40–100 GeV, and saw a slight effect from statistical fluctuations in the background-dominated tails, however overall the behaviour was the same.

As expected, the shape of the m_{vis} peak is affected by the presence of background; comparing, for example, the blue signal and the yellow total simulation, they show similar changes as a result of α but have quite different measures of the moments. However, the points of intersection—a rough indicator of the final

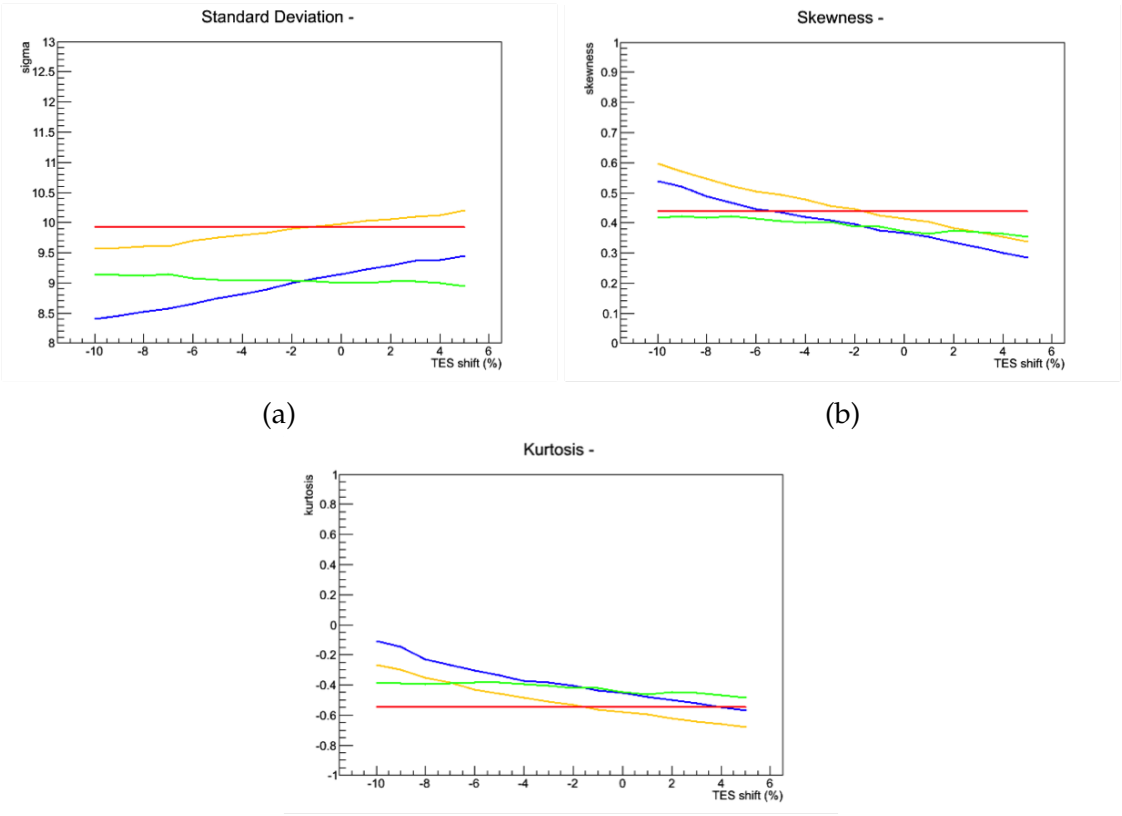

(a) (b)

(c)

Figure 5.6: The higher moments ((a) standard deviation, (b) skewness, (c) kurtosis) of the data (red line), simulation (yellow line), data - background (green line) and $Z \to \tau_{\text{lep}}\tau_{\text{had}}$ signal (blue line), for $m_{\text{vis}} \in [50, 90]$ GeV.

value of α—of the $Z \to \tau_{\text{lep}}\tau_{\text{had}}$ and data - background, and of total simulation and data, align reasonably well in each moment plot (and, to a lesser degree, across moments), suggesting that either choice of exactly what comparison to make will give similar results for the optimal correction to the TES. In other words, the proposed method of fitting the peak with a function that appropriately fits the shape as well as the peak position, is robust against the behaviour of the backgrounds. From hereon, we choose to compare the $Z \to \tau_{\text{lep}}\tau_{\text{had}}$ signal against data - background, so eq. 5.8 becomes

$$\mathit{diff} = \mathit{est}_{\text{data-bkg}} - \mathit{est}_{Z\to\tau_{\text{lep}}\tau_{\text{had}}} \,. \tag{5.9}$$

The functions are fitted to the visible mass distribution, these are shown in fig. 5.7, where the top row shows the fits to the $Z \to \tau_{\text{lep}}\tau_{\text{had}}$ signal and the bottom row shows the fits to data - background.

The difference variable defined in eq. 5.9 is shown in fig. 5.8, for the τ_{had} having one or three associated charged tracks, and the inclusive case. The p_{T} of the hadronic taus has been shifted according to eq. 5.2 with α (labeled in the figure as 'TEC shift') varied from -5% to 5% in steps of 1%. The final value of the TES correction is obtained by calculating where a linear fit of all the points crosses the x-axis. (A study was performed to determine whether it was better to find this intersection using a linear fit of all points between α = -10% and α = 5%, or a point-by-point interpolation; the difference in the final TES correction was found to be insignificant.) All estimators show similar behaviour and predict reasonably close corrections to the TES, which is taken as a sign of the robustness of this method. This is especially true for the case of one associated track; the case of three associated tracks case has less agreement among the estimators, due to smaller statistics.

The bifurcated Gaussian fit shows good agreement with the distribution in the sides of the peak (see figs. 5.7(b) and (g)), however the peak itself shows a slight negative bias in both the signal and data - background distributions. The same is true for the bifurcated Crystal Ball function (figs. 5.7(d) and (i)), which we can see in fig. 5.8 as these two estimators give linear distributions that are positively biased relative to the alternative estimators. Therefore, both estimators are discarded.

The convolution of a Gaussian and a Breit-Wigner (figs. 5.7(a) and (f)), and the Crystal Ball function (figs. 5.7(c) and (h)), both estimate the peak postion better, however neither fits the extreme ends of the distribution particularly well, and both slightly overestimate the height of the peak compared to the distribution they are fitting.

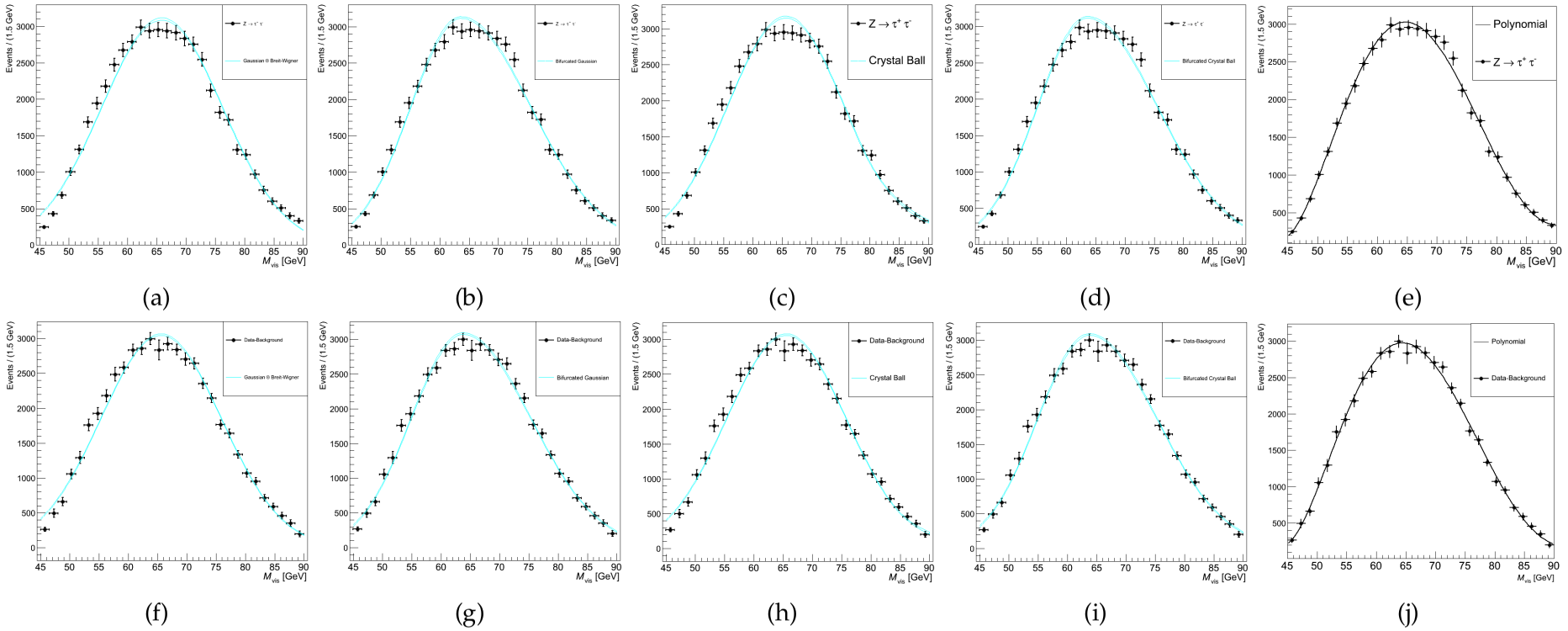

Figure 5.7: Fits to the m_{vis} distribution of the $Z \to \tau_{\text{lep}}\tau_{\text{had}}$ signal (top row) and data-background (bottom row) for the Gaussian convolved with a Breit-Wigner function (a,f), the bifurcated Gaussian (b,g), the Crystal Ball function (c,h), the bifurcated Crystal Ball function (d,i), and the 5^{th} order polynomial (e,j). The fit is performed in the range 45 – 90 GeV. Produced by F. Nuti, with whom this work was performed.

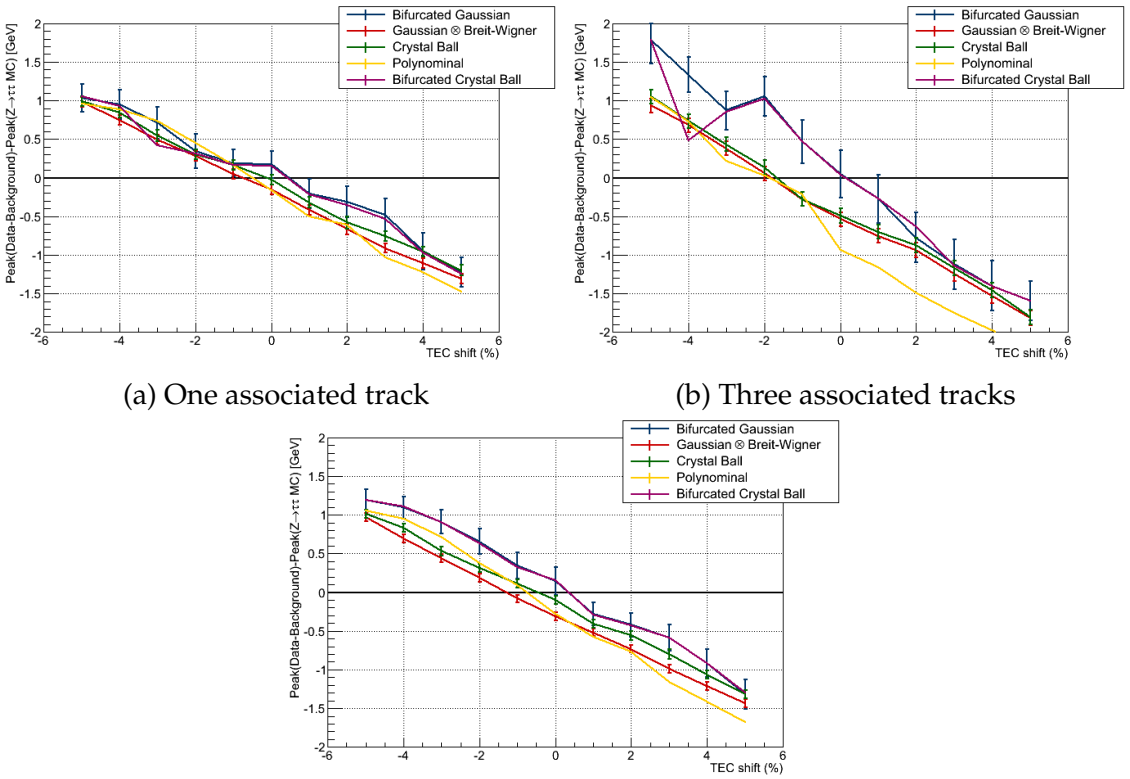

(a) One associated track

(b) Three associated tracks

(c) Inclusive

Figure 5.8: The difference in each estimator of data-background and $Z \to \tau_{\text{lep}}\tau_{\text{had}}$ signal, as a function of the TES correction shift (called α in the text), for τ_{had} candidates with one (a) and three (b) associated tracks, and inclusive (c).

The 5^{th} order polynomial does the best job of fitting the distributions both in the peak position and in the sides of the distribution (see figs. 5.7(e) and (j)), confirmed by a χ^2 test normalised to the number of degrees of freedom in the fit.

Each of the three unbiased fits give similar results for the preferred TES correction, with the result from the polynomial fit lying between the other two. Therefore, the peak position of the polynomial is considered to be the best estimator, and is used to obtain the final result for the TES correction.

5.2.5 Statistical uncertainties: the toys method

The statistical uncertainty from data on the TES correction is determined as follows. Each bin of the observed visible mass distribution is treated as a Gaussian distribution centred on the number of recorded events in that bin, N_{bin}, and with a width of the Poissonian uncertainty, $\sqrt{N_{\text{bin}}}$. A new visible mass distribution is created by randomly drawing from each bin in turn, and this is performed 1000 times to produce 1000 'pseudo-experiments'. A new value of α is obtained from each pseudo-experiment, and the obtained α values build up a distribution of approximately Gaussian shape; see fig. 5.9(a). The standard deviation of this distribution is taken as the statistical uncertainty arising from data.

The procedure for the statistical uncertainty in simulation is very similar, but instead the uncertainty in each bin of the visible mass distribution is taken from the statistical uncertainties of each estimated background contribution, added in quadrature. The distribution of α values is shown in fig. 5.9(b).

The final statistical uncertainties in the one- and three-associated track cases are found to be 1.3% and 1.4% respectively.

5.2.6 Systematic uncertainties

Systematic uncertainties in this analysis arise from several different sources. In each case, a pseudo-experiment is generated where the affected variable is varied up or down within its uncertainty, and the resulting variation in the value of the TES correction is measured. These uncertainties, divided according to the number of charged tracks associated to the τ_{had}, are listed in table 5.4. The sources are described below; note that the uncertainties on each variable, with the exception of the fitting procedure, were obtained by other members of the ATLAS Collaboration.

Uncertainties on the scale factors used in the background estimation are listed in table 5.3, and the resulting systematic uncertainties on α are listed in the first six rows of table 5.4. The dominant scale factor uncertainty is due to r_{QCD}, which is used to scale the relatively large SS background and which appears multiple

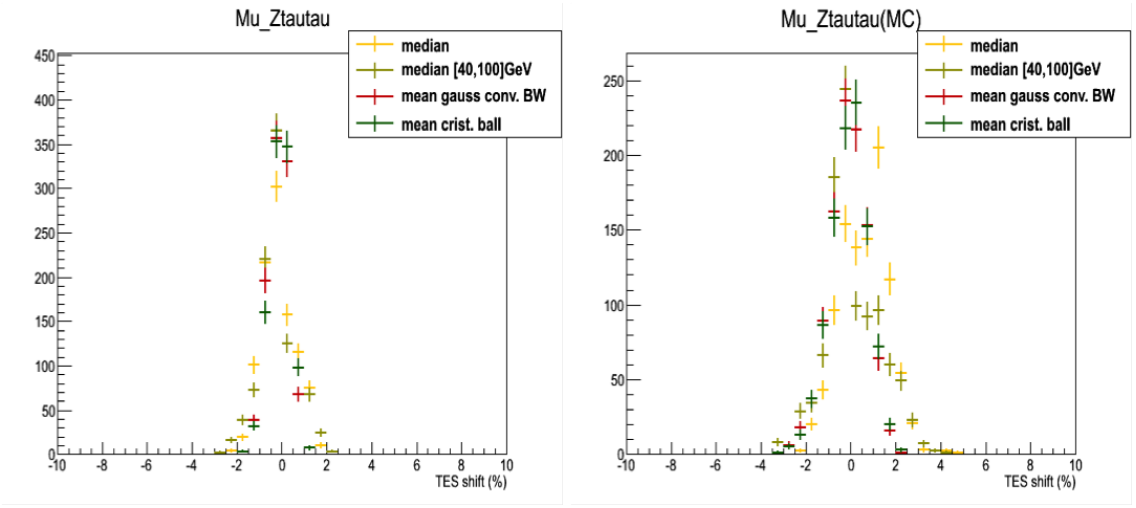

(a) (b)

Figure 5.9: The distributions of the TES correction α obtained from 1000 pseudo-experiments generated from (a) data and (b) simulation.

times in eq. 5.7; this contributes uncertainties on α of $\sim$0.3 and $\sim$0.1 in the one- and three-associated tracks respectively.

The muon trigger efficiency is measured with a tag-and-probe method using $Z \to \mu\mu$ events; a scale factor is obtained and used to correct the simulated trigger efficiency and bring it in line with that observed in data. The muon ID (isolation) scale factor similarly corrects the muon reconstruction (isolation) efficiency in simulation to that observed in data, and is measured (along with the associated uncertainty) in $J/\psi \to \mu\mu$ and $Z \to \mu\mu$ events. Muon momenta in simulation are corrected in both scale and resolution, according to

$$p_{\mathrm{T}}^{\mathrm{corr.}} = p_{\mathrm{T}}^{\mathrm{sim.}} \cdot s \cdot (1 + \Delta p_1 G(0,1) + p_{\mathrm{T}} \cdot \Delta p_2 G(0,1)) \tag{5.10}$$

where s is a scale correction, $\Delta p_{1,2}$ are momentumum resolution parameters and $G(0,1)$ is a random draw from a Gaussian distribution with standard deviation equal to 1. The scale and resolution parameters and associated uncertainties are measured in $Z \to \mu\mu$ events in data and simulation. See refs. [176] and [228] for further detail on systematics associated to the muon. The muon resolution contributes the largest uncertainty to α of $\sim$0.3 in the three-track case, the one-track case has contributions of $\sim$0.1 from both resolution and trigger scale factor uncertainties.

The $E_{\mathrm{T}}^{\mathrm{miss}}$ also has scale and resolution corrections applied, which are considerably more complicated to obtain due to the nature of its piecemeal construction. All reconstructed objects in an event which contribute to the $E_{\mathrm{T}}^{\mathrm{miss}}$ (through their negatively-inverted transverse momenta) have their own scale and resolution corrections applied, and the jets and additional SoftTerm contribution are consid-

Source	Uncertainty [%]	
	1 track	3 tracks
r_{QCD}	0.28	0.09
k_{OS}^{W}	0.01	0.04
k_{SS}^{W}	0.02	0.06
$k_{Z\to\ell\ell\text{+jets}}$	< 0.01	0.01
k_{OS}^{top}	0.03	0.06
k_{SS}^{top}	0.01	< 0.01
Muon trigger scale factor	0.12	0.06
Muon ID scale factor	< 0.01	< 0.01
Muon isolation scale factor	0.01	< 0.01
Muon resolution	0.11	0.32
$E_{\text{T}}^{\text{miss}}$ resolution	0.19	0.25
$E_{\text{T}}^{\text{miss}}$ scale	0.07	0.1
Fit procedure	0.5	0.5
Total	0.6	0.7

Table 5.4: The contribution to the systematic uncertainty from each source, separated according to number of associated tracks.

erably affected by pileup, requiring an additional correction. The reconstruction performance for events with true $E_{\text{T}}^{\text{miss}}$ is measured in events with $W \to \ell\nu$ in the final state. The resulting scale and resolution uncertainties on the TES correction are dominated by the $E_{\text{T}}^{\text{miss}}$ resolution, which contributes $\sim$0.2.

The fitting procedure described in sec. 5.2.4 makes the largest contribution to the systematic uncertainty, of 0.5 in both the one- and three-associated track cases. Specifically, uncertainties were derived from changing the range of the fit ($m_{\text{vis}} \in$ [45, 90], [50, 85] and [40, 95] GeV were all tested), from comparing data against simulation or $Z \to \tau_{\text{lep}}\tau_{\text{had}}$ against data - background, and from the difference between α obtained with the initial sample and from the toys average.

We checked the systematic uncertainty due to signal mismodeling by the generator by generating $Z \to \tau_{\text{lep}}\tau_{\text{had}}$ samples with JIMMY performing the parton shower and underlying event processes rather than PYTHIA6, and comparing the resulting TES correction. This was compatible with our final result, within the statistical uncertainty of the new signal sample. We performed a similar process with the $W(\to \ell\nu)$+jets background, and again found a compatible result within

Tau ID	Region	Recommended TES correction
	$\|\eta_\tau\| < 2.5$	α = -0.6% $\pm$ 0.9% (stat) $\pm$ 0.6% (syst)
	$\|\eta_\tau\| < 0.8$	α = -0.4% $\pm$ 1.5% (stat) $\pm$ 0.8% (syst)
medium	$0.8 < \|\eta_\tau\| < 2.5$	α = -0.7% $\pm$ 1.2% (stat) $\pm$ 0.6% (syst)
	1 track ($\|\eta_\tau\| < 2.5$)	α = -0.8% $\pm$ 1.3% (stat) $\pm$ 0.6% (syst)
	3 tracks ($\|\eta_\tau\| < 2.5$)	α = -1.1% $\pm$ 1.4% (stat) $\pm$ 0.7% (syst)
tight	$\|\eta_\tau\| < 2.5$	α = -1.1% $\pm$ 1.0% (stat) $\pm$ 0.6% (syst)

Table 5.5: The recommended TES corrections, split according to tau ID, number of associated tracks and $|\eta_\tau|$.

the statistical uncertainty. Therefore, no generator systematic is included in the total uncertainty.

As noted at the beginning of this chapter, the method described here can only account for differences between data and simulation, and not for differences between the reconstructed and true visible energy of the hadronic tau; the uncertainties described above are not sufficient as an uncertainty on the absolute TES. However, the alternative deconvolution method, mentioned in sec. 5.2, does account for the additional uncertainties (arising from the non-closure and pileup), and so we take these directly from that analysis and sum them in quadrature with the uncertainties measured in the *in situ* analysis, to obtain the final estimated uncertainty.

5.2.7 TES correction recommendations

The preliminary set of recommendations were divided according to detector region and number of associated tracks in the case of *medium* tau ID. A recommendation was also obtained for the case of *tight* tau ID, but only as an inclusive case due to the reduced statistics. These recommendations are summarised in table 5.5.

The final recommendations, as listed in ref. [1], are presented as inclusive in $|\eta|$ but separated according to number of associated tracks. These recommendations are chosen to be *positive* and to be applied to the momentum of hadronic taus in data, in order to obtain agreement between data and simulation. The TES corrections are α = 0.8% $\pm$ 1.3% (stat) $\pm$ 0.6% (syst) for τ_{had} with one associated track, and α = 1.1% $\pm$ 1.4% (stat) $\pm$ 0.7% (syst) for τ_{had} with three associated tracks.

Chapter 6

The ATLAS mono-Z (leptonic) analysis

This chapter provides detail on the ATLAS mono-$Z(\to \ell^+\ell^-)$ + $E_{\mathrm{T}}^{\mathrm{miss}}$ analysis, which was performed using the 20.3 fb^{-1} of data collected by the ATLAS detector at a centre-of-mass energy of 8 TeV in Run I. The chapter is based on the published result of ref. [3], and follows closely the ATLAS-internal support note of ref. [2].

The work was performed by the ATLAS mono-Z analysis team, of which the author was a member in the later stages in the analysis. The author worked primarily on the interpretation of the result in the simplified model framework, discussed in detail in sec. 6.8; all other work described here is provided for context of the analysis.

Several models of dark matter (DM) are included in this analysis:

- the Effective Field Theory (EFT) models (discussed in detail in sec. 3.1) that couple the DM fermions with Standard Model (SM) quarks via a contact interaction, included here as a generic DM model and for comparison against and combination with the mono-jet channel, where the strongest results for these models are obtained;

- the $ZZ\chi\bar{\chi}$ EFT models, including the dimension-5, and minimal- and maximal-mixing dimension-7 operators (see sec. 3.2). Such models are best studied in the mono-Z channel, driving the importance of this channel in DM collider searches;

- the Majorana DM variant of the tS simplified model discussed in sec. 3.3.2. This was the first study of a t-channel simplified model within an ATLAS mono-X analysis, and its inclusion here was based on the study in ref. [127] of such a model in the leptonic mono-Z channel.

For each model, an upper limit on the cross section for the mono-Z process is obtained, and in the case of the simplified model, converted to a limit on the DM-mediator-quark coupling, $g_{q\chi}$. This is also compared with the lower coupling limit calculated from the relic density measurement, and is described in the last section of this chapter.

Each model produces a mono-Z signal through emission of a Z boson, either from one of the incoming quarks or, in the case of the tS model, from the $SU(2)$ doublet mediator. The specific signal studied in this analysis consists of two DM particles manifesting in the detector as missing transverse momentum, back-to-back with a boosted Z boson decaying to two charged leptons, either e^+e^- or $\mu^+\mu^-$. The advantage of using charged leptons in the signal, compared to jets, is that they are comparatively easy to reconstruct in the detector, with well-measured and calibrated momenta (see sec. 4.3 for the details on lepton reconstruction). In addition, a jet veto can be used to remove the large multi-jet background. However, the smaller cross section of the mono-Z process (compared to the mono-jet) is a disadvantage; a full comparison between these mono-X channels is the subject of the next chapter in this thesis.

This chapter will proceed as follows. The recorded data, simulated SM background and simulated signal samples will be detailed in sec. 6.1, and the object definitions and event selection discussed in secs. 6.2 and 6.3 respectively. The estimation of the SM backgrounds is explained in sec. 6.4, along with the uncertainty estimations in sec. 6.5. A brief overview of the resulting model-independent limits is provided in sec. 6.6, considered in the EFT context in sec. 6.7, and a more complete discussion of the tS simplified model and its constraints is the topic of sec. 6.8.

6.1 Data and simulated samples

6.1.1 Data sample

The mono-Z analysis was performed with the full ATLAS 2012 dataset, recorded during collisions with a centre-of-mass energy of 8 TeV. In total, 22.8 fb^{-1} of data was recorded, however a fraction of that was collected under imperfect conditions (when, for example, one or more of the subdetectors was not operating correctly[1], or the event record was corrupted). A list of all useable data samples from each data-taking period is known as a Good Runs List (GRL). The standard

[1]This being said, small temporary failures in the detector occur quite frequently, affecting only a minor section of the subdetector, and can be accounted for by including such dead regions into the simulation; only more significant failures will render the data unuseable.

GRL for physics analyses at the end of Run I was used in this analysis, known as the ALL_GOOD GRL[2], containing a total integrated luminosity of 20.3 fb^{-1}.

6.1.2 Signal samples

As discussed in sec. 3.1, the D1, D5, D9 and D11 operators can be used as representatives of the remaining EFT operators: in a collider mono-X context, the D1 operator behaves kinematically similarly to the D2, D3 and D4 operators (which are velocity-suppressed in direct detection experiments), and so on. This can be seen in figs. 6.1(a)–(c), which show the normalised $E_{\mathrm{T}}^{\mathrm{miss}}$ distribution for each operator (for a DM mass of 200 GeV), along with the dominant irreducible SM background, $ZZ \to \ell^+\ell^-\nu\bar{\nu}$. The D1, D5 and D9 EFT operators are therefore chosen for study in this analysis.

Fig. 6.1(d) shows the $E_{\mathrm{T}}^{\mathrm{miss}}$ distribution for the three $ZZ\chi\bar{\chi}$ operators; note that the minimal- and maximal-mixing dimension-7 operators have the same normalised shape. Fig. (e) compares the tS model (in pink, labeled m_η) with the EFT operators, and is clearly most similar to the D5 operator, as expected. Much more detail on the tS model and its behaviour will be provided at the end of this chapter, in sec. 6.8.

Four representative DM masses were chosen for each model, with an additional mass included in the $ZZ\chi\bar{\chi}$ operator case as a stronger dependence on the DM mass was observed for the cross section. These are listed in tables 6.1, 6.2 and 6.3. Each EFT operator was generated with a suppression scale value of Λ = 1 TeV, which does not affect the kinematic behaviour, only the cross section. The mediator mass and coupling parameters in the case of the tS model were a little more complicated. A range of mediator masses was chosen for each DM mass, as the model behaviour is dependent on this explicit mediator mass. Each (m_χ, M_{med}) sample was generated with a single coupling value, $g_{q\chi}$, chosen in each case such that the model would contribute a density approximately equal to that of the observed relic density today, based on details in ref. [127]. However, after further work done in this area (in particular, see the following chapter) we recognise that this is a fairly arbitrary choice.

The EFT DM signal samples were generated with MADGRAPH5 [146] for the matrix element calculation and PYTHIA6.426 [144] for showering and hadronisation. The MSTW2008LO Parton Distribution Function (PDF) [141] and AU2

[2] https://twiki.cern.ch/twiki/bin/viewauth/AtlasProtected/GoodRunListsForAnalysis*

*Note that this URL is accessible only to members of the ATLAS Collaboration; it is included here for completeness, and for possible use as a reference for such ATLAS members. The same applies to similar links throughout this thesis.

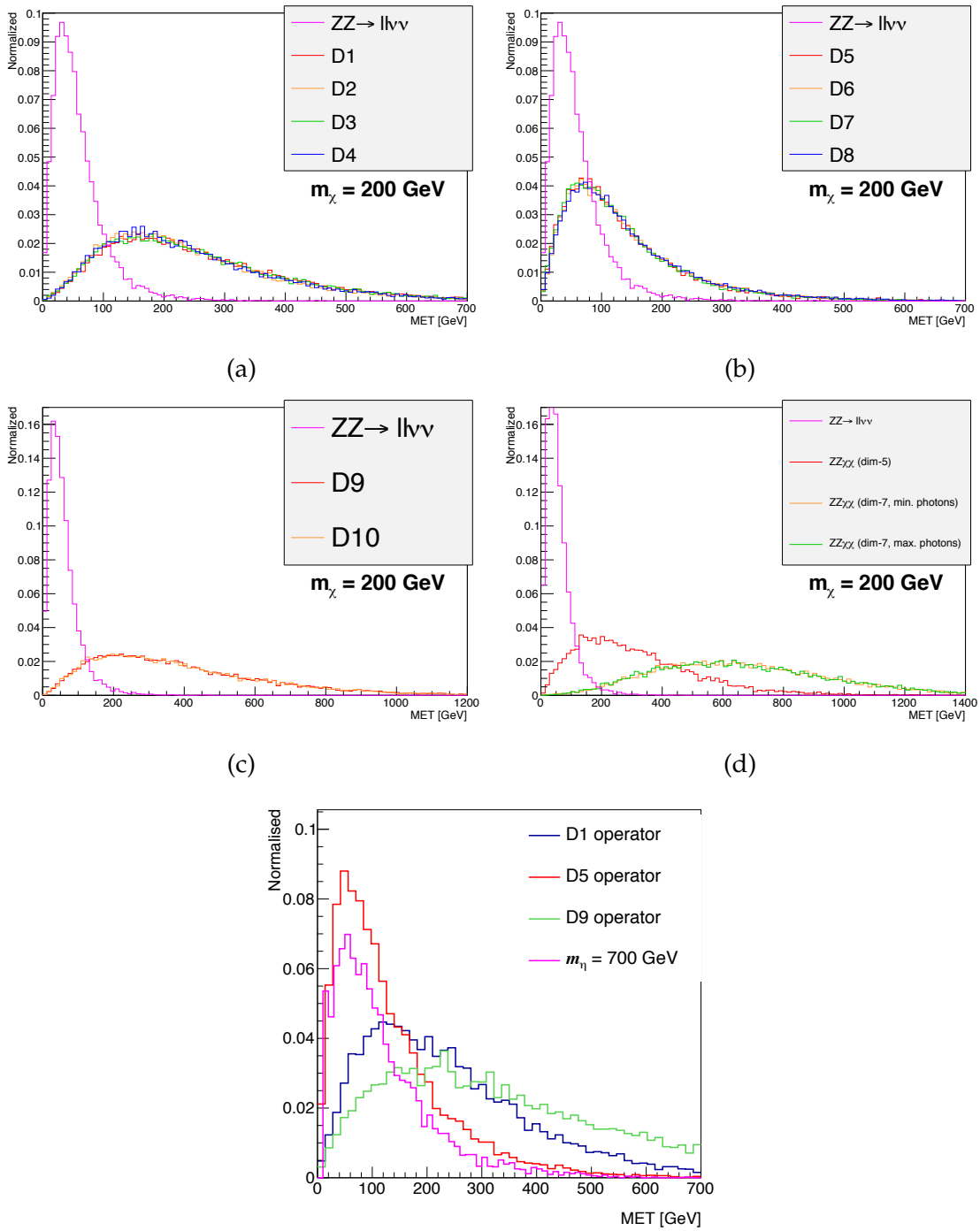

Figure 6.1: The $E_{\mathrm{T}}^{\mathrm{miss}}$ shape of all EFT operators for a DM mass of 200 GeV, compared against the main background of this analysis, $ZZ \to \ell^+\ell^-\nu\bar{\nu}$ (a)–(d). Fig. (e) shows the tS model (in pink, labeled m_η), with a clearly similar shape to the D5 operator. Taken from ref. [2].

Model	Parameters	Cross section [fb]
D1	m_χ = 10 GeV, Λ = 1 TeV	9.85×10^{-7}
D1	m_χ = 200 GeV, Λ = 1 TeV	3.52×10^{-7}
D1	m_χ = 400 GeV, Λ = 1 TeV	8.37×10^{-8}
D1	m_χ = 1000 GeV, Λ = 1 TeV	1.01×10^{-9}
D5	m_χ = 10 GeV, Λ = 1 TeV	7.12×10^{0}
D5	m_χ = 200 GeV, Λ = 1 TeV	5.59×10^{0}
D5	m_χ = 400 GeV, Λ = 1 TeV	3.12×10^{0}
D5	m_χ = 1000 GeV, Λ = 1 TeV	2.49×10^{-1}
D9	m_χ = 10 GeV, Λ = 1 TeV	$1.24\times10^{+2}$
D9	m_χ = 200 GeV, Λ = 1 TeV	$8.92\times10^{+1}$
D9	m_χ = 400 GeV, Λ = 1 TeV	$4.75\times10^{+1}$
D9	m_χ = 1000 GeV, Λ = 1 TeV	3.41×10^{0}

Table 6.1: The EFT signal samples generated for study in the ATLAS mono-$Z \to \ell^+\ell^-$ analysis, their parameters and resulting cross sections for the process $pp \to Z\chi\bar{\chi}$.

Model	Parameters	Cross section [fb]
$ZZ\chi\chi$ dim-5	m_χ = 10 GeV, Λ = 1 TeV	1.94×10^{-5}
$ZZ\chi\chi$ dim-5	m_χ = 50 GeV, Λ = 1 TeV	1.22×10^{-5}
$ZZ\chi\chi$ dim-5	m_χ = 200 GeV, Λ = 1 TeV	2.44×10^{-6}
$ZZ\chi\chi$ dim-5	m_χ = 400 GeV, Λ = 1 TeV	4.10×10^{-7}
$ZZ\chi\chi$ dim-5	m_χ = 1000 GeV, Λ = 1 TeV	2.97×10^{-9}
$ZZ\chi\chi$ dim-7 (max γ)	m_χ = 10 GeV, Λ = 1 TeV	3.09×10^{0}
$ZZ\chi\chi$ dim-7 (max γ)	m_χ = 200 GeV, Λ = 1 TeV	1.99×10^{0}
$ZZ\chi\chi$ dim-7 (max γ)	m_χ = 400 GeV, Λ = 1 TeV	8.27×10^{-1}
$ZZ\chi\chi$ dim-7 (max γ)	m_χ = 1000 GeV, Λ = 1 TeV	2.26×10^{-2}
$ZZ\chi\chi$ dim-7 (min γ)	m_χ = 10 GeV, Λ = 1 TeV	2.42×10^{-1}
$ZZ\chi\chi$ dim-7 (min γ)	m_χ = 200 GeV, Λ = 1 TeV	1.56×10^{-1}
$ZZ\chi\chi$ dim-7 (min γ)	m_χ = 400 GeV, Λ = 1 TeV	6.54×10^{-2}
$ZZ\chi\chi$ dim-7 (min γ)	m_χ = 1000 GeV, Λ = 1 TeV	1.85×10^{-3}

Table 6.2: The $ZZ\chi\chi$ EFT signal samples generated, their parameters and the resulting cross sections for the process $pp \to Z\chi\bar{\chi}$.

Model	Parameters	Cross section [fb]
tS (Maj)	m_χ = 10 GeV, M_η = 200 GeV, $g_{q\chi}$ = 2	4.51×10^{1}
tS (Maj)	m_χ = 10 GeV, M_η = 500 GeV, $g_{q\chi}$ = 3	2.58×10^{1}
tS (Maj)	m_χ = 10 GeV, M_η = 700 GeV, $g_{q\chi}$ = 4	3.18×10^{1}
tS (Maj)	m_χ = 10 GeV, M_η = 1000 GeV, $g_{q\chi}$ = 6	5.44×10^{1}
tS (Maj)	m_χ = 200 GeV, M_η = 500 GeV, $g_{q\chi}$ = 2	1.2×10^{0}
tS (Maj)	m_χ = 200 GeV, M_η = 700 GeV, $g_{q\chi}$ = 2	5.9×10^{-1}
tS (Maj)	m_χ = 200 GeV, M_η = 1000 GeV, $g_{q\chi}$ = 2	2.5×10^{-1}
tS (Maj)	m_χ = 400 GeV, M_η = 500 GeV, $g_{q\chi}$ = 2	1.7×10^{-1}
tS (Maj)	m_χ = 400 GeV, M_η = 700 GeV, $g_{q\chi}$ = 2	1.1×10^{-1}
tS (Maj)	m_χ = 400 GeV, M_η = 1000 GeV, $g_{q\chi}$ = 2	6×10^{-2}
tS (Maj)	m_χ = 1000 GeV, M_η = 1200 GeV, $g_{q\chi}$ = 2	4.1×10^{-4}

Table 6.3: The t-channel simplified model signal samples generated, and their parameters. Note the cross sections here include the branching fraction of Z to charged leptons, that is, for the process $pp \to Z\chi\bar{\chi} \to \ell^+\ell^-\chi\bar{\chi}$.

MSTW2008LO tune [229] were used. The tS simplified model samples were generated later, and used MADGRAPH5 and PYTHIA8 [222]. For each model and every point in parameter space, 10 000 events were generated.

Comparison of FastSim and FullSim

The detector simulation was performed with Atlfast-II (AFII) [166] (to produce so-called *FastSim* samples), a faster, more approximate simulation of the particle interactions with the detector material than is obtained with GEANT4 [165] (see sec. 4.2.5). To check that this approximation was acceptable, three EFT model samples and two $ZZ\chi\bar{\chi}$ model samples were also simulated fully with the GEANT4 reconstruction (known as *FullSim* samples), and their performance at each point in the event selection (described later in sec. 6.3, and only up to the $E_{\mathrm{T}}^{\mathrm{miss}}$ cut) compared against that for the FastSim samples. In the electron channel, the acceptance (that is, the percentage of events passing the selection) of the FullSim sample was consistently higher by approximately 5% or less, while in the muon channel the difference was less than 4% but in either direction. Additionally, the $E_{\mathrm{T}}^{\mathrm{miss}}$ distributions were compared (following selection of events containing exactly two oppositely-charged leptons), which found that the FastSim treatment produced a $E_{\mathrm{T}}^{\mathrm{miss}}$ distribution with a slightly higher mean than the FullSim treatment, but the difference was less than 1% in the electron channel, and smaller again in the muon channel.

6.1.3 Background samples

The dominant SM background processes in this analysis are the $ZZ \to \ell^+\ell^-\nu\bar{\nu}$ and $WZ \to \ell\nu\ell^+\ell^-$ processes, with additional contributions from Z+jets (including $Z \to \tau^+\tau^-$), W+jets, WW, and top events. The background estimation in each signal region is described in detail in sec. 6.4, and includes some estimations taken directly from simulation and others from data-driven methods. However, all background samples were simulated initially, as described below, and are summarised in table 6.4.

The $qq \to WZ$ and $qq \to ZZ$ background samples were produced with POWHEGBOX v1.0 [152]. The $gg \to WW$ sample was produced with `GG2WW` v2 [160], while the $gg \to ZZ$ contribution was included simply by rescaling the $qq \to ZZ$ sample by 6%. All used the CT10 PDF and AUET2 CT10 tune.

The Z+jets, W+jets and $W\gamma$ + jets SM samples were generated with the leading order (LO) generator ALPGEN v2.14 [153], using the CTEQ6L1 PDF [140] and AUET2 CTEQ6L1 tune [219]. The t-channel single top sample was generated with

ACERMC v2 [154, 155], while the s-channel single top, $t\bar{t}$, Wt and $qq \to WW$ samples used the MC@NLO v4.03 generator [156, 157]. All used the CT10 PDF [142] and AUET2 CT10 tune.

The Z+jets sample used PYTHIA6.426 [144] for both showering and the underlying event, while $qq \to WZ$ and $qq \to ZZ$ used PYTHIA8 [145]. All other samples used HERWIG v6.5.20 [158] for showering, and JIMMY v4.31 [159] for the underlying event. QED radiative corrections for all samples were implemented using PHOTOS v3.0 [161] or PHOTOS++ v3.0 [162], and tau decays were handled with TAUOLA v1.04 [163]. GEANT4 was used to simulate the interaction between the truth-level decay products and the detector material.

In all cases, the samples were generated with the in-time pileup conditions that were expected in data, and reweighting was applied to the average number of interactions per bunch crossing, denoted μ, to match data (see sec. 4.1) in the case of discrepancies between data and Monte Carlo (MC) simulation. More specifically, the in-time pileup depends on the instantaneous luminosity, which was not constant during all data-taking; different MC samples were generated with various amounts of pileup, and all were reweighted such that μ was the same as in data. Additionally, μ was scaled by a factor of 1.18 to account for enhancement from minimum bias, following the studies of the $ZH \to \ell\ell$ + *invisible* analysis [230], which has a similar final state.

Finally, several of the cross sections were scaled by a value in each case, called the k-factor, which corrects the LO cross sections to next-to-leading-order (NLO) or next-to-next-to-leading-order (NNLO) where possible.

6.2 Trigger and object definitions

Details of the trigger and object definitions used in this analysis are provided below.

6.2.1 Trigger

All events (data and simulated) are required to pass an initial trigger selection, as discussed in sec. 4.2.4. While a $E_{\mathrm{T}}^{\mathrm{miss}}$-based trigger does exist, it only uses $E_{\mathrm{T}}^{\mathrm{miss}}$ calculated with information from the calorimeter, and as such, muons are not included in the $E_{\mathrm{T}}^{\mathrm{miss}}$ definition. As muons are important in this analysis (particularly in the $\mu^+\mu^-$ channel), a $E_{\mathrm{T}}^{\mathrm{miss}}$-based trigger would therefore not be appropriate, as consistency between the analysis $E_{\mathrm{T}}^{\mathrm{miss}}$ (which does include the muon contribution) and the trigger $E_{\mathrm{T}}^{\mathrm{miss}}$ is required to ensure the analysis is performed with a fully-efficient trigger. Instead, a combination of lepton triggers is utilised.

SM process	Generator	PDF	tune	showering	underlying event	k-factor
Z + jets	ALPGEN v2.14	CTEQ6L1	AUET2 CTEQ6L1	PYTHIA6.426	PYTHIA6.426	1.18
W + jets	ALPGEN v2.14	CTEQ6L1	AUET2 CTEQ6L1	HERWIG v6.5.20	JIMMY v4.31	1.19
$W\gamma$ + jets	ALPGEN v2.14	CTEQ6L1	AUET2 CTEQ6L1	HERWIG v6.5.20	JIMMY v4.31	1.15
$t\bar{t}$	MC@NLO v4.03	CT10	AUET2 CT10	HERWIG v6.5.20	JIMMY v4.31	1.0
single top (s-channel)	MC@NLO v4.03	CT10	AUET2 CT10	HERWIG v6.5.20	JIMMY v4.31	1.0
single top (t-channel)	ACERMC v2	CT10	AUET2 CT10	HERWIG v6.5.20	JIMMY v4.31	1.0
Wt	MC@NLO v4.03	CT10	AUET2 CT10	HERWIG v6.5.20	JIMMY v4.31	1.0
$qq \to WW$	MC@NLO v4.03	CT10	AUET2 CT10	HERWIG v6.5.20	JIMMY v4.31	1.0
$qq \to WZ$	POWHEGBOX v1.0	CT10	AUET2 CT10	PYTHIA8	PYTHIA8	1.0
$qq \to ZZ$	POWHEGBOX v1.0	CT10	AUET2 CT10	PYTHIA8	PYTHIA8	1.0
$gg \to WW$	GG2WW	CT10	AUET2 CT10	HERWIG v6.5.20	JIMMY v4.31	1.0
$gg \to ZZ$	included by scaling $qq \to ZZ$ up by 6%					

Table 6.4: The generators used to simulate the SM background samples for the mono-Z analysis. All used PHOTOS++ v3.0 [162] to compute QED radiative corrections, and TAUOLA v1.04 [163] to handle tau decays where necessary.

Three possible electron triggers are used in the dielectron stream. The first, referred to as `EF_e24vhi_medium1`, requires an electron passing the offline *medium*++ identification with $p_{\mathrm{T}} > 24$ GeV at Event Filter (EF) level. Additional requirements are applied to the hadronic core isolation and track isolation, which can lead to inefficiency at very high p_{T}. This is compensated for by the second trigger, referred to as `EF_e60_medium1`, which also requires a *medium*++ electron but with no isolation requirements, satisfying $p_{\mathrm{T}} > 60$ GeV and so increasing sensitivity to the high p_{T} range. The third trigger instead increases sensitivity at lower p_{T}, it requires two electrons, each satisfying the *loose*++ identification criteria, with p_{T} at the EF level greater than just 12 GeV. The same hadronic core isolation is required. This trigger is called `EF_2e12Tvh_loose1`.

Similarly, in the dimuon channel there are three possible triggers used, with p_{T} thresholds of 24 GeV, 36 GeV and 13 GeV. The first two require the muon satisfy the criteria for *tight* identification, while just the first also requires track isolation; the lowest-threshold trigger requires two muons. These triggers are referred to as `EF_mu24i_tight`, `EF_mu36_tight` and `EF_2mu13`.

All triggers are unprescaled. To avoid overlap between the two streams, events which fire both an electron and a muon trigger are vetoed.

6.2.2 Electrons

Two types of electron are defined: *signal* and *veto* electrons.

Signal electrons pass the *medium*++ identification criteria, and satisfy $E_{\mathrm{T}} > 20$ GeV and $|\eta| < 2.47$. They must be isolated, which is tested by requiring that the p_{T} sum of all tracks in the inner detector (ID) within $\Delta R = 0.2$ of the electron track and satisfying $p_{\mathrm{T}} > 1$ GeV, be less than 10% of the electron transverse energy. Electrons within $\Delta R < 0.2$ of a selected muon are removed, to avoid including events where the electron has been produced through radiation from a muon. Similarly, electrons within $\Delta R < 0.4$ of a selected jet are also removed.

Veto electrons are defined far more loosely, and are used (as described in sec. 6.3) to veto events containing a third lepton. They pass *loose*++ identification criteria and satisfy $p_{\mathrm{T}} > 7$ GeV.

6.2.3 Muons

STACO combined muons are used, as described in sec. 4.3.2. As with electrons, both *signal* and *veto* muons are defined.

Signal muons must satisfy $p_{\mathrm{T}} > 20$ GeV and $|\eta| < 2.5$. To remove cosmic ray muons, tracks are required to have originated at the primary vertex, using $|z_0| <$ 10mm and $|d_0| <$ 1mm. Just as for the electron isolation, the p_{T} sum of all ID

tracks within ΔR = 0.2 of the muon track which satisfy $p_{\mathrm{T}} > 1$ GeV must be less than 10% of the muon p_{T}. Muons within $\Delta R < 0.4$ of a selected jet are removed.

Veto muons are required to pass a lower cut on the transverse momentum, $p_{\mathrm{T}} > 7$ GeV.

6.2.4 Jets

Jets are used as a veto object in this analysis. They are reconstructed with the anti-k_{T} algorithm with a radius parameter of 0.4, and are calibrated to the EM+JES scale (see sec. 4.3.3). Jets are required to satisfy $p_{\mathrm{T}} > 25$ GeV and $|\eta| < 2.5$.

The jet vertex fraction (JVF) is used to characterize the association of a jet to the primary vertex, and is defined as the p_{T} sum of tracks associated to the jet *and* to the primary vertex, divided by the p_{T} sum of all tracks associated to the jet. The JVF for selected jets with $p_{\mathrm{T}} < 50$ GeV and $|\eta| < 2.4$ is required to be greater than 0.5, thereby reducing the number of pileup jets included in the selection.

6.2.5 Missing transverse momentum

The `RefFinal` $E_{\mathrm{T}}^{\mathrm{miss}}$ definition, as described in sec. 4.3.5, is used in this analysis, with one minor change: that tau leptons in the $E_{\mathrm{T}}^{\mathrm{miss}}$ are required to pass the *tight* definition (this is *medium* in the default `RefFinal` definition), but are only scaled to the Local Hadronic Calibration (LC) scale, *not* the Tau Energy Scale (TES) scale. Because the analysis does not identify taus (particularly not hadronically-decaying taus) but instead treat them as jets, and subsequently selects events based on the $E_{\mathrm{T}}^{\mathrm{miss}}$ and absence of a jet, treating the tau differently within the analysis and the $E_{\mathrm{T}}^{\mathrm{miss}}$ could introduce a bias. Scaling both jets and tau-jets to the same scale in the $E_{\mathrm{T}}^{\mathrm{miss}}$ definition is therefore the preferred approach.

6.3 Event selection

The selection of events, and optimisation of that selection, shall be discussed in this section.

The cuts are designed to select events containing a Z boson that has decayed leptonically to a pair of electrons or a pair of muons, as well as a large amount of missing transverse momentum (which 'hides' the invisible DM pair in our signal). The charged lepton pair should be reconstructed into the Z with an invariant mass close to the Z mass, and a transverse momentum that is balanced in magnitude and direction against a significant amount of $E_{\mathrm{T}}^{\mathrm{miss}}$.

6.3.1 Quality cuts

Firstly, events are required to satisfy basic quality criteria:

- have at least one reconstructed vertex with ≥ 3 associated tracks satisfying $p_{\mathrm{T}} > 400$ MeV, to remove the non-collision background,
- reject events where data from the LAr or Tile subdetectors has been flagged as corrupted, and
- reject events containing any jet with $p_{\mathrm{T}} > 20$ GeV and $|\eta| < 4.5$ which has been characterised as 'bad' by the Jet/$E_{\mathrm{T}}^{\mathrm{miss}}$ group of ATLAS, to ensure the $E_{\mathrm{T}}^{\mathrm{miss}}$ calculation is not biased.

6.3.2 Cut optimisation

We note first that when the optimisation of this analysis was being performed, the tS simplified model had not yet been included as one of the DM models, and so was not included in the set of signals studied in this section. However, as described in chapter 3, it is known to demonstrate similar kinematic behaviour to the D5 EFT model, with some variation as the mediator mass decreases.

The following variables are physically motivated as described below, and give continuous distributions requiring optimisation of the selection:

- $\Delta\phi(\vec{E}_{\mathrm{T}}^{\mathrm{miss}}, \vec{p}_{\mathrm{T}}^{Z})$: motivated as the invisible χ particles (which make up the bulk of the $E_{\mathrm{T}}^{\mathrm{miss}}$) should be travelling back-to-back with the recoiling Z boson in the transverse plane, so we expect a separation in ϕ of close to π radians;
- $|p_{\mathrm{T}}^{Z} - E_{\mathrm{T}}^{\mathrm{miss}}|/p_{\mathrm{T}}^{Z}$: the transverse momenta of the reconstructed Z and the χ pair are expected to be balanced in magnitude as well as direction, so this fractional p_{T} difference should be small;
- $|\eta^{Z}|$: the analysis requires transversely-boosted Z bosons, and thus large $E_{\mathrm{T}}^{\mathrm{miss}}$, so this variable should not be too large. In addition, it is used in the Z+jets background estimation procedure (see sec. 6.4) to clearly define the control region (CR);
- $E_{\mathrm{T}}^{\mathrm{miss}}$: fig. 6.1 suggests most signal samples have a harder $E_{\mathrm{T}}^{\mathrm{miss}}$ distributions than the dominant irreducible background[3] of $ZZ \to \ell^{+}\ell^{-}\nu\bar{\nu}$, so a relatively high lower bound on the $E_{\mathrm{T}}^{\mathrm{miss}}$ is expected.

[3]Irreducible here indicates that the background has the same final state as our signal (two same-flavour leptons and missing energy), and so can't be significantly reduced through selection cuts alone.

The first three variables are optimised with the significance, σ, approximated by

$$\sigma \approx \frac{n_S}{\sqrt{n_B}} \ , \tag{6.1}$$

an approximation which is valid when the number of background events (n_B) is much greater than the number of signal events (n_S) and so the background uncertainty can be neglected. These variables and their significance at each cut value are shown in fig. 6.2. However, as the $E_{\mathrm{T}}^{\mathrm{miss}}$ distribution of the backgrounds falls off much faster than that of the DM signal, this approximation is not valid for large $E_{\mathrm{T}}^{\mathrm{miss}}$ and the significance is instead approximated by

$$\sigma \approx \frac{n_S}{\sqrt{n_B + \Delta n_B}} \ , \tag{6.2}$$

where now the background uncertainty Δn_B is taken into account. A variable proportional to this significance is shown for the D5 and $ZZ\chi\chi$ (minimal-interference) EFT models as a function of the $E_{\mathrm{T}}^{\mathrm{miss}}$ cut in fig. 6.3.

Relatively conservative values are chosen for the final selection cuts for two reasons. Firstly, there is variation within the different model signals, bounded by the D5 and the minimum-interference $ZZ\chi\chi$ models, so a conservative cut choice in each case means the same signal region can be defined for all models. Secondly, the significance is maximised at extreme values of $\Delta\phi(\vec{E}_{\mathrm{T}}^{\mathrm{miss}}, \vec{p}_{\mathrm{T}}^{\ell\ell})$ and $|p_{\mathrm{T}}^{\ell\ell} - E_{\mathrm{T}}^{\mathrm{miss}}|/p_{\mathrm{T}}^{\ell\ell}$, but since these are sensitive to the modeling of the $E_{\mathrm{T}}^{\mathrm{miss}}$ in simulation, applying the selection at those extremes would make the optimisation process dependent on the $E_{\mathrm{T}}^{\mathrm{miss}}$ systematic uncertainties.

Further, discrete selections are not optimised, but are motivated on physical grounds:

- veto events containing a third, more loosely defined lepton, so as to suppress the diboson background ($WZ \to \ell'\nu\ \ell^+\ell^-$ and $ZZ \to \ell^+\ell^-\ \ell'^+\ell'^-$);
- veto events containing a jet, so as to suppress the top-quark pair background ($t\bar{t} \to W^+\bar{b}\ W^-b \to \ell^+\bar{\nu}\bar{b}\ \ell^-\nu b$).

6.3.3 Final selection

The final event selection is as follows:

- exactly 2 same-flavour, opposite-sign leptons (i.e. an e^+e^- pair *or* a $\mu^+\mu^-$ pair),

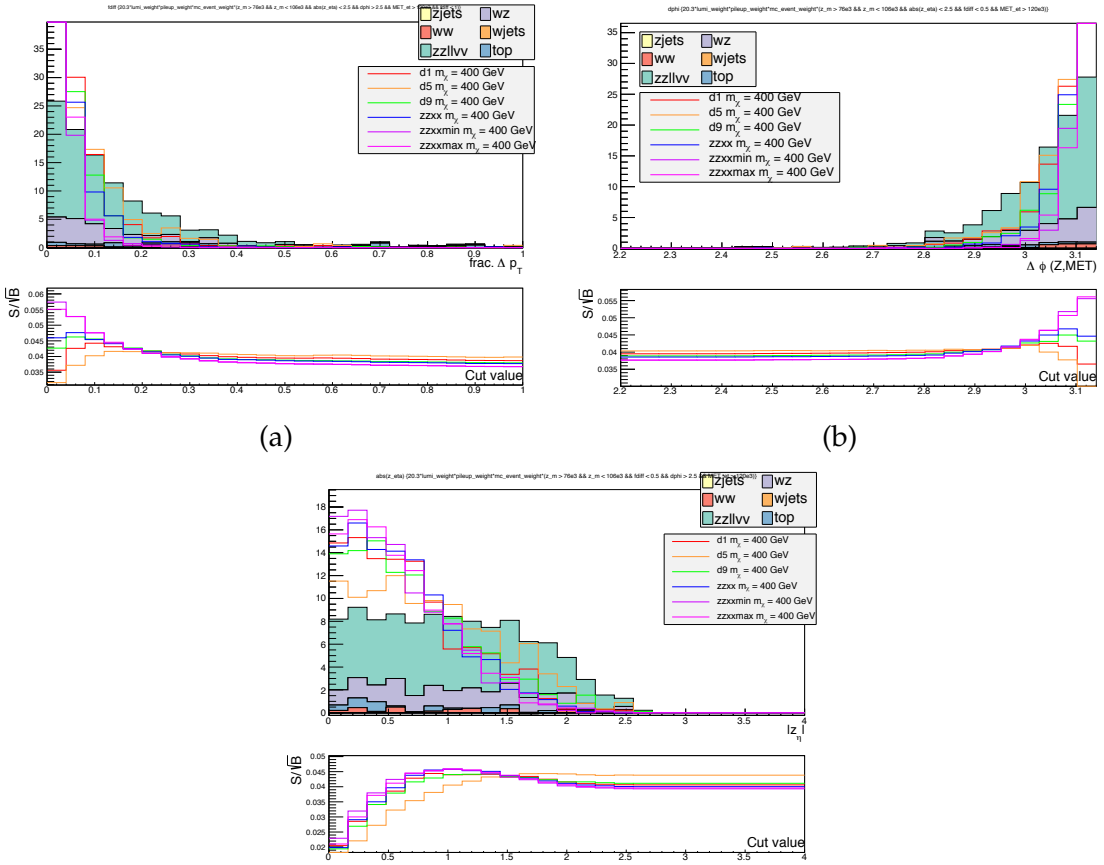

(a) (b)

(c)

Figure 6.2: Comparison of a subset of DM signals and SM background estimations for the continuous variables of interest, optimised with $\sigma \approx n_S/\sqrt{n_B}$ which is shown in the lower panels as a function of the cut value. All analysis cuts (as listed in sec. 6.3) are applied except for the variable shown in each case. Taken from ref. [2].

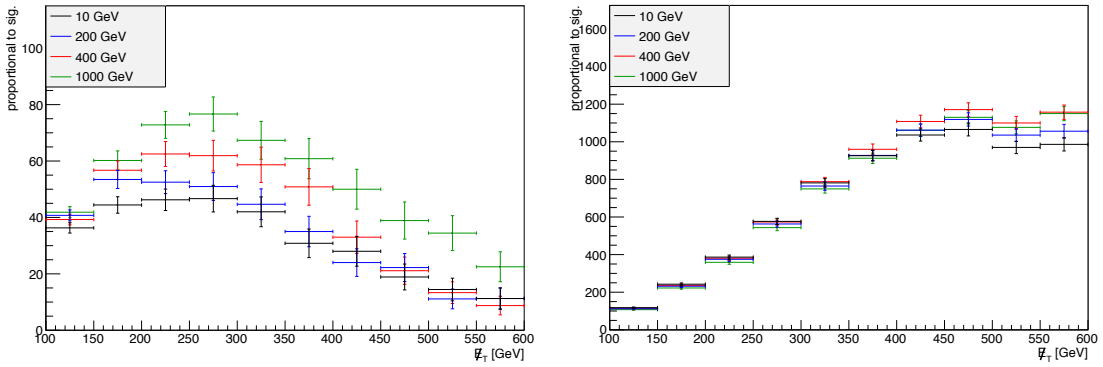

(a) (b)

Figure 6.3: Comparison of the significance ($\sigma \approx n_S/\sqrt{n_B + \Delta n_B}$) of the D5 (left) and minimal-interference $ZZ\chi\chi$ (right) models of DM for a varying $E_{\mathrm{T}}^{\mathrm{miss}}$ cut. Other EFT models were tested and shown to lie within the extreme cases shown here. Taken from ref. [2].

- $m^Z \in$ [76, 106] GeV,
- $|\eta^Z| < 2.5$,
- $\Delta\phi(\vec{E}_{\mathrm{T}}^{\mathrm{miss}}, \vec{p}_{\mathrm{T}}^{Z}) > 2.5$,
- $|p_{\mathrm{T}}^{Z} - E_{\mathrm{T}}^{\mathrm{miss}}|/p_{\mathrm{T}}^{Z} < 0.5$,
- veto events that contain a third *veto* lepton, as defined in secs. 6.2.2 and 6.2.3,
- veto events containing a *veto* jet, as defined in sec. 6.2.4, and
- $E_{\mathrm{T}}^{\mathrm{miss}} > 150$, 250, 350, 450 GeV

where m^Z is the invariant mass of the lepton pair, and the four $E_{\mathrm{T}}^{\mathrm{miss}}$ cuts define four (non-orthogonal) signal regions.

Figs. 6.4 and 6.5 show the relevant kinematic distributions following selection of exactly two electrons or two muons. With the exception of the top two plots of fig. 6.4, which depict the $E_{\mathrm{T}}^{\mathrm{miss}}$ distribution, all plots are shown with $E_{\mathrm{T}}^{\mathrm{miss}} <$ 150 GeV; these are known as *blinded* plots, and are designed to provide information on the variables of interest, without comparing the data and simulated backgrounds in the intended signal regions before the simulated backgrounds have been properly estimated (as discussed in the following section), to avoid biasing the analysis.

6.4 Backgrounds

The estimation of number of SM background events entering the signal region (SR) is an important component of any experimental analysis. While some backgrounds are well-modeled by MC simulation, others are known to be imperfectly simulated, as can be shown by the poor agreement with measured data in dedicated CRs designed to be dominated by the background process of interest. This is often related to whether the distribution of interest, in this case the $E_{\mathrm{T}}^{\mathrm{miss}}$, is real (such as that resulting from high-energy neutrinos) in which case it is generally well-modeled, or fake (such as when a jet's energy is mismeasured), in which case it is not.

The dominant background in this analysis is the irreducible $ZZ \to \ell^+\ell^-\ \nu\bar{\nu}$ background, in which the $E_{\mathrm{T}}^{\mathrm{miss}}$ contribution is real and due to the momentum carried away by the neutrinos. $WZ \to \ell\nu\ \ell^+\ell^-$ events, in which one of the leptons is not identified, also have a real $E_{\mathrm{T}}^{\mathrm{miss}}$ component. Both of these backgrounds are estimated with MC, and validated in dedicated 3- and 4-lepton CRs.

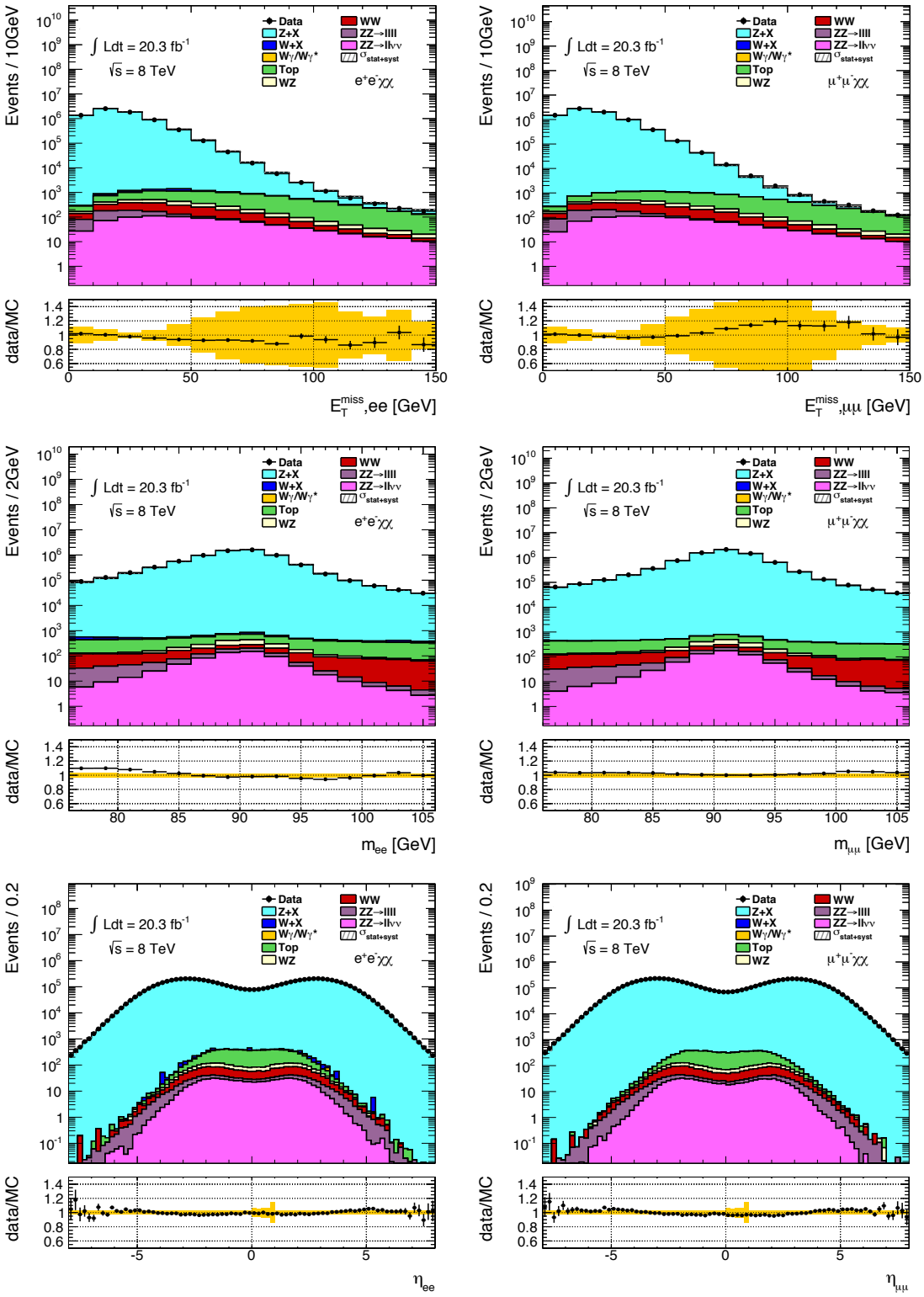

Figure 6.4: The $E_{\mathrm{T}}^{\mathrm{miss}}$ (top), lepton pair invariant mass (middle) and η (bottom) distributions, in events with exactly two oppositely-charged electrons (left) or muons (right). The $E_{\mathrm{T}}^{\mathrm{miss}}$ distribution is shown following application of the Z mass window requirement, while the invariant mass and η distributions are for events with $E_{\mathrm{T}}^{\mathrm{miss}} < 150$ GeV. Taken from ref. [2].

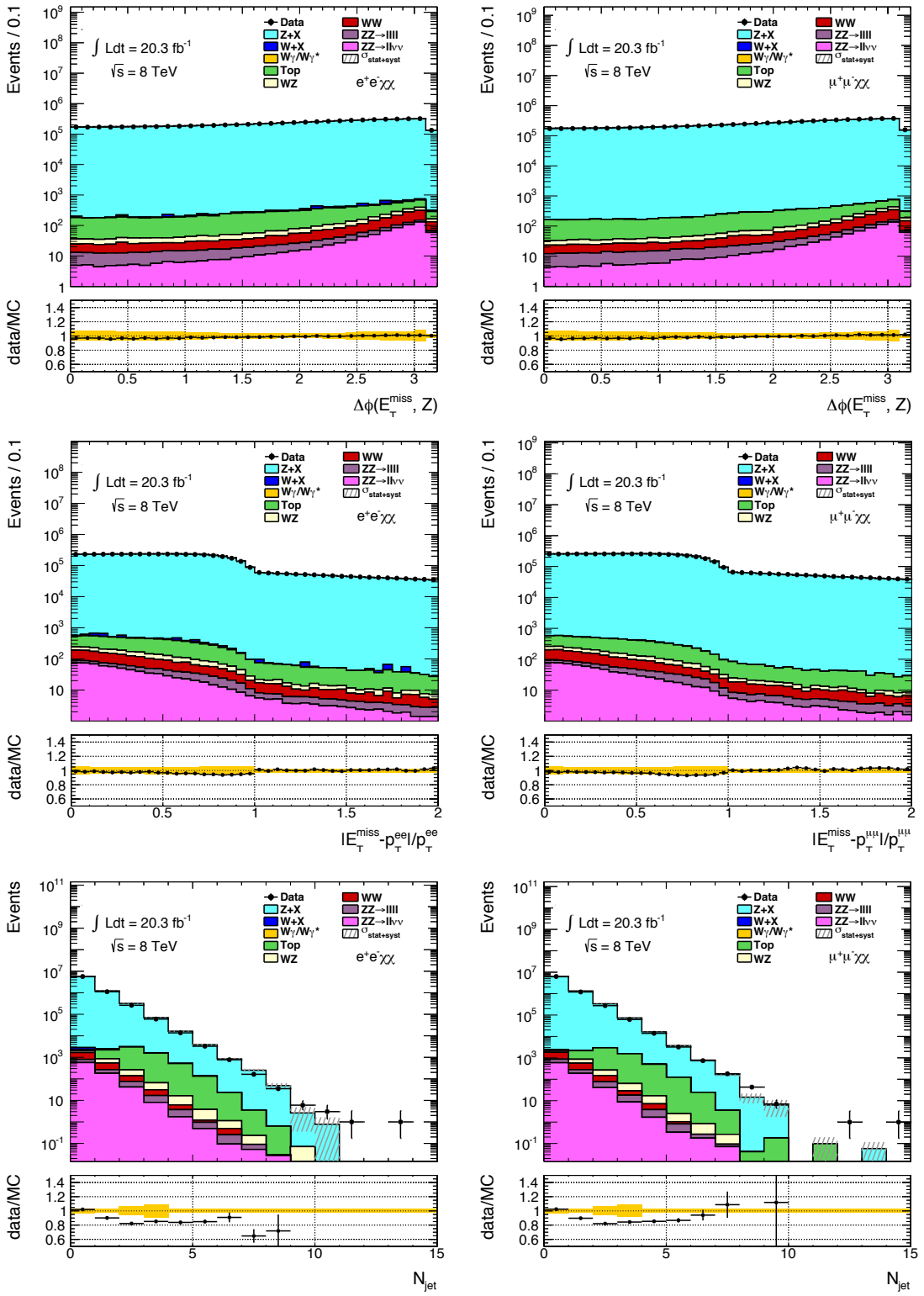

Figure 6.5: Distributions of $\Delta\phi(Z, E_{\mathrm{T}}^{\mathrm{miss}})$ (top), fractional p_{T} (middle) and jet multiplicity (bottom), in events with exactly two oppositely-charged electrons (left) or muons (right). All plots are shown following application of the Z mass window requirement and $E_{\mathrm{T}}^{\mathrm{miss}} < 150$ GeV. Taken from ref. [2].

The Z+jets, W+jets, WW, top and $\tau\tau$ backgrounds, on the other hand, are all estimated using data-driven methods. The Z+jets background estimate is performed two ways, using the *ABCD* method with two uncorrelated kinematic variables, or fitting a function to the $\Delta\phi(Z, E_{\mathrm{T}}^{\mathrm{miss}})$ distribution in bins of $E_{\mathrm{T}}^{\mathrm{miss}}$, and extrapolating from the low-$E_{\mathrm{T}}^{\mathrm{miss}}$ region into the high-$E_{\mathrm{T}}^{\mathrm{miss}}$ SR. The W+jets background also uses an extrapolation to the high-$E_{\mathrm{T}}^{\mathrm{miss}}$ region, within a CR scaled to the SR. The WW, top and $\tau\tau$ estimates take advantage of lepton universality, which says that the number of ee or $\mu\mu$ events from each production mode should be half that of $e\mu$ events.

Each of the background estimation methods is described in further detail in the following sections.

6.4.1 The Z + jets background

This background comes from a real Z decaying leptonically, and some amount of fake $E_{\mathrm{T}}^{\mathrm{miss}}$ resulting from the mismeasurement of jet energies. Because the $E_{\mathrm{T}}^{\mathrm{miss}}$ is not real, it is harder to make an accurate estimate with MC; additionally, the available MC statistics are limited in the high $E_{\mathrm{T}}^{\mathrm{miss}}$ region (our signal regions), leading to large statistical uncertainties. Therefore, a data-driven estimate is desirable.

In fact, the Z+jets background contribution is estimated from data in two ways, both using the low $E_{\mathrm{T}}^{\mathrm{miss}}$ region (where Z+jets dominates) and extrapolating to the signal regions: an ABCD method using the uncorrelated $E_{\mathrm{T}}^{\mathrm{miss}}$ and η^Z variables, and a fit to a function of $E_{\mathrm{T}}^{\mathrm{miss}}$ and $\Delta\phi(Z, E_{\mathrm{T}}^{\mathrm{miss}})$. The result from the former method is used as the central value of the background estimate, while the difference from the result of the latter method is taken as a systematic uncertainty.

The *ABCD* method

In this method, one SR and three CRs are defined according to cuts on the $E_{\mathrm{T}}^{\mathrm{miss}}$ and an uncorrelated variable, in this case, the pseudorapidity of the leptonic Z boson (η^Z); see table 6.5 for the definitions of the regions A, B, C and D. Other kinematic variables of the Z were tested, however $|\eta^Z|$ has the smallest correlation, 1.3% in 1.1fb^{-1} of data. Specifically, $|\eta^Z|$ is cut at 2.0, while the $E_{\mathrm{T}}^{\mathrm{miss}}$ is cut at some value X; ordinarily this would be set to the lower bound of each signal region (i.e. at 150, 250, 350 and 450 GeV), however the number of Z+jets events in the regions with $E_{\mathrm{T}}^{\mathrm{miss}} > X$ start to become very small, and large statistics are desired to estimate this background. Therefore, a set of 'provisional' signal regions are defined with $X \in [30, 80]$ GeV, the number of Z+jets events in each is estimated using the $ABCD$ method (described below), and then these are fitted

	$\lvert\eta^{\ell\ell}\rvert < 2.5$	$\lvert\eta^{\ell\ell}\rvert > 2.5$
$E_{\mathrm{T}}^{\mathrm{miss}} > X$	A	C
$E_{\mathrm{T}}^{\mathrm{miss}} < X$	B	D

Table 6.5: The four regions used in the ABCD method, where $E_{\mathrm{T}}^{\mathrm{miss}}$ and $|\eta^{\ell\ell}|$ are approximately uncorrelated variables. Multiple values for X are used, and the resulting distribution of numbers of events in the region A are extrapolated into the SRs.

as a function of X and extrapolated into the true signal regions, where X= 150, 250, 350 and 450 GeV.

In each region of table 6.5, all other SR cuts are applied, other than the $E_{\mathrm{T}}^{\mathrm{miss}}$ and $|\eta^{Z}|$ cuts *and* the cuts on the fractional p_{T} and $\Delta\phi(Z, E_{\mathrm{T}}^{\mathrm{miss}})$. The latter two cuts are not included so as to ensure there are still many events in each of the CRs, and a selection efficiency of 0.099$\pm$ 0.001 (which accounts for these two cuts) is applied to the Z+jets events in the provisional SRs before the extrapolation to the real SRs is performed.

The number of events in the signal region, region A, is calculated by

$$n(A) = \frac{n(B) \times n(C)}{n(D)} \ . \tag{6.3}$$

However, this does not yet take into account the purity of Z+jets events in each of the regions. This purity is denoted α and is the fraction of Z+jets events in the total background in each region, estimated using MC:

$$\alpha = \frac{N_{Z\text{+jets}}}{\sum_i N_i} \tag{6.4}$$

where $i = WW, WZ, ZZ(\rightarrow \ell\ell\ell'\ell', \ell\ell\nu\nu), W\gamma, t\bar{t}, W$+jets and Z+jets. The purity in regions B and D is found to be consistent with 1, however in region C it varies from 99.8% at X = 40 GeV to 88% at X = 100 GeV. The purity in region A is therefore exactly the purity of region C, and so the estimated number of Z+jets events in region A is corrected from eq. 6.3 to

$$n(A) = \frac{n(B) \times n(C) \times \alpha}{n(D)} \ . \tag{6.5}$$

Fig. 6.6, taken from ref. [2], shows the full data set as a function of $E_{\mathrm{T}}^{\mathrm{miss}}$ and $|\eta^{\ell\ell}|$ in the di-muon channel; it also indicates the signal and control regions for X = 60 GeV, the event count in regions B, C and D, and the estimated number of Z+jets events in region A calculated according to eq. 6.5.

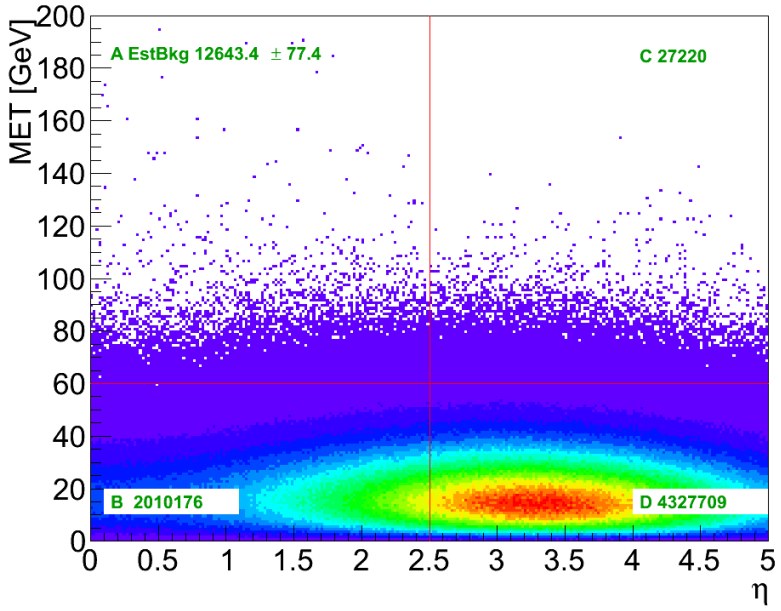

Figure 6.6: $E_{\mathrm{T}}^{\mathrm{miss}}$ vs $|\eta^{\ell\ell}|$ in the di-muon channel, for 20.3 fb^{-1} of data. The four regions of the *ABCD* method are marked by the red lines (for an arbitrary $E_{\mathrm{T}}^{\mathrm{miss}}$ cut at 60 GeV). The event count in each CR, as well as the estimate in the SR following eq. 6.5, are also shown. Taken from ref. [2].

The fitted $\Delta\phi$ method

This method takes advantage of the fact that the fake $E_{\mathrm{T}}^{\mathrm{miss}}$ in Z+jets events can be distinguished from true $E_{\mathrm{T}}^{\mathrm{miss}}$ in the signal or real-$E_{\mathrm{T}}^{\mathrm{miss}}$ backgrounds (such as $ZZ \to \ell\ell\nu\nu$), by comparing kinematic distributions that feature this variable. $\Delta\phi(Z, E_{\mathrm{T}}^{\mathrm{miss}})$ is chosen as it is sharply peaked around π in events with real $E_{\mathrm{T}}^{\mathrm{miss}}$, but more spread out in events where the fake $E_{\mathrm{T}}^{\mathrm{miss}}$ has a random component.

In this method, the distribution of $\Delta\phi(Z, E_{\mathrm{T}}^{\mathrm{miss}})$ in low-$E_{\mathrm{T}}^{\mathrm{miss}}$ data events (expected to be dominated by the Z+jets background) is fitted with a function in bins of $E_{\mathrm{T}}^{\mathrm{miss}}$, then extrapolated into the high-$E_{\mathrm{T}}^{\mathrm{miss}}$ signal regions. This method is validated in MC as described below, and a systematic is determined based on the presence of other backgrounds within the low-$E_{\mathrm{T}}^{\mathrm{miss}}$ control region. The fitting function is a Gaussian of the form

$$f_{\Delta\phi}(x) = A + B \exp\left(-\frac{(x-\pi)^2}{2\sigma^2}\right) , \tag{6.6}$$

where A can be interpreted as the fraction of events with fake $E_{\mathrm{T}}^{\mathrm{miss}}$ in random directions, B as the fraction from mismeasured jets back-to-back with the leptonically-decaying Z, and σ as the width of the distribution. Fig. 6.7 demonstrates the geometric interpretation of these parameters as they are fitted against the $\Delta\phi(\vec{E}_{\mathrm{T}}^{\mathrm{miss}}, \vec{p}_{\mathrm{T}}^{\,Z})$ distribution in bins of low $E_{\mathrm{T}}^{\mathrm{miss}}$.

The fitting variables are dependent on the $E_{\mathrm{T}}^{\mathrm{miss}}$ range, shown explicitly in

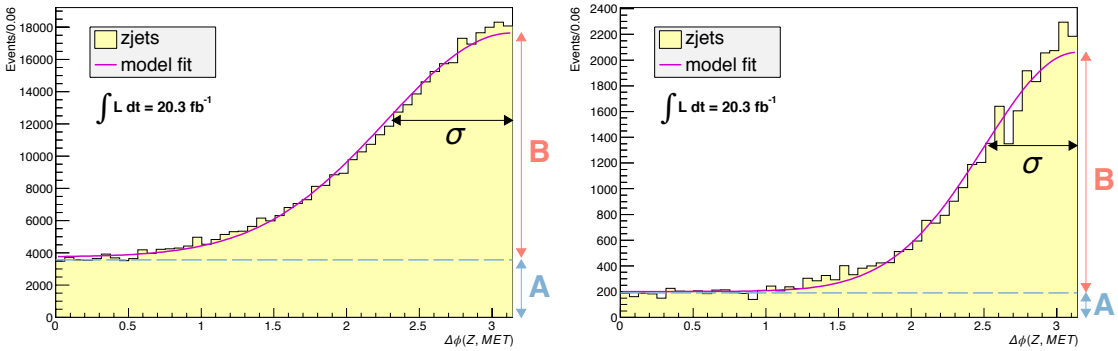

(a) 20 GeV $< E_{\mathrm{T}}^{\mathrm{miss}} <$ 30 GeV (b) 40 GeV $< E_{\mathrm{T}}^{\mathrm{miss}} <$ 50 GeV

Figure 6.7: The $\Delta\phi(\vec{E}_{\mathrm{T}}^{\mathrm{miss}}, \vec{p}_{\mathrm{T}}^{Z})$ distribution in two $E_{\mathrm{T}}^{\mathrm{miss}}$ bins, with a Gaussian fitted according to eq. 6.6. All signal region cuts are applied except those on $E_{\mathrm{T}}^{\mathrm{miss}}$ and $\Delta\phi$. Taken from ref. [2].

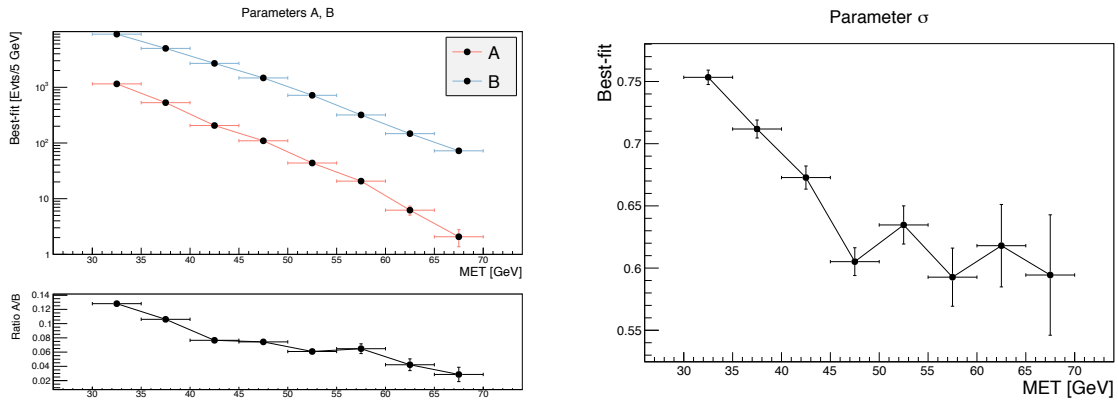

Figure 6.8: The Gaussian fit parameters A, B (left) and σ (right) of eq. 6.6 as a function of the $E_{\mathrm{T}}^{\mathrm{miss}}$, in the dielectron channel. All three parameters are subsequently modeled as exponentials. Taken from ref. [2].

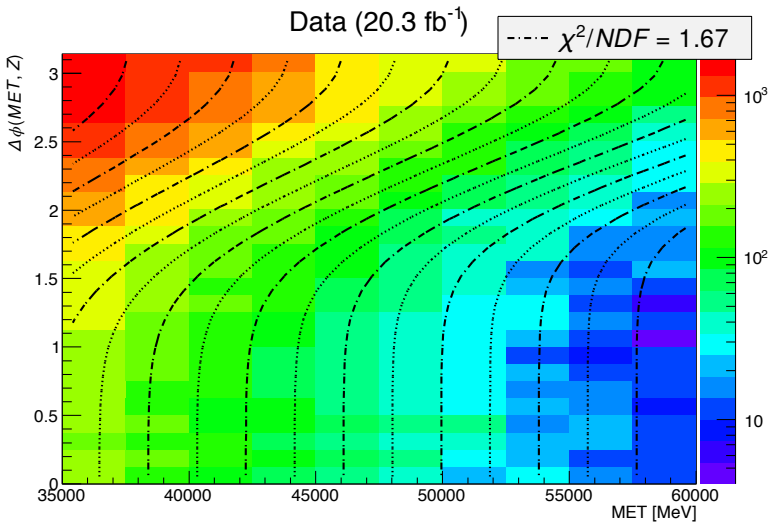

Figure 6.9: 3D distribution of data events in the dielectron channel, shown as a function of $E_{\mathrm{T}}^{\mathrm{miss}}$ and $\Delta\phi(Z, E_{\mathrm{T}}^{\mathrm{miss}})$, and fitted by eq. 6.7 with a reduced χ^2 of 1.67. Taken from ref. [2].

fig. 6.8 for pure Z+jets MC in the di-electron channel. The value of A/B decreases for events in bins of greater $E_{\mathrm{T}}^{\mathrm{miss}}$, since a higher $E_{\mathrm{T}}^{\mathrm{miss}}$ cut implies events with more boosted Z bosons are selected, due to the inclusion of the fractional p_{T} cut ($|p_{\mathrm{T}}^{Z} - E_{\mathrm{T}}^{\mathrm{miss}}|/p_{\mathrm{T}}^{Z} < 0.5$); this also decreases the Gaussian width σ. The parameters A, B and σ are all modeled as exponential functions of $E_{\mathrm{T}}^{\mathrm{miss}}$ of the form $\exp(a_0 + a_1 x)$, and so the fitting function of eq. 6.6 now becomes a function of two parameters ($\Delta\phi(\vec{E}_{\mathrm{T}}^{\mathrm{miss}}, \vec{p}_{\mathrm{T}}^{Z})$ and $E_{\mathrm{T}}^{\mathrm{miss}}$), and takes the form

$$f_{\Delta\phi, E_{\mathrm{T}}^{\mathrm{miss}}}(x, y) = \exp(a_0 + a_1 y) + \exp\left(b_0 + b_1 y - \frac{(x-\pi)^2}{2\exp(s_0 + s_1 y)^2}\right) . \tag{6.7}$$

The 3D distribution of events in the e^+e^- channel for all data with 35 GeV $\leq E_{\mathrm{T}}^{\mathrm{miss}} \leq$ 60 GeV is shown in fig. 6.9, and the function of eq. 6.9 was fitted with a reduced χ^2 (that is, χ^2 divided by the total number of degrees of freedom) of 1.67. In data, uncertainty in the fitting parameters is considered a statistical uncertainty as it results from the limited statistics.

The final estimate of background events from Z+jets processes is found by integrating the fitted function eq. 6.7 over the signal region, according to

$$\int_{2.5}^{\pi}\int_{X}^{\infty} f_{\Delta\phi, E_{\mathrm{T}}^{\mathrm{miss}}}(x, y)\,dx\,dy \ , \tag{6.8}$$

where X is the lower bound on the $E_{\mathrm{T}}^{\mathrm{miss}}$ defining each SR. Only SR1 (with $E_{\mathrm{T}}^{\mathrm{miss}} >$ 150 GeV) gives a non-negligible contribution from the Z+jets background. To estimate the systematic uncertainty that arises from treating the low-$E_{\mathrm{T}}^{\mathrm{miss}}$ control

region as entirely Z+jets events, and thereby ignoring the (small) contribution from other background sources, the fitting procedure and background estimation is performed on MC, where the MC is either a pure Z+jets sample or includes all backgrounds.

6.4.2 The W+jets background

The W+jets events that enter the signal region do so when one of the jets is misidentified as an electron or muon of opposite sign to the true muon produced by the W decay, and the real and fake leptons are reconstructed into a fake Z boson close to the Z mass. The $E_{\mathrm{T}}^{\mathrm{miss}}$ in this background is real, from the neutrino produced in W decay, and peaks at half the transverse mass of the W. Because the likelihood of a jet faking an electron is an order of magnitude greater than the likelihood of it faking a muon, only the electron case is considered.

For the estimation of this background, a data-driven method is used, whereby a CR enriched in W+jets events is defined, and scaled to the number of events expected in the SR, as defined by MC. The $E_{\mathrm{T}}^{\mathrm{miss}}$ distribution is fitted in the low-$E_{\mathrm{T}}^{\mathrm{miss}}$ region, and extrapolated into the high-$E_{\mathrm{T}}^{\mathrm{miss}}$ SR, to estimate the number of W+jets events in the SR. This is described in further detail below.

The W+jets CR is defined by inverting the selection criteria for the second electron, while still requiring that the first electron pass the standard electron criteria. The second electron is then required to pass the *loose*++ criteria but *fail* the *medium*++; the isolation requirement is also inverted, that is, the vector p_{T} sum of all inner-detector tracks within a cone of ΔR = 0.2 of the electron track should be *greater* than 10% of the E_{T} of the electron. Finally, the jet overlap removal step is removed.

In data, these criteria yield approximately 54,000 events. The default electron selection (i.e. two good electrons) is applied to the W+jets MC (scaled for cross section), and yields 2,300 events. The normalisation of data events is therefore defined to be 2300/54000 = 0.043, and is applied to the $E_{\mathrm{T}}^{\mathrm{miss}}$ distribution from data in the CR, which is depicted in the fig.6.10(a).

Two fitting functions are derived to fit to the data. The first is commonly used to describe the falling $E_{\mathrm{T}}^{\mathrm{miss}}$ spectrum of a dijet function [231]:

$$f_{E_{\mathrm{T}}^{\mathrm{miss}}}(x) = a(1-x)^b(x^{-c+d\ln(x)}) \ . \tag{6.9}$$

However, fitting studies indicated that parameter b had the largest uncertainty and would return values close to 0, and it was decided to set this equal to 0 for subsequent fits, which still yields a reasonable reduced χ^2. The second function is a simple power law, given by

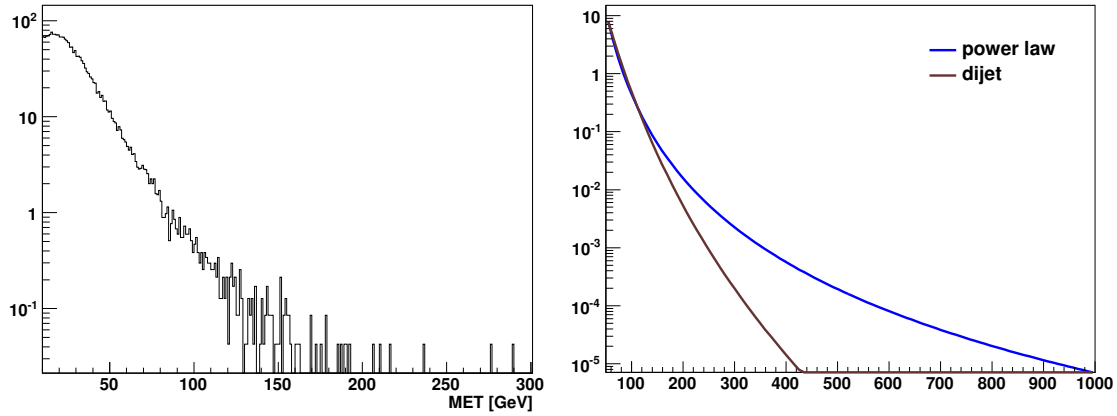

(a) (b)

Figure 6.10: The $E_{\mathrm{T}}^{\mathrm{miss}}$ distribution of data in the W+jets CR, which inverts the *medium*++ identification criterion for the second electron in the dielectron channel (a), and the two fitting functions that were tested (b). While the two functions agree for $E_{\mathrm{T}}^{\mathrm{miss}} < 150$ GeV (where most events in the CR lie), they diverge significantly in the high-$E_{\mathrm{T}}^{\mathrm{miss}}$ region. Taken from ref. [2].

$$g_{E_{\mathrm{T}}^{\mathrm{miss}}}(x) = ax^b \ . \tag{6.10}$$

The two functions are fitted in several ranges of $E_{\mathrm{T}}^{\mathrm{miss}}$, and the range giving the best χ^2/NDF is chosen in each case; the dijet function is therefore fitted in the range 30–300 GeV (giving χ^2/NDF = 0.89) and the power law function is fitted in the range 50–300 GeV (χ^2/NDF = 0.84). The parameters giving these best fits are listed in table 6.6. The two functions are then extrapolated to $E_{\mathrm{T}}^{\mathrm{miss}}$ = 1 TeV, and are shown in fig. 6.10(b). The estimated number of W+jets events in the SR background is then found by integrating the function over the range X–1 TeV (where X = 150, 250, 350 and 450 GeV for each SR), and multiplying that value by 0.22, which was calculated as the fraction of events that passed the remaining SR selection. Notably, the two possible functions give quite different distributions over the range 200–1000 GeV, so the more conservative power law function is used to calculate the W+jets background estimate, while the difference from the dijet function value is taken as a systematic uncertainty. Only SR1 gives a non-negligible estimate of the W+jets background.

6.4.3 The WW, top and $\tau\tau$ backgrounds

The contribution from the WW, top ($t\bar{t}$, Wt and s- and t-channel single-top) and $Z \to \tau\tau$ backgrounds is estimated using a data-driven method that takes advantage of the lepton branching ratios in each case. Specifically, at truth-level,

function	parameter	value
dijet	a	$9.7\times10^{-4} \pm 4\times10^{-4}$
	b	0 (fixed)
	c	-8.39 $\pm$ 0.22
	d	-1.54 $\pm$ 0.03
power law	a	$1.7\times10^{9} \pm 0.5\times10^{9}$
	b	-4.80 $\pm$ 0.07

Table 6.6: The parameters giving the best fit to the falling $E_{\mathrm{T}}^{\mathrm{miss}}$ distribution of fig. 6.10(a), as described by the functions in eqs. 6.9 and 6.10. The functions were then extrapolated into the signal region to estimate the contribution of the W+jets background.

$$N_{e\mu}^{\text{truth}} = 2 \times N_{ee}^{\text{truth}} = 2 \times N_{\mu\mu}^{\text{truth}} \ . \tag{6.11}$$

At reconstruction-level, muons and electrons have different reconstruction efficiencies, which needs to be taken into account. The method uses events requiring exactly one electron and one muon reconstructed within the Z boson mass window, and estimates the number of di-electron and di-muon events from these backgrounds according to

$$N_{ee}^{\text{est}} = N_{e\mu}^{\text{data,corr}} \times k_{ee}, \text{ where } k_{ee} = \frac{1}{2}\sqrt{\frac{N_{ee}^{\text{data}}}{N_{\mu\mu}^{\text{data}}}} \tag{6.12}$$

and

$$N_{\mu\mu}^{\text{est}} = N_{e\mu}^{\text{data,corr}} \times k_{\mu\mu}, \text{ where } k_{\mu\mu} = \frac{1}{2}\sqrt{\frac{N_{\mu\mu}^{\text{data}}}{N_{ee}^{\text{data}}}} \tag{6.13}$$

where $N_{e\mu}^{\text{data,corr}}$ is the number of $e\mu$ events observed in the CR after subtraction of other backgrounds which may contribute to the $e\mu$ CR, estimated with MC. These other backgrounds are dominated by WZ events but also include ZZ, W+jets, Z+jets and $W\gamma$; in total they contribute less than 3% following all selection cuts.

Fig. 6.11(a) shows the invariant mass of the $e\mu$ pair within the Z mass window, while (b) shows the high-$E_{\mathrm{T}}^{\mathrm{miss}}$ region; both the mass window and $E_{\mathrm{T}}^{\mathrm{miss}} > 120$ GeV cuts are applied. This background is dominated by WW and top events, and good agreement with data (including after all other selections are applied) is observed.

The uncertainties of the data-driven method are dominated by the statistical uncertainty due to the small number of events in the CR—after the full selec-

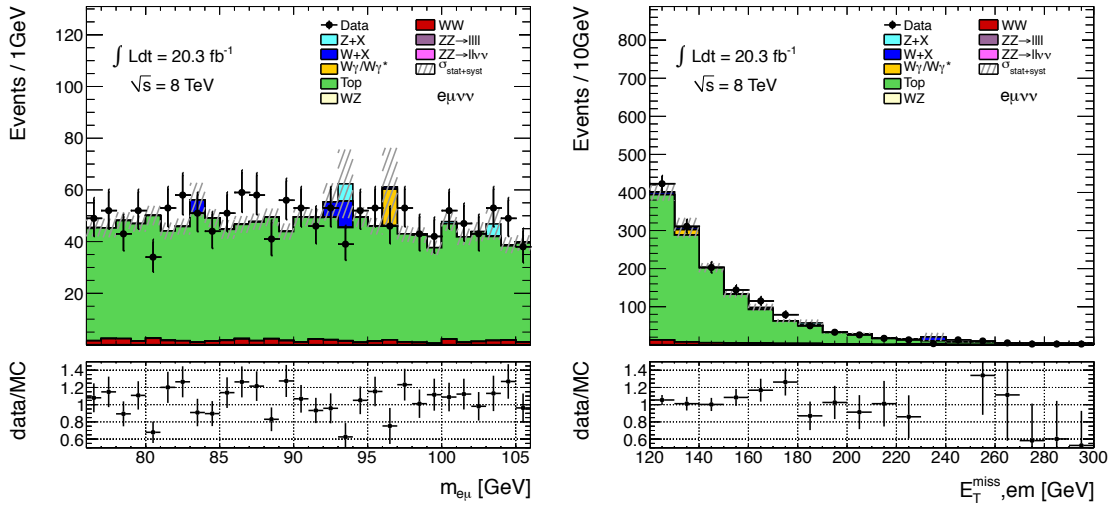

(a) (b)

Figure 6.11: The lepton pair invariant mass (a), and the high-$E_{\mathrm{T}}^{\mathrm{miss}}$ (b) distributions in the $e\mu$ CR. The mass window cut and $E_{\mathrm{T}}^{\mathrm{miss}} > 120$ GeV cuts have been applied. Taken from ref. [2].

tion is applied (including a $E_{\mathrm{T}}^{\mathrm{miss}}$ cut at 120 GeV), only 12 $e\mu$ events are observed in data. Statistical uncertainties from the subtracted additional backgrounds are also included.

Systematic uncertainties are estimated from three sources. An MC closure test is performed, where the method described by eqs. 6.12 and 6.13 is applied to pure MC, and the values of N_{ee}^{est} and $N_{\mu\mu}^{\mathrm{est}}$ obtained are compared with the MC direct estimate, yielding a difference of 1.3% in both electron and muon channels. This difference is taken as a systematic uncertainty.

The values of k_{ee} and $k_{\mu\mu}$ are compared in data and MC, and the differences taken as additional systematics. These are 4.6% and 4.7% in the electron and muon channels respectively. Systematic uncertainties on the subtracted MC backgrounds are estimated to be 10.4% for the WZ and ZZ backgrounds, 30% for the W+jets and $W\gamma$ backgrounds, and 13% for the Z+jets background; these are linearly summed and propagated through the calcualtion.

Finally, the estimated background using the data-driven method described above is cross-checked against the estimate from MC. Uncertainties in the MC are split into the associated statistical uncertainties of the WW, top and $Z \to \tau\tau$ MC samples, and systematic uncertainties due mainly to the Jet Energy Scale (JES) and Jet Energy Resolution (JER) uncertainties in the jet veto for the top events and difference in predicted and measured cross section for WW events. The data-driven and fully-simulated methods give background estimates that are consistent, and so the estimate from the data-driven method is used as the final estimate for the WW, top and $\tau\tau$ backgrounds.

	3-lepton CR	4-lepton CR
MC	331 ± 13	119.5 ± 1.35
Data	335	148

Table 6.7: Data and MC comparison for the 3-lepton and 4-lepton CRs.

6.4.4 The ZZ and WZ backgrounds

The WZ and ZZ background contributions are estimated from simulation, and validated in CRs with three and four charged leptons respectively. The WZ CRs contain either eee, $ee\mu$, $e\mu\mu$ or $\mu\mu\mu$, while the ZZ CRs contain either four electrons, four muons, or two of each flavour. WZ events can also appear in the 4-lepton CRs with a fake lepton, and conversely ZZ events can contribute to the 3-lepton CRs if a lepton is not properly identified. $t\bar{t}$ and Z+jets events can contibute to both types of CRs with one or two additional fake leptons.

The fake contribution is poorly modeled in MC, however most fake lepton events are removed with the application of the Z mass window cut. The 3-lepton CRs also have $E_{\mathrm{T}}^{\mathrm{miss}} > 80$ GeV applied, this is not needed in the 4-lepton CR as the overall fake contribution is small (particularly from the $t\bar{t}$ and Z+jets backgrounds, which need to fake two leptons).

Table 6.7 indicates the total number of events in the 3-lepton and 4-lepton CRs in both MC and data, while figs. 6.12 and 6.13 show the $E_{\mathrm{T}}^{\mathrm{miss}}$ distribution in each of the CRs separately, following the invariant mass selection. In all cases, reasonable agreement is observed between MC and data.

The systematic uncertainty is obtained through comparison of two MC generators with very high statistics. A million $ZZ \to \ell\ell\nu\nu$ events were produced with POWHEGBOX v1.0, along with 830k ZZ events produced with SHERPA v1.4.1 [147] (using massive b and c quarks). The acceptance at truth level for each SR was calculated and compared between the two samples, and it was found that the difference in each SR was within a few percentage points of 35%. This value is therefore taken as a flat systematic for all signal regions, for both ZZ and WZ backgrounds.

6.4.5 Summary of backgrounds

The final estimated backgrounds from each source, in each of the four SRs, are listed in tables 6.12 and 6.13. The total estimate of the SM background is found by summing the MC WZ and ZZ contributions and the data-driven WW, top, Z+jets and W+jets contributions. Further details about the systematic uncertain-

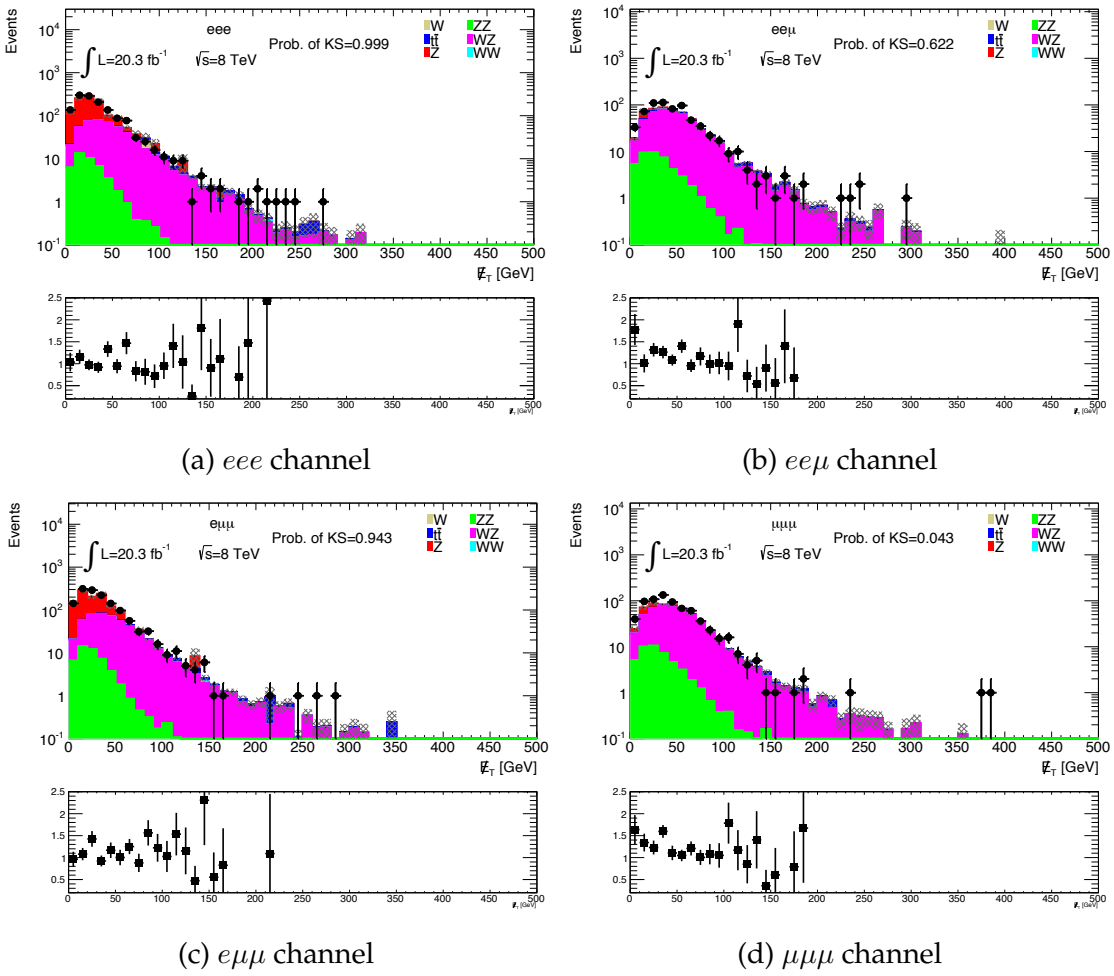

(a) eee channel

(b) $ee\mu$ channel

(c) $e\mu\mu$ channel

(d) $\mu\mu\mu$ channel

Figure 6.12: Comparison of data and MC in the $E_{\mathrm{T}}^{\mathrm{miss}}$ distribution of the 3-lepton CRs, used for validating the WZ MC background estimation. Only the Z mass window selection has been applied. Taken from ref. [2].

ties is found in the following section.

6.5 Systematic uncertainties

The mono-Z analysis is subject to systematic biases, both from experimental and theoretical sources. These are addressed through the inclusion of systematic uncertainties, some of which have already been described in the previous section. Additional sources of systematic uncertainty, both experimental and theoretical, are described in detail below.

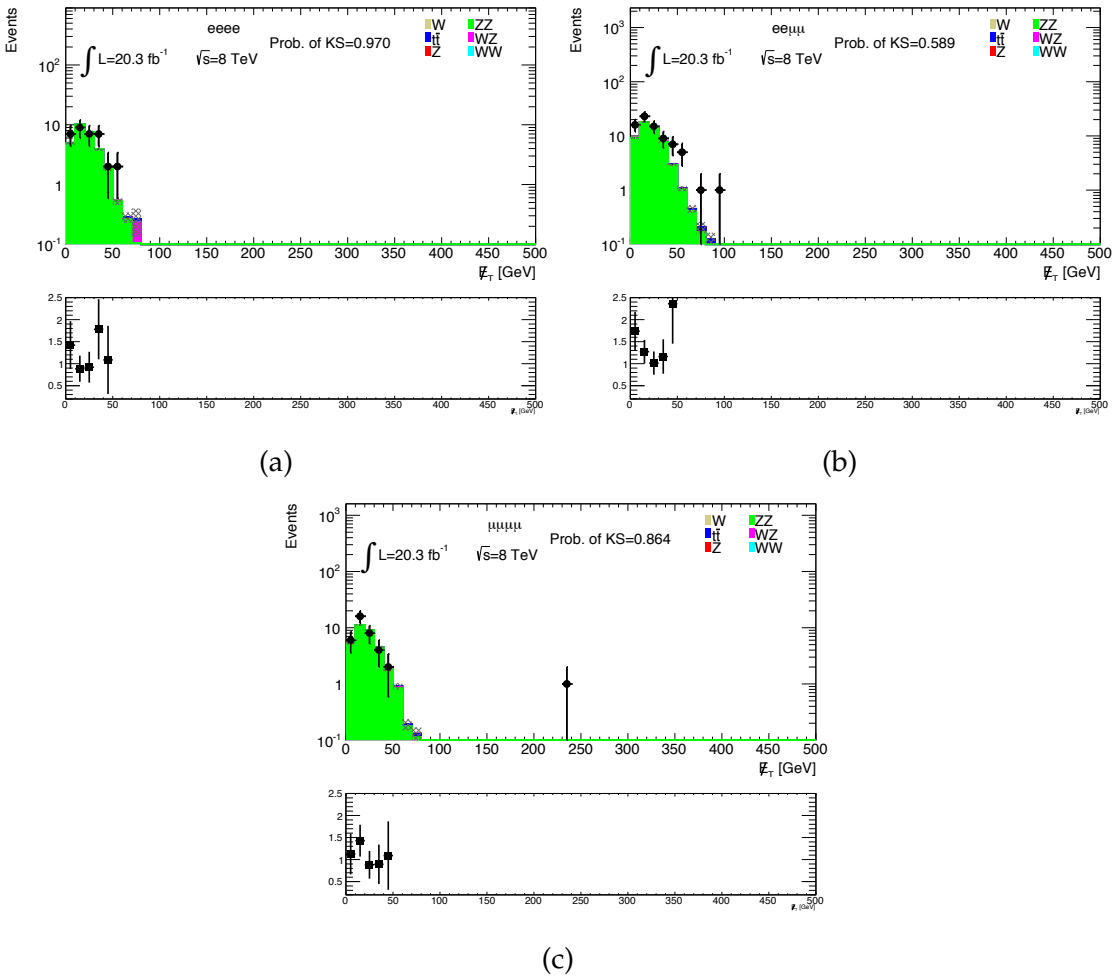

(a) (b)

(c)

Figure 6.13: Comparison of data and MC in the $E_{\mathrm{T}}^{\mathrm{miss}}$ distribution of the 4-lepton CRs, used for validating the ZZ MC background estimation. Only the Z mass window selection has been applied. Taken from ref. [2].

6.5.1 Experimental systematic uncertainties

Electrons

Systematic uncertainties from electrons arise from four sources, the reconstruction and identification efficiencies, and the energy scale and resolution. Leptons are used explicitly in the SRs to reconstruct the Z boson, as well as a veto object, and to define some of the CRs used in the data-driven background estimations; they are also used in calculating the $E_{\mathrm{T}}^{\mathrm{miss}}$. Variations in their identification and energy can cause events to migrate in and out of the signal and control regions. There are therefore many points where these uncertainties enter the analysis, and in fact they are one of the dominant experimental sources of uncertainty on the SM background estimations.

Scale factors, with associated systematic uncertainties, are derived by the ATLAS performance group, to account for differences in the reconstruction and

identification efficiencies between simulation and data, see ref. [170]. The uncertainty for each electron from either source is calculated following ATLAS recommendations and using centrally-provided software tools [4]. The efficiency scale factor is varied up or down by 1σ, and the event yield is recalculated. The symmetrised difference in the event yields about the nominal yield is taken as the systematic uncertainty in the efficiency.

The uncertainties on the energy scale and resolution result from a few different sources, see ref. [173] for details. Similar to the efficiency uncertainties, software tools[5] are utilised, which vary each source up or down within its uncertainty and propagate the effect through the analysis.

The resulting systematic uncertainties on the two largest backgrounds, ZZ and WZ are shown in table 6.8, and are dominated by the electron energy scale (up to 3%) and reconstruction efficiency ($\sim$2%).

Muons

The systematic uncertainties from muons are similar to those from electrons, arising from the reconstruction efficiency, and the p_{T} scale and resolution. See ref. [176] for details of the uncertainty sources. These are implemented with the use of software tools[6], which again vary each source up or down within its uncertainty.

The p_{T} resolution uncertainty is estimated separately for the ID and muon spectrometer (MS) track variations, and the maximum of the two is taken as the systematic uncertainty.

The muon uncertainties listed in table 6.8 are dominated by the p_{T} scale and resolution.

Jets

While jets are used as a veto object in this analysis, they are important for calculation of the $E_{\mathrm{T}}^{\mathrm{miss}}$ in each event, and so contribute a significant uncertainty to the analysis. Three main sources of systematic uncertainty apply to jets, originating from the uncertainties on the JES, the JER, and the JVF (see secs. 4.3.3 and 6.2.4).

The systematic uncertainty from the JES is complex as it arises from over 50 sources, most of which are related to the *in situ* calibration of jets in data [116]. The

[4] https://twiki.cern.ch/twiki/bin/viewauth/AtlasProtected/EfficiencyMeasurements2012

[5] https://twiki.cern.ch/twiki/bin/viewauth/AtlasProtected/EnergyScaleResolutionRecommendations

[6] https://twiki.cern.ch/twiki/bin/viewauth/AtlasProtected/MCPAnalysisGuidelinesData2012

total JES uncertainty for each jet is calculated following ATLAS recommendations and using centrally-provided software tools[7], and is also propagated to the $E_{\mathrm{T}}^{\mathrm{miss}}$ calculation. The uncertainty on the background estimates is calculated by varying the JES up or down within its uncertainty, and re-calculating the background estimate in the SR.

The uncertainties from the JER and JVF are also calculated with software tools[8][9]. The jet energy resolution is varied up by 1σ, implemented as a smearing of the jet energy, and the resulting uncertainty is symmetrized to represent a $\pm 1\sigma$ uncertainty. The jet vertex fraction, which has a nominal value of 0.5, is varied up or down around this value (see ref. [232]). In both cases, the effect is propagated to the $E_{\mathrm{T}}^{\mathrm{miss}}$ calculation and then through the analysis.

The resulting uncertainties from the JES, JER and JVF are listed in table 6.8, note that these also include the impact on the $E_{\mathrm{T}}^{\mathrm{miss}}$ calculation. The uncertainties are larger for the WZ background, because this background enters the SR when one of the leptons is not identified, often when it has been misreconstructed as a jet. The JES contributes the largest systematic uncertainty, up to 2.4% in the ZZ background and up to 4.1% in the WZ background. However, the jet-related uncertainties on the other backgrounds are reduced, as they are estimated using data-driven methods where the uncertainties are mostly cancelled out.

Missing transverse momentum

As the $E_{\mathrm{T}}^{\mathrm{miss}}$ is a composite object, the $E_{\mathrm{T}}^{\mathrm{miss}}$ uncertainty arises from multiple sources such as the leptons and jets, discussed above, that contribute to its calculation. The systematic uncertainties from variations in those object measurements have been discussed (see above), and are included in the uncertainties attributed to those sources. Only the SoftTerm component on the $E_{\mathrm{T}}^{\mathrm{miss}}$, introduced in sec. 4.3.5, is treated independently and discussed here.

The SoftTerm is the contribution from soft jets and other topoclusters not associated to any reconstructed object, and calibrated to the LC scale. Uncertainties arise from the MC modeling and pileup effects, see ref. [197] for details. The recommended scale and resolution uncertainties are applied with the appropriate tool[10], varying the source up or down within its uncertainty and propagating the result through the analysis chain.

[7] https://twiki.cern.ch/twiki/bin/viewauth/AtlasProtected/JetUncertainties

[8] https://twiki.cern.ch/twiki/bin/viewauth/AtlasProtected/JetEnergyResolutionProvider2012

[9] https://twiki.cern.ch/twiki/bin/view/AtlasProtected/JVFUncertaintyTool

[10] https://twiki.cern.ch/twiki/bin/viewauth/AtlasProtected/MissingETUtility

Syst. source	ZZ			WZ		
	ee	$\mu\mu$	combined	ee	$\mu\mu$	combined
e energy smearing	0.34	0.05	0.19	1.47	0.37	0.68
e energy scale	2.33	0.05	1.16	2.95	0.34	1.13
e identification efficiency	1.77	0.00	0.88	1.82	0.00	0.81
e reconstruction efficiency	2.01	0.00	1.00	2.08	0.00	0.93
μ momentum smearing (ID)	0.14	0.13	0.06	1.53	0.01	0.69
μ momentum smearing (MS)	0.00	0.33	0.16	0.00	1.00	0.55
μ momentum scale	0.00	0.77	0.38	0.61	1.35	1.02
μ reconstruction efficiency	0.00	0.64	0.32	0.00	0.64	0.35
JER	0.17	0.66	0.42	2.89	2.18	2.49
JES	1.68	2.32	1.85	1.78	4.09	2.60
JVF	0.26	0.26	0.24	1.47	0.77	0.66
$E_{\mathrm{T}}^{\mathrm{miss}}$ SoftTerm resolution	0.45	0.31	0.38	0.92	1.35	1.07
$E_{\mathrm{T}}^{\mathrm{miss}}$ SoftTerm scale	0.31	1.05	0.68	4.02	1.02	2.36
total	3.99	2.87	2.77	7.20	5.33	5.03

Table 6.8: The sources of systematic uncertainty for the ZZ and WZ simulated background estimates, with a $E_{\mathrm{T}}^{\mathrm{miss}}$ cut at 120 GeV.

The total experimental uncertainties for the ZZ and WZ backgrounds, in the four SRs, are summarised in table 6.9.

The combined experimental sources of systematic uncertainty on the D5 EFT model signal in the four SRs are listed in table 6.10. Explicit uncertainties for the tS simplified model were not estimated, due to its late inclusion in the analysis, but instead the D5 uncertainties were used, due to the similarities in behaviour of the two models, particularly in the heavy-mediator limit.

Luminosity

The uncertainty on the luminosity is 2.8%, measured with the method detailed in ref. [233]. This affects the normalisation of simulated sources, and is small compared to the other systematic sources of uncertainty.

m_χ	$E_{\mathrm{T}}^{\mathrm{miss}} > 150$ GeV			$E_{\mathrm{T}}^{\mathrm{miss}} > 250$ GeV		
	ee	$\mu\mu$	combined	ee	$\mu\mu$	combined
ZZ	4.7	3.6	3.3	9.2	6.4	5.8
WZ	20.1	7.5	10.3	34.3	16.3	10.3
m_χ	$E_{\mathrm{T}}^{\mathrm{miss}} > 350$ GeV			$E_{\mathrm{T}}^{\mathrm{miss}} > 450$ GeV		
	ee	$\mu\mu$	combined	ee	$\mu\mu$	combined
ZZ	11.7	11.9	8.6	13.8	5.0	8.0
WZ	2.3	0.7	0.9	2.3	0.0	2.3

Table 6.9: The experimental systematic uncertainties on the ZZ and WZ background estimates in the signal regions.

m_χ	$E_{\mathrm{T}}^{\mathrm{miss}} > 150$ GeV			$E_{\mathrm{T}}^{\mathrm{miss}} > 250$ GeV		
	ee	$\mu\mu$	combined	ee	$\mu\mu$	combined
10 GeV	8.8	7.4	5.7	10.1	13.8	8.1
200 GeV	4.6	5.8	4.3	6.0	8.3	5.5
400 GeV	3.0	2.9	2.3	4.9	5.5	4.0
1000 GeV	5.9	5.4	4.6	5.7	10.6	6.1
m_χ	$E_{\mathrm{T}}^{\mathrm{miss}} > 350$ GeV			$E_{\mathrm{T}}^{\mathrm{miss}} > 450$ GeV		
	ee	$\mu\mu$	combined	ee	$\mu\mu$	combined
10 GeV	21.5	44.9	17.8	23.7	2.3	19.2
200 GeV	10.6	6.0	6.6	24.2	9.8	17.0
400 GeV	10.6	8.0	7.9	20.7	8.0	12.8
1000 GeV	7.4	17.2	8.8	8.3	18.2	8.1

Table 6.10: The experimental systematic uncertainty estimates derived for the D5 signal MC sample. Note that these uncertainties are also used for the tS simplified model.

Source	$E_{\mathrm{T}}^{\mathrm{miss}} > 150$ GeV			$E_{\mathrm{T}}^{\mathrm{miss}} > 250$ GeV		
	$qq \to ZZ$	$gg \to ZZ$	combined	$qq \to ZZ$	$gg \to ZZ$	combined
PDF	7.55	14.6	7.97	9.13	17.5	9.63
QCD	1.39	40.6	3.74	1.67	47.3	4.41
Source	$E_{\mathrm{T}}^{\mathrm{miss}} > 350$ GeV			$E_{\mathrm{T}}^{\mathrm{miss}} > 450$ GeV		
	$qq \to ZZ$	$gg \to ZZ$	combined	$qq \to ZZ$	$gg \to ZZ$	combined
PDF	10.6	20.3	11.2	11.7	22.2	12.3
QCD	1.94	53.7	5.05	2.13	58.3	5.50

Table 6.11: The theory systematic uncertainties (from PDF and QCD scale choices) as percentages for the ZZ MC background estimation.

Pileup

Pileup reweighting was applied to MC samples to better match the pileup conditions observed in data, and included a systematic uncertainty. However, the resulting systematic is negligible compared to other systematic sources, and so is ignored.

6.5.2 Theoretical systematic uncertainties

Theoretical uncertainties for the dominant ZZ background are also included, and are listed in table 6.11. These arise from choices of the PDF and factorisation and renormalisation scales. The uncertainties are taken from section 11.3.4 of ref. [234] (which studies the $H \to ZZ$ process), and propagated to the background estimate in each signal region.

The only exception is for the $qq \to ZZ$ scale uncertainty, which is estimated with samples generated in POWHEGBOX and PYTHIA8, with *dynamic*[11] QCD factorisation and normalisation scales varied up and down by a factor of 2. This leads to uncertainties smaller by factor of $\sim$3 than those predicted by ref. [234], a result of both the dynamic scale and study of the process $ZZ \to \ell^+\ell^-\nu\bar{\nu}$ rather than $ZZ \to e^+e^-\mu^+\mu^-$.

[11]The dynamic scales μ_{F} and μ_{R} are set to the mass m_{ZZ}, while the *fixed* scales used in ref. [234] are set to the Z mass.

6.6 Limits on new physics

The finalised SM background estimations in the four signal regions, along with their associated uncertainties, are listed in tables 6.12 and 6.13. Distributions of the dilepton invariant mass, the $E_{\mathrm{T}}^{\mathrm{miss}}$ and the jet multiplicity, comparing the SM background estimate against the observed data, are shown in fig. 6.14. No significant deviation from the expected background is observed.

Also included in tables 6.12 and 6.13 are the expected and observed upper limits on the number of signal events, N_{sig}. These are calculated at 95% confidence level with the CL_{S} method [235] with the use of the HistFitter package [236], using events observed in data to calculate the observed limit, and assuming only the SM background is observed to calculate the expected limit. When the yield from simulation is zero, the Feldman-Cousins confidence interval [237] is used to evaluate the uncertainty. Note that these limits on N_{sig} do not take into account uncertainties on the signal modeling.

6.7 Limits on contact operator models

6.7.1 Limit calculation

Converting the model-independent limits on the number of new physics events, N_{sig}, to a model-dependent limit on the cross section for a given process, depends on knowledge of the acceptance and efficiency of that model within the analysis. The acceptance, $\mathcal{A}$, is the fraction of events *at truth level* that pass the analysis selection, while the efficiency, ϵ, is a measure of how well the reconstructed events match those at truth level:

$$\begin{aligned} \mathcal{A} &= \frac{N(\text{truth-level analysis selection})}{N(\text{all generated events})} \\ \epsilon &= \frac{N(\text{reco.-level analysis selection})}{N(\text{truth-level analysis selection})} \end{aligned} \tag{6.14}$$

Note that ϵ is not a true efficiency, as the events in the numerator are not necessarily completely a subset of events in the denominator.

In practice, $\mathcal{A}$ and ϵ are treated together as a single variable $\epsilon \times \mathcal{A}$, calculated as the number of signal events at reconstruction level that pass the analysis selection divided by the total number generated, with uncertainties included.

The limit on the cross section for a model with a given $\epsilon \times \mathcal{A}$ is calculated according to

	Background sources						
	ZZ	WZ	WW	top	$Z \to \tau\tau$ + jets	Z + jets	W + jets
				$E_{\mathrm{T}}^{\mathrm{miss}} > 150$ GeV			
MC estimate	41.4±0.9±15.0	8.0±0.7±3.0	0.4±0.2	1.0±0.5	$0^{+3.6}_{-0.0}$	$0^{+3.6}_{-0.0}$	0
DD estimate	-	-		1.9±1.4±0.1		0.1±0.01±0.10	0.52±0.02±0.31
Total estimate				51.9±1.8±18.0			
Observed				45			
Limit on $N_{\mathrm{sig}}^{\mathrm{exp}}$				34.4			
Limit on $N_{\mathrm{sig}}^{\mathrm{exp}}$				31.3			
				$E_{\mathrm{T}}^{\mathrm{miss}} > 250$ GeV			
MC estimate	6.4±0.4±2.4	0.8±0.2±0.3	$0.0^{+0.1}_{-0.0}$	$0.0^{+1.0}_{-0.0}$	$0^{+3.6}_{-0.0}$	$0^{+3.6}_{-0.0}$	0
DD estimate	-	-		$0.0^{+0.65}_{-0.65}$		negligible	negligible
Total estimate				7.2±0.8±2.7			
Observed				3			
Limit on $N_{\mathrm{sig}}^{\mathrm{exp}}$				8.4			
Limit on $N_{\mathrm{sig}}^{\mathrm{exp}}$				6.4			

Table 6.12: Total estimated backgrounds from both MC and data-driven methods, along with associated statistical and systematic uncertainties, for the first two signal regions. Also shown are the recorded events in data, along with the expected and observed upper limits on the number of signal events. Adapted from ref. [2].

	Background sources						
	ZZ	WZ	WW	top	$Z \to \tau\tau$ + jets	Z + jets	W + jets
				$E_{\mathrm{T}}^{\mathrm{miss}} > 350$ GeV			
MC estimate	$1.3 \pm 0.2 \pm 0.5$	$0.2 \pm 0.1 \pm 0.1$	$0.0^{+0.1}_{-0.0}$	$0.0^{+1.0}_{-0.0}$	$0^{+3.6}_{-0.0}$	$0^{+3.6}_{-0.0}$	0
DD estimate	-	-		$0.0^{+0.65}_{-0.65}$		negligible	negligible
Total estimate				$1.4 \pm 0.7 \pm 0.5$			
Observed				0			
Limit on $N_{\mathrm{sig}}^{\mathrm{exp}}$				4.2			
Limit on $N_{\mathrm{sig}}^{\mathrm{exp}}$				3.1			
				$E_{\mathrm{T}}^{\mathrm{miss}} > 450$ GeV			
MC estimate	$0.32 \pm 0.08 \pm 0.12$	$0.06 \pm 0.06 \pm 0.02$	$0.0^{+0.1}_{-0.0}$	$0.0^{+1.0}_{-0.0}$	$0^{+3.6}_{-0.0}$	$0^{+3.6}_{-0.0}$	0
DD estimate	-	-		$0.0^{+0.65}_{-0.65}$		negligible	negligible
Total estimate				$0.38 \pm 0.66 \pm 0.14$			
Observed				0			
Limit on $N_{\mathrm{sig}}^{\mathrm{exp}}$				3.2			
Limit on $N_{\mathrm{sig}}^{\mathrm{exp}}$				3.0			

Table 6.13: Same as table 6.12, but for the two higher-$E_{\mathrm{T}}^{\mathrm{miss}}$ signal regions. Adapted from ref. [2].

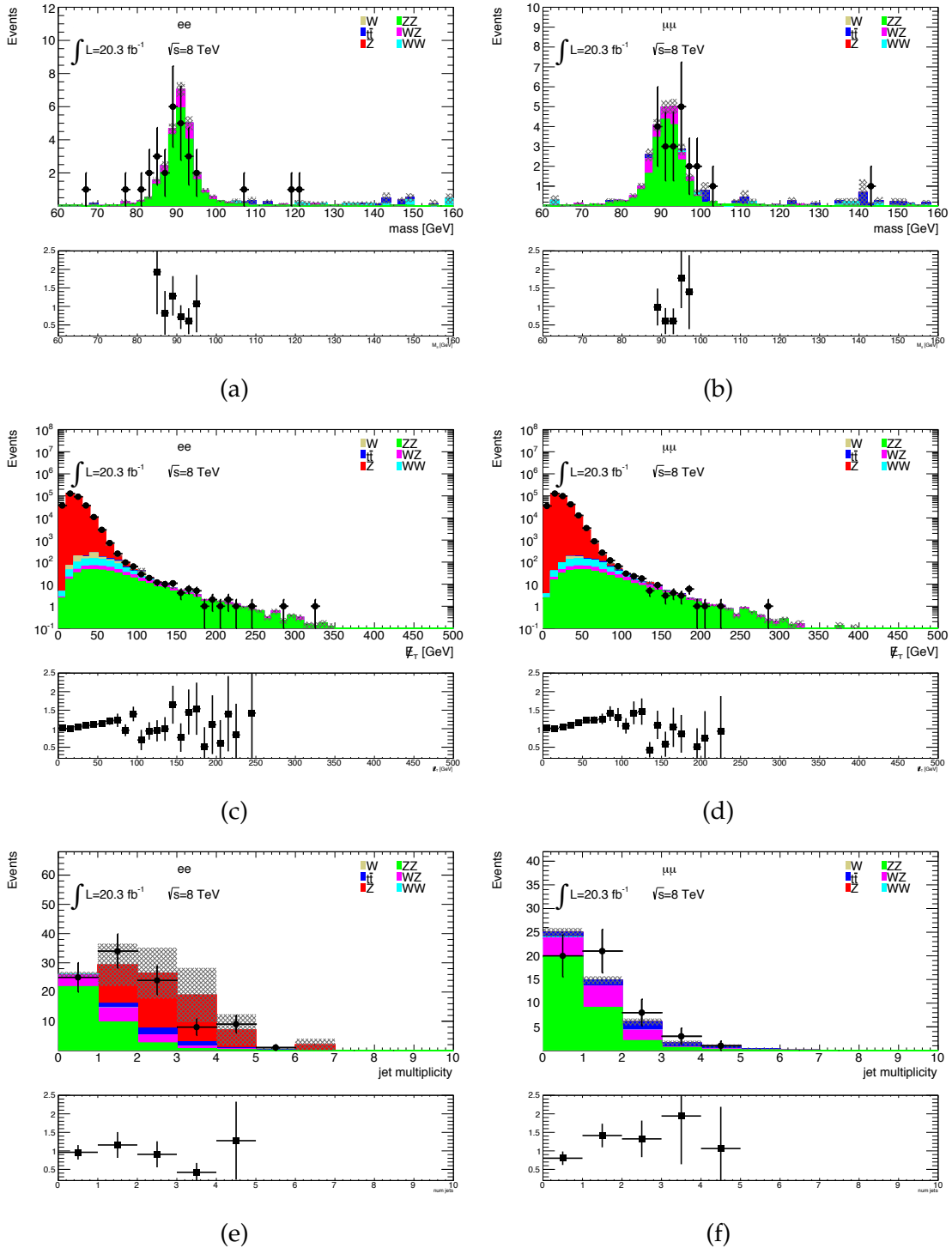

Figure 6.14: The distributions of dilepton invariant mass (top), $E_{\mathrm{T}}^{\mathrm{miss}}$ (middle) and veto jet multiplicity (bottom) showing the expected backgrounds (coloured) and observed data (black circles) for the ee channel (left) and the $\mu\mu$ channel (right). All selections except the cut on the variable plotted are applied. Taken from ref. [2].

Model	m_χ [GeV]	Best SR	$\sigma_{\text{lim}}^{\text{exp}}$ [fb]	$\sigma_{\text{lim}}^{\text{obs}}$ [fb]
D1	10	$E_{\text{T}}^{\text{miss}} > 250$ GeV	4.8	3.8
D1	200	$E_{\text{T}}^{\text{miss}} > 250$ GeV	3.3	2.6
D1	400	$E_{\text{T}}^{\text{miss}} > 350$ GeV	2.5	1.9
D1	1000	$E_{\text{T}}^{\text{miss}} > 350$ GeV	1.9	1.4
D5	10	$E_{\text{T}}^{\text{miss}} > 250$ GeV	15.2	11.9
D5	200	$E_{\text{T}}^{\text{miss}} > 250$ GeV	11.6	9.2
D5	400	$E_{\text{T}}^{\text{miss}} > 250$ GeV	9.6	7.5
D5	1000	$E_{\text{T}}^{\text{miss}} > 250$ GeV	8.8	6.9
D9	10	$E_{\text{T}}^{\text{miss}} > 350$ GeV	1.5	1.1
D9	200	$E_{\text{T}}^{\text{miss}} > 350$ GeV	1.4	1.0
D9	400	$E_{\text{T}}^{\text{miss}} > 350$ GeV	1.4	1.0
D9	1000	$E_{\text{T}}^{\text{miss}} > 350$ GeV	1.4	1.0

Table 6.14: Expected and observed upper limits on the cross section for each EFT sample, and the SR in which the best expected limit was obtained.

$$\sigma_{\text{lim}}^{\text{exp,obs}} = \frac{N_{\text{sig}}^{\text{exp,obs}}}{\mathcal{L} \times \epsilon \times \mathcal{A}} \ , \tag{6.15}$$

where $\mathcal{L}$ is the total integrated luminosity. These limits are shown for the D1, D5 and D9 operators, as well as the three $ZZ\chi\chi$ operators, in tables. 6.14 and 6.15 and fig. 6.15.

Since the cross section for the D1, D5 and D9 EFT operators is proportional to Λ^{-2p}, and the kinematic behaviour (and therefore $\epsilon \times \mathcal{A}$) is independent of Λ, we can convert the limit on the cross section to a limit on the suppression scale Λ, using

$$\Lambda_{\text{lim}} = \Lambda_{\text{gen}} \times \left(\frac{\sigma_{\text{gen}}}{\sigma_{\text{lim}}} \right)^{\frac{1}{2p}} \ , \tag{6.16}$$

where σ_{gen} and σ_{lim} are the generated and limiting cross sections respectively, Λ_{gen} is the suppression scale of the generated samples (in this case, 1 TeV), and p is 3 for the D1 operator and 2 for the D5 and D9 operators (see table 3.1 in sec. 3.1.1). The resulting lower limits on Λ are shown in fig. 6.16. Note that there is no check on the validity of these limits as described in sec. 3.1.2, since unfortunately this work was published before such concerns were raised.

Model	m_χ [GeV]	Best SR	$\sigma_{\text{lim}}^{\text{exp}}$ [fb]	$\sigma_{\text{lim}}^{\text{obs}}$ [fb]
$ZZ\chi\chi$ dim-5	10	$E_{\text{T}}^{\text{miss}} > 350$ GeV	6.1	4.5
$ZZ\chi\chi$ dim-5	50	$E_{\text{T}}^{\text{miss}} > 350$ GeV	4.5	3.3
$ZZ\chi\chi$ dim-5	200	$E_{\text{T}}^{\text{miss}} > 350$ GeV	1.8	1.3
$ZZ\chi\chi$ dim-5	400	$E_{\text{T}}^{\text{miss}} > 350$ GeV	1.3	1.0
$ZZ\chi\chi$ dim-5	1000	$E_{\text{T}}^{\text{miss}} > 450$ GeV	1.1	1.0
$ZZ\chi\chi$ dim-7 (max γ)	10	$E_{\text{T}}^{\text{miss}} > 450$ GeV	1.00	0.91
$ZZ\chi\chi$ dim-7 (max γ)	200	$E_{\text{T}}^{\text{miss}} > 450$ GeV	0.95	0.86
$ZZ\chi\chi$ dim-7 (max γ)	400	$E_{\text{T}}^{\text{miss}} > 450$ GeV	0.93	0.85
$ZZ\chi\chi$ dim-7 (max γ)	1000	$E_{\text{T}}^{\text{miss}} > 450$ GeV	0.92	0.83
$ZZ\chi\chi$ dim-7 (min γ)	10	$E_{\text{T}}^{\text{miss}} > 450$ GeV	1.00	0.91
$ZZ\chi\chi$ dim-7 (min γ)	200	$E_{\text{T}}^{\text{miss}} > 450$ GeV	0.96	0.87
$ZZ\chi\chi$ dim-7 (min γ)	400	$E_{\text{T}}^{\text{miss}} > 450$ GeV	0.93	0.85
$ZZ\chi\chi$ dim-7 (min γ)	1000	$E_{\text{T}}^{\text{miss}} > 450$ GeV	0.94	0.85

Table 6.15: Expected and observed upper limits on the cross section for each $ZZ\chi\bar{\chi}$ operator sample, and the SR in which the best expected limit was obtained.

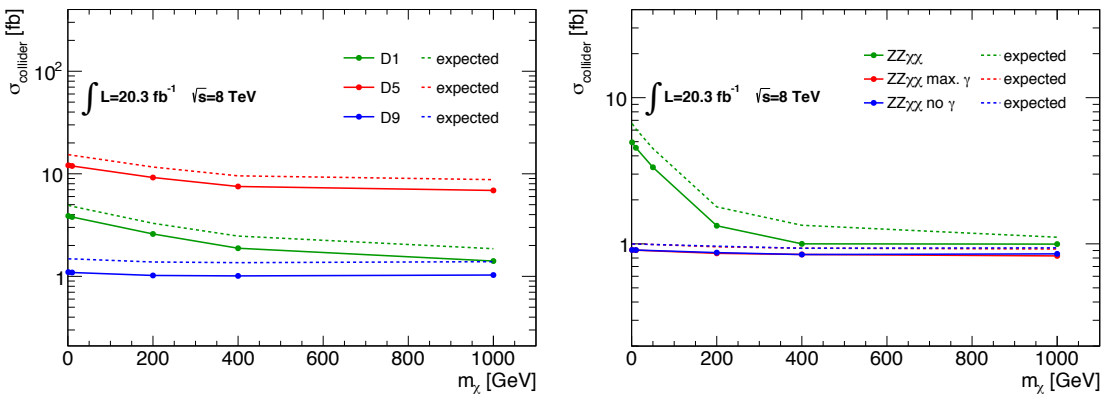

(a) (b)

Figure 6.15: The upper limits on the cross section for the EFT models of DM, as a function of DM mass. Taken from ref. [2].

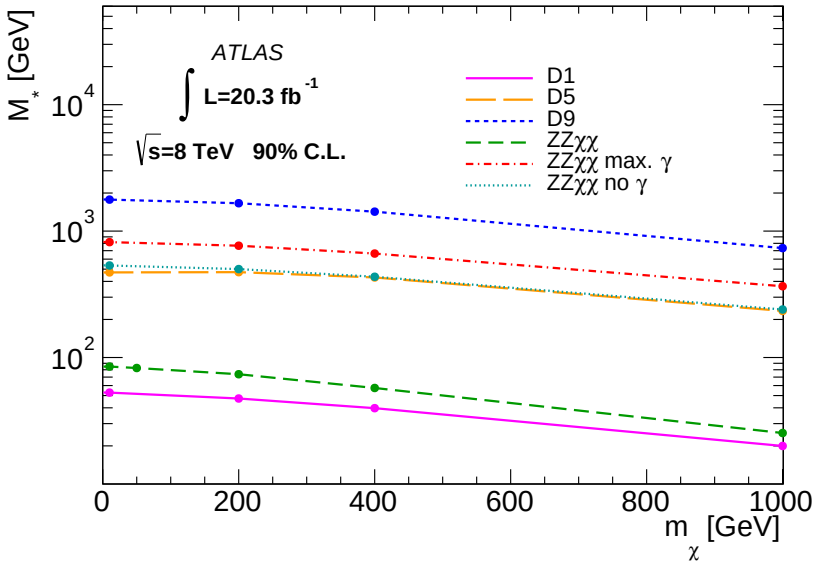

Figure 6.16: Observed 90%C.L. lower limits on the suppression scale Λ (labeled as $M_\star$ in the figure) for the EFT models considered in this analysis. Taken from ref. [3].

Finally, as has been noted previously, the advantage of an EFT is that simple comparison across different experimental types is possible. The limits from the production process in a collider, as has been described here, can be converted to limits on the χ-nucleon scattering cross section which is the signal in direct detection experiments, via eqs. 3.1 and 3.2 in sec. 3.1.1. The resulting limits on the scattering cross section are shown in figs. 6.17(a) and (b) (for spin-independent and spin-dependent scattering respectively), and compared against the limits from ATLAS mono-jet [109] and mono-$W/Z(\rightarrow jj)$ [238] analyses, and the CoGENT [239], XENON100 [85], CDMS [87, 240] LUX [86], COUPP [241], SIMPLE [242], PICASSO [243], and IceCube [88] experiments, as they were at the time this work was finalised in 2013.

6.8 Limits on the tS simplified model

The work of the author within this analysis effort was to include a study of a simplified model, which was one of the first cases of such a model within an ATLAS mono-X analysis. The model included is the t-channel model discussed in sec. 3.3, included following the work of ref. [127], with a Majorana fermion[12]

[12] As discussed in sec. 3.3, this decision is motivated by the parallel simplified model in the Minimal Supersymmetric Simplified Model (MSSM), where the neutralino and squark doublet play the roles of the DM and mediator respectively. However, it affects only the cross section and not the kinematic behaviour of the model.

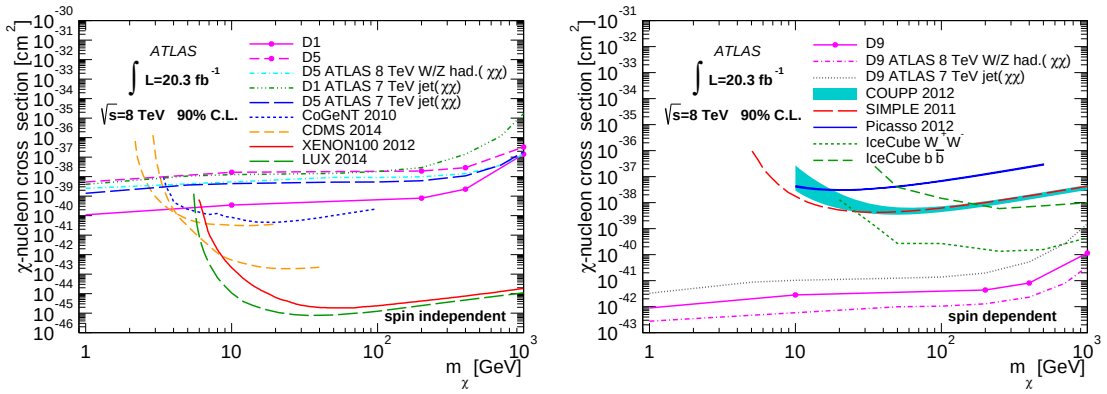

(a) (b)

Figure 6.17: Observed 90%C.L. upper limits on the χ-nucleon scattering cross section as a function of m_χ for the spin-independent (left) and spin-dependent (right) EFT operators. The limits are compared with results from the ATLAS hadronically-decaying mono-W/Z analysis [238], and mono-jet [109] analyses, CoGeNT [239], XENON100 [85], CDMS [87, 240], LUX [86], COUPP [241], SIMPLE [242], PICASSO [243], and IceCube [88]. These limits are shown as they are given in the corresponding publications and are only shown for comparison with the results from this analysis, since they are obtained assuming the interactions are mediated by operators different from those used for the ATLAS limits. Taken from ref. [3].

DM particle χ, coupled to the first two[13] generations of left-handed quarks via a single scalar mediator doublet ϕ:

$$\mathcal{L}_{tS} = g_{q\chi} \sum_{i=1,2} \phi \bar{Q}^i_L \chi + \text{h.c.} \, . \tag{6.17}$$

As well as emission of a Z boson from one of the incoming quarks, the weak isospin charge of the SU(2) doublet mediator also allows it to radiate a Z, providing an additional diagram for the mono-Z signal; both diagrams are shown in fig. 6.18. Note that the anti-quark can also (of course) radiate the Z, and so corresponding u-channel diagrams, where the incoming quarks are swapped, also contribute.

Kinematic distributions of leading lepton p_{T}, η, ϕ, Z invariant mass and $E_{\mathrm{T}}^{\mathrm{miss}}$ are shown in fig. 6.19 (created at truth-level) for m_χ = 200 GeV and M_{med} = 700 GeV, and compared with the D1, D5 and D9 operators with the same DM mass. Here, the correspondance between the tS simplified model and the D5 effective operator is clearly evident, particularly in the lepton p_{T} and η distributions, where the EFT operators are distinguishable. The $E_{\mathrm{T}}^{\mathrm{miss}}$ plot demonstrates that the simplified model does still vary from the D5 model, due to the fact that this point

[13] While the number of generations to which the DM couples has minimal impact on the collider phenomenology, it is significant for the relic density calculation; see sec. 6.8.1.

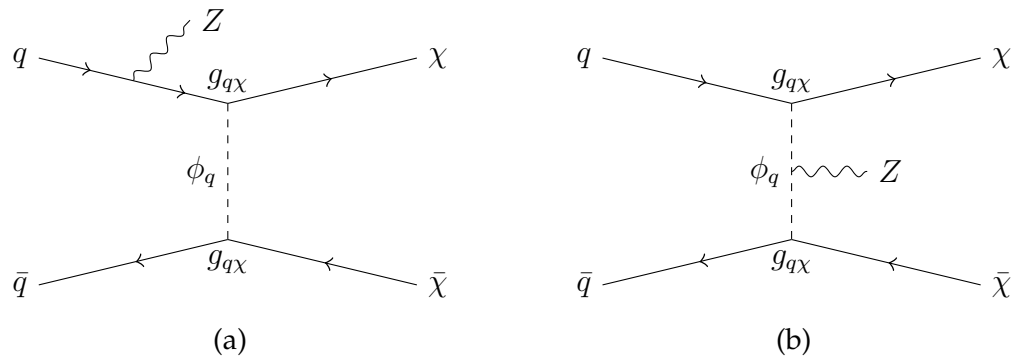

Figure 6.18: Emission of Z boson, leading to the mono-Z + $E_{\mathrm{T}}^{\mathrm{miss}}$ signal, can be from either an incoming quark (left) *or* from the scalar mediator SU(2) doublet (right) in the tS simplified model.

in parameter space is *not* in the heavy-mediator limit, that is, M_{med} is not much larger than m_χ.

The set of DM masses included in this analysis were chosen to match those studied in the EFT models, $m_\chi \in$ [10, 200, 400, 1000] GeV. Where the EFTs used Λ = 1 TeV, here we have two degrees of freedom: M_{med} and $g_{q\chi}$. We choose to fix a single coupling for each DM mass and include a range of mediator masses, because while the mediator will affect the kinematic behaviour, the couplings are only expected to scale the cross section (further details on this topic are provided in the next chapter). The masses chosen are listed in table 6.16, along with the value of $\mathcal{A} \times \epsilon$ for each sample in the four SRs. Note the very low acceptances in the two hardest-$E_{\mathrm{T}}^{\mathrm{miss}}$ SRs (SR3 and SR4).

The limits on the cross section for the tS model are calculated using the method described in sec. 6.7.1 and using eq. 6.15. The upper limits in tables 6.12 and 6.13 are not quite the values that are used, as these don't include the signal uncertainties which are dependent on the model. Instead, the values listed in table 6.17 are used, which are calculated using the signal systematic uncertainties that had already been obtained from the D5 model, used due to its similarity to the tS simplified model. Only the first two signal regions are listed, as the latter signal regions had $E_{\mathrm{T}}^{\mathrm{miss}}$ cuts that were quite hard compared to the model $E_{\mathrm{T}}^{\mathrm{miss}}$ distributions, and so in these SRs the model had very low acceptance.

The limits on the cross section are shown in table 6.18. Note the 'best' signal region is chosen as that which gives the strongest expected limit. The limits are plotted in figs. 6.20 and 6.21. In these plots, the cross section is scaleable by varying the coupling $g_{q\chi}$ (as $\sigma \sim g_{q\chi}^4$), and the point where the theoretical cross section intersects the observed limit indicates the limiting value of, say, M_{med} (labeled m_η in the figures).

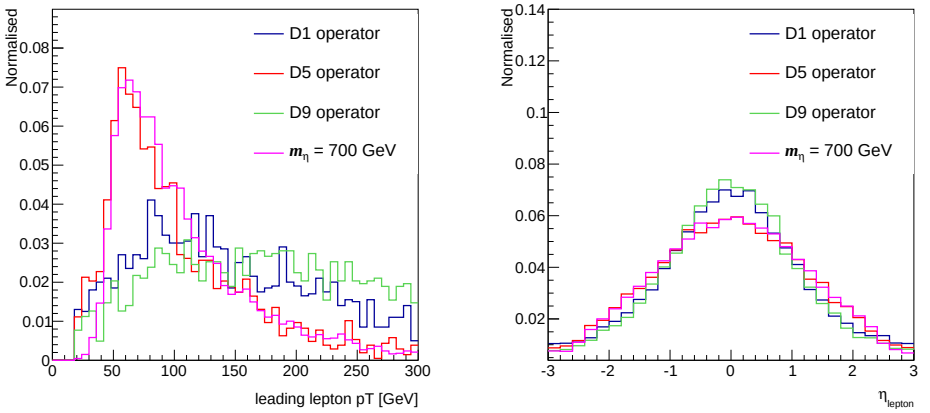

(a)

(b)

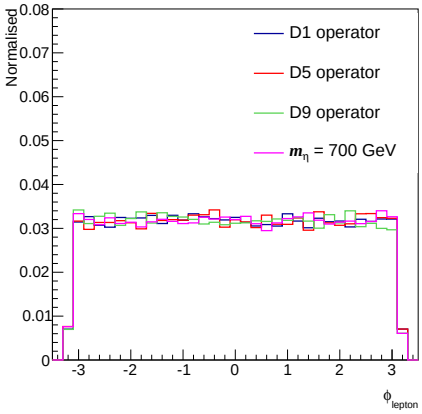

(c)

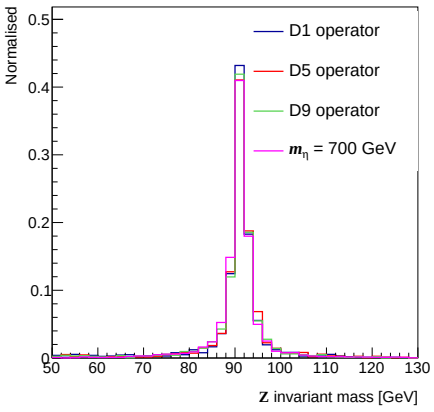

(d)

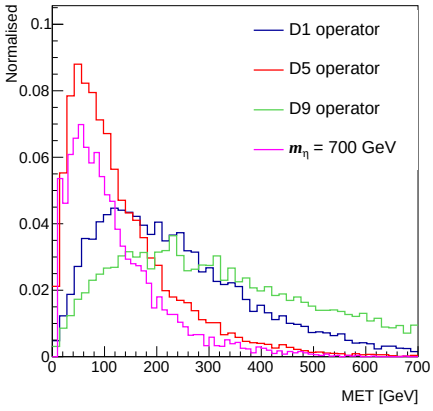

(e)

Figure 6.19: Distributions of the leading lepton p_{T} (a), η (b), ϕ (c), the two-lepton invariant mass (d), and $E_{\mathrm{T}}^{\mathrm{miss}}$ (e), comparing the D1, D5 and D9 EFT operators against the tS simplified model, with a mediator mass (labeled m_η) of 700 GeV. All models use m_χ = 200 GeV.

m_χ [GeV]	M_{med} [GeV]	$\epsilon \times \mathcal{A}$			
		SR1	SR2	SR3	SR4
10	200	4.4±0.2	1.1±0.1	0.4±0.1	0.0±0.0
10	500	5.7±0.2	1.8±0.1	0.6±0.1	0.2±0.0
10	700	5.5±0.2	1.8±0.1	0.5±0.1	0.1±0.0
10	1000	6.9±0.3	1.9±0.1	0.5±0.1	0.1±0.0
200	500	8.4±0.3	3.3±0.2	1.1±0.1	0.3±0.1
200	700	8.3±0.3	2.8±0.2	0.9±0.1	0.3±0.1
200	1000	8.5±0.3	3.0±0.2	0.9±0.1	0.3±0.1
400	500	9.7±0.3	3.4±0.2	1.4±0.1	0.5±0.1
400	700	8.7±0.3	3.5±0.2	1.3±0.1	0.3±0.1
400	1000	8.8±0.3	3.2±0.2	1.2±0.1	0.4±0.1
1000	1200	10.4±0.3	4.4±0.2	1.2±0.1	0.4±0.1

Table 6.16: The DM and mediator masses of the tS model included in this analysis, and their corresponding acceptances in each of the four SRs. The uncertainties are statistical.

	$E_{\text{T}}^{\text{miss}} > 150$ GeV	$E_{\text{T}}^{\text{miss}} > 250$ GeV
Limit on $N_{\text{sig}}^{\text{exp}}$	35.2	8.6
Limit on $N_{\text{sig}}^{\text{obs}}$	31.8	6.7

Table 6.17: Expected and observed limits on number of signal events for the relevant signal regions, calculated using the systematic uncertainty from the D5 signal sample.

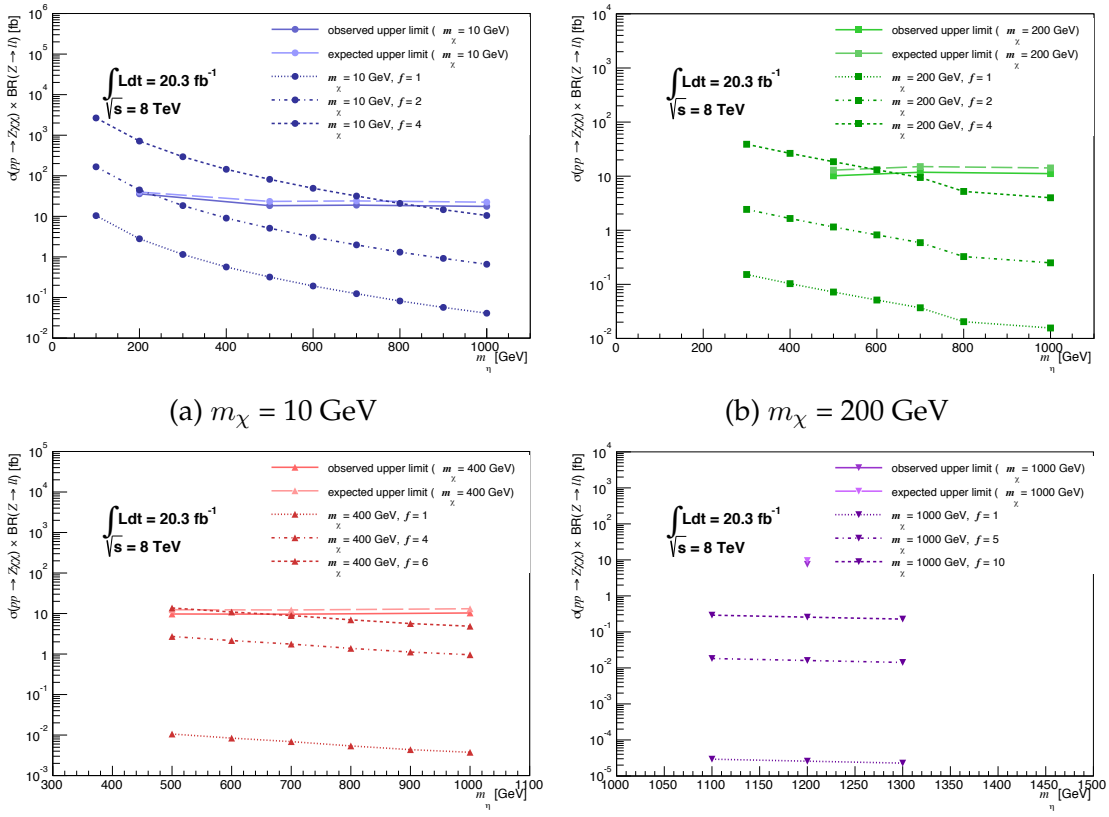

(a) m_χ = 10 GeV

(b) m_χ = 200 GeV

(c) m_χ = 400 GeV

(d) m_χ = 1000 GeV

Figure 6.20: The observed and expected upper limits (shown in bold) on the cross section ($\sigma(pp \to Z\chi\chi)$) times leptonic branching fraction for each DM mass studied, as a function of the mediator mass (labeled m_η) compared with the simulated value for some representative couplings. The point of intersection with the observed limit gives the lower bound on the mediator mass for a fixed DM mass and coupling.

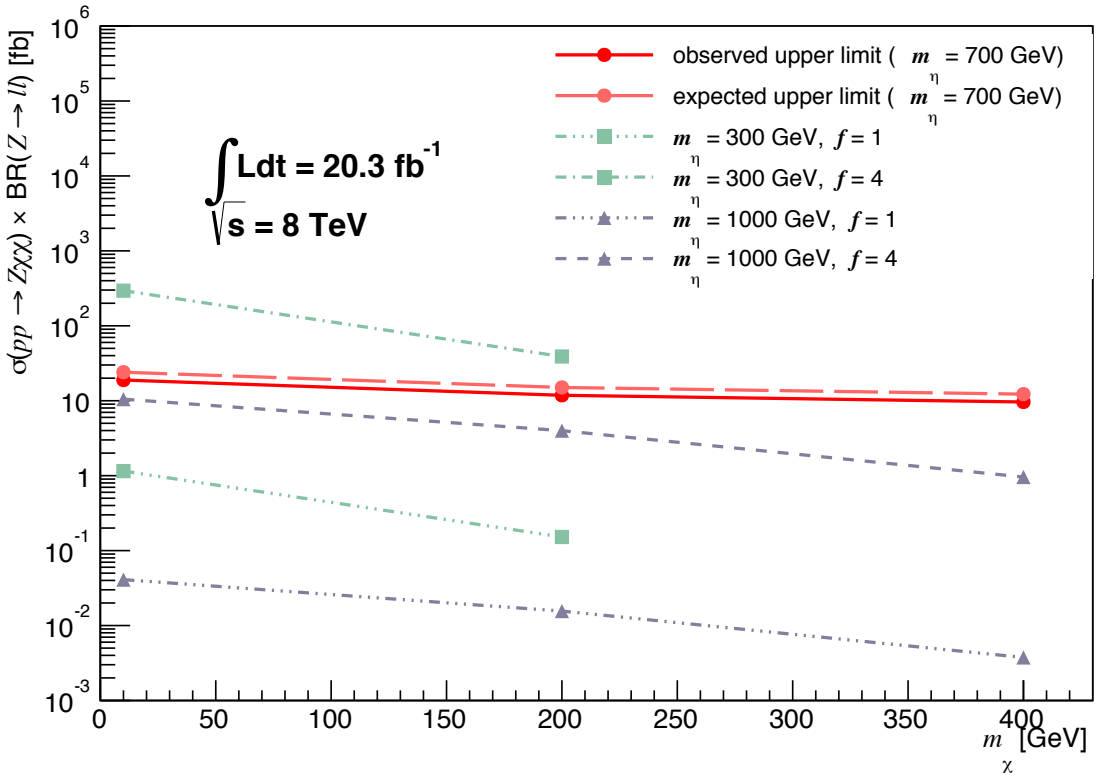

Figure 6.21: The observed and expected upper limits on the cross section times leptonic branching fraction shown in red, compared with the simulated value for mediator masses of 300 GeV (in green) and 1000 GeV (in purple), as a function of the DM mass.

m_χ [GeV]	M_{med} [GeV]	Best SR	$\sigma_{\text{lim}}^{\text{exp}}$ [fb]	$\sigma_{\text{lim}}^{\text{obs}}$ [fb]
10	200	$E_{\text{T}}^{\text{miss}} > 150$ GeV	39.8	35.9
10	500	$E_{\text{T}}^{\text{miss}} > 250$ GeV	23.4	18.4
10	700	$E_{\text{T}}^{\text{miss}} > 250$ GeV	24.0	18.9
10	1000	$E_{\text{T}}^{\text{miss}} > 250$ GeV	22.4	17.6
200	500	$E_{\text{T}}^{\text{miss}} > 250$ GeV	12.9	10.2
200	700	$E_{\text{T}}^{\text{miss}} > 250$ GeV	15.0	11.8
200	1000	$E_{\text{T}}^{\text{miss}} > 250$ GeV	14.2	11.2
400	500	$E_{\text{T}}^{\text{miss}} > 250$ GeV	12.4	9.7
400	700	$E_{\text{T}}^{\text{miss}} > 250$ GeV	12.3	9.6
400	1000	$E_{\text{T}}^{\text{miss}} > 250$ GeV	13.1	10.3
1000	1200	$E_{\text{T}}^{\text{miss}} > 250$ GeV	9.6	7.5

Table 6.18: The best expected and observed upper limits on the tS model cross section, and the corresponding SRs where these were obtained.

Extension of parameter space

Toward the end of this analysis, it was decided to extend the range of mediator masses up to 1200 GeV for the DM masses below 1000 GeV, resulting in a more consistent parameter space. As such samples were not initially simulated, and more time than was needed to do so was available, we investigated an alternative method of estimating the values of $\mathcal{A} \times \epsilon$ at reconstruction-level. (The cross sections are easily obtainable through local simulation to truth-level of the parameter points.)

The proposed method was to plot the value of $\mathcal{A} \times \epsilon$ as a function of mediator mass for each DM mass, and look for an obvious trend which could be fitted and extrapolated to M_{med} = 1200 GeV. The values of $\mathcal{A} \times \epsilon$ in the first two signal regions, along with the statistical uncertainties, are plotted in fig. 6.22. In each case, the variable is either approximately flat, or has a slight upward trend; the exception is for $m_\chi = 400$ GeV, which has a very slight downward trend between $M_{\text{med}} = 700$ and 1000 GeV, but it is flat within uncertainties. Therefore, we take the value of $\mathcal{A} \times \epsilon$ at $M_{\text{med}} = 1000$ GeV and apply it to $M_{\text{med}} = 1200$ GeV in each case, since this gives a conservative result in the case of the observed slight upward trend. This makes sense if we look at the kinematic behaviour for different masses, of which

the $E_{\mathrm{T}}^{\mathrm{miss}}$ is plotted at truth-level in fig. 6.23 for each DM mass. There is very little variation demonstrated, and so it is unsurprising that there is little variation in the acceptances. In fact, this fact could have been exploited by using a single fully-reconstructed sample to obtain an acceptance which would be applied to a range of mediator masses; alternately, a larger range such that more variation starts to arise could have been studied. Unfortunately such considerations were not recognised until after this analysis was established.

Conversion to limits on the coupling

The final upper limits on $g_{q\chi}$ are listed in the third column of table 6.19 for each mass point. These are calculated according to

$$g_{q\chi}^{\mathrm{lim}} = g_{q\chi}^{\mathrm{gen}} \times \left(\frac{\sigma^{\mathrm{gen}}}{\sigma^{\mathrm{lim}}}\right)^{\frac{1}{4}} \tag{6.18}$$

where σ^{gen} and σ^{lim} are the generated and limiting (at 95%C.L.) cross sections respectively, and $g_{q\chi}^{\mathrm{gen}}$ is the coupling of the initially-generated sample. The limits are also plotted in fig. 6.24 (ignoring the black line, which is explained in the next section). The white region corresponds to $M_{\mathrm{med}} < m_{\chi}$, a region of parameter space that is not included in this model following the assumption that the DM particle be the lightest, stable, new particle. The hatched region (where $M_{\mathrm{med}} \gtrsim m_{\chi}$) is valid parameter space, however we explicitly do not say anything about the limit on the coupling in this region as we did not consider any points within the region, and there were concerns that additional, unconsidered effects might arise due to the degenerative nature of the DM and mediator masses. Finally, the shaded region is created with an interpolation between the points for which the limits on $g_{q\chi}$ exist, with strongest limits at low DM and mediator masses.

6.8.1 Relic density considerations

The final column of table 6.19 corresponds to a *lower* limit on the coupling $g_{q\chi}$, obtained through a relic density calculation requiring that the dark matter relic density contributed by this model is exactly equal to the total observed relic density $\Omega_{\mathrm{DM}}h^2 \sim 0.11$. The value of $g_{q\chi}$ obtained is a lower limit since a smaller value does not provide the required interaction between pairs of DM particles such that they would annihilate away sufficiently; that is, a smaller coupling would lead to a larger relic density than is observed today. However, this does assume that the DM *only* interacts with quarks—if, on the other hand, it is also able to annihilate away to leptons (for example), that would allow the coupling $g_{q\chi}$, which only controls the strength of the annihilation to quarks, to decrease, while not affecting

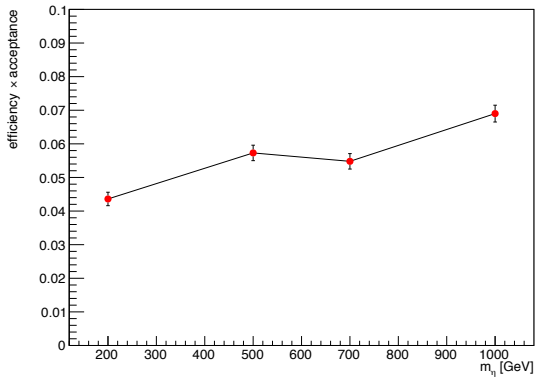

(a) m_χ = 10 GeV, SR1

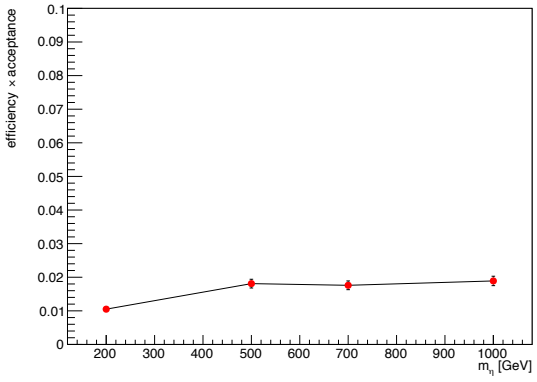

(b) m_χ = 10 GeV, SR2

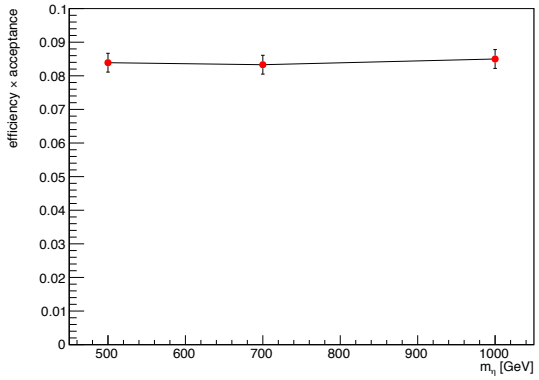

(c) m_χ = 200 GeV, SR1

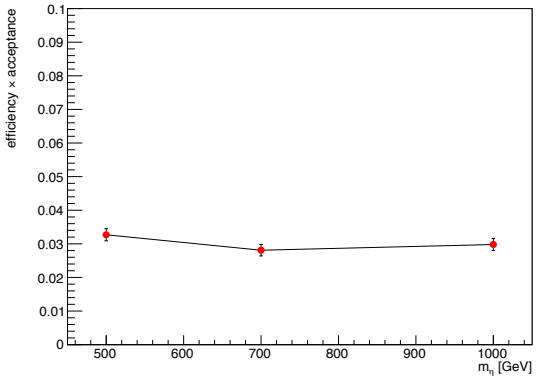

(d) m_χ = 200 GeV, SR2

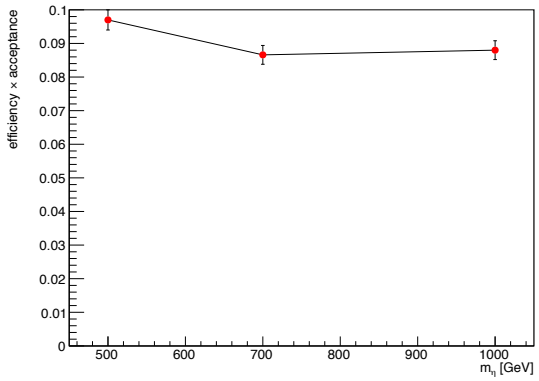

(e) m_χ = 400 GeV, SR1

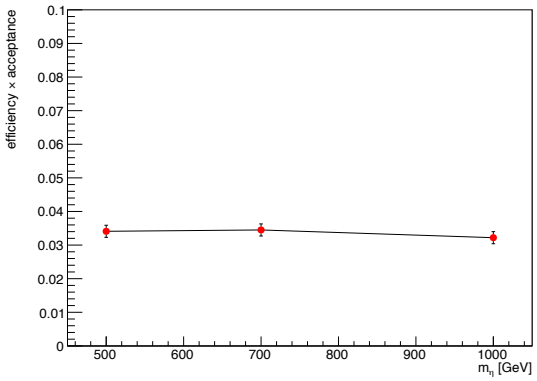

(f) m_χ = 400 GeV, SR2

Figure 6.22: The distribution of $\mathcal{A} \times \epsilon$ as a function of M_{med} (labeled m_η) in SRs 1 (left) and 2 (right), for m_χ = 10 GeV (top), 200 GeV (middle) and 400 GeV (bottom). The uncertainties are statistical.

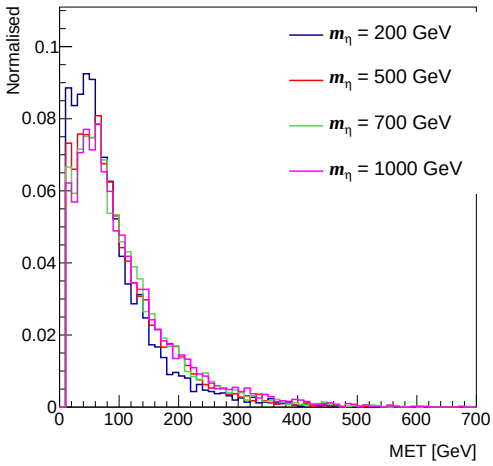

(a) m_χ = 10 GeV.

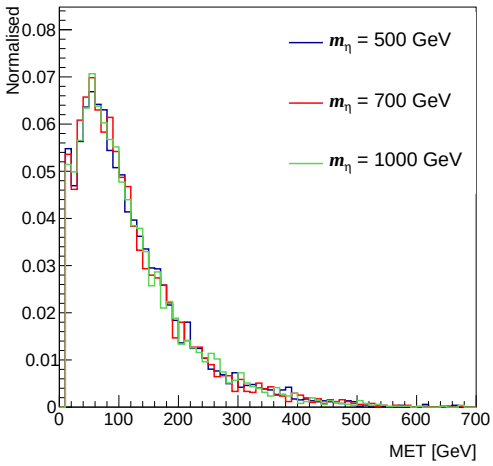

(b) m_χ = 200 GeV.

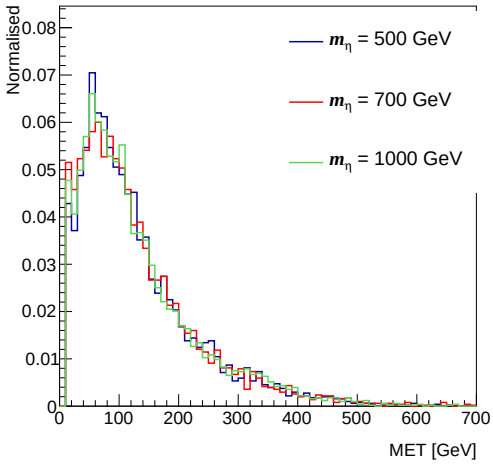

(c) m_χ = 400 GeV.

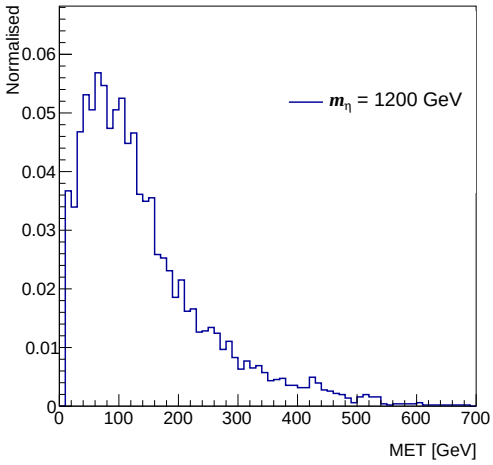

(d) m_χ = 1000 GeV.

Figure 6.23: The $E_{\mathrm{T}}^{\mathrm{miss}}$ distribution of the tS model for different DM masses (shown at truth-level), indicating that the kinematic behaviour of the model is reasonably independent of the mediator mass for the range of masses shown.

the collider studies described.

The relic density calculation proceeds following the method of refs. [56, 127, 244], using a semi-analytic solution to the co-moving Boltzmann equation, and doubling the annihilation cross section to allow for the additional annihilation to charm and strange quarks. This doubling of the cross section is valid as it is independent of the quark masses, since they are negligible compared to the momentum transfer in the annihilation process. The code for this process was provided by a colleague, and the underlying physics is as follows.

The cross section for two Majorana DM particles annihilating to a pair of quarks is given by [44]

$$\sigma v = \frac{g_{q\chi}^4 m_\chi^2 (m_\chi^4 + M_{\text{med}}^4)}{4(m_\chi^2 + M_{\text{med}}^2)^4 \pi} v^2 + \mathcal{O}(v^4) \tag{6.19}$$

where three quark colours and four quark channels have been included. Note that the s-wave term (a in the expansion $\sigma = a + bv^2 + \mathcal{O}(v^4)$) is helicity-suppressed and so vanishes in the $m_q \to 0$ limit assumed here, a result of the Majorana nature of the DM particle.

The relic density of a relic DM particle was discussed in sec. 2.2.2 and restated here, it is expressed as [55]

$$\Omega_{\text{DM}} h^2 \simeq \frac{1.07 \times 10^9 \text{GeV}^{-1}}{M_{\text{Pl}}} \frac{x_F}{\sqrt{g_F^*}} \frac{1}{(a + 3b/x_F)} \ , \tag{6.20}$$

where M_{Pl} is the Planck mass (1.22×10^{19} GeV). g_F^* counts the number of relativistic degrees of freedom, and is taken directly from ref. [244]. $x_F \equiv m_\chi / T_F$ where T_F is the freeze-out temperature of the relic particle χ, and is estimated through iteration of the following equation:

$$x_F = \ln \left[c(c+2) \sqrt{\frac{45}{8}} \frac{g}{2\pi^3} \frac{m_\chi M_{\text{Pl}} (a + 6b/x_F)}{(g_F^*)^{1/2} x_F^{1/2}} \right] \ , \tag{6.21}$$

where c is a constant of order one determined by matching the late-time and early-time solutions—in this case it is equal to $\sqrt{2} - 1$.

The coupling limit is then obtained for given values of m_χ and M_{med} through iterative testing of couplings $g_{q\chi}$ until eq. 6.21 is satisfied and eq. 6.20 gives the observed relic density. The limiting coupling values are listed in the final column of table 6.19.

These lower limits on the couplings are interpolated across the (m_χ, M_{med}) parameter space, which along with the interpolation of the upper collider limits, results in upper and lower limit surfaces. The intersection between these surfaces, that is, where the upper and lower limits are equal, is shown as the black line in

m_χ [GeV]	M_{med} [GeV]	collider limit on $g_{q\chi}$	relic density limit on $g_{q\chi}$
10	200	1.89	1.30
10	500	2.76	3.25
10	700	3.51	4.54
10	1000	4.53	6.48
10	1200	5.26	7.78
200	500	3.41	3.99
200	700	4.23	5.23
200	1000	5.17	7.19
200	1200	5.86	8.53
400	500	5.50	3.73
400	700	6.11	4.48
400	1000	7.24	5.71
400	1200	8.15	6.38
1000	1200	23.3	5.84

Table 6.19: The 95%C.L. upper limit on the coupling from this analysis (third column), and the allowed coupling minimum allowed coupling that satisfies relic density constraints (fourth column), where the total relic density is assumed to be $\Omega_{\text{DM}}h^2 \simeq 0.11$.

fig. 6.24. The region to the left of the line is where the lower limit on the relic density is higher than the upper limit from the collider studies, and therefore this region would be excluded under the assumption that the DM only interacts with quarks as described by this model. However, as noted above, if the DM could also interact with leptons or bosons, the relic density constraint is relaxed and the parameter space becomes viable again.

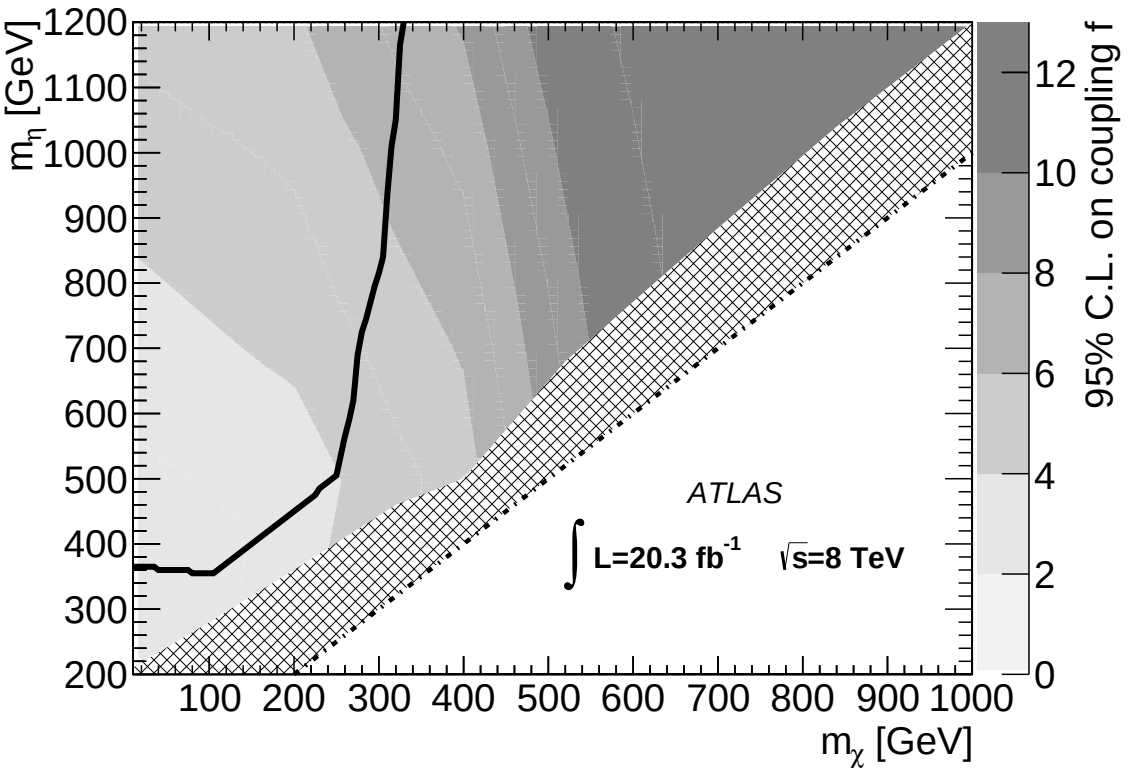

Figure 6.24: The 95%C.L. upper limits on the coupling of the tS model, $g_{q\chi}$ (labeled f), plotted as a function of the DM and mediator masses. The black line indicates where the upper limit from this mono-Z analysis intersects the lower limit from a relic density calculation. The hatched region indicates valid parameter space that was not considered in this analysis.

Chapter 7

Reinterpreting the ATLAS Run I mono-X searches

In this chapter, we use results from Run I ATLAS mono-X analyses to place constraints on the three phenomenologically distinct cases of a simplified model (SiM) that were introduced in chapter 3, namely, the sV, sA and tS models (see eqs. 3.12, 3.13 and 3.14). As previously noted, the sV and sA models correspond to the simplest UV-completions of the D5 (vector) and D8 (axial-vector) effective operators in the s-channel, while in the heavy mediator limit, the operator describing the tS model can be Fierz transformed into a combination of operators D5 to D8[1].

The models are constrained using public results from mono-X + missing transverse energy ($E_{\mathrm{T}}^{\mathrm{miss}}$) searches conducted by the ATLAS Collaboration. Specifically, we focus on searches where X is either a parton (manifesting in the detector as a narrow-radius jet), a leptonically-decaying Z boson (manifesting as two opposite-sign same-flavor leptons), or a hadronically-decaying W or Z boson (manifesting as a large-radius jet). The purpose of this work is to strengthen existing SiM limits using the full 20.3 fb^{-1} of Run I ATLAS data, and to explore an enhanced parameter space with respect to the mediator and dark matter (DM) masses and the relative strength of the couplings to the visible and dark sectors. We choose to treat the mediator width as the minimal value naturally arising, which is more realistic than a fixed width. Lastly, we provide a cross-check and comparison of the performance of the three targeted collider detection channels, and compare against relic density and direct detection constraints.

The remainder of the chapter is organised as follows. Sec. 7.1 describes the

[1]The D5 and D8 operators form a nice starting point in the analysis of SiMs as they have been studied exhaustively in the past (see refs. [11, 12, 14, 16, 115, 119, 120, 245, 246] among others). This attention is motivated by the fact that collider limits for the D5 (D8) operator can be readily transformed into limits on spin-independent (spin-dependent) DM-nucleon scattering and vice versa.

parameter space included in this study, and discusses the impact of a narrow t-channel mediator width in the mono-jet channel. Sec. 7.2 outlines the techniques used to recast mono-X + $E_{\mathrm{T}}^{\mathrm{miss}}$ limits on the visible cross section for any new physics process into constraints on SiMs, and specifically on the couplings g_q, g_χ and $g_{q\chi}$, while sec. 7.3 provides details on the three mono-X channels. Lastly, our results are presented in sec. 7.4 along with a discussion of the implications of this work.

7.1 Simplified model phenomenology

7.1.1 The mono-X + $E_{\mathrm{T}}^{\mathrm{miss}}$ signatures

Section 3.3.2 of chapter 3 provides a comprehensive overview of the sV, sA and tS SiMs studied in this work, and figs. 3.7 and 3.8 show the possible tree-level processes for emission of a jet, photon or electroweak (EW) boson. A very brief summary is as follows.

The mono-X + $E_{\mathrm{T}}^{\mathrm{miss}}$ signal (abbreviated to mono-X) is a popular collider signal in the search for new physics, particularly in the search for dark matter. Since DM particles are not expected to interact with detector material, they appear as missing transverse energy when balanced against a visible object, X, that is radiated from the initial or intermediate state. For the s-channel SiMs, only initial-state radiation is permitted; see figs. 7.1a and 7.1b for examples. For the tS model, radiation of a gluon, photon or EW boson is permitted both from initial state partons (fig. 7.1c) or from the mediator (fig. 7.1d). Note that these diagrams do not comprise a comprehensive set.

The most likely scenario at the Large Hadron Collider (LHC) is the production of a jet alongside the invisible DM pair (labeled $\chi\bar{\chi}$), as a result of the strong coupling and prevalence of partons in the initial state. However, to fully exploit the potential of the ATLAS detector to record and identify a vast array of particle types, we also consider two additional channels. Firstly, we take advantage of the relative cleanliness and simplicity of leptons in the leptonically-decaying mono-Z ($\rightarrow \ell^+\ell^-$) channel. We also take advantage of the large hadronic branching fraction, and developing jet-identification techniques for boosted EW bosons, in the hadronically-decaying mono-W/Z ($\rightarrow jj$) channel[2]. In both cases, the large multi-jet background is reduced, and complications in jet production such as parton-matching can be ignored, making these an interesting alternative to the mono-jet channel where speed, efficiency and a reduction in jet-associated uncertainties

[2]In addition, one of the first Run II dark matter search results from ATLAS was from this channel [5], released during the preparation of this work, and described in the following chapter.

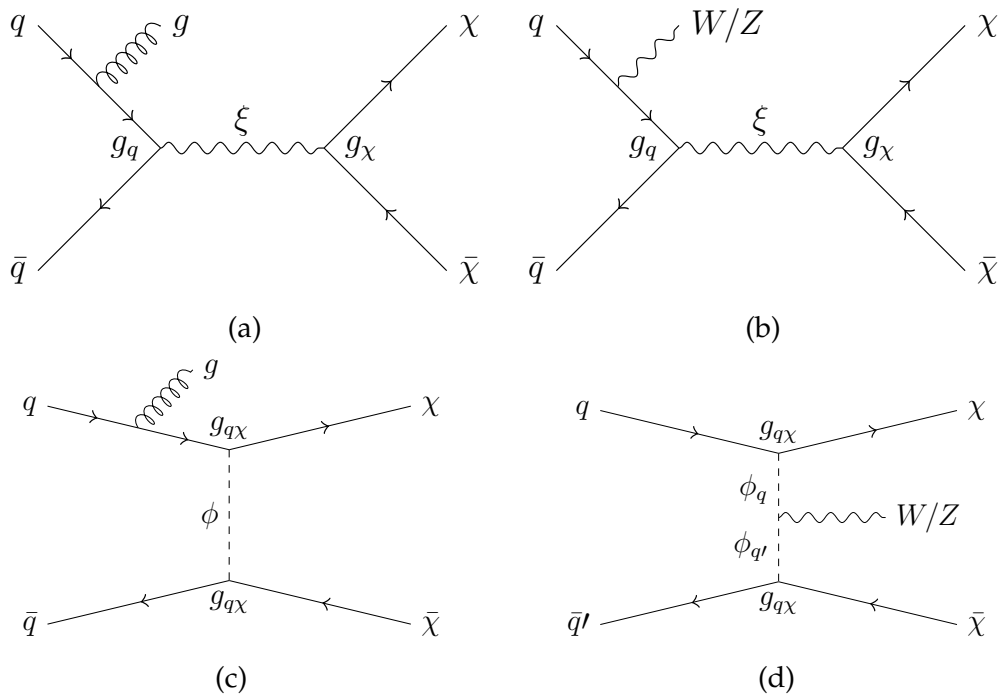

Figure 7.1: A representative subset of dark matter pair-production processes with a gluon or W/Z boson in the final state for the s-channel (a,b) and t-channel (c,d) models. Note that other diagrams are possible, including initial state radiation of a gauge boson, and internal bremsstrahlung of a gluon.

may make up for a loss in sensitivity.

7.1.2 Mass and coupling points

A representative set of dark matter and mediator masses, listed in table 7.1, are chosen for study in each detection channel. DM masses of 3, 30 and 300 GeV are also included in the mono-Z channel, where ease of production permits finer granularity in the mass parameter space. All (m_χ, M_{med}) combinations are allowed in the sV and sA models, while in the tS model M_{med} must be greater than m_χ to ensure stability of the DM particle. The couplings g_q and $g_{q\chi}$ are set to unity, while the DM-mediator coupling in the s-channel models, g_χ, is varied from 0.2 to 5. The mediator masses are chosen to cover a broad range of parameter space and to coincide with predominantly three regimes: (near-)degenerate ($M_{\text{med}} \approx m_\chi$), on-shell ($M_{\text{med}} \geq 2m_\chi$) and off-shell ($M_{\text{med}} < 2m_\chi$).

7.1.3 Impact of the mediator width

The natural mediator widths for the sV, sA and tS models are given in chapter 3 in eqns. 3.16, 3.17 and 3.18 respectively. It is important to ensure that the mediator width is treated appropriately, as it impacts both the cross section cal-

m_χ [GeV]	M_{med} [GeV]	s-channel		t-channel
		g_q	g_χ	$g_{q\chi}$
1, (3), 10, (30), 100, (300), 1000	1, 2, 10, 20, 100, 200, 1000, 2000	1	0.2, 0.5, 1, 2, 5	1

Table 7.1: Mass and coupling points chosen for the analysis of simplified dark matter models. Values in brackets are only included in the mono-Z channel. The mediator masses are primarily representative of three regimes: (near-)degenerate ($M_{\text{med}} \approx m_\chi$), on-shell ($M_{\text{med}} \geq 2m_\chi$) and off-shell ($M_{\text{med}} < 2m_\chi$). For the t-channel model, $M_{\text{med}} > m_\chi$ is required to ensure stability of the DM particle.

culation and, in some cases, the kinematic behaviour of the model. In most cases however, we can take advantage of the fact that for each point in (m_χ, M_{med}) parameter space, the mediator width (and therefore the couplings) do not greatly affect a model's kinematic behaviour. This is demonstrated in fig. 7.2, where we plot a simplified $E_{\text{T}}^{\text{miss}}$ distribution (as a proxy for the full selection in each analysis) for the sV (representing both the sV and sA models) and tS models for two mass points and a demonstrative set of couplings such that $\Gamma < M_{\text{med}}/2$. The $E_{\text{T}}^{\text{miss}}$ distribution is predominantly independent of the mediator width for the s-channel models in the mono-jet channel, and all models in the mono-Z[3] channel. For the s-channel models, the same result was found by ref. [15], which provides a set of recommendations for the usage of simplified models for DM searches in Run II. As described below, this independence of the kinematic spectrum on the width, and therefore the couplings, allows a simplification of the limit calculation used in sec. 7.2.2.

However, there is the notable exception of the tS model in the mono-jet channel, showing a clear variation in the kinematic behaviour, which can be attributed to additional diagrams (accessible only in this channel) featuring a gluon in the initial state and subsequently allowing the mediator to go on-shell. These diagrams are discussed and shown in, for example, ref. [41]. The kinematics of these diagrams with an on-shell mediator are much more sensitive to variations in the width.

In the cases where the kinematic distribution is independent of the width, we assume that the impact of the selection cuts in each channel is unchanged by the couplings. In this case, the following relations approximately hold:

[3]In this discussion, the mono-W/Z channel can be assumed to follow the same logic as for the mono-Z channel.

$$\sigma \propto \begin{cases} g_q^2 g_\chi^2/\Gamma & \text{if } M_{\text{med}} \geq 2m_{\text{DM}} \\ g_q^2 g_\chi^2 & \text{if } M_{\text{med}} < 2m_{\text{DM}} \end{cases} \tag{7.1}$$

in the sV and sA models [34], and

$$\sigma \propto g_{q\chi}^4 \tag{7.2}$$

in the tS model. When valid, these approximations allow us to greatly simplify our limit calculations, and for this reason, we restrict our primary results to regions of parameter space where $\Gamma/M_{\text{med}} < 0.5$ (see sec. 7.2.2 for further details of the limit-setting calculation).

The generator treatment of the mediator as a Breit-Wigner propagator, rather than a true kinetic propagator, breaks down for large widths [26, 34]. More problematically, it was noted by refs. [26, 34] that the Breit-Wigner propagator breaks down in the $m_{\text{DM}} \gg M_{\text{med}}$ region even if Γ/M_{med} is small. To correct for this we follow ref. [34], and rescale the cross section in the $m_{\text{DM}} > M_{\text{med}}$ region by a factor which takes into account the error introduced by the use of a Breit-Wigner propagator by the generator. The factor is found by convolving the PDF with both the kinetic and Breit-Wigner propagators in turn and taking the ratio at each mass point. We approximate the kinetic propagator by making the substitution $M_{\text{med}}\Gamma(M_{\text{med}}) \to s\Gamma(\sqrt{s})/M_{\text{med}}$ in the Breit-Wigner propagator.

A full study of the tS model within the mono-jet channel, where altering the coupling can lead to changed kinematic behaviour, has been performed elsewhere [41], and requires the production of individual samples for each coupling point. This, combined with the challenges associated with including differing orders of α_s, make the generation process computationally expensive compared to the mono-Z and mono-W/Z channels. We therefore exclude an analysis of the tS model in the mono-jet channel in this work.

7.2 Recasting mono-X constraints

The procedure for recasting existing mono-X analyses to obtain SiM constraints follows a simple cut-and-count methodology. Firstly, signal events are simulated (described below in section 7.2.1) with object p_{T} smearing applied to approximate the detection efficiency of the ATLAS detector, ϵ. The event selection criteria of the mono-X analysis of interest is then applied to the simulated signal samples. Events surviving the selection criteria are counted to determine the likelihood of a dark matter event being observed (referred to as the acceptance, $\mathcal{A}$), which is then used in combination with channel-specific model-independent limits on

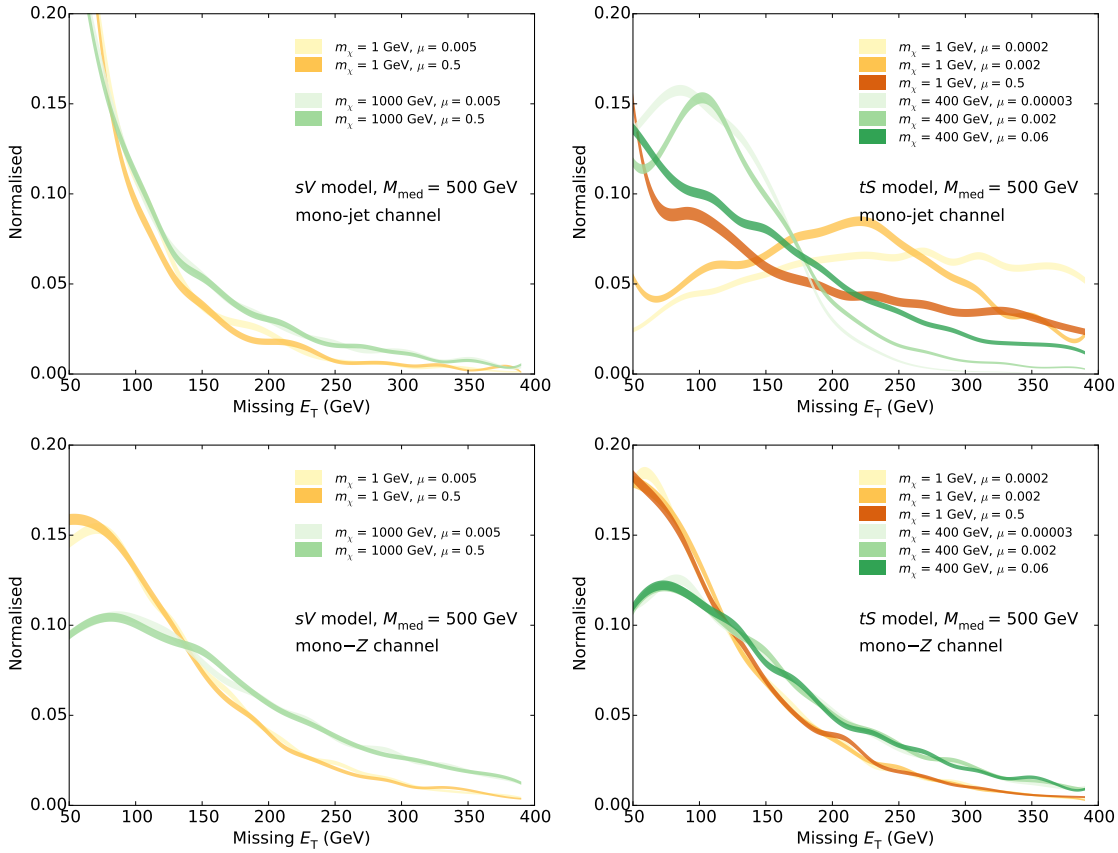

Figure 7.2: The $E_{\mathrm{T}}^{\mathrm{miss}}$ distribution of the sV and tS models in the mono-jet and mono-Z channels, for some example masses. The parameter μ is defined as Γ/M_{med}, and is used to demonstrate the impact of a changing width; the tS model in the mono-jet channel shows a clear width dependence, while all other model/channel combinations show behaviour that is independent of the width for the parameter space considered. The widths are obtained with couplings of 0.1, 1 and 5 where $\mu < 0.5$ remains true.

new physics events to constrain the parameter space of a given model.

In this paper, mono-jet limits are derived from a search for new phenomena conducted by the ATLAS Collaboration using pp collisions at $\sqrt{s} = 8$ TeV as described in ref. [115]. Similarly, the leptonic mono-Z and hadronic mono-W/Z constraints are derived from ATLAS dark matter searches that were optimised for the D1, D5 and D9 effective operators [3, 238], the former of which was the subject of the previous chapter. These analyses are described in further detail in secs. 7.3.1, 7.3.2 and 7.3.3 respectively.

7.2.1 Signal simulation

Monte Carlo simulated event samples are used to model the expected signal for each channel and for each SiM. Leading order matrix elements for the process $pp \to X + \chi\bar{\chi}$ (where X is specifically one or two jets[4], a Z boson decaying to two charged leptons, or a hadronically-decaying W or Z boson) are first simulated using MADGRAPH_aMC@NLO v2.2.2 [247] with the MSTW2008lo68cl PDF [141]. During this stage, the renormalisation and factorisation scales are set to the default sum of $\sqrt{m^2 + p_{\mathrm{T}}^2}$ for all particles in the final state. Showering and hadronisation are then performed by PYTHIA8.201 [222] with the appropriate PDF and using the ATLAS UE Tune AU2-MSTW2008LO [229]. Reconstruction of small-radius jets (hereon referred to just as 'jets') for the mono-jet channel is performed by FASTJET [248] using the anti-k_{T} algorithm with radius parameter R = 0.4. Similarly, reconstruction of large-radius jets for the mono-W/Z channel is performed using the Cambridge-Aachen (C/A) algorithm with R = 1.2. The latter channel also includes a mass-drop filtering procedure (see sec. 4.3.3) with μ_{12} = 0.67 and minimum momentum balance $\sqrt{y_{\mathrm{min}}}$ = 0.4, which favours large-R jets with two balanced subjets, consistent with the decay of an EW boson to a boosted di-jet pair. Lastly, the detector response is approximated by applying a Gaussian smearing factor to the p_{T} of all leptons and jets.

Parton matching scheme

When a hard process includes one or more jets (such as a mono-jet event), some method is required to separate the partons produced in that hard process (described by the matrix element, which diverges as partons become soft and collinear) from those produced by the soft process (described by the parton showering, which breaks down for hard and widely-separated jets). A one-parton event produced in MADGRAPH can be showered in PYTHIA to produce two jets, a final state which is indistinguishable from a two-jet event produced in MADGRAPH;

[4]Jets are seeded by any parton excluding the (anti-)top quark.

therefore, matching of partons between the two generators is necessary to ensure hard and soft processes are treated correctly and to avoid double-counting jets. In very simplistic terms, a cutoff or *matching scale* is a threshold above which only MADGRAPH is permitted to produce partons and below which only PYTHIA is allowed to produce jets.

In the ATLAS mono-jet analysis, matching of partons generated in MADGRAPH to jets generated in PYTHIA is performed using the MLM scheme [249], with *two* matching scales, or values of 'QCUT', per mass/coupling point. In combination, the QCUT values span a broad kinematic range with a cut placed on the leading jet p_{T} per event to avoid double-counting. This treatment aims to both enhance the statistics in the high $E_{\mathrm{T}}^{\mathrm{miss}}$ signal regions and to mitigate the impact of the matching scale on the shape of the p_{T} and $E_{\mathrm{T}}^{\mathrm{miss}}$ distributions; that is, to reduce the uncertainty in those areas of parameter space where the transferred momentum is significantly larger or smaller that the QCUT value. For the analysis of SiMs in this work, we use instead a single matching scale of 80 GeV. The need for a second, high $E_{\mathrm{T}}^{\mathrm{miss}}$ QCUT is compensated for by the generation of increased events per mass and coupling sample. Furthermore, any effects introduced by this simplified procedure are accounted for by a conservative estimation of the uncertainties on the final limits as discussed in sec. 7.2.2. Though not ideal, this approach suitably reproduces the results of the ATLAS mono-jet analysis for the masses of interest (see sec. 7.3.1). Importantly, it also reduces the complexity and computational expense involved in estimating limits for the mono-jet channel.

7.2.2 Limit calculations

A summary of the procedure employed to calculate the 95% confidence level (C.L.) limits on the coupling parameter $\sqrt{g_q g_\chi}$ is provided below, where this parameter can be replaced with $g_{q\chi}$ for the tS model, and Λ in the validation of the mono-jet analysis.

For each SiM, the nominal limit is calculated by taking the model-independent upper limit on the visible cross section, $\sigma \times \mathcal{A} \times \epsilon$, from each analysis, dividing by the value of $\mathcal{A} \times \epsilon$ coming from signal MC (which is taken as a single parameter for each point) to obtain the limiting cross section σ_{lim}, and rearranging eq. 7.1 to convert to a limit on the couplings. In the s-channel on-shell case, the width can be expressed as a function of g_q and the ratio g_χ/g_q, which simplifies the calculation. We arrive at

$$\sqrt{g_q g_\chi}_{\rm lim} = \begin{cases} \sqrt{g_q g_\chi}_{\rm gen} \times (\sigma_{\rm lim}/\sigma_{\rm gen})^{\frac{1}{2}} & \text{if } M_{\rm med} \geq 2m_{\rm DM} \ (s-\text{channel}) \\ \sqrt{g_q g_\chi}_{\rm gen} \times (\sigma_{\rm lim}/\sigma_{\rm gen})^{\frac{1}{4}} & \text{if } M_{\rm med} < 2m_{\rm DM} \end{cases} \tag{7.3}$$

where $\sqrt{g_q g_\chi}_{\rm gen}$ and $\sigma_{\rm gen}$ are the input couplings and generated cross section (taken at PYTHIA-level), respectively.

The signal region in each case is chosen based on where the best 'expected' limit lies, where that limit is calculated assuming that exactly the expected SM background is observed.

Uncertainty estimation

Our nominal limits rely on both $\sigma_{\rm gen}$ and $\mathcal{A} \times \epsilon$ and so are subject to systematic uncertainties which derive from our choice of signal generation procedure. For our signal samples, there are three key sources of systematic uncertainty: the factorisation and renormalisation scales, the strong coupling constant (α_s) and the choice of Parton Distribution Function (PDF). Note that all uncertainties resulting from the experimental analysis are taken into account in the model-independent 95%C.L. limits that we use to calculate our limits on the SiMs.

We assess the impact of the factorisation and renormalisation default scales in a straightforward manner; by varying them simultaneously by factors of 2 ('up') and 0.5 ('down'). The systematic effects of the strong coupling constant and PDF are difficult to separate and so are treated in tandem. We assume that the systematic uncertainty introduced by α_s at matrix-element level is negligible when compared to the PDF uncertainties, as demonstrated to be valid in ref. [116]. The variation of α_s in conjunction with a change of PDF is done with the use of specific tunes in PYTHIA, which we change simultaneously with the PDF choice to estimate the uncertainty on $\sigma_{\rm gen}$. The nominal choices of PDF and tune are varied 'up' to NNPDF2.1LO PDF [250] + Monash tune [251], and 'down' to CTEQ6L1 PDF [140] and ATLAS UE AU2-CTEQ6L1 tune [229]. For the mono-jet channel, the impact of the matching scale (`QCUT`) is assessed in a manner similar to that of the factorisation and renormalisation scales. That is, we vary the `QCUT` by factors of 2 ('up' to 160 GeV) and 0.5 ('down' to 40 GeV). These systematic uncertainty sources are summarised in table 7.2.

The average variation in the nominal value of $\sigma_{\rm lim}$ (measured as a fraction of $\sigma_{\rm lim}$) resulting from each systematic source is added in quadrature and propagated to $\sqrt{g_q g_\chi}$ to obtain the total systematic uncertainty. This process is adjusted slightly to account for the inclusion of statistical uncertainties, which are estimated conservatively by taking the 95% C.L. *lower* limit on $\mathcal{A} \times \epsilon$ as calculated

main systematic sources	PDF/tune	factorisation and renormalisation scales	matching scale (mono-jet only)
variation 'up'	NNPDF2.1LO + Monash tune	2	160 GeV
nominal	MSTW2008lo68cl + ATLAS UE AU2-MSTW2008LO	1	80 GeV
variation 'down'	CTEQ6L1 + ATLAS UE AU2-CTEQ6L1	0.5	40 GeV

Table 7.2: Reading left to right, the sources of systematic uncertainty considered in this analysis. Each point in parameter space is varied up or down by one of these sources, and the systematic uncertainty is then taken from the resultant changes to the acceptance and cross section in comparison to their nominal values.

with the Wald approximation, i.e. $\mathcal{A} \times \epsilon \rightarrow (\mathcal{A} \times \epsilon) - \Delta(\mathcal{A} \times \epsilon)$. Note that the uncertainty on the luminosity is less than 3%, so is considered to be negligible in comparison to other systematic sources.

7.3 The mono-X channels

The details of each mono-X analysis, as well as the validation procedure performed for each channel, are discussed in this section. The implementation and validation of the mono-jet and mono-W/Z channels was performed by M. McDonald and J. Gramling in collaboration with the author.

7.3.1 The mono-jet channel

The ATLAS mono-jet + $E_{\mathrm{T}}^{\mathrm{miss}}$ analysis [115] was originally designed to set limits on three new physics scenarios, the most relevant of which is the production of Weakly Interacting Massive Particle (WIMP) DM within the context of a set of effective operators. The analysis also includes a brief study of a Z' DM model which is analogous to our sV model.

Signal selection is carried out based on at least one hard jet recoiling against missing energy, and is summarised in the left-hand column of table 7.3. To ensure that the correct back-to-back jet + $E_{\mathrm{T}}^{\mathrm{miss}}$ topology is selected, events are required

to have a leading jet, j_1, with $p_{\mathrm{T}} > 120$ GeV and $|\eta| < 2.0$ satisfying $p_{\mathrm{T}}^{j_1}/E_{\mathrm{T}}^{\mathrm{miss}} > 0.5$. Surviving events must then fulfill $|\Delta\phi(j, \vec{E}_{\mathrm{T}}^{\mathrm{miss}})| > 1.0$, where j is any jet with $p_{\mathrm{T}} > 30$ GeV and $|\eta| < 4.5$. This criterion reduces the multijet background contribution where the large $E_{\mathrm{T}}^{\mathrm{miss}}$ originates mainly from jet energy mismeasurements. Note that there is no upper limit placed on the number of jets per event. The contribution from the dominant background processes, W/Z+jets, is managed with a veto on events containing muons or electrons with $p_{\mathrm{T}} > 7$ GeV. Lastly, nine separate signal regions are defined with increasing lower thresholds on $E_{\mathrm{T}}^{\mathrm{miss}}$, which range from 150 GeV to 700 GeV as shown in table 7.4.

The ATLAS mono-jet analysis revealed no significant deviation of observed events from the expected Standard Model (SM) backgrounds in the 8 TeV dataset of Run I. Subsequently, model-independent limits on new physics signatures were provided in terms of the visible cross section, $\sigma \times \mathcal{A} \times \epsilon$, listed in table 7.4.

The signal simulation procedure outlined in sec. 7.2.1 and implementation of the selection criteria discussed above are validated for the mono-jet channel via reproduction of ATLAS limits on the suppression scale, $\Lambda \equiv M_{\mathrm{med}}/\sqrt{g_q g_\chi}$, for the Z' model. The details of this process are described below.

Validation of the mono-jet channel

The signal generation and selection procedures for the mono-jet channel are validated via reproduction of the ATLAS limits on $\Lambda \equiv M_{\mathrm{med}}/\sqrt{g_q g_\chi}$, for the s-channel vector SiM. A comparison of limits in SR7[5] for a representative sample of mediator masses with $m_\chi = 50$ GeV, $\Gamma = M/8\pi$ and $\sqrt{g_q g_\chi} = 1$ is presented in table 7.5. In general, good agreement is observed between the ATLAS and reproduced limits, with a maximum difference of 12%. We note that a discrepancy of a few percent is expected given the differences in signal simulation. For example, the simplified matching procedure discussed in sec. 7.2.1 introduces an additional uncertainty of approximately 25% for events with $E_{\mathrm{T}}^{\mathrm{miss}} > 350$ GeV when compared to the approach utilised by the ATLAS mono-jet group. Further uncertainties are introduced by the jet smearing approximation used in place of a full detector simulation and by the 95% C.L. estimation procedure (outlined in sec. 7.2.2) used instead of a thorough HistFitter treatment. As our results are consistently more conservative than those of the ATLAS analysis, we consider our approach to be acceptable.

[5] We use this signal region as it is the only one for which ATLAS limits are provided.

Event selection criteria		
Mono-jet channel	Mono-$Z(\to \ell^+\ell^-)$ channel	Mono-$W/Z(\to jj)$ channel
≥ 1 jet with $p_{\mathrm{T}} > 120$ GeV and $\lvert\eta\rvert < 2.0$	e^+e^- or $\mu^+\mu^-$ pair with $p_{\mathrm{T}} > 20$ GeV and $\lvert\eta\rvert \lesssim 2.5$	≥ 1 large-R jet (μ_{12} = 0.67, $\sqrt{y_{\mathrm{min}}}$ = 0.4) with $p_{\mathrm{T}} > 250$ GeV and $\lvert\eta\rvert <1.2$
	$m_{\ell\ell} \in$ [76, 106] GeV, $\lvert\eta_{\ell\ell}\rvert < 2.5$	$m_{\mathrm{jet}} \in$ [50, 120] GeV
$p_{\mathrm{T}}^{\mathrm{jet}}/E_{\mathrm{T}}^{\mathrm{miss}} > 0.5$	$\lvert p_{\mathrm{T}}^{\ell\ell} - E_{\mathrm{T}}^{\mathrm{miss}}\rvert \,/\, p_{\mathrm{T}}^{\ell\ell} < 0.5$	
$\lvert\Delta\phi(j, \vec{E}_{\mathrm{T}}^{\mathrm{miss}})\rvert > 1.0$, for any jet j satisfying $p_{\mathrm{T}} > 30$ GeV and $\lvert\eta\rvert < 4.5$	$\Delta\phi(\vec{E}_{\mathrm{T}}^{\mathrm{miss}}, p_{\mathrm{T}}^{\ell\ell}) >2.5$	
veto events containing an e or μ satisfying $p_{\mathrm{T}} > 7$ GeV	veto events containing a third e or μ satisfying $p_{\mathrm{T}} > 7$ GeV	veto events containing an e, μ or γ satisfying $p_{\mathrm{T}} > 10$ GeV and $\lvert\eta\rvert \lesssim 2.5$
	veto events containing a jet satisfying $p_{\mathrm{T}} > 25$ GeV and $\lvert\eta\rvert < 2.5$	veto events containing >1 narrow jets satisfying $p_{\mathrm{T}} > 40$ GeV, $\lvert\eta\rvert < 4.5$ and ΔR(large-R jet) > 0.9
		veto events with $\Delta\phi$(narrow jet, $\vec{E}_{\mathrm{T}}^{\mathrm{miss}}$)< 0.4
$E_{\mathrm{T}}^{\mathrm{miss}} >$ 150, 200, 250, 300, 350, 400, 500, 600, 700 GeV	$E_{\mathrm{T}}^{\mathrm{miss}} >$ 150, 250, 350, 450 GeV	$E_{\mathrm{T}}^{\mathrm{miss}} >$ 350, 500 GeV

Table 7.3: The event selection criteria for the three mono-X analyses, see text for further details.

Signal Region	$E_{\mathrm{T}}^{\mathrm{miss}}$ threshold [GeV]	$\sigma \times \mathcal{A} \times \epsilon$ [fb]
SR1	150	726 (935)
SR2	200	194 (271)
SR3	250	90 (106)
SR4	300	45 (51)
SR5	350	21 (29)
SR6	400	12 (17)
SR7	500	7.2 (7.2)
SR8	600	3.8 (3.2)
SR9	700	3.4 (1.8)

Table 7.4: The ATLAS mono-jet $E_{\mathrm{T}}^{\mathrm{miss}}$ signal regions and corresponding observed (expected) model-independent upper limits on $\sigma \times \mathcal{A} \times \epsilon$ at 95% confidence level. Adapted from ref. [115].

$M_{\mathrm{med}}^{\mathrm{gen}}$ [TeV]	$\Lambda^{95\%\mathrm{CL}}$ [GeV] (ATLAS)	$\Lambda^{95\%\mathrm{CL}}$ [GeV] (this work)	Difference [%]
0.05	91	89	2.2
0.3	1151	1041	7.3
0.6	1868	1535	11.8
1	2225	1732	12.0
3	1349	1072	6.8
6	945	769	8.5
10	928	724	10.6
30	914	722	9.6

Table 7.5: Comparison of the 95% C.L. lower limits on $\Lambda \equiv M_{\mathrm{med}}/\sqrt{g_q g_\chi}$ from this work and from the ATLAS mono-jet analysis [115]. The limits are for an s-channel vector mediator model with $m_\chi = 50$ GeV and $\Gamma = M_{\mathrm{med}}/8\pi$, and for the process $pp \to \chi\bar{\chi} + 1, 2j$ with `QCUT` = 80 GeV. Note that all samples were generated with $\sqrt{g_q g_\chi}$ = 1.

Signal Region	$E_{\mathrm{T}}^{\mathrm{miss}}$ threshold [GeV]	$\sigma \times \mathcal{A} \times \epsilon$ [fb]
SR1	150	1.59 (1.71)
SR2	250	0.291 (0.335)

Table 7.6: The ATLAS mono-Z + $E_{\mathrm{T}}^{\mathrm{miss}}$ signal regions and corresponding observed (expected) model-independent upper limits on $\sigma \times \mathcal{A} \times \epsilon$ at 95% confidence level, where those limits have been calculated in this work with HistFitter from the numbers of expected and observed events published in ref. [3].

7.3.2 The leptonic mono-Z channel

The ATLAS mono-Z + $E_{\mathrm{T}}^{\mathrm{miss}}$ analysis [3] was principally designed to constrain a set of Effective Field Theory (EFT) models of DM. As a secondary focus, it also included a short study of a t-channel SiM very similar to our tS model.

The selection criteria for this analysis are summarised in the central column of table 7.3. Electrons (muons) are required to have a p_{T} greater than 20 GeV, and $|\eta|$ less than 2.47 (2.5). Two opposite-sign, same-flavour leptons are selected, and required to have invariant mass and pseudorapidity such that $m_{\ell\ell} \in [76, 106]$ GeV and $|\eta^{\ell\ell}| < 2.5$. The reconstructed Z boson should be approximately back-to-back and balanced against the $E_{\mathrm{T}}^{\mathrm{miss}}$, ensured with the selections $\Delta\phi(\vec{E}_{\mathrm{T}}^{\mathrm{miss}}, \vec{p}_{\mathrm{T}}^{Z}) > 2.5$ and $|p_{\mathrm{T}}^{Z} - E_{\mathrm{T}}^{\mathrm{miss}}| \,/\, p_{\mathrm{T}}^{Z} < 0.5$. Events containing a jet with $p_{\mathrm{T}} > 25$ GeV and $|\eta| < 2.5$ are vetoed. Events are also vetoed if they contain a third lepton with $p_{\mathrm{T}} > 7$ GeV. The signal regions are defined by increasing lower $E_{\mathrm{T}}^{\mathrm{miss}}$ thresholds: $E_{\mathrm{T}}^{\mathrm{miss}} > 150$, 250, 350, 450 GeV.

A cut-and-count strategy is used to estimate the total observed yields and expected SM backgrounds in each signal region. The limits on $\sigma \times \mathcal{A} \times \epsilon$ are not publicly available, so we take the numbers of expected and observed events from ref. [3], along with the associated uncertainties, and convert these into model-dependent upper limits with a single implementation of the HistFitter framework [236] using a frequentist calculator and a one-sided profile likelihood test statistic (the LHC default). The results of this process are displayed in table 7.6. Note that we use signal regions 1 and 2 only, as our simplified HistFitter approach is inadequate for handling the very low numbers of events in signal regions 3 and 4. These upper limits, the mono-Z signal generation and the selection procedures are all validated through comparison of the ATLAS analysis limits on a variant of the tS model with our own limits on the same model, as described below.

m_χ [GeV]	M_{med} [GeV]	$g_{q\chi}^{95\%\text{CL}}$ (ATLAS)	$g_{q\chi}^{95\%\text{CL}}$ (this work)	Difference [%]
10	200	1.9	2.0	5.3
	500	2.8	3.2	14.3
	700	3.5	4.4	25.7
	1000	4.5	5.2	15.6
200	500	3.4	4.0	17.6
	700	4.2	4.5	7.1
	1000	5.2	5.3	1.9
400	500	5.5	5.7	3.6
	700	6.1	6.5	6.6
	1000	7.2	7.4	2.8
1000	1200	23.3	24.1	3.4

Table 7.7: Comparison of the 95% C.L. upper limit on $g_{q\chi}$ from this work and from the ATLAS mono-Z analysis [3]. The limits are for a variant of the t-channel scalar mediator model with Majorana DM for the process $pp \to \chi\bar{\chi} + Z(\to e^+e^-/\mu^+\mu^-)$.

Validation of the leptonic mono-Z channel

The ATLAS mono-Z results include an upper limit on the coupling $g_{q\chi}$ for a t-channel SiM similar to our tS model, and so it is this model which we use to validate our signal generation and selection procedures. Note that the following differences exist: the ATLAS model includes just two mediators (up- and $down$-type) where we consider six, the DM particle is taken to be Majorana where we assume Dirac, and the couplings $g_{t,b\chi}$ are set to zero where we have universal coupling to all three quark generations. The validation model therefore has increased mediator widths (which have been demonstrated not to impact the model behaviour in the mono-boson channel), and loses the very small contribution to the cross section from third-generation quarks; these are sub-leading order effects.

Table 7.7 shows the 95% C.L. upper limits on $g_{q\chi}$ that we calculate using our own generation procedure (and the values in table 7.6), compared with the limits taken from the ATLAS analysis. Also shown is the difference as a percentage of the ATLAS limit. We see reasonable agreement; most of the 11 points in parameter space are within 10% of the ATLAS limits, and all are within 26%. Additionally, our results are consistently more conservative, which again is to be expected given the less sophisticated nature of our generation procedure. As in the case of

the mono-jet validation, the differences stem from the use of p_{T} smearing applied to the leptons (rather than a full reconstruction simulation) and from the simplified treatment of systematics; we also obtained $\sigma \times \mathcal{A} \times \epsilon$ independently using the publically-available results.

7.3.3 The hadronic mono-W/Z channel

The ATLAS mono-W/Z + $E_{\mathrm{T}}^{\mathrm{miss}}$ search [238] was aimed at constraining the spin-independent effective operators C1, D1, and D5, and the spin-dependent operator D9. The search was originally designed to exploit what was thought to be the constructive interference of W boson emission from up-type and down-type quarks with opposite-sign operator coefficients, leading to DM production wherein the mono-W channel is dominant. Recent studies [252] have revealed this scenario to violate gauge invariance and so we ignore it in this analysis.

The mono-W/Z event selection is carried out as follows. Large-radius jets are selected using a mass-drop filtering procedure (see secs. 7.2.1 and 4.3.3) to suppress non-W/Z processes. Events are required to contain at least one large-R jet with $p_{\mathrm{T}} >$ 250 GeV, $|\eta| <$ 1.2 and a mass, m_{jet}, within a 30-40 GeV window of the W/Z mass (i.e. $m_{\mathrm{jet}} \in [50, 120]$ GeV). In order to reduce the $t\bar{t}$ and multijet backgrounds, a veto removes events containing a small-R jet with $\Delta\phi(\mathrm{jet}, \vec{E}_{\mathrm{T}}^{\mathrm{miss}}) < 0.4$, or containing more than one small-R jet with $p_{\mathrm{T}} >$ 40 GeV, $|\eta| <$ 4.5, and ΔR(small-R jet, large-R jet)> 0.9. Electrons, muons and photons are vetoed if their p_{T} is larger than 10 GeV and they lie within $|\eta| <$ 2.47 (electrons), 2.5 (muons), 2.37 (photons). Two signal regions are defined with $E_{\mathrm{T}}^{\mathrm{miss}} > 350$ GeV and $E_{\mathrm{T}}^{\mathrm{miss}} > 500$ GeV. These details are summarised in the right-hand column of table 7.3.

The ATLAS analysis used a shape-fit of the mass distribution of the large-R jet to set exclusion limits, however we use the published numbers of SM background and observed data events (along with the associated uncertainties) to convert to upper limits on new physics events using the HistFitter framework. For the $E_{\mathrm{T}}^{\mathrm{miss}} > 500$ GeV signal region, we obtain the limits shown in table 7.8; these are validated, along with the signal generation and selection process, as described below. We do not consider the first signal region with $E_{\mathrm{T}}^{\mathrm{miss}} > 350$ GeV in the recasting procedure, since the cut-and-count limits extracted could not be convincingly validated. The high $E_{\mathrm{T}}^{\mathrm{miss}}$ signal region was found to be optimal for most operators studied by the ATLAS analysis.

Signal Region	$E_{\mathrm{T}}^{\mathrm{miss}}$ threshold [GeV]	$\sigma \times \mathcal{A} \times \epsilon$ [fb]
SR2	500	1.35 (1.34)

Table 7.8: The ATLAS mono-W/Z $E_{\mathrm{T}}^{\mathrm{miss}}$ signal region considered in this work and corresponding observed (expected) model-independent upper limits on $\sigma \times \mathcal{A} \times \epsilon$ at 95% confidence level, where those limits have been adapted from the numbers of expected and observed events in ref. [238] using HistFitter.

EFT operator	m_χ [GeV]	$\Lambda^{90\%\mathrm{CL}}$ [GeV] (ATLAS)	$\Lambda^{95\%\mathrm{CL}}$ [GeV] (this work)	Difference [%]
D9	1	2400	2221	7.4
D5	1	570	499	12.5

Table 7.9: Comparison of the 95% C.L. lower limits on Λ from this work and from the ATLAS mono-W/Z analysis [238]. The limits correspond to the process $pp \to \chi\bar{\chi} + W/Z\ (\to jj)$.

Validation of the hadronic mono-W/Z channel

The event generation and selection procedures for the mono-W/Z channel are validated via reproduction of the ATLAS limits on Λ for the D5 and D9 effective operators with $m_\chi = 1$ GeV, using the upper limits on $\sigma \times \mathcal{A} \times \epsilon$ listed in table 7.8. We see agreement within 12.5% and 7.4% respectively, where the ATLAS limits are consistently stronger, as shown in table 7.9. The relative sizes of the discrepancies are expected given that only low-$E_{\mathrm{T}}^{\mathrm{miss}}$ limits are available for the D5 operator while we use the high-$E_{\mathrm{T}}^{\mathrm{miss}}$ signal region in our recast. Note that a general discrepancy of a few percent is expected for both operators for the reasons discussed in secs. 7.3.1 and 7.3.2, and also because we use a cut-and-count approach while the ATLAS limits are extracted using a shape-fit. Furthermore, the ATLAS limits are quoted at 90% C.L. while ours are calculated at 95% C.L.

7.4 Results

7.4.1 Limits on the couplings $\sqrt{g_q g_\chi}$

The 95% confidence level upper limits on the sV and sA model coupling combination $\sqrt{g_q g_\chi}$, and the tS model coupling $g_{q\chi}$, obtained from each of the mono-X channels, are presented in figs. 7.3–7.8. These quantities were evaluated as described in sec. 7.2.2 (including statistical and systematic uncertainties), and corre-

spond to the best limits of each signal region tested.

In each plot, limits are shown ranging from <0.01 to the upper perturbative limit for each coupling, 4π; where a limit was calculated to be larger than this, the limit is considered meaningless and the region is coloured grey. The white (hatched) regions coincide with those mass points which yield an initial (final) value of $\sqrt{g_q g_\chi}$ or $g_{q\chi}$ which fails to satisfy $\Gamma < M_{\mathrm{med}}/2$. (We observe that values for which the width is just within our upper validity bound of $M_{\mathrm{med}}/2$ may be pushed over into the invalid range with the addition of new particles, not considered here, which would serve to increase the mediator width.) When g_χ/g_q = 0.2, only the mono-jet channel produces limits which survive this requirement, and so these are shown separately in fig. 7.7.

Detailed comments specific to each channel are provided below, however some trends are channel-independent. For the sV model, strong limits exist when $M_{\mathrm{med}} > 2m_\chi$ as the mediator can go on-shell, thereby enhancing the cross section. The sA model limits are generally similar to the sV model limits except in the region corresponding to $m_\chi \gtrsim \sqrt{4\pi} M_{\mathrm{med}}/g_\chi^{\mathrm{gen}}$ where g_χ^{gen} is the DM coupling used at the generator level. We remove this region in the sA model to avoid violating perturbative unitarity, which can lead to an unphysical enhancement of the cross section when the DM mass is much larger than the mediator mass [35–37]. The upper limit on $\sqrt{g_q g_\chi}$ is relatively constant across values of g_χ/g_q, as is expected when the coupling (and hence the width) has been demonstrated to have little effect on kinematic behaviour (see sec. 7.1.3), and using the assumptions of eq. 7.1. As the ratio increases, points in the region $M_{\mathrm{med}} > m_\chi$ disappear as the initial value, $g_q = 1$, leads to a failure of the width condition. However, one could easily choose a smaller initial value of g_q to recover these points, and we suggest that the limits in this region would be quite similar to those seen in the g_χ/g_q = 0.2 and 0.5 cases.

The constraints on the coupling strength are weaker when m_χ or M_{med} is large (>100 GeV) owing to suppression of the cross section. In this region, the constraints are expected to improve at higher centre-of-mass energies. For small DM masses with an off-shell mediator, the $E_{\mathrm{T}}^{\mathrm{miss}}$ distribution is softer, therefore results in this region of parameter space are limited by statistical uncertainties associated with the tail-end of the distribution. This region of parameter space would benefit from further optimisation of event selection in analyses aimed at the study of simplified models, as we expect to see in the upcoming Run II results.

These mono-X searches are complementary to direct searches for the mediator via di-jet resonances [130, 253–255]. These have been used to study SiMs in, for example, refs. [26, 36, 41]. Di-jet studies search for the signature of a direct mediator decay into standard model particles, generally assuming a narrow res-

onance. These constraints can be stronger than mono-X constraints, particularly when the width is small and when the coupling to quarks is large relative to the coupling to DM. Mono-X searches however have the advantage for larger values of g_χ/g_q and smaller mediator masses, since smaller g_q couplings can avoid the di-jet constraints.

We now examine channel-specific trends.

Mono-jet channel

The mono-jet channel upper limits on the coupling combination $\sqrt{g_q g_\chi}$ for the sV and sA models are displayed in the left-hand column of figs. 7.3-7.6, for $g_\chi/g_q =$ 0.5, 1, 2 and 5 respectively (where the ratio of 5 is only shown for the sV model, due to a lack of meaningful results in the sA model). The $g_\chi/g_q = 0.2$ case is shown separately in fig. 7.7, as these limits are only meaningful within this channel.

As expected, the mono-jet channel produces the strongest coupling limits for both s-channel models, which are better than those from the next-best mono-Z channel by a factor of a few. For these models, the weakest limits result for large m_χ or large M_{med}, and in fact are so weak that they are pushed into the region of invalidity where $\Gamma > M_{\text{med}}/2$. Although the acceptance is considerably higher when both m_χ and M_{med} are large compared to low masses, the cross section is sufficiently small so as to nullify any gain. Within the valid region ($m_\chi \in [1, 100]$ GeV and $M_{\text{med}} \in [1, 200]$ GeV), the limit on $\sqrt{g_q g_\chi}$ generally ranges from 0.1 to 0.7, with a handful of on-shell masses reaching a limit of $\sim$0.05 in the large g_χ/g_q case. In the large g_χ/g_q scenario, limits for $m_\chi = 1000$ GeV start to become valid; where $\sqrt{g_q g_\chi}$ remains constant but g_χ/g_q increases, the value of g_q is pushed downward and so the width, which is dominated by decays to SM particles, decreases with respect to M_{med}.

The uncertainties on the limits for both s-channel models are dominated by contributions from the matching scale at acceptance-level, and generally range from $\sim$5% to 46%.

Mono-Z(lep) channel

The simplicity of the mono-Z channel relative to the mono-jet channel, and the ease of signal simulation at MADGRAPH level allowed us to study a finer granularity of points in the mass parameter space. The resulting limits on the sV and sA models are shown in the central column of figs. 7.3-7.6. While the behaviour of the limits as g_χ/g_q is varied is similar to that within the mono-jet channel, the mono-Z limits are overall weaker by a factor of a few.

The total relative uncertainties on $\sqrt{g_q g_\chi}$ for the s-channel models are generally within 10%, but can range up to 80% in a few cases where m_χ is small; they are in general split equally between statistical and systematic contributions.

The advantage of the mono-boson channels is in the study of the tS model; since this was not included in the mono-jet channel the strongest limits are obtained with the mono-Z analysis, and are shown in the left-hand side of fig. 7.8. Note that, in comparison to the s-channel models, the limits have weakened by a factor of 10. This is the result of an orders-of-magnitude weaker cross section and the inability of the mediator to go on-shell in this channel. We find stronger limits for smaller m_χ and M_{med} masses, where larger cross sections compensate for lower acceptances at these points. Overall, the uncertainties contribute less than 10%.

Mono-W/Z(had) channel

The limits on the couplings of the sV, sA and tS models, obtained within the mono-W/Z channel, are shown in the right-hand column of figs. 7.3-7.8. This channel was included for comparison with the leptonic mono-Z channel in particular, but a coarser selection of masses was chosen as the limits were initially found to be somewhat weaker. Additionally, further estimates were made: a) as the kinematic behaviour is reasonably independent of the couplings, a single acceptance was found for each (m_χ, M_{med}) combination and applied to each value of g_χ/g_q, and b) complete systematic uncertainties were generated for a subset of masses and compared to those from the mono-Z channel, then from this comparison the mono-Z systematic uncertainties were multiplied by 2 and applied to the mono-W/Z limits. As a result, the limits obtained in this channel are not intended to be rigorously quantitative; rather, they are used to indicate qualitatively how the channel compares.

The ATLAS mono-W/Z analysis (and in particular the higher $E_{\mathrm{T}}^{\mathrm{miss}}$ signal region) was not optimised for a SiM interpretation, and much of the parameter space produced insignificant numbers of events passing the event selection, with up to 200 thousand events generated. Generally, the limits are a factor of a few weaker than those from the mono-Z channel, which is both consistent with the limits on the EFT models studied in the ATLAS analyses, and expected following our use of a cut-and-count interpretation, rather than a shape analysis, of the mono-W/Z public results.

In some cases the limits become comparable with the mono-Z channel, suggesting that more statistics and an improved treatment of systematic uncertainties would bring these closer in line with that channel.

Overall, the uncertainties from this channel lie within 5–50%, most of the time being within 10–30%. Generally, both statistical and systematic uncertainties contribute in a similar manner. A few points are clearly limited by the generated statistics, resulting in a statistical error of up to 90%. Points with high m_χ and low M_{med} tend to have larger systematic uncertainties.

7.4.2 Comparison with relic density constraints

This section and that below describe work performed by T. Jacques in collaboration with the author.

In figs. 7.3–7.8 we show lines where the constraint on the coupling corresponds to the coupling strength that would reproduce the correct DM relic density if DM is a thermal relic of the early universe. For points diagonally above and to the left of the solid purple line, the LHC constraints naively rule out the couplings leading to the correct relic density. Below and to the right of this line the relic density coupling is still allowed. In some cases the intercept does not pass through a significant number of data points surviving the quality criteria outlined in previous sections. In these cases the line is not shown.

The relic density for a WIMP was discussed in sec. 2.2.2; the approach is summarised again below, with an alternative formalism that was used in this work. The measured abundance is approximately related to the unknown self-annihilation cross section via:

$$\Omega_{\text{DM}}h^2 \simeq \frac{2 \times 2.4 \times 10^{-10}\,\text{GeV}^{-2}}{\langle\sigma v\rangle_{\text{ann}}}. \tag{7.4}$$

This is used with measurements of the DM abundance by Planck, $\Omega^{\text{obs}}_{\text{DM}}h^2 = 0.1199 \pm 0.0027$ [256], to find $\langle\sigma v\rangle_{\text{ann}} \simeq 4.0 \times 10^{-9}$ GeV^{-2} for thermal relic DM.

This relation is only approximately accurate, and so we use the micrOMEGAs code [257] to determine the coupling strength leading to the correct relic density for each model. This technique was verified against the semi-analytic technique outlined in e.g. ref. [258].

If the DM mass lies at the electroweak scale, the thermal relic scenario provides a natural explanation for the observed DM density. The coupling strengths leading to the correct relic density are therefore a natural benchmark with which to compare constraints from collider (and indeed direct detection) searches. However the relic density couplings should by no means be regarded as serious constraints. If DM is not produced thermally or there is an unknown effect which modifies the evolution of the density with temperature, then eq. 7.4 breaks down. Additionally, in the scenario where we assume DM to be a thermal relic, we ig-

nore the possibility of there being other annihilation channels and other beyond-SM particles contributing to the DM abundance, which, if taken into account, would also invalidate eq. 7.4.

7.4.3 Comparison with direct detection constraints

In figs. 7.3–7.8 we also show the intercept line where constraints from direct detection experiments are equivalent to our mono-X constraints. Below and to the right of the dashed purple line, direct detection constraints are stronger while above and to the left of this line, the LHC gives the stronger limit. As with the relic density contours, we do not show the intercept where it does not pass through sufficient valid data points. We use the toolset from ref. [259] to convert the strongest available direct detection constraints, which are from the LUX 2013 dataset [86], onto constraints on our models.

Compared to direct detection, the mono-X collider limits perform relatively better for the sA model than for the sV model. This is because the axial-vector coupling leads to a suppressed scattering rate in direct detection experiments while collider searches are relatively insensitive to the difference between the vector and axial-vector couplings. In the non-relativistic limit, the tS model leads to a mix of both suppressed and unsuppressed operators.

The direct detection constraints assume that the DM candidate under consideration contributes 100% of the local DM density, while the mono-X constraints make no assumptions about either the local DM density or overall abundance. In this sense the mono-X limits remain useful even in those regions of parameter space where they are not as strong as those from direct detection.

7.5 Reinterpretation summary

In this chapter we examined a set of three simplified dark matter models, extracting constraints from ATLAS Run I mono-X plus missing energy searches featuring the associated production of a mono-jet, mono-$Z(\rightarrow$ leptons), or mono-$W/Z(\rightarrow$ hadrons). We explored a parameter space where both the DM and mediator masses span $\mathcal{O}$(GeV)–$\mathcal{O}$(TeV), and considered ratios of g_χ/g_q of 0.2, 0.5, 1, 2 and 5 in the s-channel models.

Rather than setting limits in the $M_{\rm med} - m_{\rm DM}$ plane for a fixed value of the coupling strength, we instead constrained the coupling strength as a function of both $M_{\rm med}$ and $m_{\rm DM}$ in a 3D plane. Whilst this approach necessitates the introduction of some approximations, it also allows for a thorough examination of the interplay between the DM production cross section and the free parameters of

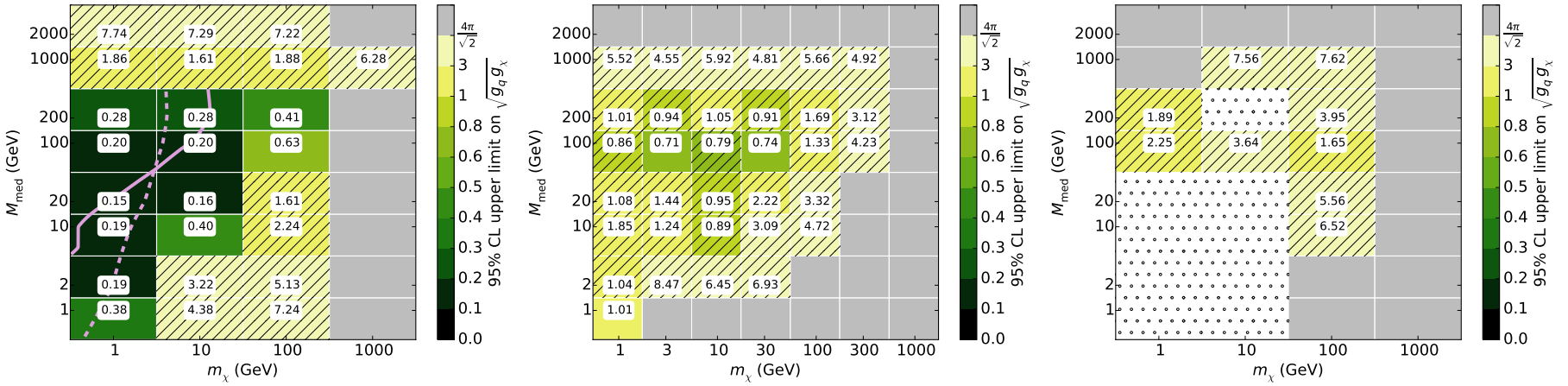

(a) sV model, $g_\chi/g_q = 0.5$, mono-jet channel. (b) sV model, $g_\chi/g_q = 0.5$, mono-Z channel. (c) sV model, $g_\chi/g_q = 0.5$, mono-W/Z channel.

(d) sA model, $g_\chi/g_q = 0.5$, mono-jet channel. (e) sA model, $g_\chi/g_q = 0.5$, mono-Z channel. (f) sA model, $g_\chi/g_q = 0.5$, mono-W/Z channel.

Figure 7.3: Upper limits on the coupling for the s-channel models in the mono-jet (left), mono-Z (centre) and mono-W/Z (right) channels, for g_χ/g_q = 0.5. The grey region represents the parameter space where no meaningful limit was obtained. The hatched region represents a limit which leads to a width greater than $M_{\text{med}}/2$, so the validity of the calculation begins to fail. The dotted region represents parameter space where insufficient statistics were available. The purple dashed line shows the threshold where direct detection constraints become stronger than the mono-X constraint. Similarly the solid purple line shows where relic density constraints become stronger than mono-X constraints. See the text for further details.

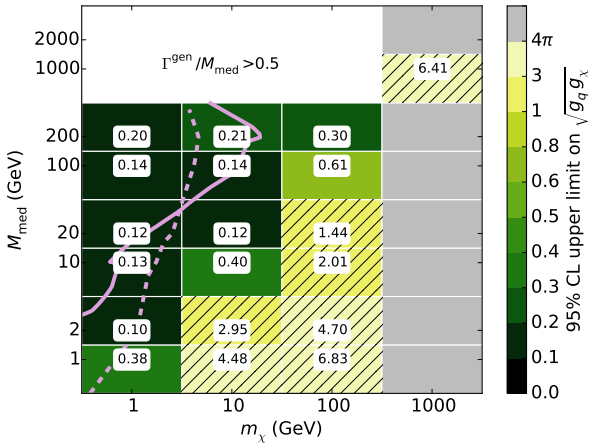

(a) sV model, $g_\chi/g_q = 1$, mono-jet channel.

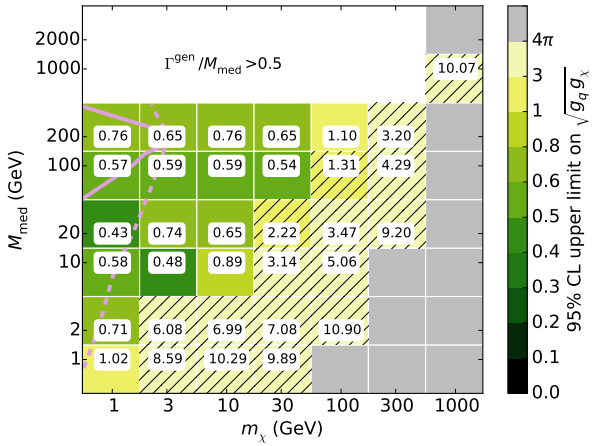

(b) sV model, $g_\chi/g_q = 1$, mono-Z channel.

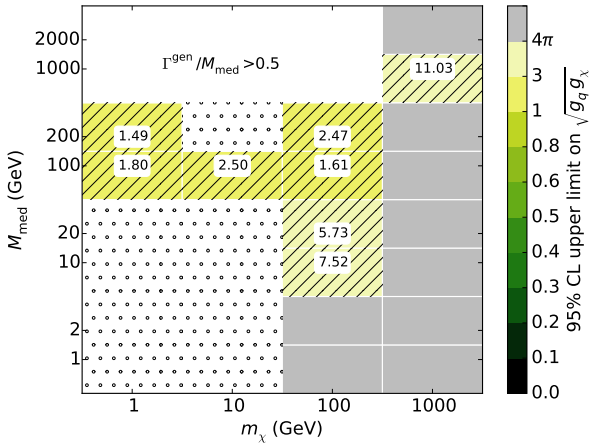

(c) sV model, $g_\chi/g_q = 1$, mono-W/Z channel.

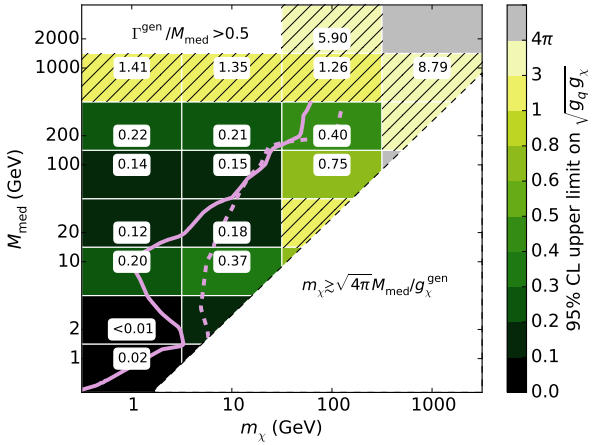

(d) sA model, $g_\chi/g_q = 1$, mono-jet channel.

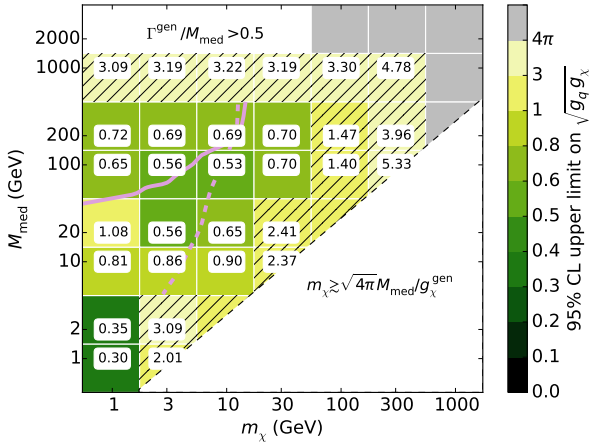

(e) sA model, $g_\chi/g_q = 1$, mono-Z channel.

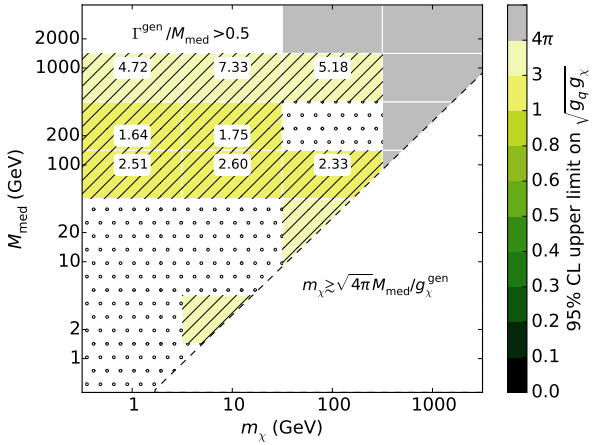

(f) sA model, $g_\chi/g_q = 1$, mono-W/Z channel.

Figure 7.4: Upper limits on the couplings for the s-channel models in the mono-jet (left), mono-Z (centre) and mono-W/Z (right) channels, for $g_\chi/g_q = 1$. Refer to fig. 7.3 for details.

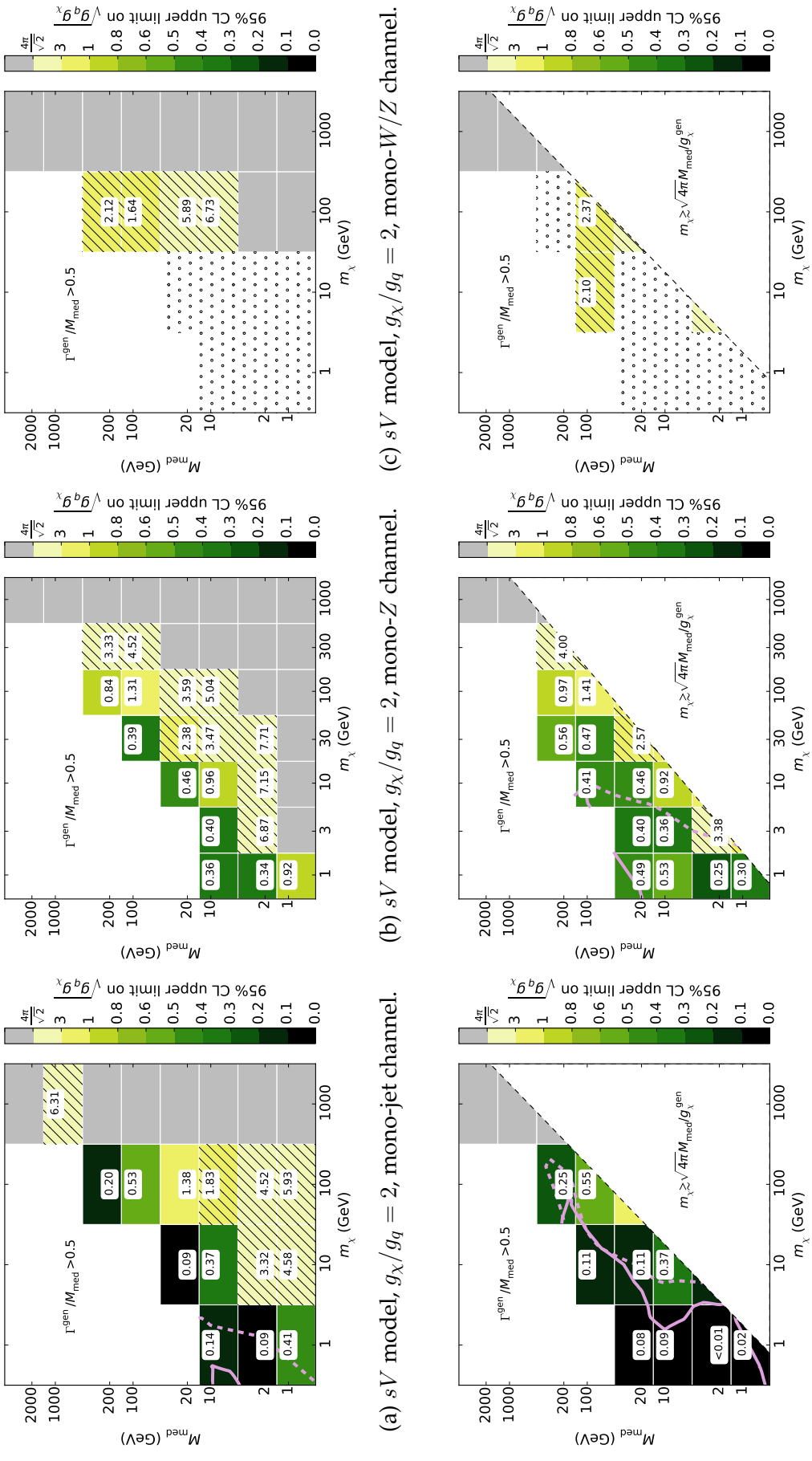

(a) sV model, $g_\chi/g_q = 2$, mono-jet channel. (b) sV model, $g_\chi/g_q = 2$, mono-Z channel. (c) sV model, $g_\chi/g_q = 2$, mono-W/Z channel.

(d) sA model, $g_\chi/g_q = 2$, mono-jet channel. (e) sA model, $g_\chi/g_q = 2$, mono-Z channel. (f) sA model, $g_\chi/g_q = 2$, mono-W/Z channel.

Figure 7.5: Upper limits on the coupling for the s-channel models in the mono-jet (left), mono-Z (centre) and mono-W/Z (right) channels, for $g_\chi/g_q = 2$. Refer to fig. 7.3 for details.

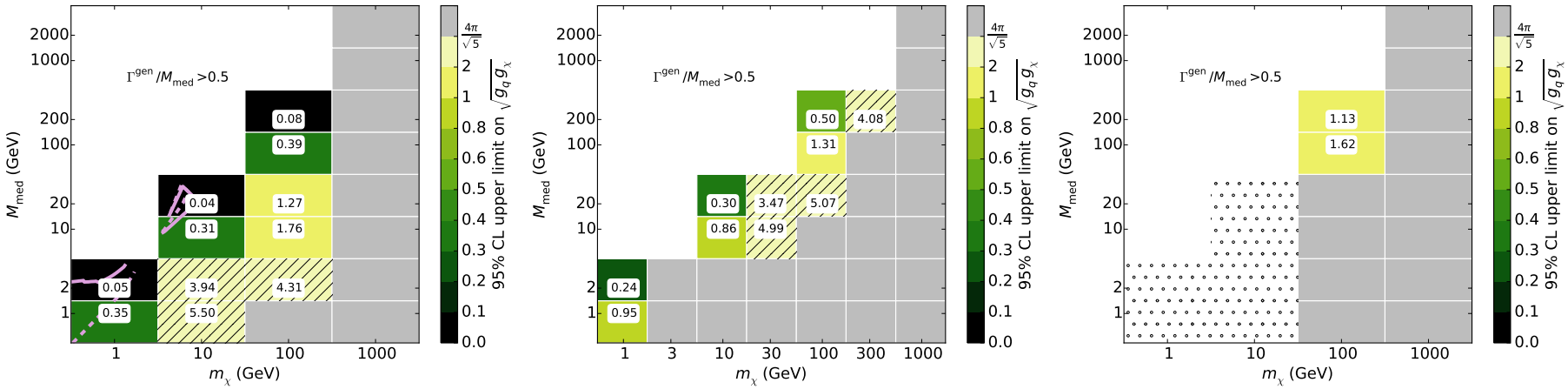

(a) sV model, $g_\chi/g_q = 5$, mono-jet channel. (b) sV model, $g_\chi/g_q = 5$, mono-Z channel. (c) sV model, $g_\chi/g_q = 5$, mono-W/Z channel.

Figure 7.6: Upper limits on the coupling for the sV model in the mono-jet (left), mono-Z (centre) and mono-W/Z (right) channels, for $g_\chi/g_q = 5$. Refer to fig. 7.3 for details.

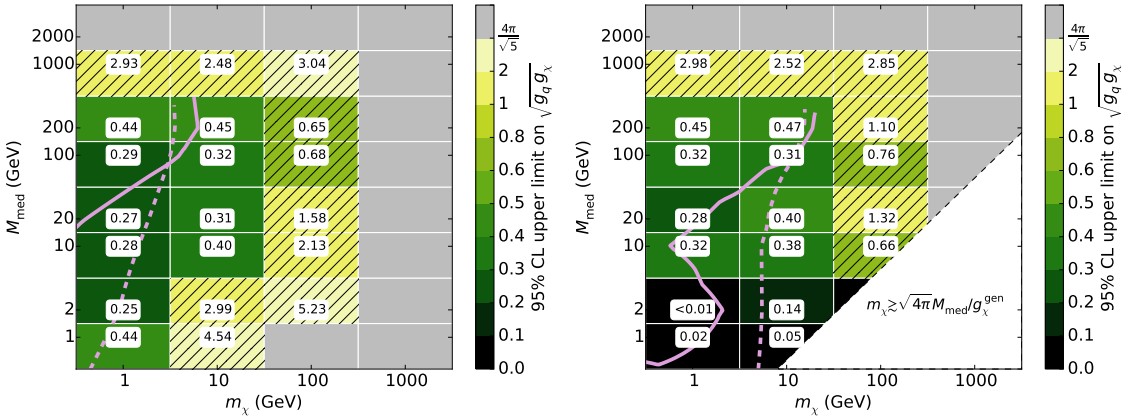

(a) sV model, $g_\chi/g_q = 0.2$, mono-jet channel.

(b) sA model, $g_\chi/g_q = 0.2$, mono-jet channel.

Figure 7.7: Upper limits on the coupling for the s-channel models in the mono-jet channel, for $g_\chi/g_q = 0.2$. Refer to fig. 7.3 for details.

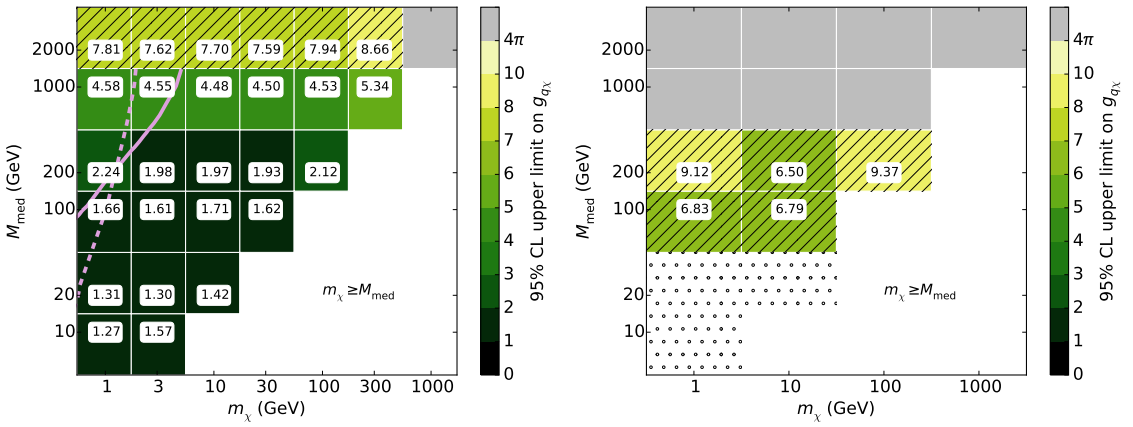

(a) tS model, mono-Z channel.

(b) tS model, mono-W/Z channel.

Figure 7.8: Upper limits on the coupling $g_{q\chi}$ for the t-channel model in the mono-Z (left) and mono-W/Z (right) channels. Refer to fig. 7.3 for details.

the models.

As expected, the mono-jet channel was found to yield the strongest limits on vector and axial-vector SM and DM couplings to a vector mediator exchanged in the s-channel. This channel is also found to perform well for small values of g_χ. The limits obtained in the mono-Z channel, in comparison, are generally weaker by a factor of a few, while the mono-W/Z results are weaker again. This is partly due to our conservative estimations of the systematic uncertainties and partly due to limited statistics resulting from a harder $E_{\mathrm{T}}^{\mathrm{miss}}$ selection cut. The width effects associated with the t-channel exchange of an $SU(2)$ doublet scalar mediator are observed to vanish in both the mono-Z and mono-W/Z channels, greatly simplifying the analysis of this model and confirming these as straightforward and competitive channels for future collider DM detection.

Where the axial-vector model is not excluded by perturbative unitarity requirements, we find the coupling limits to be on par with those of the vector model within each analysis channel. Weaker limits are found for the t-channel model, a result of cross section suppression not present in the s-channel models.

Finally, we compared our limits to constraints from relic density and direct detection; although each search is subject to a different set of assumptions, this demonstrates the complementarity and impressive reach of simplified models as a tool for the interpretation of collider DM searches.

Chapter 8

The ATLAS mono-W/Z (hadronic) analysis

The ATLAS mono-$W/Z(\rightarrow jj)$ + $E_{\mathrm{T}}^{\mathrm{miss}}$ search for dark matter (DM) produced one of the first publicly released DM results from Run II of the Large Hadron Collider (LHC). The preliminary result from this search, using the first 3.2 fb^{-1} of data collected at 13 TeV, was released as a conference note (see ref. [5]). This chapter closely follows this reference, as well as ATLAS-internal details in ref. [6].

The previous chapter described a recasting of the constraints from three ATLAS Run I mono-X + $E_{\mathrm{T}}^{\mathrm{miss}}$ analyses, one of which was the mono-W/Z search, where the radiated W or Z boson decays to hadrons. This chapter follows the ATLAS analysis in Run II for the same signal, where a hadronically-decaying electroweak (EW) boson is produced back-to-back with a large amount of missing transverse momentum (representing the invisible DM). The alternative, a leptonic decay of the boson, is described in chapter 6 in the case of the mono-$Z(\ell\ell)$, or in ref. [260] in the case of mono-$W(\ell\nu)$. W and Z bosons decay to hadrons 67% and 70% of the time respectively [48], so while the advantage of the relative simplicity of leptons is lost, a gain is made in statistics.

The hadronic decay of the W and Z bosons is to a pair of quarks, which then hadronise to form two jets depositing their energy in the calorimeter. The masses of the bosons are only separated by $\sim$11 GeV, so the mass peaks in a distribution of the total mass of the produced jets would overlap, making it difficult to distinguish a hadronic W from a hadronic Z. Since the signal in each case is so similar, an analysis is therefore designed which searches for a signal of *either* boson.

Such an analysis does not look for two jets + $E_{\mathrm{T}}^{\mathrm{miss}}$, however; the background from quantum chromodynamics (QCD) processes would be very large, and instead we can exploit the common origin of the jets. The jets from the decay of the boson, which is often boosted as it is required to be back-to-back with a large

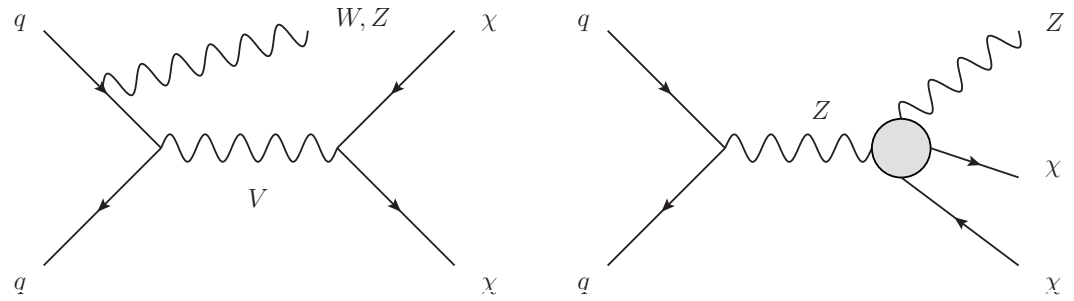

Figure 8.1: A mono-boson process from the sV simplified model (left) and $ZZ\chi\bar{\chi}$ contact operator (right) studied in the preliminary mono-W/Z analysis.

amount of $E_{\mathrm{T}}^{\mathrm{miss}}$, are usually quite collinear and can be reconstructed as a single, large-radius jet (rather than using a narrow-jet algorithm which best captures QCD jets). Additionally, the large-R jet from a hadronically-decaying EW boson typically has a two-pronged substructure; the energy is grouped around two axes within the jet, which wouldn't necessarily be resolvable as two separate narrow jets. The considerable advances by many researchers that have been made in the identification and tagging of hadronically-decayed bosons are exploited in this analysis, and will be described in a later section.

The analysis described in this chapter and in ref. [5] is a preliminary study, and the mono-W/Z analysis remains an on-going work, being performed by other members of the ATLAS mono-W/Z group. Only one simplified model recommended by the Dark Matter Forum Report [15] is included, with the expectation that others will be studied at a later time. The included simplified model is the sV model, described by eq. 3.12 in sec. 3.3, where a vector mediator couples to a quark pair and a DM pair, and is exchanged in the s-channel. As both the mediator and the DM are uncharged, uncoloured Standard Model (SM) singlets, a W or Z boson can only be radiated from one of the initial-state quarks to produce the signal. This process is shown in fig. 8.1(a). As has been discussed previously, the strongest limits for this model are expected to be obtained in the mono-jet channel, however a combination of limits from multiple channels is desirable to improve on the limit from any single channel, and so the simplified models are recommended to be included in all available analyses.

A 7-dimension $ZZ\chi\bar{\chi}$ model, discussed in sec. 3.2, is also included in this analysis; it couples the DM directly to a Z boson via a contact interaction. As opposed to the simplified model, which is most strongly constrained through the mono-jet channel, a mono-Z channel is the optimum way to hunt for the $ZZ\chi\bar{\chi}$ model. The mono-Z signal process is depicted in fig. 8.1(b).

The analysis uses a combined profile likelihood fit [261] in a set of signal and control regions to constrain the background estimations consistently across all regions, and to extract the signal strength (an overall normalisation on the signal, denoted μ). The input to this fitting procedure is the standard $E_{\mathrm{T}}^{\mathrm{miss}}$ in the signal region (SR), and a 'modified $E_{\mathrm{T}}^{\mathrm{miss}}$', also written as $E_{\mathrm{T,\,no\,}\mu}^{\mathrm{miss}}$ and calculated as the vector sum of the $E_{\mathrm{T}}^{\mathrm{miss}}$ and the p_{T} of all muons, which is obtained in each control region (CR). This variable will be described in further detail in sec. 8.2.

The remainder of the chapter will proceed as follows. The data and simulated SM background and signal samples will first be described in sec. 8.1. The object definitions and event selection are explained in secs. 8.2 and 8.3 respectively. The background estimations are covered in sec. 8.4, followed by the systematic uncertainty estimations in sec. 8.5. The profile likelihood method and resulting limits are discussed in sec. 8.6.

The author's main contribution to this work was in the two 1-lepton control regions, and providing feedback on the development of the software framework and the analysis. Details of the rest of the analysis is provided for context, and to make sense of the final result, which is a limit on the signal strength of the DM models.

8.1 Data and simulated samples

8.1.1 Data sample

This analysis uses 3.2 fb^{-1} of physics data recorded by the ATLAS detector at $\sqrt{s}$ = 13 TeV during 2015. All data was collected with a 25ns spacing between proton bunches. As described in sec. 6.1.1, the list of all useable data samples from each data-taking period is known as a Good Runs List (GRL); the GRL used in this analysis was the ALL_GOOD_25NS list.[1]

Trigger choice and efficiency

Events are selected in both data and Monte Carlo (MC) using a trigger based on missing transverse momentum, known as the HLT_XE80 trigger. This trigger reconstructs the $E_{\mathrm{T}}^{\mathrm{miss}}$ by summing the energies of all calorimeter cells, where those energies are calibrated at the electromagnetic (EM) scale and satisfy $|E| > 2\sigma$ and $E > -5\sigma$ (where σ is the standard deviation of the cell noise); it then selects events where the trigger-level $E_{\mathrm{T}}^{\mathrm{miss}}$ is greater than 80 GeV. Notably, since muons

[1] https://twiki.cern.ch/twiki/bin/view/AtlasProtected/GoodRunListsForAnalysisRun2

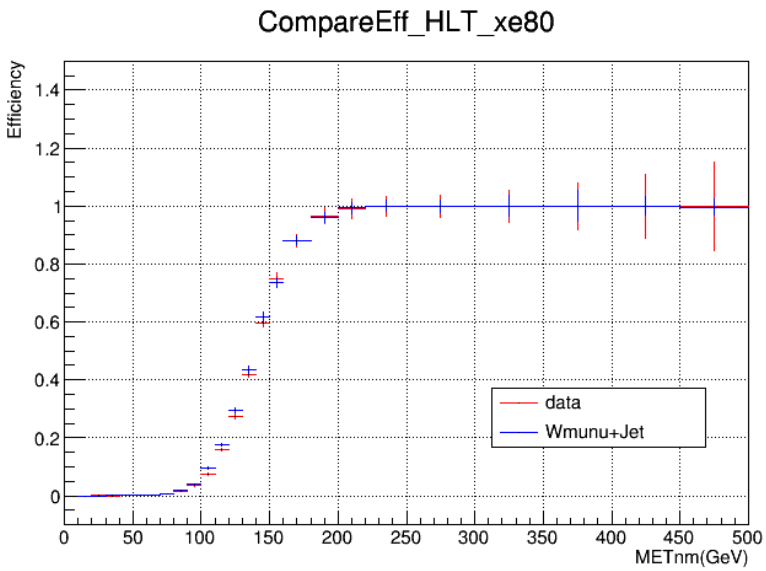

Figure 8.2: The trigger efficiency for events in data and W+jets Monte Carlo for events seeded with one lepton triggers. Taken from ref. [6].

tend to pass through the calorimeters before being absorbed in the muon spectrometer, this trigger-level $E_{\mathrm{T}}^{\mathrm{miss}}$ therefore does not take the muons into account, and so is similar to the modified $E_{\mathrm{T,\,no}\,\mu}^{\mathrm{miss}}$ mentioned in the introduction.

Because the trigger-level $E_{\mathrm{T}}^{\mathrm{miss}}$ does not include muon contributions, events that contain a muon can be used to measure the efficiency of the HLT_XE80 trigger. These events, collected by one of the muon triggers that are fully efficient for low muon p_{T} thresholds, allow the offline $E_{\mathrm{T}}^{\mathrm{miss}}$ to be reconstructed and summed with the p_{T} of all muons in the event; it can then be checked whether the HLT_XE80 trigger was passed, and the efficiency measured as a function of the modified $E_{\mathrm{T}}^{\mathrm{miss}}$. This procedure was performed with both data and the $W(\rightarrow \mu\nu)$+jets MC, and the efficiency turn-on curve is shown in fig. 8.2. The trigger is found to be fully efficient at $E_{\mathrm{T,\,no}\,\mu}^{\mathrm{miss}} \simeq 200$ GeV.

8.1.2 Signal samples

Points in parameter space for the sV and $ZZ\chi\bar{\chi}$ signal models were chosen for study based on the recommendations of the Dark Matter Forum Report for these models, and are listed for the sV model in tables 8.1 and 8.2, corresponding to the mono-Z and mono-W channels respectively, and for the $ZZ\chi\bar{\chi}$ model in table 8.3.

The matrix element for these signals was calculated with MADGRAPH5, and the showering and hadronisation processes were performed with PYTHIA8[2]. The NNPDF30_lo Parton Distribution Function (PDF) [262] was used, and the cross

[2]Refer to sec. 4.2.5 for an overview of the event simulation steps and software

sections (also listed in the tables) were calculated to leading order (LO) accuracy. In all sV cases, coupling values of g_q = 0.25 and g_χ = 1.0 were used, while the suppression scale for the Effective Field Theory (EFT) was set to Λ = 3 TeV.

The $E_{\mathrm{T}}^{\mathrm{miss}}$ distributions for the simplified model, assuming a $pp \to Z(\to jj) + \chi\bar{\chi}$ process, are shown in fig. 8.3. The $E_{\mathrm{T}}^{\mathrm{miss}}$ and leading jet pseudorapidity distributions for the $ZZ\chi\bar{\chi}$ model are shown in fig. 8.4.

8.1.3 Background samples

The main background process for the hadronic mono-W/Z analysis is $Z(\to \nu\nu)$+jets, where a large-R jet is reconstructed from one or more of the jets. Another major background results from $W(\to \ell\nu)$+jets events, where the charged lepton is not reconstructed, and together with the neutrino looks like a large amount of $E_{\mathrm{T}}^{\mathrm{miss}}$. Also included are $t\bar{t}$ events (where one t decays hadronically and the other leptonically), while single-top and diboson production processes make minor contributions to the SM background. Multi-jet events produced by QCD processes are generally quite poorly modeled by MC; while in this analysis the QCD background was simulated and compared against data, it was ultimately considered negligible following the application of 'anti-QCD' cuts to be described in sec. 8.3.

The simulation of the relevant backgrounds is described in detail below.

The Z+jets and W+jets MC samples were generated with the SHERPA 2.1.1 [147] generator, using the CT10 PDF [142]. Here, the matrix element for events with $\leq$ 2 partons was calculated at next-to-leading-order (NLO), while for three or four partons, a LO calculation was used. The events were then normalised to the next-to-next-to-leading-order (NNLO) cross section.

All top processes ($t\bar{t}$, Wt and s- and t-channel single-top production) were generated by POWHEG [148–151], with the CT10 and CTEQ6L1 [140] PDFs. Showering, hadronisation and the underlying event were all handled by PYTHIA6 [144]. The $t\bar{t}$ cross sections were generated to NNLO or next-to-next-to-leading-log (NNLL) accuracy [264], while single-top processes are at NLO.

The diboson backgrounds (WW, WZ and ZZ) were also generated with SHERPA and the CT10 PDF, with cross sections calculated at NLO. The multi-jet background was generated by PYTHIA8 [145], using the NNPDF23_lo PDF [265], and the cross section was calculated just to LO.

The background generation processes are summarised in table 8.4.

Model (process)	m_χ [GeV]	M_{med} [GeV]	Cross section [fb]
sV (mono-Z)	1	10	$1.18 \times 10^{+5}$
sV (mono-Z)	1	100	$4.78 \times 10^{+3}$
sV (mono-Z)	1	300	$6.49 \times 10^{+2}$
sV (mono-Z)	1	2000	1.64×10^{0}
sV (mono-Z)	10	10	$1.23 \times 10^{+3}$
sV (mono-Z)	10	100	$4.77 \times 10^{+3}$
sV (mono-Z)	10	10000	1.93×10^{-4}
sV (mono-Z)	50	10	$7.17 \times 10^{+1}$
sV (mono-Z)	50	95	$4.04 \times 10^{+2}$
sV (mono-Z)	50	300	$6.45 \times 10^{+2}$
sV (mono-Z)	150	10	6.90×10^{0}
sV (mono-Z)	150	295	$9.55 \times 10^{+1}$
sV (mono-Z)	150	1000	$2.48 \times 10^{+1}$
sV (mono-Z)	500	10	1.66×10^{-1}
sV (mono-Z)	500	995	5.23×10^{0}
sV (mono-Z)	500	2000	1.54×10^{0}
sV (mono-Z)	500	10000	1.10×10^{-4}
sV (mono-Z)	1000	10	6.46×10^{-3}
sV (mono-Z)	1000	1000	9.48×10^{-3}
sV (mono-Z)	1000	1995	3.30×10^{-1}

Table 8.1: The sV simplified model parameters, and associated cross sections, for the process $pp \to Z(jj)\chi\bar{\chi}$. In all cases, g_q = 0.25 and g_χ = 1.0.

Model (process)	m_χ [GeV]	M_{med} [GeV]	Cross section [fb]
sV (mono-W)	1	10	$3.38 \times 10^{+5}$
sV (mono-W)	1	100	$1.32 \times 10^{+4}$
sV (mono-W)	1	300	$1.79 \times 10^{+3}$
sV (mono-W)	1	2000	4.54×10^{0}
sV (mono-W)	10	10	$3.41 \times 10^{+3}$
sV (mono-W)	10	100	$1.32 \times 10^{+4}$
sV (mono-W)	10	10000	5.26×10^{-4}
sV (mono-W)	50	10	$1.99 \times 10^{+2}$
sV (mono-W)	50	95	$1.12 \times 10^{+3}$
sV (mono-W)	50	300	$1.78 \times 10^{+3}$
sV (mono-W)	150	10	$1.89 \times 10^{+1}$
sV (mono-W)	150	295	$2.63 \times 10^{+2}$
sV (mono-W)	150	1000	$6.80 \times 10^{+1}$
sV (mono-W)	500	10	4.57×10^{-1}
sV (mono-W)	500	995	$1.43 \times 10^{+1}$
sV (mono-W)	500	2000	4.27×10^{0}
sV (mono-W)	500	10000	2.98×10^{-4}
sV (mono-W)	1000	10	1.76×10^{-2}
sV (mono-W)	1000	1000	2.59×10^{-2}
sV (mono-W)	1000	1995	9.15×10^{-1}

Table 8.2: The sV simplified model parameters, and associated cross sections, for the process $pp \to W(jj)\chi\bar{\chi}$. In all cases, g_q = 0.25 and g_χ = 1.0.

Model (process)	m_χ [GeV]	Cross section [fb]
$ZZ\chi\bar{\chi}$ (mono-Z)	1	1.07×10^{-3}
$ZZ\chi\bar{\chi}$ (mono-Z)	10	1.07×10^{-3}
$ZZ\chi\bar{\chi}$ (mono-Z)	50	1.02×10^{-3}
$ZZ\chi\bar{\chi}$ (mono-Z)	150	8.39×10^{-4}
$ZZ\chi\bar{\chi}$ (mono-Z)	500	2.94×10^{-4}
$ZZ\chi\bar{\chi}$ (mono-Z)	1000	5.39×10^{-5}

Table 8.3: The $ZZ\chi\bar{\chi}$ EFT model parameters, and associated cross sections, for the process $pp \to Z(jj)\chi\bar{\chi}$. In all cases, Λ = 3 TeV.

SM process	Generator	Order of cross section	PDF
W+jets	SHERPA	NNLO	CT10
Z+jets	SHERPA	NNLO	CT10
$t\bar{t}$	POWHEG + PYTHIA6	NNLO + NNLL	CT10 + CTEQ6L1
single top ($Wt/s/t$-channel)	POWHEG + PYTHIA6	NLO	CT10 + CTEQ6L1
diboson (WW, WZ, ZZ)	SHERPA	NLO	CT10
multi-jet	PYTHIA8	LO	NNPDF23_lo

Table 8.4: Summary of the generation processes for all SM backgrounds.

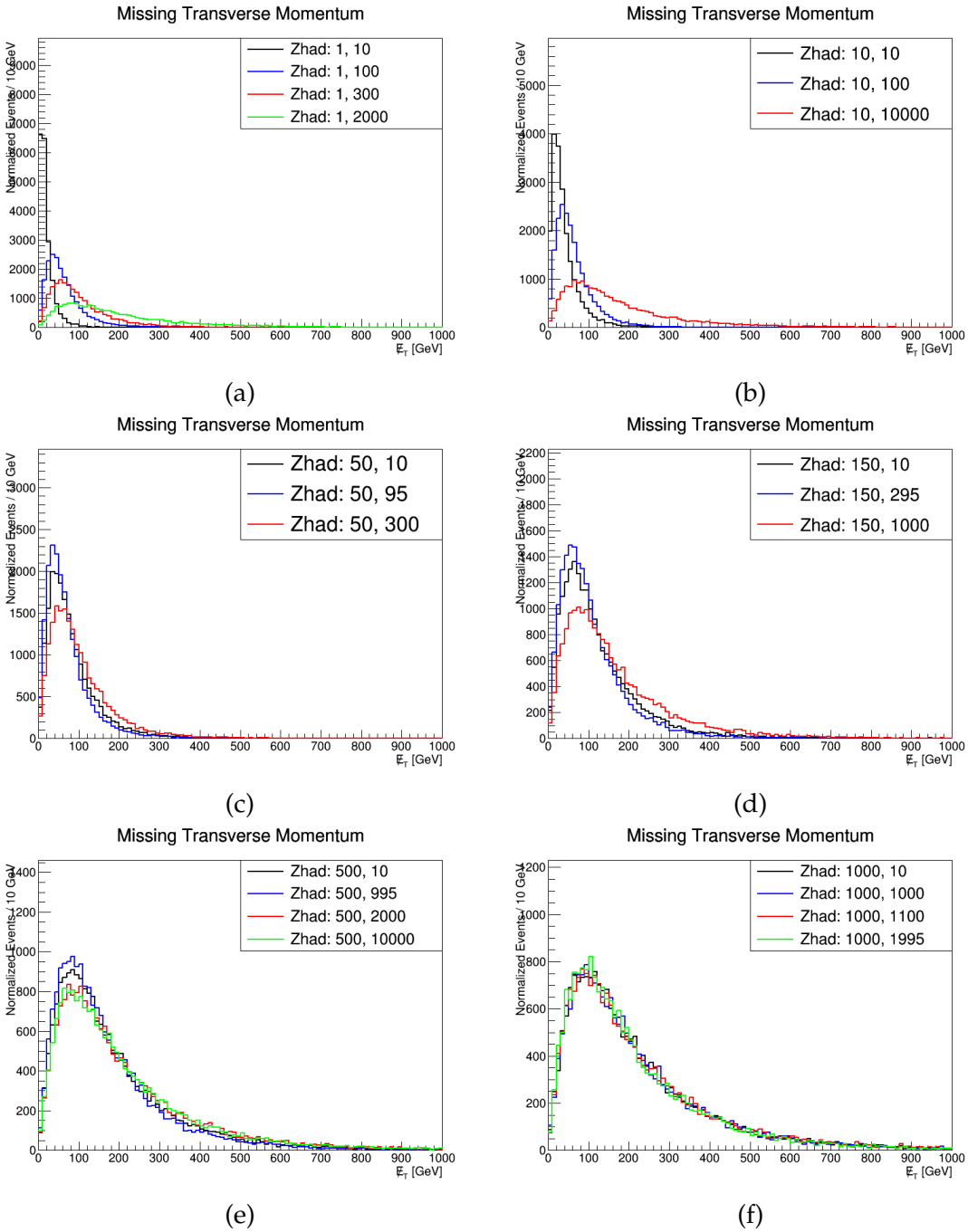

Figure 8.3: The $E_{\mathrm{T}}^{\mathrm{miss}}$ distributions at truth-level for the sV model produced via $pp \to Z(jj) + \chi\bar{\chi}$, for the set of masses listed in table 8.1. Similar distributions exist for the case of $pp \to W(\to jj) + \chi\bar{\chi}$, and so are not shown here. Taken from ref. [263].

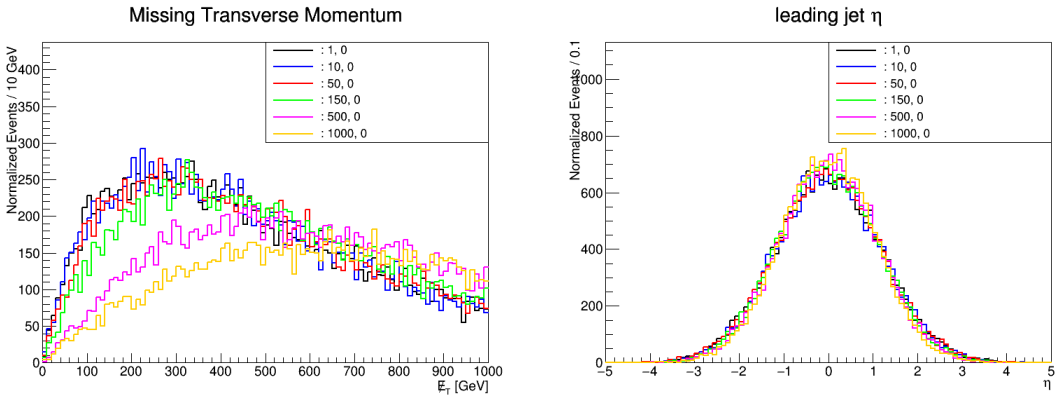

(a) (b)

Figure 8.4: The $E_{\mathrm{T}}^{\mathrm{miss}}$ and $\eta^{\text{leading jet}}$ distributions at truth-level for the dimension-7 $ZZ\chi\bar{\chi}$ models produced via $pp \to Z(jj) + \chi\bar{\chi}$, for the set of masses listed in tables 8.1 and 8.3. Similar distributions exist for the mono-W process in the sV model case, but are not shown here. Taken from ref. [263].

8.2 Object definitions

The object definitions for the mono-$W/Z(\to jj)$ analysis are summarised in this section.

8.2.1 Jets

Three jet definitions are used in the analysis, referred to as *large-R* jets, *narrow* jets and *track* jets, which serve to identify hadronically-decaying bosons, remove the multi-jet background, and separate the two 1-lepton control regions, respectively. They are described in detail below.

Large-R jets

In this analysis, the large-R jets in the signal model come from the decay of a boosted hadronically-decaying W or Z boson; these produce two jets (usually coming from the hadronisation of two light quarks from the $W/Z \to jj$ decay) that are quite collinear due to the boost of the boson, and so are generally reconstructed as a single, large-radius jet, with a 2-prong internal structure. The selection of the large-R signal jets is therefore designed to reflect this, as follows.

The large-R jets [186, 266] are initially reconstructed using the anti-k_{T} algorithm, with a radius parameter of R = 1.0; they are then groomed with a trimming procedure [187], which serves to reduce the impact of pileup, the underlying event and soft radiation by removing the energy deposited by these effects. The trimming process reclusters the constituents of the large-R jet using the k_{T} algorithm [180] and a subjet-radius of R_{sub} = 0.2, then removes subjets with a p_{T}

less than 5% of the original jet p_{T} (f_{cut} = 5%). The total four-vector of the resulting jet is obtained by summing the four-vectors of the constituents that remain following the trimming, and the calibration of the jet p_{T} and mass (to the Jet Energy Scale (JES) and Jet Mass Scale (JMS) respectively), as well as the substructure selection described below, are all performed *after* the jet has been trimmed.

This choice of jet produced by the clustering algorithm and grooming procedure is known as an `R2` jet, and it is a point of difference from the Run I mono-W/Z (hadronic) analysis, which used the Cambridge-Aachen (C/A) algorithm with R = 1.2 to cluster the jets, and a mass-drop filtering procedure to groom them. However, the choice for this Run II analysis was made on the basis of the recommendations of a study reported in ref. [266], which compared the different options for boosted boson identification, and which is discussed in further detail below. From hereon in this chapter, large-R jets are assumed to have undergone the grooming process, so `R2` and 'large-R' are used interchangeably.

The large-R jets are required to satisfy $p_{\mathrm{T}} > 200$ GeV (the mass calibration is only recommended for jets with transverse momenta above this value) and $|\eta| < 2.0$ (to ensure good overlap between the inner detector (ID) and hadronic calorimeter). They are then subjected to a tagging algorithm, which identifies them as having come from a W or Z boson with an efficiency of $\sim 50\%$ at all jet momenta. The tagging algorithm is described in the next subsection, and is based around a symmetric jet mass window of width 30 GeV centred on the calibrated boson mass, and a p_{T}-dependent cut on the jet substructure variable D_2 which is designed to select jets with two concentrations of energy.

Boosted boson tagging

This section describes the boosted boson tagging method and derivation used in the analysis, following ref. [266]; it is not work that the author was involved in but is included to provide clarity on the meaning of and motivation behind the boson tagging variables.

The recommendations for boosted boson tagging for Run II comes from a simulation-based study by the ATLAS jet substructure group and published in ref. [266][3], which studied four large-R jet reconstruction and grooming algorithms in combination with a jet mass window and three possible jet substructure variables to identify the best method for tagging hadronically-decaying boosted bosons. The (uncalibrated) jet mass distribution following the trimming process for the `R2` jet is shown in fig. 8.6; the p_{T} dependence that can be seen disappears following the jet mass calibration, leaving an average jet mass distribution that

[3]The performance of the jet substructure variables discussed here was studied with early Run II data and published in ref. [267].

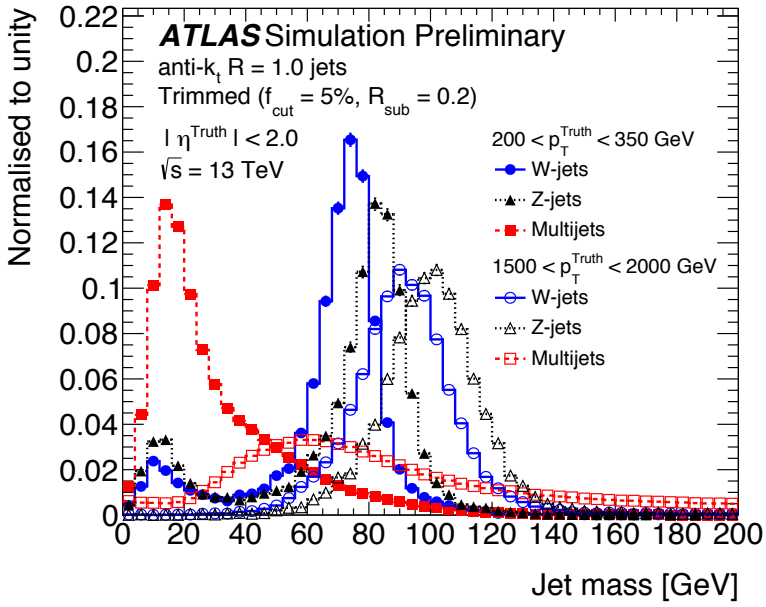

Figure 8.5: The uncalibrated leading R2 jet mass distributions for W+jets, Z+jets and multi-jet simulated events, where the leading jet was reconstructed with the anti-$k_T$algorithm with a radius parameter of R = 1.0, and trimmed with parameters R_{sub} = 0.2 and f_{cut} = 5%. Taken from ref. [266].

is almost flat with respect to p_T (meaning a fixed mass window cut can be applied). The other reconstruction algorithms studied used a C/A algorithm and pruning [188, 189] or split-filtering [190] methods, and are not discussed further here.

The average jet mass ($\langle M \rangle$) distribution for R2 jets produced by simulated W and Z decays was found to be approximately flat as a function of jet p_T following jet mass calibration, and so a jet mass window cut of $\langle M \rangle \pm$ 15 GeV was recommended [266], leading to an efficiency varying from 55-80% due to the changing mass resolution in this range.

The best substructure variable, when combined with the jet mass window cut, was found to be the D_2 variable proposed in refs. [268, 269], and defined as

$$D_2^{(\beta)} = \frac{e_3^{(\beta)}}{(e_2^{(\beta)})^3} \ , \tag{8.1}$$

where $e_n^{(\beta)}$ is an n-point energy correlation function (ECF) as defined below, and β is an angular exponent required to be greater than 0 for infra-red and collinear (IRC) safety [269].

The n-point ECFs are IRC safe observables that are sensitive to the n-prong substructure of a jet. The relevant functions for identifying a 2-prong jet in a hadron collider are [269]

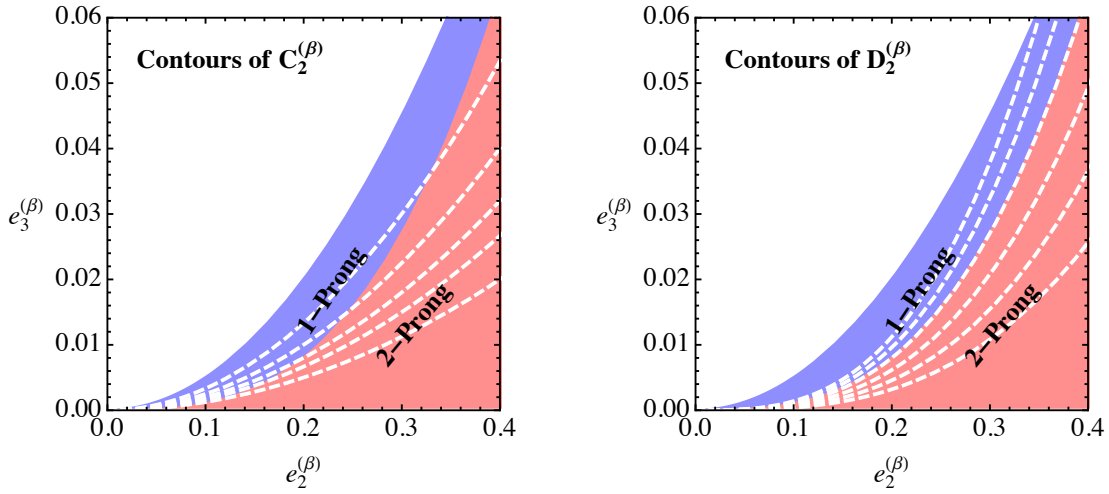

Figure 8.6: The phase space defined by the 2- and 3-point ECFs, showing contours of constant $C_2^{(\beta)}$ (left) and $D_2^{(\beta)}$ (right) and the regions corresponding to 1-prong and 2-prong jets. Taken from ref. [268].

$$
\begin{aligned}
e_2^{(\beta)} &= \frac{1}{p_{\mathrm{T}J}^2} \sum_{1 \le i < j \le n_J} p_{\mathrm{T}i} p_{\mathrm{T}j} R_{ij}^{(\beta)} \ , \\
e_3^{(\beta)} &= \frac{1}{p_{\mathrm{T}J}^3} \sum_{1 \le i < j < k \le n_J} p_{\mathrm{T}i} p_{\mathrm{T}j} p_{\mathrm{T}k} R_{ij}^{\beta} R_{ik}^{\beta} R_{jk}^{\beta} \ ,
\end{aligned}
\tag{8.2}
$$

where J is the large-R jet, n_J is the number of particles within the jet, $p_{\mathrm{T}i}$ is the transverse momentum of particle i and R_{ij} is the angular separation between particles i and j in the azimuth-rapidity plane ($R_{ij}^2 = (\phi_i - \phi_j)^2 + (y_i - y_j)^2$).

In the ATLAS boson-tagging studies, β is set equal to 1, and the superscript is dropped.

The ECFs can be combined in a slightly different, dimensionless variable C_2, defined as [270]

$$
C_2^{(\beta)} = \frac{e_3^{(\beta)}}{(e_2^{(\beta)})^2} \ . \tag{8.3}
$$

Fig. 8.6 shows the phase space defined by the 2- and 3-point ECFs $e_2^{(\beta)}$ and $e_3^{(\beta)}$, and the regions occupied by 1- and 2-prong jets. Lines of constant $D_2^{(\beta)}$ (right) clearly lie within a single region, whereas lines of $C_2^{(\beta)}$ (left) pass through both regions, meaning the former variable is the better discriminant for separating 2-prong and 1-prong jets consistently[4].

An alternative jet substructure variable included in Run I boson tagging studies in the N-subjettiness ratio τ_{21} [268]. The N-subjettiness of a jet can be con-

[4]The C_2 is still a strong discriminating variable when used with a tight jet mass cut [270], however a study by the CMS Collaboration found it to be sensitive to pileup [271].

sidered as the degree to which a jet's substructure resembles $\leq N$ subjets, and is defined by [272, 273]

$$\tau_N^{(\beta)} = \sum_i p_{\mathrm{T}i} \min\{R_{1,i}^{\beta}, R_{2,i}^{\beta}, ..., R_{N,i}^{\beta}\} \ , \tag{8.4}$$

where i runs over all particles in the jet and $R_{A,i}$ is the angular separation between particle i and one of the N subjets. If a jet has N subjets, τ_{N-1} should be much larger than τ_N, and so the discriminating variable that is used specifically for 2-prong jets is the ratio

$$\tau_{21}^{(\beta)} = \frac{\tau_2^{(\beta)}}{\tau_1^{(\beta)}} \ . \tag{8.5}$$

The authors of ref. [266] compared the D_2, C_2 and τ_{21} substructure variables, and found the D_2 variable to provide the best background rejection given a 50% signal efficiency, when applied to `R2` jets, and proposed this as the preliminary recommended tag for Run II analyses. This combination of the jet reconstruction and grooming algorithm `R2` and substructure variable D_2 is known as the (delightfully named) `R2`D_2 tagger.

The nominal performance of the `R2`D_2 tagger is an efficiency of 50% and a background rejection (defined as 1 - $\epsilon_{\text{background}}$) of 98%; this is achieved by applying a cut on the large-R jet mass of within 15 GeV of the W or Z mass, as well as a p_{T} dependent cut on D_2 with a functional form (as recommended by the authors in the jet substructure group) of

$$\begin{aligned} D_2(p_{\mathrm{T}}) \ < & 1.00068 - 0.00038526 \times p_{\mathrm{T}} + 2.43073 \times 10^{-6} \times p_{\mathrm{T}}^2 \\ & - 2.11884 \times 10^{-9} \times p_{\mathrm{T}}^3 + 6.23008 \times 10^{-13} \times p_{\mathrm{T}}^4 \end{aligned} \tag{8.6}$$

in the case of the W tagger, and

$$\begin{aligned} D_2(p_{\mathrm{T}}) \ < & 1.26233 - 0.00175091 \times p_{\mathrm{T}} + 4.54697 \times 10^{-6} \times p_{\mathrm{T}}^2 \\ & - 3.48375 \times 10^{-9} \times p_{\mathrm{T}}^3 + 9.30225 \times 10^{-13} \times p_{\mathrm{T}}^4 \end{aligned} \tag{8.7}$$

in the case of the Z tagger. These functional forms were derived to result in an approximately flat 50% signal efficiency for both W and Z bosons as a function of p_{T}.

The final selections for tagged large-R jets in the mono-W/Z analysis are summarised in table 8.5.

Tagger requirements	W-tagging	Z-tagging
Jet type	anti-k_{T} (R = 1.0), LCTopo-type jet, trimmed (R_{subjet} = 0.2, f_{cut} = 5%)	
Kinematics	$p_{\mathrm{T}} > 200$ GeV, $\lvert\eta\rvert < 2.0$	
Jet mass cut	83.1993 ± 15 GeV	93.4007 ± 15 GeV
D_2 cut	see eq. 8.6	see eq. 8.7

Table 8.5: The large-R jet definitions, kinematic selection and boosted boson tagging criteria. Note that jet mass and p_{T} calibration are performed following the trimming procedure.

Narrow jets

Small-radius jets (referred to as small-R or narrow jets) are used in this analysis mainly as a handle to reject the multi-jet background. Like the large-R jets, they are reconstructed with the anti-k_{T} algorithm but with a radius parameter of R = 0.4. The four-vector is corrected for beamspot, and the jet energy is calibrated to the JES, estimated from studies with 8 TeV data and checked against simulation of 13 TeV events [181, 184, 185].

If the jet lies within $|\eta| < 2.5$, it is required to satisfy $p_{\mathrm{T}} > 20$ GeV, while if it lies within $2.5 < |\eta| < 4.5$, there is a higher p_{T} cut at 30 GeV. Relatively low-p_{T} jets ($p_{\mathrm{T}} < 50$ GeV) satisfying $|\eta| < 2.4$ are particularly susceptible to contamination from pileup jets, and so are required to be associated to the primary vertex through the jet vertex tagger (JVT) algorithm [274], a likelihood-based method that uses a combination of tracking variables.

A summary of the small-R jet selection is shown in table 8.6.

Track jets

Track jets are used in this analysis to define the 1-lepton CRs (used to estimate the W+jets and $t\bar{t}$ background contributions, described in sec. 8.4.2), as they can be identified as having come from a b-hadron or not, thereby providing a handle to separate the regions populated by $t\bar{t}$ and W+jets events respectively. They are reconstructed with the anti-k_{T} algorithm with a radius parameter of R = 0.2, but using tracks in the ID that are required to have originated from the primary vertex (with the impact parameter cut $|z_0 \sin\theta| < 3$mm) and satisfying other track quality requirements (see ref. [275]). These requirements reduce tracks from pileup ver-

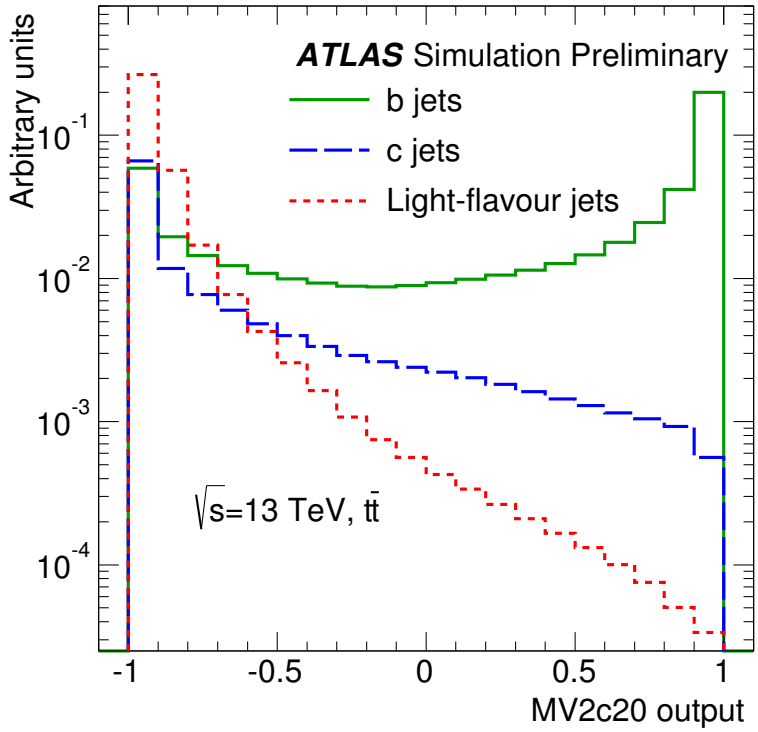

Figure 8.7: The MC2c20 distribution for a set of simulated $t\bar{t}$ events at 13 TeV. Jets originating from a b-hadron generally have a higher MC2c20 score than jets from a c- or light-quard. Taken from ref. [276].

tices while remaining highly efficient for tracks originating at the hard-scattering vertex. The track jets are required to satisfy $p_{\mathrm{T}} > 10$ GeV, and $|\eta| < 2.5$. They are then tested for having originated from a b-hadron, through use of the MC2c20 algorithm which uses a boosted decision tree (BDT) trained on a b-jets signal with light-flavour[5] jets and c-jets as background [276]. Fig. 8.7, taken from ref. [276], shows the MC2c20 distribution for a set of $t\bar{t}$ events simulated at 13 TeV. The track jets in this analysis are considered to have been 'b-tagged' if they satisfy MC2c20 $>$ -0.3098, a working point shown to be 70% efficient for identifying b-jets in a simulated $t\bar{t}$ sample. To avoid counting b-jets produced in Z boson decays, we ignore track jets that are associated to the leading large-R jet, where the association is tested with the ghost-association process [199, 200, 277]. This is a method of matching up tracks to clusters in the calorimeter, which sets the p_{T} of all tracks to 1 eV before adding them to the list of inputs for jet finding, thereby allowing identification of which tracks contribute to which clusters without affecting the reconstruction of the calorimeter jets.

A summary of the track jet and b-tagging selection is shown in table 8.6.

[5]Light jets originate from u-, d- or s-quarks or gluons.

Object	Type/quality cuts	Kinematics	Notes
small-R jets	anti-k_{T} (R = 0.4) EMTopo-type jet	$p_{\mathrm{T}} > 20$ GeV if $\lvert\eta\rvert < 2.5$ $p_{\mathrm{T}} > 30$ GeV if $2.5 \leq \lvert\eta\rvert < 4.5$	if $p_{\mathrm{T}} < 50$ GeV and $\lvert\eta\rvert < 2.4$, $JVT > 0.64$
track jets	anti-k_{T} (R = 0.2) using ID tracks	$p_{\mathrm{T}} > 10$ GeV $\lvert\eta < 2.5$	b-tagged if MV2c20 > -0.3098, ignore if ghost-associated to leading large-R jet

Table 8.6: The definitions and selections of the small-R and track jets used in the mono-$W/Z(\to jj)$ analysis.

8.2.2 Leptons

Leptons are used as the main handle to define the CRs that constrain the main backgrounds, which are defined as having one or two charged leptons. Leptons also serve to ensure the analysis is orthogonal to VV search channels within ATLAS such as $WZ \to \ell\nu qq$ and $ZZ \to \ell\ell\nu\nu$. The requirements for muons and electrons are described below, and summarised in table 8.7.

Muons

Muons are used in this analysis both as veto objects in the SR, and to define the 1- and 2-lepton CRs, to be defined further in sec. 8.3. Three definitions are used, outlined below, following the recommendations of the Muon Combined Performance group within the ATLAS Collaboration.

Loose muons satisfy *loose* identification critera [175], and are also loosely isolated from any nearby track activity in the ID, tested by summing the p_{T} of all good-quality tracks within a cone of R = 0.3 of the muon track and defined to be 99% efficient. They must satisfy $p_{\mathrm{T}} > 7$ GeV and $|\eta| < 2.7$. *Medium* muons satisfy the *loose* identification criteria, but must pass stronger kinematic constraints, $p_{\mathrm{T}} >$ 25 GeV and $|\eta| < 2.5$. *Tight* muons must be isolated in the EM calorimeter in addition to the track-based isolation, tested by summing the energy of topological clusters around the muon within a cone of R = 0.2. The combined efficiency of the tight isolation is 95%.

Object	Type/quality cuts	Kinematics
loose muons	*loose* identification, loose isolation (ID)	$p_{\mathrm{T}} > 7$ GeV, $\lvert\eta\rvert < 2.7$
medium muons	*loose* identification, loose isolation (ID)	$p_{\mathrm{T}} > 25$ GeV, $\lvert\eta\rvert < 2.5$
tight muons	*loose* identification, tight isolation (ID and calo)	$p_{\mathrm{T}} > 25$ GeV, $\lvert\eta\rvert < 2.5$
electrons	*loose* identification, loose track isolation	$p_{\mathrm{T}} > 7$ GeV, $\lvert\eta\rvert < 2.47$

Table 8.7: The definitions of leptons used in the mono-$W/Z(\rightarrow jj)$ analysis.

Electrons

Electrons are used in this analysis only as veto objects, and so a loose definition (which has high efficiency but low purity) is required. Electrons satisfy the *loose* identification criteria, following the recommendations of the ATLAS e/γ performance group and described in ref. [171], and also have a loosely isolated ID track requirement, similar to the *loose* muon isolation but with a cone size of R = 0.2. They are required to satisfy $p_{\mathrm{T}} > 7$ GeV and $|\eta| < 2.47$.

8.2.3 Missing transverse energy

The missing transverse energy vector, $\vec{E}_{\mathrm{T}}^{\mathrm{miss}}$, is obtained as described in sec. 4.3.5, using the reconstructed and calibrated physics objects (including electrons, muons and jets) along with any additional reconstructed tracks that are not associated to any other object (known as the track-based soft term (TST) contribution) [196, 198, 278] . These tracks are required to be consistent be having originated at the primary vertex, to reduce the effect of pileup contributions. The track missing transverse momentum, $\vec{p}_{\mathrm{T}}^{\mathrm{miss}}$, is calculated entirely with reconstructed tracks in the ID.

As noted in the introduction to this chapter, the vector sum of the $\vec{E}_{\mathrm{T}}^{\mathrm{miss}}$ and the $\vec{p}_{\mathrm{T}}$ of all muons is an important variable measured in the CRs and input into the combined profile likelihood fit. This is denoted $E_{\mathrm{T,\,no\,}\mu}^{\mathrm{miss}}$, and is calculated by

$$E_{\mathrm{T,\,no\,}\mu}^{\mathrm{miss}} \equiv |\vec{E}_{\mathrm{T}}^{\mathrm{miss}} + \sum_{\text{all muons}} \vec{p}_{\mathrm{T}}| \ . \tag{8.8}$$

Events are collected with the HLT_XE80 trigger (introduced in sec. 8.1.1), which

Object	Type/quality cuts	Notes
$\vec{E}_{\mathrm{T}}^{\mathrm{miss}}$	TST $E_{\mathrm{T}}^{\mathrm{miss}}$	$\vec{E}_{\mathrm{T,\,no}\,\mu}^{\mathrm{miss}} \equiv \vec{E}_{\mathrm{T}}^{\mathrm{miss}} + \sum_{\mathrm{all}\,\mu} \vec{p}_{\mathrm{T}}$ trigger fully efficient when $E_{\mathrm{T,\,no}\,\mu}^{\mathrm{miss}} > 200$ GeV
$\vec{p}_{\mathrm{T}}^{\mathrm{miss}}$	track-based $E_{\mathrm{T}}^{\mathrm{miss}}$	

Table 8.8: The missing transverse momentum variables included in the mono-$W/Z(\to jj)$ analysis.

does not include the contribution from muons and so can be considered a trigger-level version of $E_{\mathrm{T,\,no}\,\mu}^{\mathrm{miss}}$. This was shown in fig. 8.2 to be fully efficient for $E_{\mathrm{T,\,no}\,\mu}^{\mathrm{miss}} \gtrsim$ 200 GeV. The $E_{\mathrm{T,\,no}\,\mu}^{\mathrm{miss}}$ variable also allows us to estimate the $E_{\mathrm{T}}^{\mathrm{miss}}$ distribution in the $Z(\to \nu\bar{\nu})$+jets background by studying the $Z(\to \mu^+\mu^-)$+jets events instead.

A summary of the missing transverse energy objects is found in table 8.8.

8.2.4 Overlap removal

Baseline overlap removal requirements are applied by the calibrated framework that is used to create the samples used in this analysis[6]. Two additional requirements are applied: large-R and small-R jets are not included if they overlap an electron, according to ΔR(electron, jet) within 1.0 and 0.4 respectively.

8.3 Event selection

The signal region event selection is designed to select events containing a large-R jet tagged as coming from the hadronic decay of a boosted W or Z boson, as well as a large amount of missing transverse energy and no leptons.

8.3.1 Quality cuts

All events should first pass the baseline selection:

- the HLT_XE80 trigger is used to collect events,
- the event should contain a primary vertex,
- the event is vetoed if any jet is tagged as a BadLoose jet as described in ref. [279] to ensure the $E_{\mathrm{T}}^{\mathrm{miss}}$ is well-measured, and

[6] https://twiki.cern.ch/twiki/bin/viewauth/AtlasProtected/CxAODFramework

- the event should contain at least one large-R jet.

Data events are also required to be included in the ALL_GOOD_25NS GRL (introduced in sec. 8.1.1) and events are vetoed if the Tile or LAr data is affected by noise bursts, or the semiconductor tracker (SCT) event flag shows an error.

8.3.2 Signal region

Events in the signal region are vetoed if they contain any *loose* leptons. They are also required to satisfy $E_{\mathrm{T}}^{\mathrm{miss}} > 250$ GeV. Most of the multi-jet background (also referred to as the QCD background) is removed by imposing a high $E_{\mathrm{T}}^{\mathrm{miss}}$ cut, however a significant amount remains as a result of dijet events with a mismeasured jet resulting in a large $E_{\mathrm{T}}^{\mathrm{miss}}$. These events are removed by imposing three 'anti-QCD' cuts described below:

- $p_{\mathrm{T}}^{\mathrm{miss}} > 30$ GeV: mis-measured jets in the calorimeter will still have well-reconstructed tracks in the ID, so the track-based missing transverse momentum won't be as large as the $E_{\mathrm{T}}^{\mathrm{miss}}$;
- $\Delta\phi(\vec{E}_{\mathrm{T}}^{\mathrm{miss}}, \vec{p}_{\mathrm{T}}^{\mathrm{miss}}) < \pi/2$: real missing transverse momentum should point in the same direction in both calorimeter- and track-based measurements, however in the case of a mis-measured jet, these will not align;
- min$[\Delta\phi(\vec{E}_{\mathrm{T}}^{\mathrm{miss}}, p_{\mathrm{T}}(\text{small-}R\text{ jets}))] > 0.6$: the $E_{\mathrm{T}}^{\mathrm{miss}}$ vector will point in approximately the direction of the lower-p_{T} jet in the case where one of the jets is mis-measured, so these events are removed. (Events containing no small-R jets are assigned a default value of π.)

Finally, events in the SR are required to pass a logical OR of the W- and Z-tagging, as summarised in table 8.5. The complete list of selection criteria for the SR are listed in table 8.9, along with the dedicated CRs for the main backgrounds, discussed in the following section.

8.4 Backgrounds

The shape of the dominant W, Z and $t\bar{t}$ SM background contributions are taken from simulation, however the normalisation of each is a free parameter of the profile-likelihood fit, described in sec. 8.6.1. The diboson and single-top backgrounds are estimated directly from simulation, while the multi-jet background is negligible.

The dominant backgrounds are studied in dedicated CRs, containing exactly one or two muons, and the $E_{\mathrm{T,\,no}\,\mu}^{\mathrm{miss}}$ distribution in each is used as the input to the fit, as the comparison between simulation and data within uncertainties is used to constrain the normalisation of each consistently. A 0-lepton validation region, where the W/Z boson mass window requirement is inverted, is also defined.

8.4.1 2-lepton control region

The dominant background comes from Z+jets processes, where the Z decays to neutrinos which are invisible to the detector. These events can be studied with similar events with the Z instead decays to two charged leptons (in this case muons), and adding the muons back into the $E_{\mathrm{T}}^{\mathrm{miss}}$ term so that they become 'hidden' and are a source of $E_{\mathrm{T}}^{\mathrm{miss}}$. This is of course the modified $E_{\mathrm{T}}^{\mathrm{miss}}$ term $E_{\mathrm{T,\,no}\,\mu}^{\mathrm{miss}}$, so is consistent with the calorimeter-based $E_{\mathrm{T}}^{\mathrm{miss}}$ used by the trigger. The resulting $E_{\mathrm{T,\,no}\,\mu}^{\mathrm{miss}}$ spectrum can be included in the combined fit to constrain the $Z(\rightarrow \text{invisible})$+jets background.

The 2-lepton CR is therefore designed to obtain a sample rich in Z+jets events, where the Z decays leptonically and a 'fake' large-R jet is reconstructed. It should be close to the SR, but non-overlapping.

Following application of the HLT_XE80 trigger, events are required to contain exactly two muons (one *medium* and one at least *loose*) which together have an invariant mass within 25 GeV of the Z boson mass. They should also satisfy $E_{\mathrm{T,\,no}\,\mu}^{\mathrm{miss}} > 200$ GeV (to ensure the trigger is fully efficient), $p_{\mathrm{T,\,no}\,\mu}^{\mathrm{miss}} > 30$ GeV (an anti-QCD cut), and have at least one large-R jet that passes the jet substructure (D_2) cut. Because the large-R doesn't result from true hadronic decay of the Z, the mass window requirement is relaxed to retain a large number of events in this CR.

Fig. 8.8 shows a collection of kinematic distributions with various selections applied, and compares data and simulation.

8.4.2 1-lepton control regions

Control regions for the W+jets and $t\bar{t}$ background processes are known together as the 1-lepton CRs. They are defined by the presence of a single muon so that a cut on the $E_{\mathrm{T,\,no}\,\mu}^{\mathrm{miss}}$ can be applied to ensure the trigger is fully efficient.

Diagrams depicting the explicit processes are shown in fig. 8.9, and selections should therefore be designed to reflect these topologies. W+jets events constitute a background to the $t\bar{t}$ CR and vice versa; to make sure that events don't fall into both CRs and so enter the combined fit twice, a method is required to enforce the two CRs are orthogonal. We use b-tagged jets as a handle to do this, as a b-quark

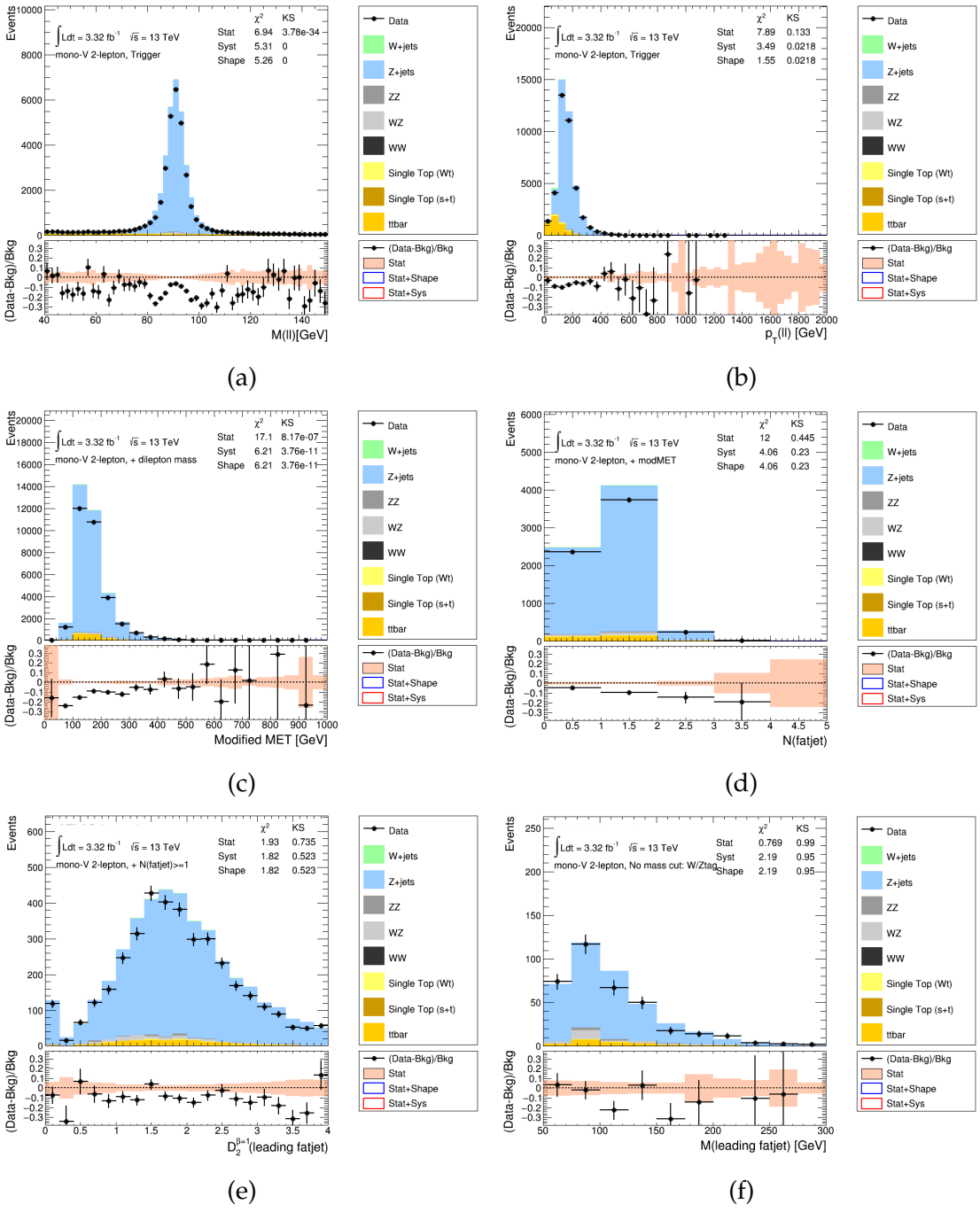

Figure 8.8: Kinematic distributions for the 2-lepton CR. The dilepton invariant mass (a) and dilepton p_{T} (b) after the trigger and two lepton requirements, the $E^{\mathrm{miss}}_{\mathrm{T,\,no}\,\mu}$ distribution after the dilepton mass cut (c), the large-R jet multiplicity after the cuts on $E^{\mathrm{miss}}_{\mathrm{T,\,no}\,\mu}$ and p_{T} (d), the D_2 distribution with all selections except the substructure cut (e), and the leading large-R jet mass following all selections (f). Taken from ref. [6].

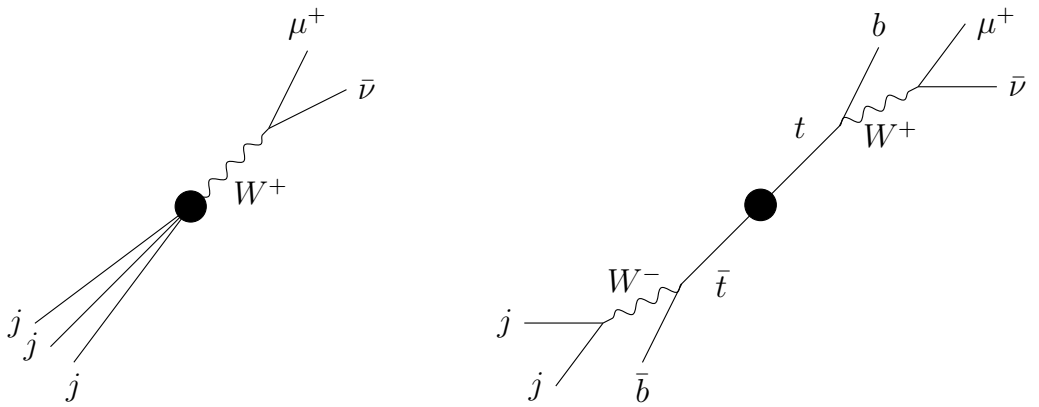

Figure 8.9: The W+jets (left) and $t\bar{t}$ (right) processes that are dominant in each of the 1-lepton CRs. The black dot represents the production mechanism, as only the resulting final states are of interest here. Note that the charge-conjugate processes are implied.

is always produced in the decay of a top quark, but rarely appears in the hadronic activity of a W+jets event.

The following subsections describe the preliminary development of the 1-lepton CRs individually, and summarise the final selection.

W+jets CR

The W+jets signal, shown in fig. 8.9(a), is tagged with a leptonically-decaying W boson. The W is produced in association with one or more jets that are reconstructed as a large-R jet, that is required to satisfy at least the D_2 requirement to remain close to the SR selection. The preliminary studies described here were performed for testing in a blinded validation region where the boson mass-window selection of the SR is inverted (see further description below), and so the central large-R jet mass region is also blinded by removing events with $60 < m_{\text{large-}R\text{ jet}} < 110$ GeV. Initally, the lepton was not restricted to be a muon only, as the significance of the $E^{\text{miss}}_{\text{T, no }\mu}$ variable as the final input to the fit had not been fully developed.

As stated above, the handle used to separate the W+jets CR from the $t\bar{t}$ CR was the presence of a b-tagged jet, however the definition of such a jet was still flexible in the early stages of this analysis. Studies were performed with track- and calorimeter-based narrow jet definitions, and the degree of overlap with the large-R jet that was permitted, which is particularly relevant to the following $t\bar{t}$ CR. We also investigated whether additional hadronic activity outside the reconstructed large-R jet should be permitted, through a restriction on the number of non-b-tagged narrow jets not overlapping the large-R jet.

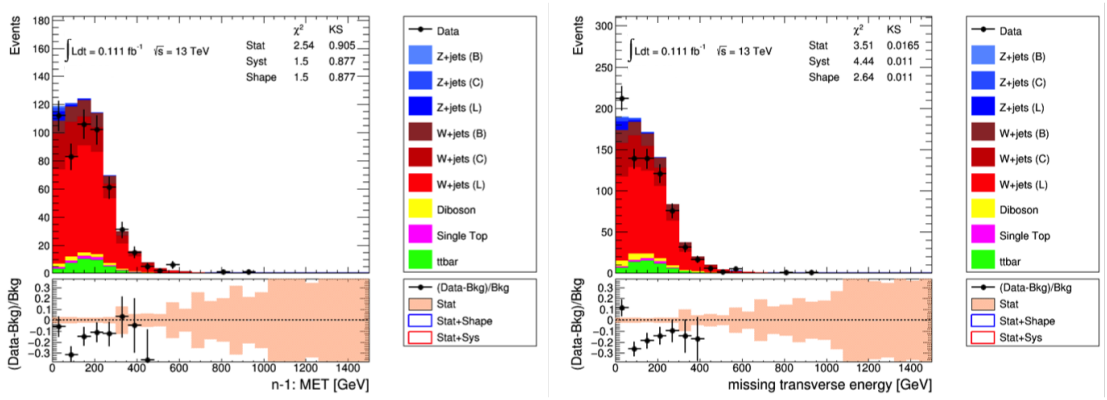

(a) (b)

Figure 8.10: Preliminary plots of the $E_{\mathrm{T}}^{\mathrm{miss}}$ distribution in the W+jets CR, where events with more than one additional non-b-tagged jet are removed (left), and where this veto is no longer included (right). Only 0.11 fb^{-1} of data is shown, with statistical uncertainties.

The transverse mass was considered in both 1-lepton CRs as a way to select events containing a W boson; it is defined as

$$m_{\mathrm{T}} = \sqrt{2p_{\mathrm{T}}^{\ell} \cdot E_{\mathrm{T}}^{\mathrm{miss}}(1 - \cos\Delta\phi(\ell, E_{\mathrm{T}}^{\mathrm{miss}}))}\,, \tag{8.9}$$

and peaks at around 80 GeV for W+jets events. The cut $m_{\mathrm{T}} > 40$ GeV was therefore included.

It was found that the inclusion of a veto on the number of additional non-b-tagged narrow jets did not improve the signal-to-background ratio in the CR, but reduced the number of events entering the CR by approximately 40%. This can be seen in fig. 8.10, where fig.(a) shows events where only one additional non-b-tagged jet is permitted, and fig.(b) is the same distribution with that veto removed. Note these are early plots, with only 0.11 fb^{-1} of data available. This cut is therefore not included in the final selection.

The preliminary set of cuts was:

- HLT_XE80 trigger acceptance,
- exactly 1 electron *or* muon,
- ≥ 1 large-R jet ($p_{\mathrm{T}} > 250$ GeV, $|\eta| < 1.2$),
- $E_{\mathrm{T,\,no\,}\mu}^{\mathrm{miss}} > 40$ GeV,
- $m_{\mathrm{T}} > 40$ GeV,
- no b-tagged track jets,
- large-R jet passing D_2 cut, and

- large-R jet in mass sidebands (since the analysis was not yet unblinded).

A set of N - 1 plots, where each of the selections listed above has been applied except that affecting the displayed variable, are shown in fig. 8.11. Note these plots have only 1.4 fb^{-1} of data, and all uncertainties are statistical.

$t\bar{t}$ CR

The $t\bar{t}$ process, depicted in fig. 8.9(b), consists of two b-quarks producing b-jets, a large-R jet produced from decay of one W boson, and a second W decaying leptonically. While electrons were also being included as the charged lepton, better agreement between simulation and data was observed in the muon channel, which was therefore preferred even before the $E^{\text{miss}}_{\text{T, no }\mu}$ variable was explicitly included. The large-R jet was required to pass the D_2 cut, and a cut on the transverse mass m_{T} was also included to enhance the selection of events containing a W boson.

Because the signal process includes two b-quarks, events were initially required to include at least two b-tagged jets, one which was required to be overlapping the large-R jet (min(ΔR(b-tag, large-R jet)) < 1.0) and another non-overlapping (max(ΔR(b-tag, large-R jet)) > 1.0). The former requirement would therefore select events where the large-R jet was seeded by a top quark, and we can see this effect in fig. 8.12(a), where the top mass peak at 173 GeV is evident in the distribution of leading large-R jet mass. However, this implies that the substructure of the large-R jet is 3-pronged rather than the desired 2-pronged, making it less likely to pass the D_2 criterion. Removing the requirement that a b-tagged overlap the large-R jet means that the more large-R jets are instead seeded by a W boson, demonstrated in fig. 8.12(b) where the W mass peak at 80 GeV is visible.

Additionally, as the efficiency of the b-tagging is 70%, requiring two b-tagged jets results in an efficiency of close to 50%. It was therefore decided that merely requiring at least one b-tagged jet would be sufficient, and also ensure that 1-lepton events with exactly one b-tagged jet were not being thrown away unnecessarily.

The preliminary set of cuts was:

- HLT_XE80 trigger acceptance,
- exactly 1 muon,
- ≥ 1 large-R jet ($p_{\text{T}} > 250$ GeV, $|\eta| < 1.2$),
- $E^{\text{miss}}_{\text{T, no }\mu} > 40$ GeV,
- $m_{\text{T}} > 40$ GeV,

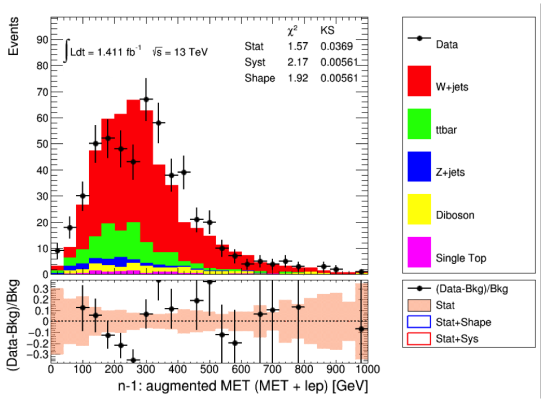

(a) The $E_{\mathrm{T,\,no}\,\mu}^{\mathrm{miss}}$ disitribution.

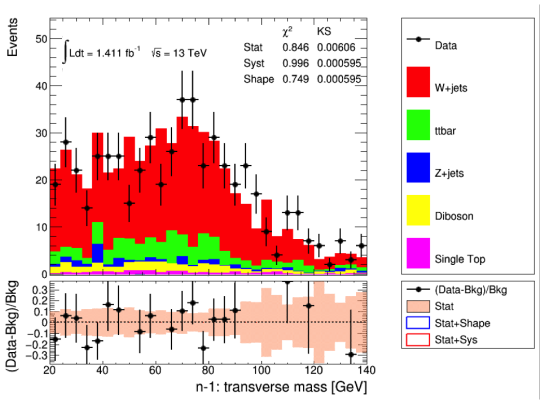

(b) The m_{T} distribution.

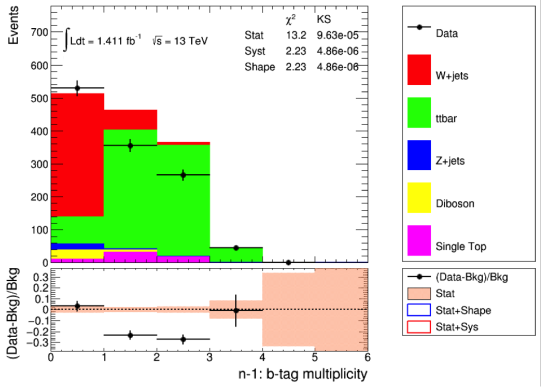

(c) The b-tagged narrow jet multiplicity.

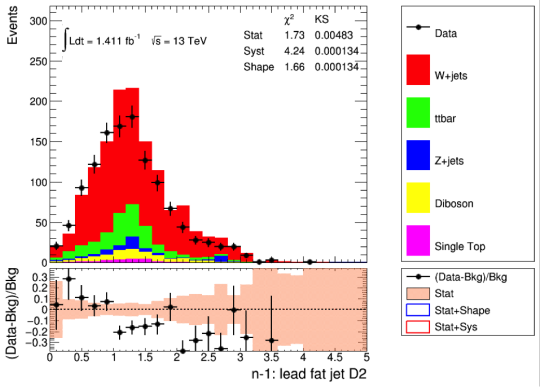

(d) The large-R jet D_2 distribution.

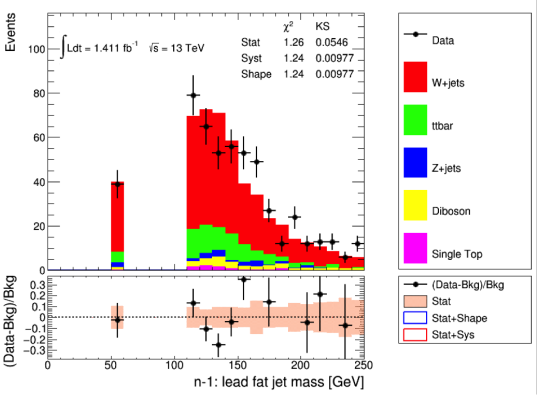

(e) The large-R jet mass distribution.

Figure 8.11: Preliminary plots in the W+jets CR, showing relevant kinematic variables with all preliminary selections applied except on the variable shown. Only 1.4 fb^{-1} of data is shown, and the plots are blinded in the W/Z mass window.

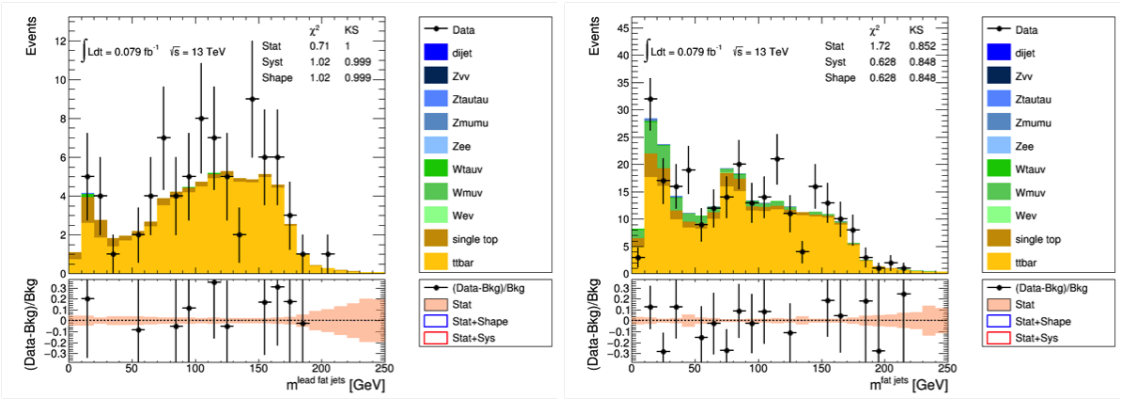

(a) (b)

Figure 8.12: Preliminary plots of the large-R jet mass, with and without requiring that one of the b-tagged jets be overlapping the leading large-R jet, revealing the top-quark mass at 173 GeV (left) and the W mass at 80 GeV (right). Only 79 pb^{-1} of data is shown, with statistical uncertainties.

- $\geq$ one b-tagged track jet, satisfying $\Delta R(b\text{-tag, large-}R\text{ jet}) > 1.0$,
- large-R jet passing D_2 cut, and
- large-R jet in mass sidebands (since the analysis was not yet unblinded).

A set of N - 1 plots, where each of the selections listed above has been applied except that affecting the displayed variable, are shown in fig. 8.13. Note these plots have only 1.4 fb^{-1} of data, and all uncertainties are statistical.

It was found that the transverse mass cut removed about 40% of events but did not improve the signal-to-background ratio when used in conjunction with the other selection criteria, and so it was removed. This cut was then also removed from the W+jets CR definition, to ensure the two 1-lepton CRs were as close as possible while also remaining orthogonal.

The final 1-lepton CRs

The final event selection criteria for the 1-lepton CRs are chosen to ensure that all events with one muon pass into exactly of the two regions, as they have identical selections but are separated according to the presence of b-tagged jets. In particular we look for b-tagged track jets (described in sec. 8.2.1), which are not ghost-associated to the leading large-R jet; such choices are made as this analysis overlaps considerably with the mono-$H(\rightarrow b\bar{b})$ analysis [280] and diboson resonance search [281], and a consistent treatment among the analyses is desirable to be able to produce consistent results and systematic uncertainties.

The final selection in both the W+jets and $t\bar{t}$ CRs is

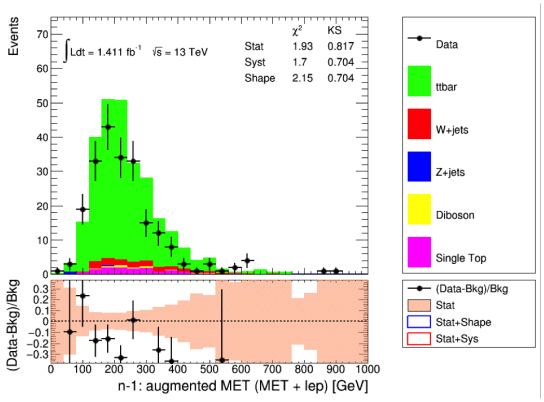

(a) The $E_{\mathrm{T,\,no}\,\mu}^{\mathrm{miss}}$ distribution.

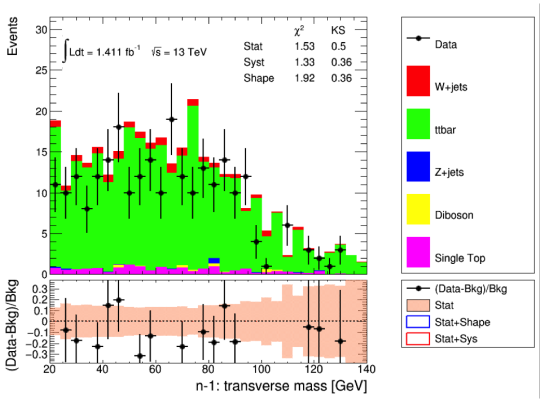

(b) The m_{T} distribution.

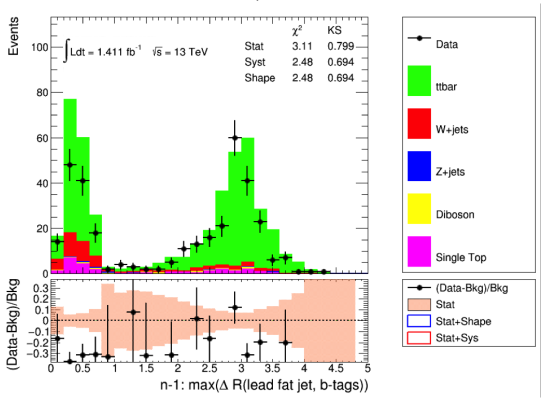

(c) The maximum separation of b-tagged jets and the leading large-R jet.

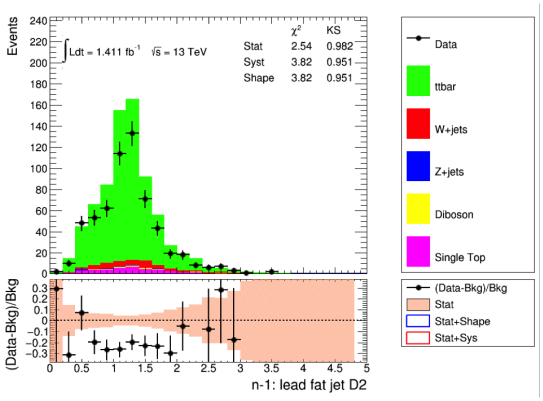

(d) The large-R jet D_2 distribution.

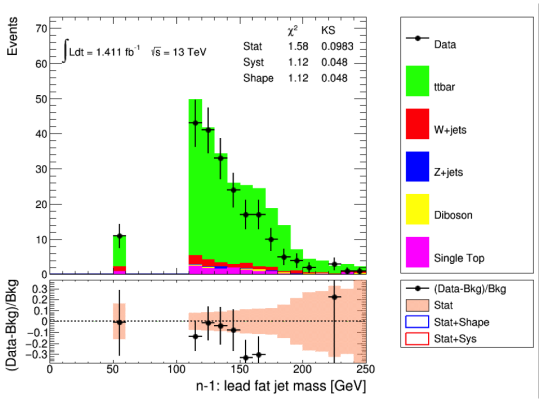

(e) The large-R jet mass distribution.

Figure 8.13: Preliminary plots in the $t\bar{t}$ CR, showing relevant kinematic variables with all preliminary selections applied except on the variable shown. Only 1.4 fb^{-1} of data is shown, and the plots are blinded in the W/Z mass window.

- HLT_XE80 trigger acceptance,
- exactly 1 *tight* muon, and no additional muons passing the *loose* definition,
- $E_{\mathrm{T,\,no}\,\mu}^{\mathrm{miss}} > 200$ GeV,
- $p_{\mathrm{T}}^{\mathrm{miss}} > 30$ GeV,
- at least 1 large-R jet,
- the large-R jet passes the D_2 substructure selection, and
- exactly 0 b-tagged track jets (W+jets CR) *or* at least 1 b-tagged track jet ($t\bar{t}$ CR), where any b-tagged track jets are not associated to the highest-p_{T} large-R jet.

Fig. 8.14 shows key kinematic distributions in the W+jets CR as the selection cuts are applied sequentially, while $N-1$ plots (where all cuts except that affecting the variable shown are applied) for the W+jets and $t\bar{t}$ CRs are shown in figs. 8.15 and 8.16 respectively. The full available dataset is used, and the plots are now unblinded.

8.4.3 Background validation region

A validation region (also referred to as the 0-lepton, or mass sideband, CR) is defined, where all selection cuts of the SR are applied *except* for the boson mass cut, which is inverted, thereby selecting events where the large-R jet mass is outside the W/Z mass window. This produces a set of events that are topologically and kinematically very similar to those in the SR, with a background composition that that is also very similar. Such events are used to test the results of the combined fit.

The $E_{\mathrm{T}}^{\mathrm{miss}}$ and large-R jet mass distributions are plotted in fig. 8.17.

All signal, control and validation regions are summarised in table 8.9.

8.5 Systematic uncertainties

This section provides details of the sources of systematic uncertainty considered in this analysis. The experimental sources of uncertainty are summarised in tables 8.10 and 8.11, which show the effect of each source as a percentage of the total number of background or signal events in each region. The theoretical uncertainties affecting the signal samples are listed in table 8.12.

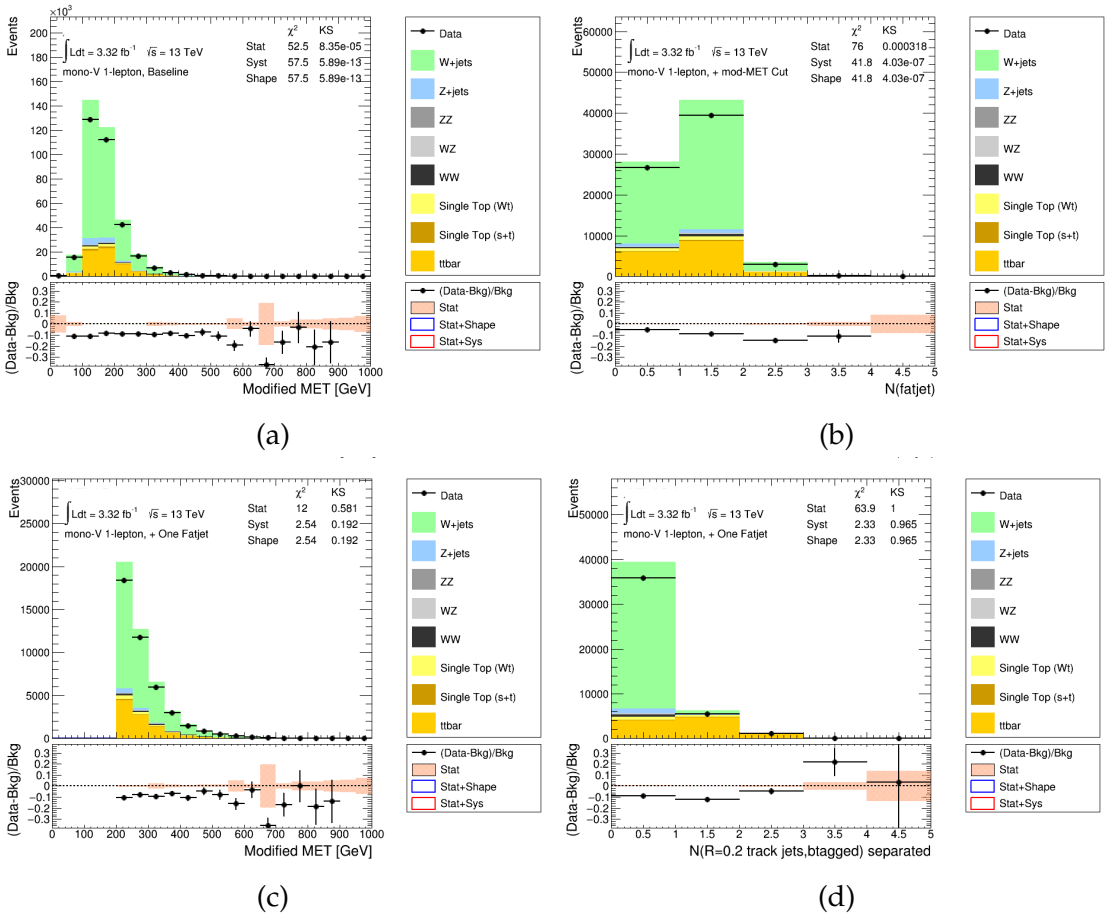

Figure 8.14: Kinematic distributions in the W+jets 1-lepton CR, plotted as the selection criteria are applied successively: the $E_{\mathrm{T,\,no}\,\mu}^{\mathrm{miss}}$ distribution following the trigg and one muon requirements (a), the large-R jet multiplicity following cuts on the $E_{\mathrm{T,\,no}\,\mu}^{\mathrm{miss}}$ and $p_{\mathrm{T}}^{\mathrm{miss}}$ (b), the $E_{\mathrm{T,\,no}\,\mu}^{\mathrm{miss}}$ distribution this time after the large-R jet requirement (c), and the b-tagged track jet multiplicity following all other selections (d).

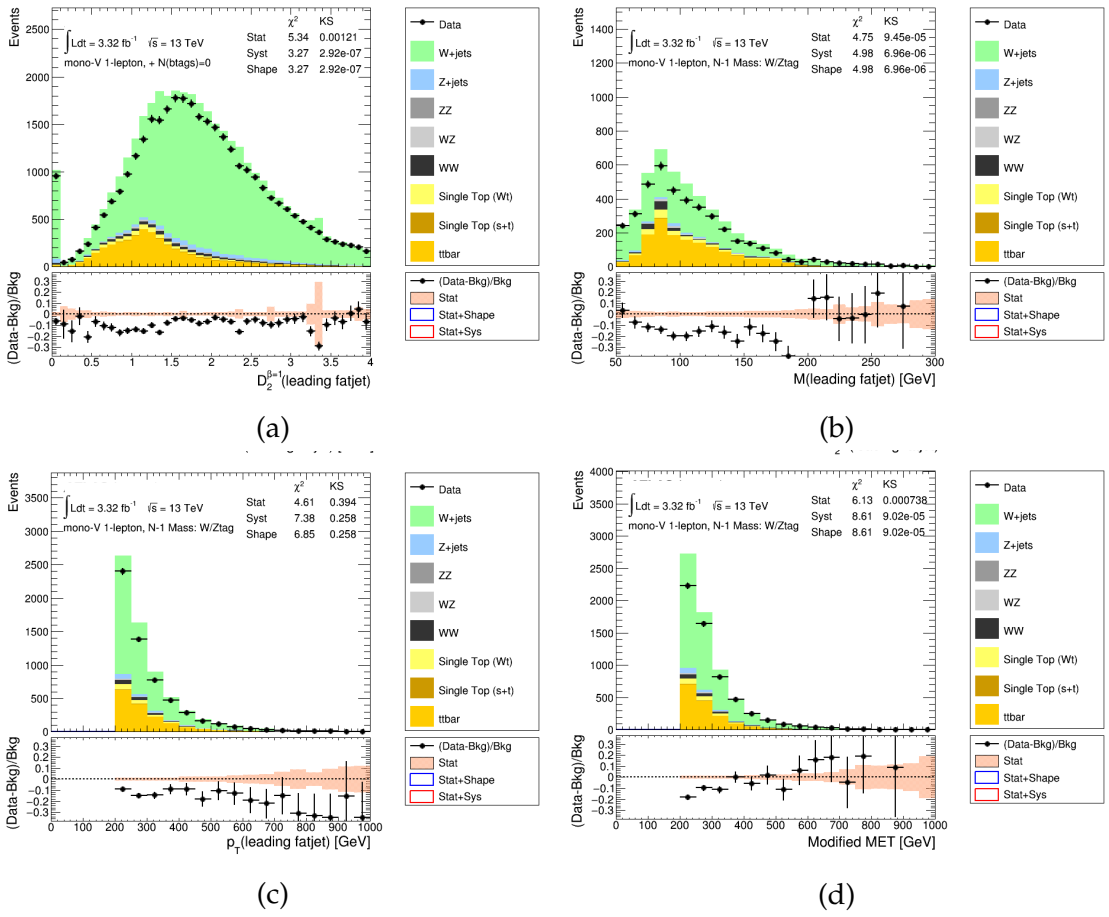

Figure 8.15: In the W+jets 1-lepton CR, the leading large-R jet D_2 (a), mass (b) and p_{T} (c) distributions, and the $E^{\mathrm{miss}}_{\mathrm{T,\,no}\,\mu}$ (d) distribution. All selections except on the variable shown are applied.

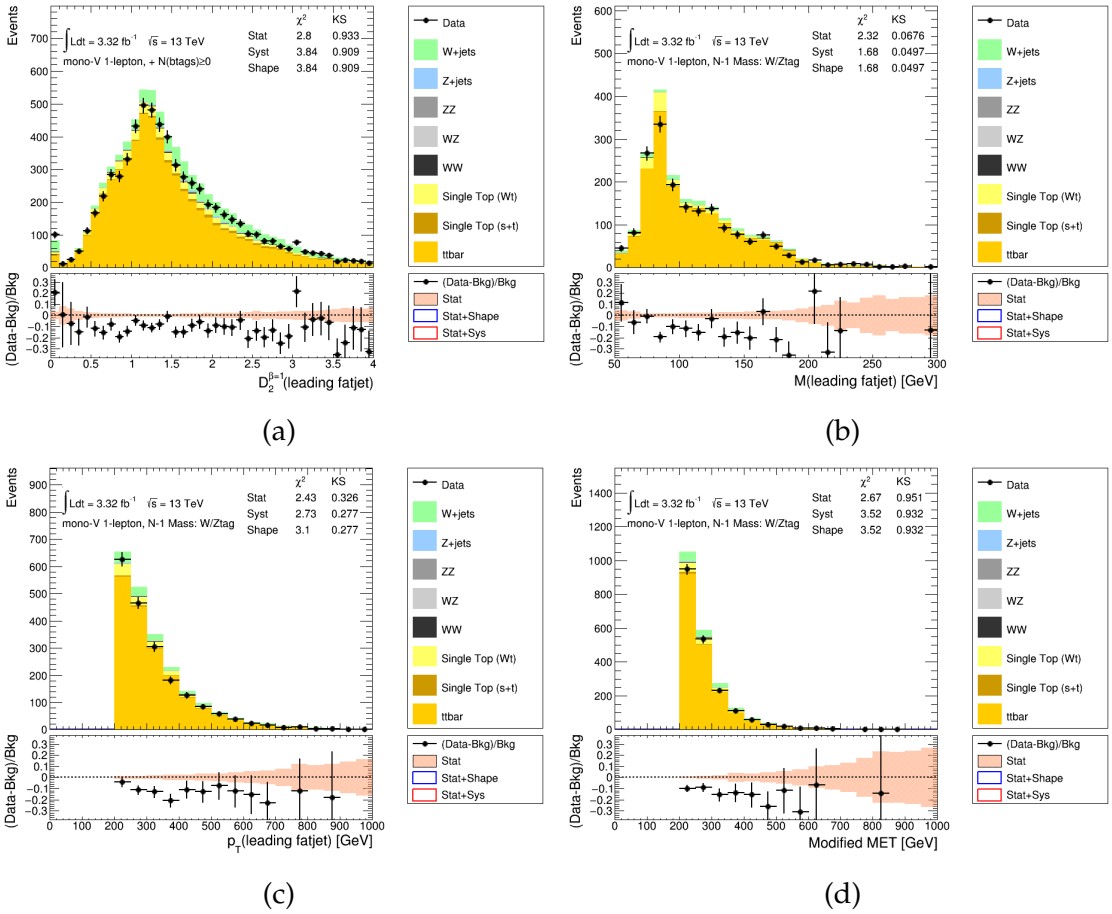

(a) (b)

(c) (d)

Figure 8.16: In the $t\bar{t}$ 1-lepton CR, the leading large-R jet D_2 (a), mass (b) and p_{T} (c) distributions, and the $E_{\mathrm{T,\,no\,}\mu}^{\mathrm{miss}}$ (d) distribution. All selections except on the variable shown are applied.

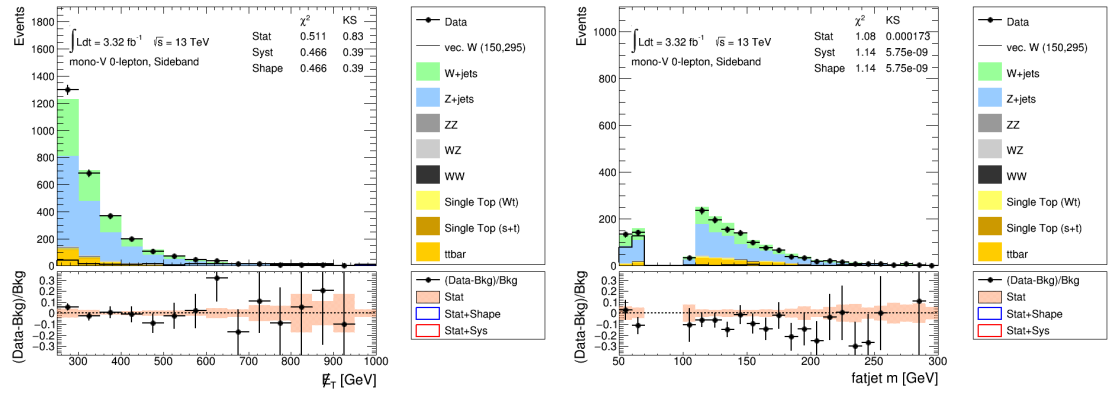

(a) (b)

Figure 8.17: The 0-lepton validation region, where all SR selections are applied except for the boson mass window cut, which is inverted. Taken from ref. [6].

Region	Usage	Selections
Signal region (0-lepton)	Search	trigger and quality cuts anti-QCD cuts no *loose* leptons $E_{\mathrm{T}}^{\mathrm{miss}} > 250$ geV D_2 tag mass tag
2-lepton Z+jets CR	Z+jets constraint	trigger and quality cuts exactly two muons (one *medium* and one at least *loose*) $m_{\mu\mu} \in [66, 116]$ GeV $E_{\mathrm{T,\,no\,}\mu}^{\mathrm{miss}} > 200$ GeV $p_{\mathrm{T,\,no\,}\mu}^{\mathrm{miss}} > 30$ GeV D_2 tag
1-lepton W+jets CR	W+jets constraint	trigger and quality cuts exactly one *tight* muon no additional *loose* muons $E_{\mathrm{T,\,no\,}\mu}^{\mathrm{miss}} > 200$ GeV $p_{\mathrm{T,\,no\,}\mu}^{\mathrm{miss}} > 30$ GeV D_2 tag no b-tagged track jets
1-lepton $t\bar{t}$ CR	$t\bar{t}$ constraint	trigger and quality cuts exactly one *tight* muon no additional *loose* muons $E_{\mathrm{T,\,no\,}\mu}^{\mathrm{miss}} > 200$ GeV $p_{\mathrm{T,\,no\,}\mu}^{\mathrm{miss}} > 30$ GeV D_2 tag at least one b-tagged track jet
0-lepton sideband region	Validation	trigger and quality cuts anti-QCD cuts no *loose* leptons $E_{\mathrm{T}}^{\mathrm{miss}} > 250$ geV D_2 tag *inverted* mass tag

Table 8.9: Summary of the signal, control and validation regions used in this analysis. Note that 'tag' here refers to either a W or a Z tag.

Note that uncertainties associated with the trigger in this analysis are assumed to be negligibly small compared to the dominant large-R jet uncertainties, and so are not included.

Large-R jets

As a groomed large-R jet is included in each of the signal and control regions, with momentum, mass and substructure calibrations applied, the modeling of these variables is the largest source of experimental systematic uncertainty in this analysis. The scale and resolution are considered for the p_{T}, mass and D_2 variables [266, 282, 283]. A cross-calibration contribution is also included. Each source is estimated following recommendations from the ATLAS Jet-$E_{\mathrm{T}}^{\mathrm{miss}}$ performance group, using centrally-provided software tools[7] to vary the relevant variable up and down within a 1σ uncertainty, and the effect is propagated through the analysis.

The jet mass resolution and D_2 scale are the largest sources of uncertainties in the SR, of approximately 10% on the signal and 13% on the background respectively. All other sources contribute uncertainties of less than 5%.

Narrow jets

As narrow jets are used mainly to reduce the multi-jet background, only uncertainties on the jet energy are considered. Uncertainties on both the JES and Jet Energy Resolution (JER) are implemented according to recommendations from the Jet-$E_{\mathrm{T}}^{\mathrm{miss}}$ performance group[8]. The 50 or so parameters which contribute to the JES uncertainty are reduced to three, known as the *strongly reduced* set of nuisance parameters, which is permitted in analyses which are demonstrated to be insensitive to (j_1, j_2) correlations arising from changes to the JES[9]. The JER uncertainty is calculated with a single nuisance parameter[10].

These contribute approximately 7% uncertainty on the background yield and $\lesssim 5\%$ on the signal yield in the SR, and only a few percent in the CRs.

[7] https://twiki.cern.ch/twiki/bin/view/AtlasProtected/JetUncertainties2015PrerecLargeR

[8] https://twiki.cern.ch/twiki/bin/view/AtlasProtected/JetEtmissRecommendationsMC15

[9] https://twiki.cern.ch/twiki/bin/viewauth/AtlasProtected/JetUncertainties2015Prerec

[10] https://twiki.cern.ch/twiki/bin/viewauth/AtlasProtected/JetResolution2015Prerecom

Track jets

Track jets that have been b-tagged are used to distinguish between the two 1-lepton CRs, and so do not affect the SR or 2-lepton CR. Only the b-tagging efficiency is included as a source of systematic uncertainty, which is implemented following the recommendations of the ATLAS Flavour Tagging performance group[11].

Missing transverse momentum

Experimental systematic uncertainties on the SoftTerm of the TST $E_{\mathrm{T}}^{\mathrm{miss}}$ come from the scale and resolution uncertainties, where the resolution is further broken into components parallel and perpendicular to the p_{T} axis (but added in quadrature in tables 8.10 and 8.11). Uncertainties the track-based missing transverse momentum, $p_{\mathrm{T}}^{\mathrm{miss}}$, are derived from a jet-by-jet uncertainty on tracks within jets. All sources are handed with a single software tool[12].

Leptons

Uncertainties are considered for electrons based on the electron reconstruction and identification scale factors[13], and the energy scale and resolution[14], using tools from the ATLAS e/γ performance group to vary each source up and down by 1σ. Muon uncertainties arise from the identification and isolation efficiencies, and the momentum scale and resolution, as recommended by the muon combined performance group[15]. As in Run I (see sec. 6.5.1), the muon p_{T} resolution uncertainty was measured in both the muon spectrometer (MS) and ID.

The dominant lepton uncertainty is from the p_{T} ID resolution, at $\lesssim 2\%$ in the 1-lepton CRs, all other contributions are at the sub-percent level.

Luminosity

The uncertainty on the measured integrated luminosity is estimated to be 5%, using special calibration data-taking runs and techniques described in ref. [233].

[11] https://twiki.cern.ch/twiki/bin/view/AtlasProtected/BTagCalib2015
[12] https://twiki.cern.ch/twiki/bin/view/AtlasProtected/MissingETSystematics
[13] https://twiki.cern.ch/twiki/bin/view/AtlasProtected/ElectronEfficiencyRun2
[14] https://twiki.cern.ch/twiki/bin/view/AtlasProtected/EGammaCalibrationRun2
[15] https://twiki.cern.ch/twiki/bin/view/AtlasProtected/MCPAnalysisGuidelinesMC15

Background modeling

Uncertainties on the modeling of the main backgrounds were estimated by generating samples with alternative generators, and comparing the resulting $E_{\mathrm{T}}^{\mathrm{miss}}$ distributions against that from the nominal generator. Specifically, MADGRAPH samples for Z+jets and W+jets processes were generated to compare with the nominal SHERPA samples, and $t\bar{t}$ samples generated with aMC@NLO [156] interfaced to HERWIG were compared with the nominal POWHEG samples. The comparisons were made in dedicated CRs, similar to the 1- and 2-lepton CRs defined in this analysis, and described further in section 9 of ref. [280].

The $E_{\mathrm{T}}^{\mathrm{miss}}$ distributions were found to be consistent within statistical uncertainties, and so the background modeling uncertainties are not included in the final analysis.

PDF, scale and tune

Uncertainties on the simulated signal are derived from the treatment of the PDF[16], the factorisation and renormalisation scales and the tune.

The PDF uncertainties arise from two sources: the uncertainty *within* a PDF set (resulting from the fitting procedure when the PDF is calculated), and the difference *between* PDF sets. Here, the baseline simulation, generated with the NNPDF30_lo_as_0130 PDF, is reweighted to both the internal NNPDF variation PDFs and to the CT14lo [284] and MMHT2014lo68cl [285] PDFs. The difference in the $E_{\mathrm{T}}^{\mathrm{miss}}$ spectra gives a measure of the uncertainty, and the largest of the intra- and inter-PDF uncertainties is taken as the systematic error. The median of the PDF uncertainty for the mono-W and mono-Z signals, for the sV simplified model, are shown binned by $E_{\mathrm{T}}^{\mathrm{miss}}$ in the first column of table 8.12.

The scale uncertainties were obtained by varying the `scalefact` parameter in MADGRAPH up and down by a factor of 2, and similarly for the `alpsfact` parameter and the Initial State Radiation (ISR) uncertainty. The tune uncertainties were obtained with five separate variations, one affecting the underlying event, one affecting the jet structure, and three affecting different aspects of jet production. These were implemented following the recommendations of the ATLAS Jets and Dark Matter working group[17]. The last two columns of table 8.12 demonstrate the effect on a mono-W signal sample, created with m_{χ} = 500 GeV and M_{med} = 10 TeV; these uncertainties on the acceptance are in the range 2–15%, and are used in the limit calculation.

[16] `https://twiki.cern.ch/twiki/bin/viewauth/AtlasProtected/PdfRecommendations`

[17] `https://twiki.cern.ch/twiki/bin/view/AtlasProtected/JDMSignalUncertainties`

Syst. source	Systematic uncertainties in the SR [%]		
	back-ground	mono-W signal	mono-Z signal
large-R jet cross calibration	1.2	2.7	1.1
large-R jet p_{T} scale	5.3	3.8	4.3
large-R jet p_{T} resolution	0.9	0.4	0.9
large-R jet mass scale	4.5	1.9	2.2
large-R jet mass resolution	2.2	11.5	8.7
large-R jet D_2 scale	13.1	9.6	7.9
large-R jet D_2 resolution	4.0	2.4	2.1
small-R jet JES	6.5	2.9	4.5
small-R jet JER	1.9	4.6	0.9
track jet b-tagging	-	-	-
$E_{\mathrm{T}}^{\mathrm{miss}}$ jet track	0.1	0.8	0.8
SoftTerm scale	0.3	0.2	0.4
SoftTerm resolution	0.3	-	0.4
electron energy scale	0.1	-	-
electron energy resolution	-	-	-
electron identification efficiency	-	-	-
μ p_{T} resolution (ID)	-	-	-
μ p_{T} resolution (MS)	-	-	-
μ p_{T} scale	-	-	-
μ isolation efficiency	-	-	-
μ identification efficiency	-	-	-
W modeling	2.1	-	-
Z modeling	3.7	-	-
$t\bar{t}$ modeling	1.8	-	-

Table 8.10: The experimental sources of systematic uncertainty in the SR, shown as a percentage of the total yield for the background, and for mono-W and mono-Z sV simplified model signals generated with m_{χ} = 500 GeV and M_{med} = 10 TeV. Uncertainties smaller than 0.05% are not shown.

Syst. source	Background syst. uncertainties [%]		
	Z+jets CR	W+jets CR	$t\bar{t}$ CR
large-R jet cross calibration	5.9	5.3	5.3
large-R jet p_{T} scale	6.5	6.9	6.9
large-R jet p_{T} resolution	0.3	0.7	-
large-R jet mass scale	-	-	-
large-R jet mass resolution	-	-	-
large-R jet D_2 scale	10.9	12.2	12.2
large-R jet D_2 resolution	5.8	5.0	4.0
small-R jet JES	1.9	1.4	1.4
small-R jet JER	0.8	0.4	0.4
track jet b-tagging	-	2.2	4.3
$E_{\mathrm{T}}^{\mathrm{miss}}$ jet track	0.7	0.7	0.7
SoftTerm scale	1.0	1.3	1.3
SoftTerm resolution	0.9	0.9	0.9
electron energy scale	-	-	-
electron energy resolution	0.1	-	-
electron identification efficiency	-	-	-
μ p_{T} resolution (ID)	0.2	1.8	1.8
μ p_{T} resolution (MS)	0.2	0.4	0.4
μ p_{T} scale	-	-	-
μ isolation efficiency	-	-	-
μ identification efficiency	-	-	-
W modeling	-	6.1	6.1
Z modeling	6.8	0.2	0.2
$t\bar{t}$ modeling	0.3	2.3	2.3

Table 8.11: The experimental sources of systematic uncertainty in the three CRs, shown as a percentage of the total yield for the SM background estimate in each region. Uncertainties smaller than 0.05% are not shown.

$E_{\mathrm{T}}^{\mathrm{miss}}$ bin	Acceptance uncertainty [%]		
	PDF	Scale	Tune
250-350	9.8	2	5
350-500	9.8	2	7
500-800	10.6	5	7
800-1500	14.9	10	10

Table 8.12: Theoretical uncertainties on the sV simplified model. The median PDF uncertainty for mono-W and mono-Z model samples is shown in the first column, the second and third columns show the uncertainty on the acceptance for a mono-W signal sample with m_{χ} = 500 GeV and M_{med} = 10 GeV. These are the signal uncertainties used in the limit calculation.

Figs. 8.18 and 8.19 show the large-R jet mass and $E_{\mathrm{T,\,no}\,\mu}^{\mathrm{miss}}$ distributions in the SR and each CR, with all statistical and systematic uncertainties included. The $E_{\mathrm{T,\,no}\,\mu}^{\mathrm{miss}}$ distributions in particular are input into the profile likelihood fit, described in the next section.

8.6 Limits

8.6.1 The profile likelihood method

A binned profile likelihood method [261] is used to constrain the dominant backgrounds and extract a signal strength. This takes as input the $E_{\mathrm{T,\,no}\,\mu}^{\mathrm{miss}}$ histograms in the SR (which, since there are no muons in the SR, is simply the $E_{\mathrm{T}}^{\mathrm{miss}}$) as well as the three dedicated CRs, and the associated uncertainties. The signal strength μ (an overall normalisation factor), along with three normalisation factors for the W, Z and $t\bar{t}$ backgrounds, are free parameters for the global fit. Note that μ = 0 indicates the background-only hypothesis, while μ = 1 indicates the nominal signal strength hypothesis.

The likelihood function is simultaneously maximized over the signal and control regions; it is defined as the product of Poissonian probabilities for all bins:

$$\mathcal{L}(\mu,\theta) = \prod_{\text{SR bins: } i} \frac{(N_{\mathrm{SR},i})^{n_i}}{n_i!} e^{-N_{\mathrm{SR},i}} \prod_{\text{CR: } j} \left(\prod_{\text{CR bins: } k} \frac{(N_{\mathrm{CR}j,k})^{n_k}}{n_k!} e^{-N_{\mathrm{CR}j,k}} \right) \tag{8.10}$$

where $N_{\mathrm{SR},i}$ is the total number of expected events in bin i of the signal region,

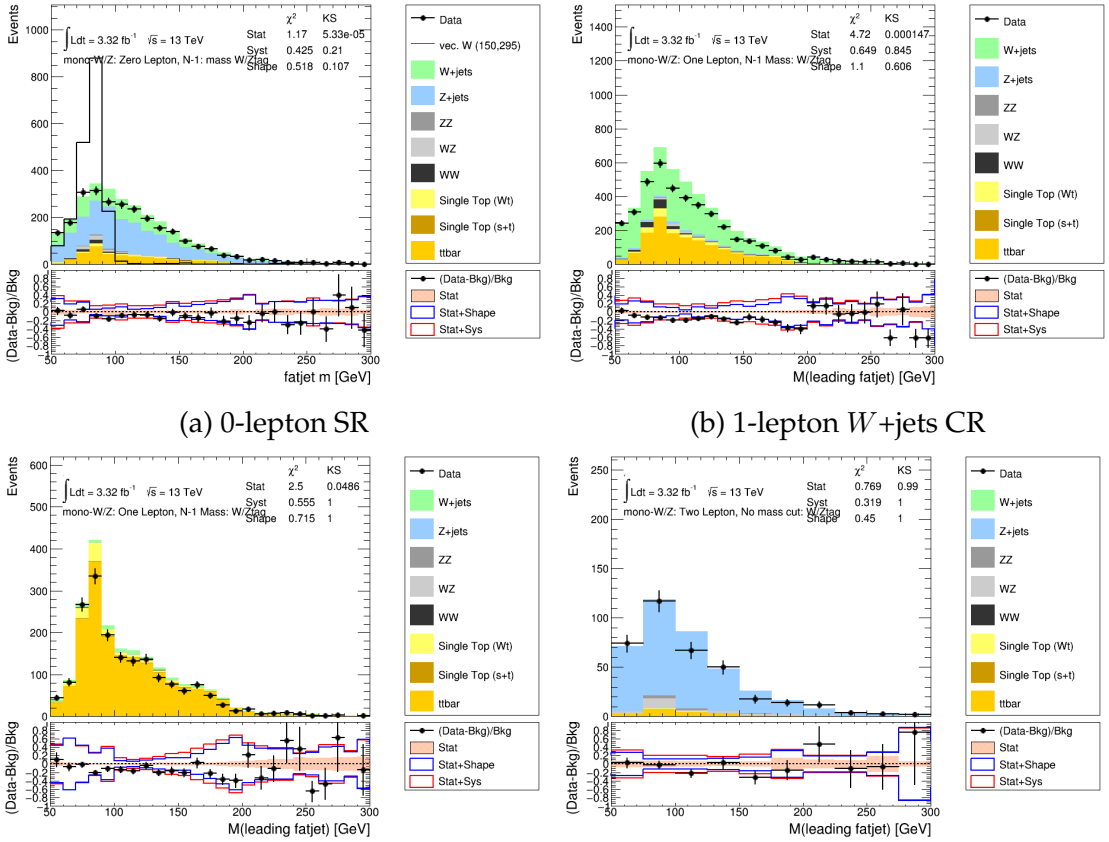

(a) 0-lepton SR

(b) 1-lepton W+jets CR

(c) 1-lepton $t\bar{t}$ CR

(d) 2-lepton Z+jets CR

Figure 8.18: The leading large-R jet mass distribution in the signal and control regions, before the likelihood fitting precedure is applied. A mono-W signal from the sV model (with m_χ = 150 GeV and M_{med} = 295 GeV) is also shown in the SR (a). Statistical and systematic uncertainties are included. Taken from ref. [6].

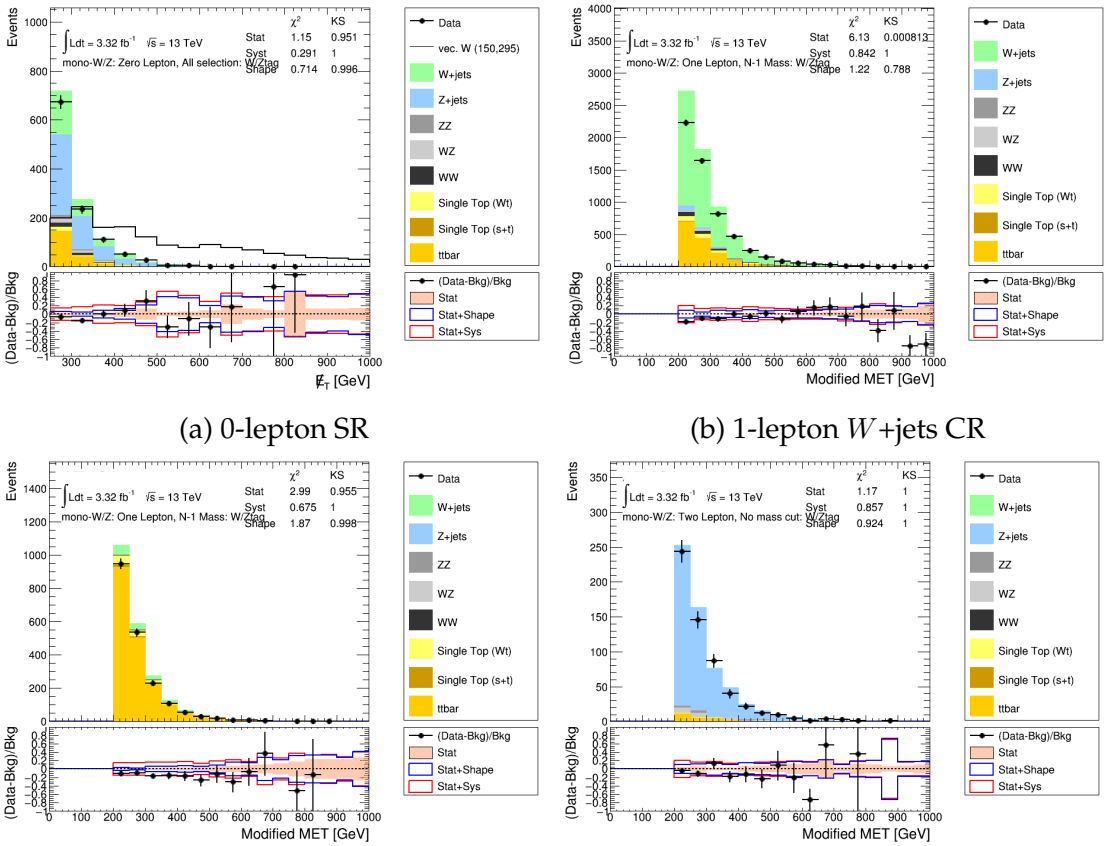

(a) 0-lepton SR

(b) 1-lepton W+jets CR

(c) 1-lepton $t\bar{t}$ CR

(d) 2-lepton Z+jets CR

Figure 8.19: The $E_{\mathrm{T,\,no\,}\mu}^{\mathrm{miss}}$ distribution in the signal and control regions, before the likelihood fitting procedure is applied. A mono-W signal from the sV model (with m_{χ} = 150 GeV and M_{med} = 295 GeV) is also shown in the SR (a). Statistical and systematic uncertainties are included. Taken from ref. [6].

and $N_{\text{CR}j,k}$ is the expected number of events in bin k of control region j. These are further defined by

$$\begin{aligned} N_{\text{SR},i} &= \mu s_i + b_i = \mu s_i + \alpha_{t\bar{t}} b_i^{t\bar{t}} + \alpha_W b_i^W + \alpha_Z b_i^Z \\ N_{\text{CR}j,k} &= b_j = \alpha_{t\bar{t}} b_{j,k}^{t\bar{t}} + \alpha_W b_{j,k}^W + \alpha_Z b_{j,k}^Z \end{aligned} \tag{8.11}$$

where $\alpha_{t\bar{t}}$, α_W and α_Z are scale factors for each of the main background types, which are allowed to float in the global fit; note that these do not vary between bins. In this way, while some amount of each different background sources will appear in each CR, they are all fitted together with a single normalisation factor extracted for each background type.

Systematic uncertainties of the signal and background are taken into account through the use of *nuisance parameters*, and are properly correlated across signal and background processes and regions. Each of the signal and background yields is parametrised according to

$$n = n_0 \times (1 + \theta \times \sigma_{\text{unc}}) \tag{8.12}$$

where n_0 is the nominal yield, θ is the nuisance parameter and σ_{unc} is the estimated uncertainty. A constraint term, $N(\tilde{\theta}|\theta)$, is added into the global likelihood to contrain the nuisance parameters, and takes the form of a Gaussian:

$$N(\tilde{\theta}|\theta) \equiv G(\tilde{\theta}|\theta, 1) = \frac{1}{\sqrt{2\pi}} e^{\frac{(\tilde{\theta}-\theta)^2}{2}} \ . \tag{8.13}$$

The nominal fit result for μ and θ_μ is obtained by maximising the likelihood function with respect to all free parameters, known as the maximised log-likelihood (MLL) value. The test statistic q_μ is constructed from the log of the profile likelihood ratio:

$$q_\mu = -2 \ln \left(\frac{\mathcal{L}(\mu, \hat{\hat{\theta}}_\mu)}{\mathcal{L}(\hat{\mu}, \hat{\theta})} \right) \ , \tag{8.14}$$

where $\hat{\mu}$ and $\hat{\theta}$ are the parameters that maximise the likelihood (with $0 \leq \hat{\mu} \leq \mu$), and $\hat{\hat{\theta}}_\mu$ are the nuisance parameter values that maximise the likelihood for a given signal strength μ. The test statistic is used to measure the compatibility of the background-only model with the observed data; a larger test statistic indicates incompatibility between the data and μ.

8.6.2 Post-fit background estimates

A background-only fit is performed with μ set to zero, and shows no deviation from the SM prediction. The extracted normalisation scale factors α_Z, α_W and $\alpha_{t\bar{t}}$,

Fit parameter	Fitted value
$\hat{\alpha}_W$	0.94 ± 0.13
$\hat{\alpha}_Z$	1.04 ± 0.15
$\hat{\alpha}_{t\bar{t}}$	0.95 ± 0.14

Table 8.13: The post-fit values and uncertainties of the background normalization factors.

Process	Events
Z+jets	519 ± 31
W+jets	326 ± 22
$t\bar{t}$ and single top	217 ± 18
Diboson	88 ± 12
Total background	1150 ± 30
Data	1143

Table 8.14: The predicted and observed numbers of events in the SR. The predicted yields are shown following the profile likelihood fit to the data in all regions.

and their associated uncertainties are listed in table 8.13, and are all consistent with unity. The $E_{\mathrm{T}}^{\mathrm{miss}}$ and $E_{\mathrm{T,\,no}\,\mu}^{\mathrm{miss}}$ distributions following the fitting procedure are shown in fig. 8.20 for each of the signal and control regions. Additionally, the post-fit yields for all backgrounds in the SR are listed alongside the number of events observed in data in table 8.14.

8.6.3 Limits on the signal strength

Finally, the fit results are used to calculate the 95%C.L. upper limits on μ for each model using the CL_{s} method [261, 286, 287]. For the sV simplified model it is kept as a limit on the signal strength, while for the $ZZ\chi\bar{\chi}$ model, these limits are translated into a constraint on the suppression scale Λ.

The sV simplified model

The upper limit on the signal strength μ is plotted in fig. 8.21, as a function of the DM and mediator masses. Note that these limits are valid for fixed coupling strengths of $g_q = 0.25$ and $g_\chi = 1.0$. They could be converted to limits on alternative coupling strengths through a rescaling, *provided* that no significant variation in

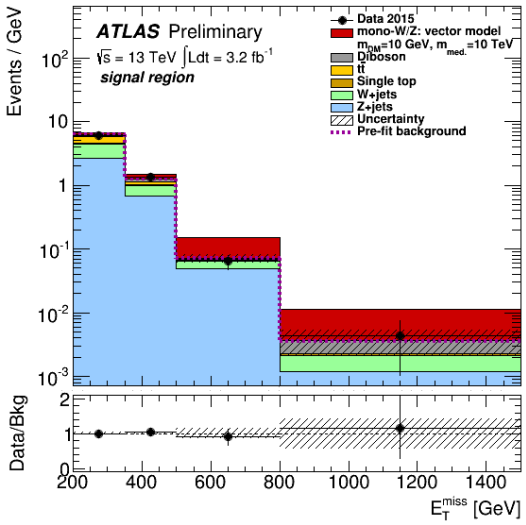

(a) 0-lepton SR

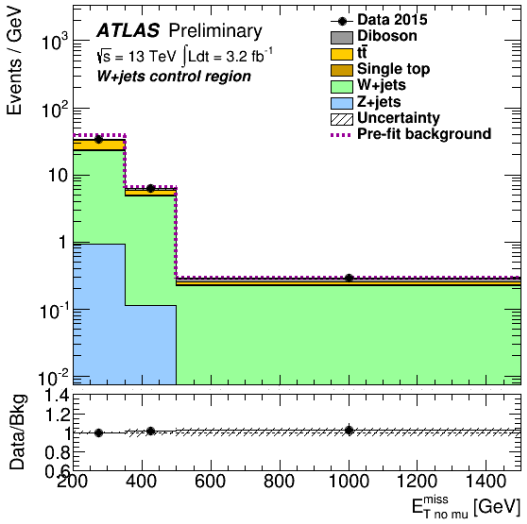

(b) 1-lepton W+jets CR

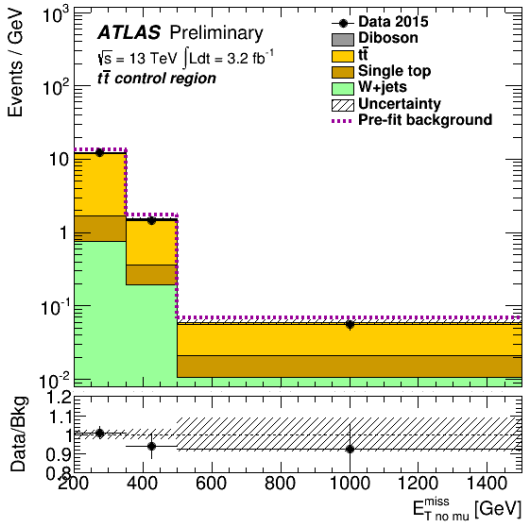

(c) 1-lepton $t\bar{t}$ CR

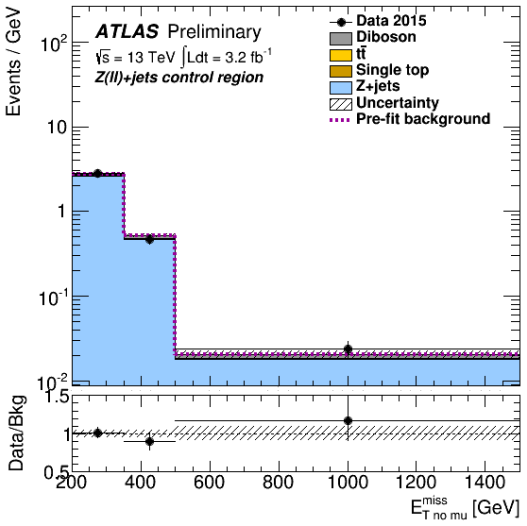

(d) 2-lepton Z+jets CR

Figure 8.20: The $E^{\text{miss}}_{\text{T, no }\mu}$ distribution in the signal and control regions, *after* the likelihood fitting procedure is applied. A mono-W/Z signal from the sV model (with m_χ = 10 GeV and M_{med} = 10 TeV) is also shown in red in the SR (a). The pre-fit background estimations are shown by the dotted line. The data and fitted simulation agree within uncertainties in all regions. Taken from ref. [5].

the kinematic behaviour through a change in the width resulted, as has been discussed in sec. 7.1.3 of chapter 7.

The weakest limits on the signal strength are for large m_χ and small M_{med}, where the mediator is considerably off-shell and the cross section is suppressed. Conversely, the strongest limits are found where the particle masses are both small and the mediator can be produced on-shell, a result of both the enhanced cross section and the harder $E_{\text{T}}^{\text{miss}}$ distribution (see fig. 8.3). Since $\mu > 1$ in all cases, no part of this model is excluded by this analysis.

This so-called *benchmark coupling* method of presenting limits for a simplified model is a clear alternative to the method used in chapters 6 and 7, which plotted limits on the coupling combination $\sqrt{g_q g_\chi}$ for particular values of the ratio g_χ/g_q (the *3D scan* method). The former method is simpler for comparing with other experiments, and requires a scan over only two parameters (the DM and mediator masses), however the choice of benchmark coupling is semi-arbitrary, and as mentioned above, is not necessarily straightforward to translate to other couplings. The latter method is easy to interpret and relevant for theorists (for whom an upper limit on a coupling is often an important result), however a comparison with other experiments is more complex and the scan over additional parameters is considerably more challenging and time- and resource-consuming. The debate within the ATLAS, CMS and theory simplified model community regarding the best way to interpolate and present such results is an on-going one, however methods such as rescaling and shaping are beginning to emerge [34, 288].

The $ZZ\chi\bar{\chi}$ model

The cross section for the dimension-7 $ZZ\chi\bar{\chi}$ model is scaled by the suppression scale Λ to the power of -6 (see eq. 3.10 in chapter 3). The signal strength is also a rescaling parameter:

$$\sigma_{\text{lim}} = \mu \times \sigma_{\text{gen}} \tag{8.15}$$

where σ_{lim} and σ_{gen} are the limiting and generated values of the cross section respectively. This then implies that

$$\Lambda_{\text{lim}} = \frac{\Lambda_{\text{gen}}}{\mu^{1/6}} \tag{8.16}$$

where Λ_{gen} was set to 3 TeV in all cases.

Fig. 8.22 plots the observed and expected lower limits on the suppression scale with 1 and 2σ uncertainties, as a function of the DM mass m_χ. This can be compared with the 'min-γ' $ZZ\chi\bar{\chi}$ signal limits in fig. 6.16 of chapter 6; even with only

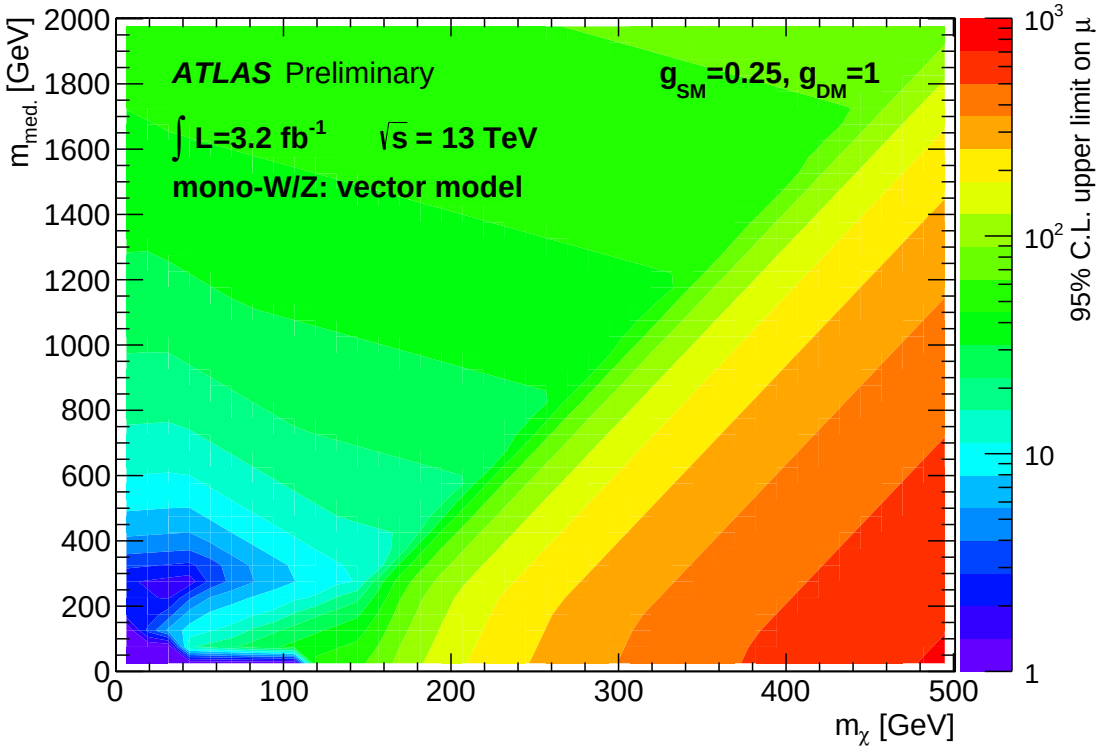

Figure 8.21: The observed 95%C.L. upper limit on the signal strength μ plotted as a function of the DM and mediator masses for the sV simplified model, as obtained with the preliminary ATLAS hadronic mono-W/Z analysis. Taken from ref. [5].

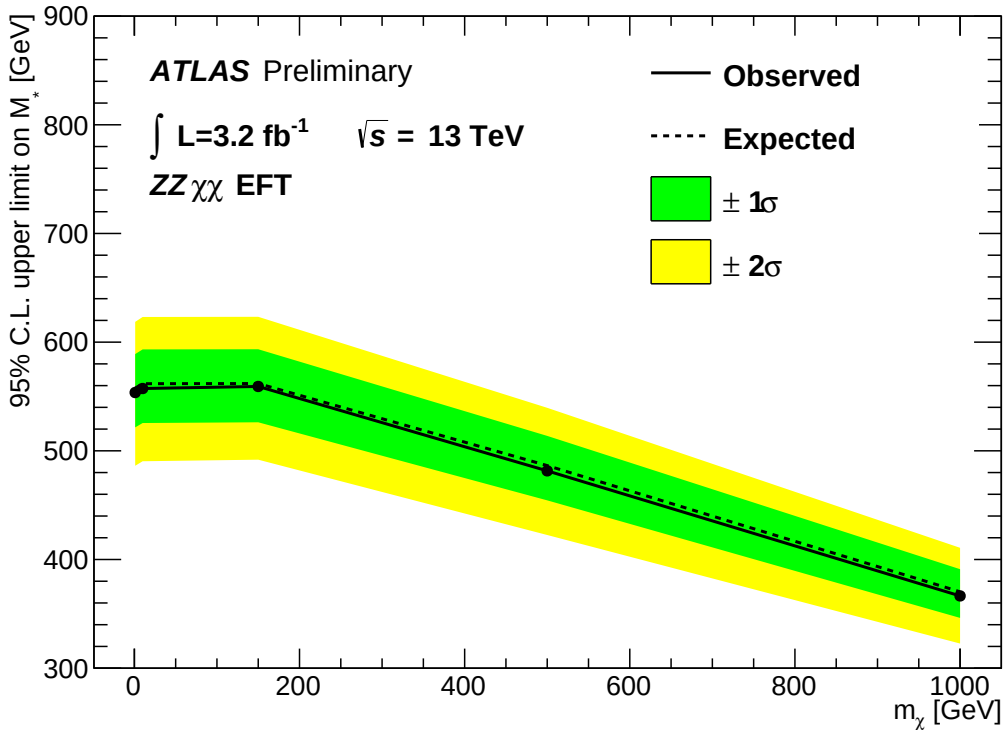

Figure 8.22: The expected and observed 95%C.L. lower limits on the suppression scale Λ (labeled $M_\star$ in the figure) plotted as a function of the DM mass for the $ZZ\chi\bar{\chi}$ EFT model, as obtained with the preliminary ATLAS hadronic mono-W/Z analysis. Taken from ref. [5].

3.2fb^{-1} of data, this 13 TeV analysis has obtained limits that are comparable (and, in fact, slightly stronger) with the 8 TeV limits of that leptonic mono-Z analysis. These limits could also be converted to the maximal-mixing case through a simple rescaling of the cross section [15], and we would expect them to be again comparable with the 'max-γ' limits in fig. 6.16.

The preliminary limits presented here are the first limits on both the sV simplified model and $ZZ\chi\bar{\chi}$ EFT released by the ATLAS Collaboration in Run II.

Chapter 9

Conclusion

The Standard Model (SM) of Particle Physics, introduced in chapter 2, is one of the most comprehensive high-precision and highly-tested theories in the field of Physics, however it is known to be incomplete as there are several open questions that it does not sufficiently address. The presence of an abundance of gravitationally-interacting particulate matter spread throughout our Universe, known as dark matter (DM), is one of the most significant of these unexplained phenomena, the evidence for which was outlined in chapter 2. The Weakly Interacting Massive Particle (WIMP) model of DM is a popular class of model, not least because of the so-called *WIMP miracle*, and because a fermionic WIMP candidate arises naturally in several of the more comprehensive models of new physics that have been developed, such as the many variations of Supersymmetry (SUSY).

If we make the assumption that DM can interact with the SM through a weakly-interacting force, three orthogonal methods of searching for DM are possible: the search for the SM products of annihilating DM (indirect detection), detection of the nuclear recoil in a target material due to the scattering of a WIMP from a nucleus (direct detection), and observation of DM produced in the annihilation of SM particles (collider searches). The focus of this thesis was a generic collider search, where DM is pair-produced in association with some visible object X, leading to the mono-X + missing transverse energy ($E_{\mathrm{T}}^{\mathrm{miss}}$) signature.

It is advantageous to be able to constrain multiple models with a single analysis; while this is not often possible with more fully-described theories like SUSY, another approach is to look for classes of DM models that add very few additional free parameters to the SM. Most commonly used is an Effective Field Theory (EFT) operator, which hides underlying physics behind a contact interaction and a suppression scale. The D1 scalar, D5 vector and D9 tensor operators couple quarks to DM fermions, and provide a phenomenologically distinct set of operators that are easily compared across experimental channels. Another alternative is the class of $ZZ\chi\bar{\chi}$ models, which couple DM directly to the Z boson at dimen-

sion 7. All of these EFT operators were described in chapter 3.

The potential problems of the EFT approach were also described in chapter 3, where if certain assumptions are made about the underlying physics, an EFT treatment can give incorrect and invalid constraints. EFTs are therefore not entirely invalid, but do require careful treatment. Iteratively rescaling the limit by the fraction of valid events is one method used to recover a useful result.

A second method is to introduce one or more further degrees of freedom, which leads to simplified models, a class of models which are not intended to describe all the new physics of a fully-realised dark matter model but which aim to capture its behaviour in the collider context. A simple set of simplified models were described in chapter 3, where a vector mediator is exchanged in the s-channel or a scalar mediator in the t-channel. A significant point of difference between the two mediator-exchange channels is the allowed emission of an X object from the t-channel coloured, charged mediator. Also demonstrated was the importance of a correct treatment of the mediator width, which can signficantly alter the kinematic behaviour of the model in the case of a narrow mediator able to go on-shell in the s-channel. This considerably complicates the analysis of the t-channel simplified model in the mono-jet channel, as described in chapter 7.

This thesis studied data produced in proton-proton collisions by the Large Hadron Collider (LHC) and collected by the ATLAS detector—the design and structure of the detector were described in chapter 4. That chapter also included details of the reconstruction and calibration of important physics objects such as leptons, jets and $E_{\mathrm{T}}^{\mathrm{miss}}$, in Run I and, following the long shutdown and detector upgrades, in Run II. All members of the ATLAS Collaboration are required to contribute to some form of performance studies, and the author's work in corrections to the calibration of the energy of hadronically-decaying taus, important for many analyses including the $H \to \tau^+\tau^-$ search, was described in chapter 5.

The ATLAS mono-$Z(\ell^+\ell^-)$ search for DM, described in chapter 6, was a study of the D1, D5 and D9 operators along with the $ZZ\chi\bar{\chi}$ EFT, for which the mono-Z channel is particularly important. The analysis was performed with the full 20.3 fb^{-1} dataset collected during Run I at a centre-of-mass energy of 8 TeV. Also included was a t-channel simplified model with Majorana fermion DM (a variant of the tS model), which is motivated by a direct parallel with SUSY where the neutralino and squark play the roles of the DM and scalar mediator respectively. Events were selected with two same-flavour opposite-sign electrons or muons, which had an invariant mass within a window of the Z boson mass, and with a momentum balanced and back-to-back with a large amount of $E_{\mathrm{T}}^{\mathrm{miss}}$. The dominant background in this analysis was the $ZZ \to \nu\bar{\nu}\,\ell^+\ell^-$ process, followed by the $WZ \to \ell\nu\,\ell^+\ell^-$ process (in which one charged lepton is not identified), both of

which were estimated with Monte Carlo (MC) simulation, and validated in a 4- and 3-lepton control region (CR) respectively. The remaining WW, top, W+jets and Z+jets backgrounds were all estimated with data-driven methods. The systematic uncertainty for the main backgrounds was dominanted by the theoretical uncertainty taken from the choice of generator (contributing 35% in each signal region), while experimentally the largest contributors were the lepton energy scales and the Jet Energy Scale (JES) and and Jet Energy Resolution (JER). The signal uncertainties for the t-channel model were taken from the D5 EFT, which has been demonstrated to be the most similar to the simplified model in the heavy mediator limit. Lower limits at 90%C.L. on the suppression scale of the EFT operators were obtained, as well as 95%C.L. upper limits on the tS model cross section and coupling strength $g_{q\chi}$. The simplified model coupling constraints were presented as a function of m_χ and M_{med}, and ranged from 1.9 at (m_χ = 10 GeV, M_{med} = 200 GeV) to 8.2 at (m_χ = 400 GeV, M_{med} = 1200 GeV); the analysis was found to be insensitive to the model when $m_\chi \geq 1000$ GeV. These constraints were also compared with the lower limits suggested by relic density calculations, and a region of parameter space ruled out under the assumption that this model of DM and its interactions with quarks is the only new physics. This was the first appearance of this t-channel simplified model in generic mono-X ATLAS analyses.

Following the conclusion of Run I and during the long shutdown, many ATLAS mono-X analyses had published limits on the EFT operators, but had included only one or two simplified models, with no consistency among the channels. The Dark Matter Forum therefore collated a list of recommended simplified models for inclusion in Run II analyses; in chapter 7, the work to constrain three of the five simplest recommended models using Run I results from the public ATLAS mono-jet, mono-$Z(\ell\ell)$ and mono-$W/Z(jj)$ analyses was described. This study involved calculating model-independent limits on the visible cross section of new physics with the use of the HistFitter software framework in some cases, and calculating a comprehensive set of theoretical uncertainties associated with the choice of Parton Distribution Function (PDF), tune and factorisation and renormalisation scales in the generation process. A framework was developed to simulate signal samples, approximate the interactions with the material of the ATLAS detector, and to calculate limits in each channel, while the framework was also validated against public results from the analyses. We found the strongest limits were obtained from a reinterpretation of results in the mono-jet channel as expected, but also concluded that the relative simplicity and cleanliness of alternative channels, and particularly the complicated behaviour of the tS model in the mono-jet channel, indicate that these channels are still extremely useful in searches for DM.

Once the LHC began colliding protons again at a centre-of-mass energy of 13 TeV in Run II, preliminary results were soon to follow, as only a few fb^{-1} of data at the higher energy were required to obtain constraints comparable to what was achieved with all the available Run I data. The preliminary mono-$W/Z(jj)$ analysis, described in chapter 8, used the first 3.2 fb^{-1} of 25ns Run II data, and was designed to search for the $ZZ\chi\bar{\chi}$ EFT operator and the sV simplified model, through use of groomed large-R jets with a mass close to W or Z mass and a 2-prong substructure, produced in association with a large amount of $E_{\mathrm{T}}^{\mathrm{miss}}$. The main backgrounds ($W$+jets, Z+jets and $t\bar{t}$) were estimated with simulation, but constrained with the use of three dedicated control regions designed to be rich in each desired background process. To ensure the analysis was studied with a fully-efficiency calorimeter-based $E_{\mathrm{T}}^{\mathrm{miss}}$ trigger, the $E_{\mathrm{T,\,no\,}\mu}^{\mathrm{miss}}$ variable was used which adds the p_{T} of all muons to the $E_{\mathrm{T}}^{\mathrm{miss}}$. This variable from each of the signal and control regions, along with all the estimated uncertainties, was input to a profile likelihood fitting procedure, to calculate scale factors for each background consistently across all regions, along with a limit on the signal strength μ. The 95% C.L. limit on μ for the sV model was presented as a function of the DM and mediator masses, for fixed coupling strengths of g_q = 0.25 and g_χ = 1.0, and found to range from close to unity for small m_χ and M_{med}, to $\mathcal{O}(50)$ for much of the parameter space; the analysis becomes insensitive to large m_χ in combination with an off-shell mediator. The limit on the $ZZ\chi\bar{\chi}$ EFT was converted to a lower limit on the suppression scale, which ranged from 560 GeV for low-mass DM to 360 GeV for m_χ = 1000 GeV. These were the first mono-X results to be publicly released with Run II data.

As further data is collected at 13 TeV, limits in all mono-X channels will continue to strengthen, as we push further into the simplified model parameter space that remains available. The High Luminosity LHC (HL-LHC), expected to increase the data produced by the LHC by approximately a factor of 10, as well as other, higher-energy collider proposals, suggest that search to produce and identify DM will continue for many years yet. We look forward to seeing what the future of collider physics holds, and perhaps even witnessing a DM discovery.

List of Acronyms

ADMX Axion Dark Matter eXperiment

AFII Atlfast-II

AMS Alpha Magnetic Spectrometer

AOD Analysis Object Data

BDT boosted decision tree

BSM Beyond the Standard Model

C/A Cambridge-Aachen

CaloTag Calorimeter Tagged

CAST CERN Axion Solar Telescope

CB ComBined

CKM Cabibbo-Kobayashi-Maskawa

CMB Cosmic Microwave Background

CR control region

CSCs Cathode Strip Chambers

D3PD Derived^3 Physics Data

DM dark matter

ECF energy correlation function

EF Event Filter

EFT Effective Field Theory

EM electromagnetic

EMB ElectroMagnetic Barrel

EMEC ElectroMagnetic EndCap

ESD Event Summary Data

EW electroweak

EWSB electroweak symmetry breaking

FCal Forward Calorimeter

GRL Good Runs List

HEC Hadronic EndCap

HL-LHC High Luminosity LHC

HLT High Level Trigger

IBL Insertable B-Layer

ID inner detector

IP interaction point

IRC infra-red and collinear

ISR Initial State Radiation

JER Jet Energy Resolution

JES Jet Energy Scale

JMS Jet Mass Scale

JVF jet vertex fraction

JVT jet vertex tagger

LAr liquid argon

LC Local Hadronic Calibration

LH left-handed

LHC Large Hadron Collider

LINAC linear accelerator

LKP Lightest Kaluza-Klein Particle

LO leading order

LSP Lightest Supersymmetric Particle

MC Monte Carlo

MDTs Monitored Drift Tubes

MLL maximised log-likelihood

MS muon spectrometer

MSSM Minimal Supersymmetric Simplified Model

MVA multivariate analysis

NLO next-to-leading-order

NNLO next-to-next-to-leading-order

NNLL next-to-next-to-leading-log

NP new physics

OS opposite-sign

PDF Parton Distribution Function

PMNS Pontecorvo-Maki-Nakagawa-Sakata

PMTs photomultiplier tubes

PS Proton Synchrotron

QCD quantum chromodynamics

QED quantum electrodynamics

RDO Raw Digital Object

RF radiofrequency

RH right-handed

RoIs regions of interest

RPCs Resistive Plate Chambers

SA Stand Alone

SCT semiconductor tracker

SHiP Search for Hidden Particles

SiM simplified model

SM Standard Model

SPS Super Proton Synchrotron

SR signal region

SS same-sign

ST Segment Tagged

STACO STAtistical COmbination

SUSY Supersymmetry

TES Tau Energy Scale

TGCs Thin Gap Chambers

TRT transition radiation tracker

TST track-based soft term

WIMP Weakly Interacting Massive Particle

WLCG Worldwide LHC Computing Grid

References

[1] The ATLAS Collaboration. "Identification and energy calibration of hadronically decaying tau leptons with the ATLAS experiment in pp collisions at $\sqrt{s}$ = 8 TeV". In: *Eur. Phys. J. C* 75 (2015), p. 303. arXiv: 1412.7086 [hep-ex] (p. v, 65, 70–72, 76, 91).

[2] A. Nelson *et. al.* "Search for dark matter in the mono-Z channel using 20.3 fb^{-1} of LHC data produced at $\sqrt{s}$ = 8 TeV collected by the ATLAS detector". eprint: ATL-COM-PHYS-2013-338. 2013 (p. v, 93, 96, 107, 109, 110, 112–115, 117, 119, 121, 122, 129–131, 133).

[3] The ATLAS Collaboration. "Search for dark matter in events with a Z boson and missing transverse momentum in pp collisions at $\sqrt{s}$ = 8 TeV with the ATLAS detector". In: *Phys. Rev. D.* 90 (2014), p. 012004. arXiv: 1404.0051 [hep-ex] (p. v, 93, 134, 135, 155, 162, 163).

[4] A.J. Brennan, M.F. McDonald, J. Gramling, T.D. Jacques. "Collide and Conquer: Constraints on Simplified Dark Matter Models using Mono-X Collider Searches". In: *JHEP* 05 (2016), p. 112. arXiv: 1603.01366 [hep-ph] (p. v).

[5] The ATLAS Collaboration. "Search for dark matter produced in association with a hadronically decaying vector boson in pp collisions at $\sqrt{s}$ = 13 TeV with the ATLAS detector at the LHC". eprint: ATLAS-CONF-2015-080. 2015 (p. vi, 150, 177, 178, 220, 222, 223).

[6] A. Nelson *et. al.* "Search for Dark Matter in association with a hadronically decaying vector boson in pp collisions at $\sqrt{s}$ = 13 TeV with the ATLAS detector". eprint: ATL-COM-PHYS-2015-1231. 2015 (p. vi, 177, 180, 198, 208, 216, 217).

[7] The ATLAS Collaboration. "Observation of a new particle in the search for the Standard Model Higgs boson with the ATLAS detector at the LHC". In: *Phys. Lett. B* 716 (2012), pp. 1–29. arXiv: 1207.7214 [hep-ex] (p. 1).

[8] The CMS Collaboration. “Observation of a new boson at a mass of 125 GeV with the CMS experiment at the LHC”. In: *Phys. Lett. B* 716 (2012), p. 30. arXiv: 1207.7235 [hep-ex] (p. 1).

[9] F. Zwicky. “Die Rotverschiebung von extragalaktischen Nebeln”. In: *Helv. Phys. Acta* 6 (1933), pp. 110–127 (p. 1).

[10] J. Goodman, M. Ibe, A. Rajaraman, W. Shepherd, T.M.P. Tait, H.-B. Yu. “Constraints on Dark Matter from Colliders”. In: *Phys. Rev. D* 82 (2010), p. 116010. arXiv: 1008.1783 [hep-ph] (p. 1, 26, 27, 29).

[11] The ATLAS Collaboration. ”Search for New Phenomena in Monojet plus Missing Transverse Momentum Final States using $10 fb^{-1}$ of pp Collisions at $\sqrt{s} = 8$ TeV with the ATLAS detector at the LHC”. eprint: ATLAS-CONF-2012-147. 2012 (p. 1, 32, 149).

[12] The CMS Collaboration. ”Search for new physics in monojet events in pp collisions at $\sqrt{s} = 8$ TeV”. eprint: CMS-PAS-EXO-12-048. 2013 (p. 1, 38, 43, 149).

[13] The ATLAS Collaboration. “Search for dark matter candidates and large extra dimensions in events with a photon and missing transverse momentum in pp collision data at $\sqrt{s} = 7$ TeV with the ATLAS detector”. In: *Phys. Rev. Lett.* 110 (2013), p. 011802. arXiv: 1209.4625 (p. 1).

[14] G. Busoni, A. De Simone, E. Morgante, A. Riotto. “On the Validity of the Effective Field Theory for Dark Matter Searches at the LHC”. In: *Phys. Lett. B* 728 (2014), 412–421. arXiv: 1307.2253 [hep-ph] (p. 2, 31, 149).

[15] D. Abercrombie *et. al.* ”Dark Matter Benchmark Models for Early LHC Run-2 Searches: Report of the ATLAS/CMS Dark Matter Forum”. 2015. arXiv: 1507.00966 (p. 2, 3, 38, 152, 178, 223).

[16] N. Zhou, D. Berge, and D. Whiteson. “Mono-everything: combined limits on dark matter production at colliders from multiple final states”. In: *Phys. Rev. D* 87 (2013), p. 095013. arXiv: 1302.3619 (p. 2, 149).

[17] P. Harris, V. V. Khoze, M. Spannowsky and C. Williams. “Constraining Dark Sectors at Colliders: Beyond the Effective Theory Approach”. In: *Phys. Rev. D* 91 (2015), p. 055009. arXiv: 1411.0535 (p. 2, 38).

[18] O. Buchmueller, M.J. Dolan, S.A. Malik, C. McCabe. “Characterising dark matter searches at colliders and direct detection experiments: Vector mediators”. In: *JHEP* 01 (2015), p. 037. arXiv: 1407.8257 [hep-ph] (p. 2, 38).

[19] A. DiFranzo, K. I. Nagao, A. Rajaraman, and T. M. P. Tait. "Simplified Models for Dark Matter Interacting with Quarks". In: *JHEP* 11 (2013), p. 014. arXiv: 1308.2679 (p. 2, 38).

[20] J. Heisig, M. Krämer, M. Pellen, C. Wiebusch. "Constraints on Majorana Dark Matter from the LHC and IceCube". In: *Phys. Rev. D* 93 (2016), p. 055029. arXiv: 1509.07867 [hep-ph] (p. 2, 38).

[21] M. Blennow, J. Herrero-Garcia, T. Schwetz and S. Vogl. "Halo-independent tests of dark matter direct detection signals: local DM density, LHC, and thermal freeze-out". In: *JCAP* 1508 (2015), p. 039. arXiv: 1505.05710 (p. 2, 38).

[22] O. Lebedev and Y. Mambrini. "Axial dark matter: The case for an invisible Z?". In: *Phys. Lett. B* 734 (2014), p. 350. arXiv: 1403.4837 (p. 2, 38).

[23] A. Alves, A. Berlin, S. Profumo and F. S. Queiroz. "Dark Matter Complementarity and the Z′ Portal". In: *Phys. Rev. D* 92 (2015), p. 083004. arXiv: 1501.03490 (p. 2, 38).

[24] A. Alves, S. Profumo and F. S. Queiroz. "The dark Z' portal: direct, indirect and collider searches". In: *JHEP* 1404 (2014), p. 063. arXiv: 1312.5281 (p. 2, 38).

[25] A. Alves, A. Berlin, S. Profumo and F. S. Queiroz. "Dirac-fermionic dark matter in $U(1)_X$ models". In: *JHEP* 1510 (2015), p. 076. arXiv: 1506.06767 (p. 2, 38).

[26] H. An, X. Ji and L. T. Wang. "Light Dark Matter and Z' Dark Force at Colliders". In: *JHEP* 1207 (2012), p. 182. arXiv: 1202.2894 (p. 2, 38, 153, 166).

[27] H. An, R. Huo and L. T. Wang. "Searching for Low Mass Dark Portal at the LHC". In: *Phys. Dark Univ.* 2 (2013), p. 50. arXiv: 1212.2221 (p. 2, 38).

[28] M. T. Frandsen, F. Kahlhoefer, A. Preston, S. Sarkar and K. Schmidt-Hoberg. "LHC and Tevatron Bounds on the Dark Matter Direct Detection Cross-Section for Vector Mediators". In: *JHEP* 1207 (2012), p. 123. arXiv: 1204.3839 (p. 2, 38).

[29] G. Arcadi, Y. Mambrini, M. H. G. Tytgat and B. Zaldivar. "Invisible Z' and dark matter: LHC vs LUX constraints". In: *JHEP* 1403 (2014), p. 134. arXiv: 1401.0221 (p. 2, 38).

[30] I. M. Shoemaker and L. Vecchi. "Unitarity and Monojet Bounds on Models for DAMA, CoGeNT, and CRESST-II". In: *Phys. Rev. D* 86 (2012), p. 015023. arXiv: 1112.5457 (p. 2, 38).

[31] M. T. Frandsen, F. Kahlhoefer, S. Sarkar and K. Schmidt-Hoberg. "Direct detection of dark matter in models with a light Z'". In: *JHEP* 1109 (2011), p. 128. arXiv: 1107.2118 (p. 2, 38).

[32] P. Gondolo, P. Ko and Y. Omura. "Light dark matter in leptophobic Z' models". In: *Phys. Rev. D* 85 (2012), p. 035022. arXiv: 1106.0885 (p. 2, 38).

[33] M. Fairbairn and J. Heal. "Complementarity of dark matter searches at resonance". In: *Phys. Rev. D* 90 (2014), p. 115019. arXiv: 1406.3288 (p. 2, 38).

[34] T. Jacques and K. Nordström. "Mapping monojet constraints onto Simplified Dark Matter Models". In: *JHEP* 06 (2015), p. 142. arXiv: 1502.05721 (p. 2, 38, 153, 221).

[35] N. F. Bell, Y. Cai and R. K. Leane. "Mono-W Dark Matter Signals at the LHC: Simplified Model Analysis". In: *JCAP* 1601 (2016), p. 051. arXiv: 1512.00476 (p. 2, 37, 38, 166).

[36] M. Chala, F. Kahlhoefer, M. McCullough, G. Nardini, K. Schmidt-Hoberg. "Constraining Dark Sectors with Monojets and Dijets". In: *JHEP* 07 (2015), p. 089. arXiv: 1503.05916 [hep-ph] (p. 2, 37, 38, 166).

[37] F. Kahlhoefer, K. Schmidt-Hoberg, T. Schwetz and S. Vogl. "Implications of unitarity and gauge invariance for simplified dark matter models". In: *JHEP* 1602 (2016), p. 016. arXiv: 1510.02110 (p. 2, 35, 37, 38, 166).

[38] Y. Bai and J. Berger. "Fermion Portal Dark Matter". In: *JHEP* 1311 (2013), p. 171. arXiv: 1308.0612 (p. 2, 38).

[39] H. An, L.-T. Wang, H. Zhang. "Dark matter with t-channel mediator: a simple step beyond contact interaction". In: *Phys. Rev. D* 89 (2014), p. 115014. arXiv: 1308.0592 [hep-ph] (p. 2, 38).

[40] S. Chang, R. Edezhath, J. Hutchinson, M. Luty. "Effective WIMPs". In: *Phys. Rev. D* 89 (2014), p. 015011. arXiv: 1307.8120v1 [hep-ph] (p. 2, 38).

[41] M. Papucci, A. Vichi, K.M. Zurek. "Monojet versus rest of the world I: t-channel Models". In: *JHEP* 11 (2014), p. 024. arXiv: 1402.2285 [hep-ph] (p. 2, 36, 38, 39, 152, 153, 166).

[42] M. Garny, A. Ibarra and S. Vogl. “Signatures of Majorana dark matter with t-channel mediators”. In: *Int. J. Mod. Phys. D* 24 (2015), p. 1530019. arXiv: 1503.01500 (p. 2, 38).

[43] M. Garny, A. Ibarra, S. Rydbeck and S. Vogl. “Majorana Dark Matter with a Coloured Mediator: Collider vs Direct and Indirect Searches”. In: *JHEP* 1406 (2014), p. 169. arXiv: 1403.4634 (p. 2, 38).

[44] N. F. Bell, J. B. Dent, A. J. Galea, T. D. Jacques, L. M. Krauss and T. J. Weiler. “W/Z Bremsstrahlung as the Dominant Annihilation Channel for Dark Matter, Revisited”. In: *Phys. Lett. B* 706 (2011), pp. 6–12. arXiv: 1104.3823 (p. 2, 38, 145).

[45] J. Abdallah et al. “Simplified Models for Dark Matter Searches at the LHC”. In: *Phys. Dark Uni.* 9-10 (2015), pp. 8–23. arXiv: 1506.03116 (p. 3).

[46] A.J. Brennan. ”A preliminary look at simplified models of dark matter”. eprint: ATL-COM-PHYS-2015-019. 2015 (p. 3).

[47] A. Purcell. ”Go on a particle quest at the first CERN webfest”. 2012. URL: https://sciencenode.org/spotlight/go-particle-quest-first-cern-hackfest.php (p. 6).

[48] Particle Data Group Collaboration. “Review of Particle Physics”. In: *Chin. Phys. C* 38 (2014), p. 090001 (p. 6, 65, 69, 70, 177).

[49] J.N. Bahcall and C. Peña-Garay. “Solar models and solar neutrino oscillations”. In: *New J. Phys.* 6 (2004), p. 63. arXiv: hep-ph/0404061 (p. 9).

[50] K. Freese. “Review of Observational Evidence for Dark Matter in the Universe and in upcoming searches for Dark Stars”. In: *Publ. Ser.* 36 (2009), pp. 113–126. arXiv: 0812.4005 [astro-ph] (p. 11).

[51] R. Tojeiro. ”Understanding the Cosmic Microwave Background Temperature Power Spectrum”. 2006. URL: http://www.roe.ac.uk/ifa/postgrad/pedagogy/2006_tojeiro.pdf (p. 13).

[52] Planck Collaboration. “Planck 2013 results. XV. CMB power spectra and likelihood”. In: *A&A* 571 (2014), A15. arXiv: 1303.5075 [astro-ph] (p. 14, 15).

[53] E. Komatsu *et. al.* “Seven-year Wilkinson Microwave Anisotropy Probe (WMAP) Observations: Cosmological Interpretation”. In: *Astrophys. J. Suppl.* 192 (2011), p. 18. arXiv: 1001.4538 [astro-ph] (p. 14).

[54] Planck Collaboration. ”Planck: Picture Gallery”. 2013. URL: http://www.cosmos.esa.int/web/planck/picture-gallery (p. 14, 15).

[55] G. Bertone, D. Hooper, J. Silk. “Particle Dark Matter: Evidence, Candidates and Constraints”. In: *Phys.Rept.* 405 (2005), pp. 279–390. arXiv: hep-ph/0404175 (p. 15, 145).

[56] G. Steigman, B. Dasgupta, J. F. Beacom. “Precise Relic WIMP Abundance and its Impact on Searches for Dark Matter Annihilation”. In: *Phys. Rev. D* 86 (2012), p. 023506. arXiv: 1204.3622v3 [hep-ph] (p. 15, 145).

[57] E. Bulbul *et. al.* “Detection of An Unidentified Emission Line in the Stacked X-ray spectrum of Galaxy Clusters”. In: *Astrophys. J.* 789 (2014), p. 13. arXiv: 1402.2301 [astro-ph.CO] (p. 16).

[58] A. Boyarsky, O. Ruchayskiy, D. Iakubovskyi and J. Franse. “Unidentified Line in X-Ray Spectra of the Andromeda Galaxy and Perseus Galaxy Cluster”. In: *Phys. Rev. Lett.* 113 (2014), p. 251301. arXiv: 1402.4119 [astro-ph.CO] (p. 16).

[59] K.N. Abazajian *et. al.* ”Light Sterile Neutrinos: A White Paper”. 2012. arXiv: 1204.5379 [hep-ph] (p. 16).

[60] S.N. Gninenko, D.S. Gorbunov, and M.E. Shaposhnikov. “Search for GeV-scale sterile neutrinos responsible for active neutrino oscillations and baryon asymmetry of the Universe”. In: *Adv. High Energy Phys.* 2012 (2012), p. 718259. arXiv: 1301.5516 [hep-ph] (p. 16).

[61] A. Harada and A. Kamada. “Structure formation in a mixed dark matter model with decaying sterile neutrino: the 3.5 keV X-ray line and the Galactic substructure”. In: *JCAP* 1601.01 (2016), p. 031. arXiv: 1412.1592 [astro-ph.CO] (p. 16).

[62] S. Horiuchi *et. al.* “Properties of resonantly produced sterile neutrino dark matter subhaloes”. In: *Mon. Not. Roy. Astron. Soc.* 456.4 (2016), pp. 4346–4353. arXiv: 1512.04548 [astro-ph.CO] (p. 16).

[63] The SHiP Collaboration. ”A facility to Search for Hidden Particles (SHiP) at the CERN SPS”. 2015. arXiv: 1504.04956 [physics.ins-det] (p. 16).

[64] L.D. Duffy and K. van Bibber. “Axions as Dark Matter Particles”. In: *New J. Phys.* 11 (2009), p. 105008. arXiv: 0904.3346 [hep-ph] (p. 16).

[65] T.M. Shokair *et. al.* "Future Directions in the Microwave Cavity Search for Dark Matter Axions". In: *Int. J. Mod. Phys.* A29 (2014), p. 1443004. arXiv: 1405.3685 [physics.ins-det] (p. 16).

[66] K. Barth *et. al.* "CAST constraints on the axion-electron coupling". In: *JCAP* 1305 (2013), p. 010. arXiv: 1302.6283 [astro-ph.SR] (p. 16).

[67] R. Bernabei *et. al.* "Search for solar axions by Primakoff effect in NaI crystals". In: *Phys. Lett.* B515 (2001), pp. 6–12 (p. 16).

[68] E. Armengaud *et. al.* "Axion searches with the EDELWEISS-II experiment". In: *JCAP* 1311 (2013), p. 067. arXiv: 1307.1488 [astro-ph.CO] (p. 16).

[69] The ATLAS Collaboration. "Summary of the searches for squarks and gluinos using $\sqrt{s}$ = 8 TeV pp collisions with the ATLAS experiment at the LHC". In: *JHEP* 10 (2015), p. 054. arXiv: 1507.05525 [hep-ex] (p. 17).

[70] The ATLAS Collaboration. "ATLAS Run 1 searches for direct pair production of third-generation squarks at the Large Hadron Collider". In: *Eur. Phys. J. C* 75 (2015), p. 510. arXiv: 1506.08616 [hep-ex] (p. 17).

[71] The ATLAS Collaboration. "Search for the electroweak production of supersymmetric particles in $\sqrt{s}$ = 8 TeV pp collisions with the ATLAS detector". In: *Phys. Rev. D* 93 (2016), p. 052002. arXiv: 1509.07152 [hep-ex] (p. 17).

[72] The ATLAS Collaboration. "Summary of the ATLAS experiment's sensitivity to supersymmetry after LHC Run 1 - interpreted in the phenomenological MSSM". In: *JHEP* 10 (2015), p. 134. arXiv: 1508.06608 [hep-ex] (p. 17).

[73] The CMS Collaboration. "Search for supersymmetry with a photon, a lepton, and missing transverse momentum in pp collisions at $\sqrt{s}$ = 8 TeV". In: *Phys. Lett. B* 757 (2016), p. 6. arXiv: 1508.01218 [hep-ex] (p. 17).

[74] The CMS Collaboration. "Search for supersymmetry in electroweak production with photons and large missing transverse energy in pp collisions at $\sqrt{s}$ = 8 TeV". In: *Phys. Lett. B* 759 (2016), p. 479. arXiv: 1602.08772 [hep-ex] (p. 17).

[75] The CMS Collaboration. "Phenomenological MSSM interpretation of CMS searches in pp collisions at $\sqrt{s}$ = 7 and 8 TeV". In: *JHEP* 10 (2016), p. 129. arXiv: 1606.03577 [hep-ph] (p. 17).

[76] T. Tait. *XXVI International Symposium on Lepton Photon Interactions at High Energies*. 2013. URL: https://indico.cern.ch/event/242095/ (p. 18).

[77] J. L. Feng. "Max-Planck-Institut für Kernphysik, Research: Dark Matter". 2016. URL: https://www.mpi-hd.mpg.de/lin/research_DM.en.html (p. 19).

[78] A.M. Green. "Astrophysical uncertainties on direct detection experiments". In: *Mod. Phys. Lett. A* 27 (2012), p. 1230004. arXiv: 1112.0524 [astro-ph] (p. 19).

[79] M. Schumann. "Dark Matter 2014". In: *EPJ Web Conf.* 96 (2015), p. 01027. arXiv: 1501.01200 [astro-ph.CO] (p. 20, 21).

[80] The XENON100 Collaboration. "Limits on spin-dependent WIMP-nucleon cross sections from 225 live days of XENON100 data". In: *Phys. Rev. Lett.* 111 (2013), p. 021301. arXiv: 1301.6620 [astro-ph.CO] (p. 20, 21).

[81] The DAMA Collaboration. "First results from DAMA/LIBRA and the combined results with DAMA/NaI". In: *Eur. Phys. J. C* 56 (2008), pp. 333–355. arXiv: 0804.2741 [astro-ph] (p. 20).

[82] The CoGeNT Collaboration. "CoGeNT: A Search for Low-Mass Dark Matter using p-type Point Contact Germanium Detectors". In: *Phys. Rev. D* 88 (2013), p. 012002. arXiv: 1208.5737 [astro-ph.CO] (p. 20).

[83] The CRESST-II Collaboration. "Results from 730 kg days of the CRESST-II Dark Matter Search". In: *Eur. Phys. J. C* 72 (2012), p. 1971. arXiv: 1109.0702 [astro-ph.CO] (p. 20).

[84] The CDMS-II Collaboration. "Silicon Detector Dark Matter Results from the Final Exposure of CDMS II". In: *Phys. Rev. Lett.* 111 (2013), p. 251301. arXiv: 1304.4279 [hep-ex] (p. 20).

[85] The XENON100 Collaboration. "Dark Matter Results from 225 Live Days of XENON100 Data". In: *Phys. Rev. Lett.* 109 (2012), p. 181301. arXiv: 1207.5988 [astro-ph.CO] (p. 20, 134, 135).

[86] The LUX Collaboration. "First results from the LUX dark matter experiment at the Sanford Underground Research Facility". In: *Phys. Rev. Lett.* 112 (2014), p. 091303. arXiv: 1310.8214 [astro-ph.CO] (p. 20, 134, 135, 170).

[87] The SuperCDMS Collaboration. "Search for Low-Mass WIMPs with SuperCDMS". In: *Phys. Rev. Lett.* 112 (2012), p. 241302. arXiv: 1402.7137 [hep-ex] (p. 20, 134, 135).

[88] The IceCube Collaboration. "Search for dark matter annihilations in the Sun with the 79-string IceCube detector". In: *Phys. Rev. Lett.* 110 (2013), p. 131302. arXiv: 1212.4097 [astro-ph] (p. 21, 134, 135).

[89] The Super-Kamiokande Collaboration. "An Indirect Search for WIMPs in the Sun using 3109.6 days of upward-going muons in Super-Kamiokande". In: *Astrophys. J.* 742 (2011), p. 78. arXiv: 1108.3384 [astro-ph.HE] (p. 21).

[90] The Fermi/LAT Collaboration. "The Large Area Telescope on the Fermi Gamma-ray Space Telescope Mission". In: *Astrophys. J.* 697 (2009), pp. 1071–1102. arXiv: 0902.1089 [astro-ph.IM] (p. 21).

[91] The AMS Collaboration. "First Result from the Alpha Magnetic Spectrometer on the International Space Station: Precision Measurement of the Positron Fraction in Primary Cosmic Rays of 0.5–350 GeV". In: *Phys. Rev. Lett.* 110 (2013), p. 141102 (p. 21).

[92] The Fermi-LAT Collaboration. "Dark Matter Constraints from Observations of 25 Milky Way Satellite Galaxies with the Fermi Large Area Telescope". In: *Phys. Rev. D* 89 (2014), p. 042001. arXiv: 1310.0828 [astro-ph.HE] (p. 21, 22).

[93] The Fermi-LAT Collaboration. "Fermi-LAT Observations of High-Energy γ-Ray Emission Toward the Galactic Center". In: *Astrophys. J.* 819.1 (2016), p. 44. arXiv: 1511.02938 [astro-ph.HE] (p. 22).

[94] T. Daylan *et. al.* "The characterization of the gamma-ray signal from the central Milky Way: A case for annihilating dark matter". In: *Phys. Dark Univ.* 12 (2016), pp. 1–23. arXiv: 1402.6703 [astro-ph.HE] (p. 22).

[95] D. Hooper and T. Linden. "On The Origin Of The Gamma Rays From The Galactic Center". In: *Phys. Rev. D* 84 (2011), p. 123005. arXiv: 1110.0006 [astro-ph.HE] (p. 22).

[96] K.N. Abazajian and M. Kaplinghat. "Detection of a Gamma-Ray Source in the Galactic Center Consistent with Extended Emission from Dark Matter Annihilation and Concentrated Astrophysical Emission". In: *Phys. Rev. D* 86 (2012). [Erratum: *Phys. Rev. D* 87, 129902 (2013)], p. 083511. arXiv: 1207.6047 [astro-ph.HE] (p. 22).

[97] L. Goodenough and D. Hooper. "Possible Evidence For Dark Matter Annihilation In The Inner Milky Way From The Fermi Gamma Ray Space Telescope". 2009. arXiv: 0910.2998 [hep-ph] (p. 22).

[98] C. Gordon and O. Macias. "Dark Matter and Pulsar Model Constraints from Galactic Center Fermi-LAT Gamma Ray Observations". In: *Phys. Rev. D* 88.8 (2013). [Erratum: *Phys. Rev. D* 89, no.4, 049901 (2014)], p. 083521. arXiv: 1306.5725 [astro-ph.HE] (p. 22).

[99] K.N. Abazajian, N. Canac, S. Horiuchi and M. Kaplinghat. "Astrophysical and Dark Matter Interpretations of Extended Gamma-Ray Emission from the Galactic Center". In: *Phys. Rev. D* 90.2 (2014), p. 023526. arXiv: 1402.4090 [astro-ph.HE] (p. 22).

[100] I. Cholis *et. al.* "The Galactic Center GeV Excess from a Series of Leptonic Cosmic-Ray Outbursts". In: *JCAP* 1512.12 (2015), p. 005. arXiv: 1506.05119 [astro-ph.HE] (p. 22).

[101] D. Gaggero, M. Taoso, A. Urbano, M. Valli and P. Ullio. "Towards a realistic astrophysical interpretation of the gamma-ray Galactic center excess". In: *JCAP* 1512.12 (2015), p. 056. arXiv: 1507.06129 [astro-ph.HE] (p. 22).

[102] Q. Yuan and B. Zhang. "Millisecond pulsar interpretation of the Galactic center gamma-ray excess". In: *JHEAp* 3-4 (2014), pp. 1–8. arXiv: 1404.2318 [astro-ph.HE] (p. 22).

[103] R. Bartels, S. Krishnamurthy and C. Weniger. "Strong support for the millisecond pulsar origin of the Galactic center GeV excess". In: *Phys. Rev. Lett.* 116.5 (2016), p. 051102. arXiv: 1506.05104 [astro-ph.HE] (p. 22).

[104] A. Rajaraman, W. Shepherd, T.M.P. Tait, A.M. Wijangco. "LHC Bounds on Interactions of Dark Matter". In: *Phys. Rev. D* 84 (2011), p. 095013. arXiv: 1108.1196 [hep-ph] (p. 26).

[105] P.J. Fox, R. Harnik, J. Kopp, Y. Tsai. "Missing Energy Signatures of Dark Matter at the LHC". In: *Phys. Rev. D* 85 (2012), p. 056011. arXiv: 1109.4398 [hep-ph] (p. 26, 30, 36, 41–43).

[106] K. Cheung, P.-Y. Tseng, Y.-L. S. Tsai, T.-C. Yuan. "Global Constraints on Effective Dark Matter Interactions: Relic Density, Direct Detection, Indirect Detection, and Collider". In: *JCAP* 1205 (2012), p. 001. arXiv: 1201.3402 [hep-ph] (p. 26).

[107] Y. Bai, P.J. Fox, R. Harnik. "The Tevatron at the Frontier of Dark Matter Direct Detection". In: *JHEP* 1012 (2010), p. 048. arXiv: 1005.3797 [hep-ph] (p. 26).

[108] The CDF Collaboration. "A search for dark matter in events with one jet and missing transverse energy in $p\bar{p}$ collisions at $\sqrt{s}$ = 1.96 TeV". In: *Phys. Rev. Lett.* 108 (2012), p. 211804. arXiv: 1203.0742 [hep-ex] (p. 26).

[109] The ATLAS Collaboration. "Search for dark matter candidates and large extra dimensions in events with a jet and missing transverse momentum with the ATLAS detector". In: *JHEP* 1304 (2013), p. 075. arXiv: 1210.4491 [hep-ex] (p. 26, 29, 134, 135).

[110] The CMS Collaboration. "Search for dark matter and large extra dimensions in monojet events in pp collisions at $\sqrt{s} = 7$ TeV". In: *JHEP* 09 (2012), p. 094. arXiv: 1206.5663 (p. 26).

[111] C.P. Burgess, M. Pospelov, T. ter Veldhuis. "The Minimal Model of Nonbaryonic Dark Matter: A Singlet Scalar". In: *Nucl. Phys. B* 619 (2001), pp. 709–728. arXiv: hep-ph/0011335 (p. 27).

[112] H. Davoudiasl, R. Kitano, T. Li, H. Murayama. "The New Minimal Standard Model". In: *Phys. Lett. B* 609 (2005), pp. 117–123. arXiv: hep-ph/0405097 (p. 27).

[113] S. Kanemura, S. Matsumoto, T. Nabeshima, N. Okada. "Can WIMP Dark Matter overcome the Nightmare Scenario?" In: *Phys. Rev. D* 82 (2010), p. 055026. arXiv: 1005.5651 [hep-ph] (p. 27).

[114] J. Goodman, M. Ibe, A. Rajaraman, W. Shepherd, T. M. P. Tait, H.-B. Yu. "Constraints on Light Majorana Dark Matter from Colliders". In: *Phys. Lett.* B695 (2011), pp. 185–188. arXiv: 1005.1286v4 [hep-ph] (p. 27).

[115] The ATLAS Collaboration. "Search for new phenomena in final states with an energetic jet and large missing transverse momentum in pp collisions at $\sqrt{s}$ = 8 TeV with the ATLAS detector". In: *Eur. Phys. J. C* 75 (2015), p. 299. arXiv: 1502.01518 [hep-ex] (p. 27, 38, 43, 44, 149, 155, 158, 161).

[116] S. Schramm. "Searching for Dark Matter with the ATLAS Detector in Events with an Energetic Jet and Large Missing Transverse Momentum". eprint: CERN-THESIS-2015-038. 2015 (p. 27, 28, 123, 157).

[117] U. Haisch, A. Hibbs and E. Re. "Determining the structure of dark-matter couplings at the LHC". In: *Phys. Rev. D* 89 (2014), p. 034009. arXiv: 1311.7131 [hep-ph] (p. 27, 28).

[118] R. Essig, J. Mardon, M. Papucci, T. Volansky, Y.-M. Zhong. “Constraining Light Dark Matter with Low-Energy e+e- Colliders”. In: *JHEP* 11 (2013), p. 167. arXiv: 1309.5084 [hep-ph] (p. 28).

[119] G. Busoni, A. De Simone, J. Gramling, E. Morgante, A. Riotto. “On the Validity of the Effective Field Theory for Dark Matter Searches at the LHC, Part II: Complete Analysis for the s-channel”. In: *JCAP* 1406 (2014), p. 060. arXiv: 1402.1275 [hep-ph] (p. 31–33, 149).

[120] G. Busoni, A. De Simone, T. Jacques, E. Morgante, A. Riotto. “On the Validity of the Effective Field Theory for Dark Matter Searches at the LHC Part III: Analysis for the t-channel”. In: *JCAP* 09 (2014), p. 022. arXiv: 1405.3101 [hep-ph] (p. 31, 149).

[121] The ATLAS Collaboration. ”Sensitivity to WIMP Dark Matter in the Final States Containing Jets and Missing Transverse Momentum with the ATLAS Detector at 14 TeV LHC”. eprint: ATL-PHYS-PUB-2014-007. 2014 (p. 33).

[122] L.M. Carpenter, A. Nelson, C. Shimmin, T.M.P. Tait, D. Whiteson. “Collider searches for dark matter in events with a Z boson and missing energy”. In: *Phys. Rev. D.* 87 (2012), p. 074005. arXiv: 1212.3352 [hep-ex] (p. 33, 34).

[123] B. Bhattacharya, J.M. Cline, A. Datta, G. Dupuis, D. London. “Quark-flavored scalar dark matter”. In: *Phys. Rev. D* 92 (2015), p. 115012. arXiv: 1509.04271 [hep-ph] (p. 35).

[124] R. M. Godbole, G. Mendiratta and T. M. P. Tait. “A Simplified Model for Dark Matter Interacting Primarily with Gluons”. In: *JHEP* 08 (2015), p. 064. arXiv: 1506.01408 (p. 35).

[125] A. Berlin, D. Hooper, S.D. McDermott. “Simplified Dark Matter Models for the Galactic Center Gamma-Ray Excess”. In: *Phys. Rev. D* 89 (2014), p. 115022. arXiv: 1404.0022 [hep-ph] (p. 35).

[126] C. Balázs, T. Li. “Simplified Dark Matter Models Confront the Gamma Ray Excess”. In: *Phys. Rev. D* 90 (2014), p. 055026. arXiv: 1407.0174 [hep-ph] (p. 35).

[127] N. Bell, A. Galea, J. Dent, T. Jacques, L. Krauss, T. Weiler. “Searching for Dark Matter at the LHC with a Mono-Z”. In: *Phys. Rev. D* 86 (2012), p. 096011. arXiv: 1209.0231v2 [hep-ph] (p. 36, 39, 93, 95, 134, 145).

[128] M. R. Buckley, D. Feld, and D. Goncalves. “Scalar Simplified Models for Dark Matter”. In: *Phys. Rev. D* 91 (2015), p. 015017. arXiv: 1410.6497 (p. 36).

[129] O. Buchmueller, M. J. Dolan, C. McCabe. "Beyond effective field theory for dark matter searches at the LHC". In: *JHEP* 01 (2014), p. 025. arXiv: 1308.6799v1 [hep-ph] (p. 41, 43, 44).

[130] The ATLAS Collaboration. "Search for new phenomena in the dijet mass distribution using $p - p$ collision data at $\sqrt{s} = 8$ TeV with the ATLAS detector". In: *Phys. Rev. D* 91 (2015), p. 052007. arXiv: 1407.1376 (p. 44, 45, 166).

[131] CERN. *TE-EPC-OMS Section Website*. 2015. URL: http://te-dep-epc-oms.web.cern.ch/te-dep-epc-oms/operation-en/operation.stm (p. 48).

[132] The ATLAS Collaboration. *Luminosity Public Results*. 2012. URL: https://twiki.cern.ch/twiki/bin/view/AtlasPublic/LuminosityPublicResults (p. 49, 50).

[133] The ATLAS Collaboration. *Luminosity Public Results Run 2*. 2015. URL: https://twiki.cern.ch/twiki/bin/view/AtlasPublic/LuminosityPublicResultsRun2 (p. 49, 50).

[134] The ATLAS Collaboration. "The ATLAS Experiment at the CERN Large Hadron Collider". In: *JINST* 3 (2008), S08003 (p. 49–53, 55, 57).

[135] H. Abreu *et. al.* "Performance of the electronic readout of the ATLAS liquid argon calorimeters". In: *JINST* 5 (2010), P09003 (p. 49).

[136] L. Evans and P. Bryant. "LHC Machine". In: *JINST* 3 (2008), S08001 (p. 50).

[137] H. Oide. "The Pixel Detector of the ATLAS experiment for Run 2 of the Large Hadron Collider". In: *JINST* 9.12 (2014), p. C12034 (p. 51).

[138] Y. Takubo. "The Pixel Detector of the ATLAS experiment for the Run 2 at the Large Hadron Collider". In: *JINST* 10.02 (2015), p. C02001. arXiv: 1411.5338 [physics.ins-det] (p. 51).

[139] The ATLAS Collaboration. "The ATLAS Simulation Infrastructure". In: *Eur. Phys. J. C* 70 (2010), pp. 823–874. arXiv: 1005.4568 (p. 58).

[140] J. Pumplin, D.R. Stump, J. Huston, H.L. Lai, P.M. Nadolsky and W.K. Tung. "New generation of parton distributions with uncertainties from global QCD analysis". In: *JHEP* 07 (2002), p. 012. arXiv: hep-ph/0201195 (p. 58, 74, 100, 157, 181).

[141] A. D. Martin, W. J. Stirling, R. S. Thorne and G. Watt. "Parton distributions for the LHC". In: *Eur. Phys. J. C* 63 (2009), pp. 189–285. arXiv: 0901.0002 (p. 58, 95, 155).

[142] H.-L. Lai, M. Guzzi, J. Huston, Z. Li, P. M. Nadolsky, J. Pumplin, C.-P. Yuan. "New parton distributions for collider physics". In: *Phys. Rev. D* 82 (2010), p. 074024. arXiv: 1007.2241 [hep-ph] (p. 58, 74, 101, 181).

[143] The ATLAS Collaboration. "ATLAS tunes of PYTHIA 6 and Pythia 8 for MC11". eprint: ATL-PHYS-PUB-2011-009. 2011 (p. 58, 74).

[144] T. Sjöstrand, S. Mrenna and P. Skands. "PYTHIA 6.4 physics and manual". In: *JHEP* 05 (2006), p. 026. arXiv: hep-ph/0603175 (p. 58, 73, 95, 101, 181).

[145] T. Sjöstrand, S. Mrenna and P. Skands. "A Brief Introduction to PYTHIA 8.1". In: *Comput. Phys. Commun.* 178 (2008), pp. 852–867. arXiv: 0710.3820 [hep-ph] (p. 58, 70, 101, 181).

[146] J. Alwall, M. Herquet, F. Maltoni, O. Mattelaer and T. Stelzer. "MadGraph 5: Going Beyond". In: *JHEP* 06 (2011), p. 128. arXiv: 1106.0522 [hep-ph] (p. 58, 95).

[147] T. Gleisberg *et. al.* "Event generation with SHERPA 1.1". In: *JHEP* 0902 (2009), p. 007. arXiv: 0811.4622 [hep-ph] (p. 59, 120, 181).

[148] S. Frixione, P. Nason, C. Oleari. "Matching NLO QCD computations with Parton Shower simulations: the POWHEG method". In: *JHEP* 0711 (2007), p. 070. arXiv: 0709.2092 [hep-ph] (p. 59, 181).

[149] S. Alioli, P. Nason, C. Oleari, E. Re. "A general framework for implementing NLO calculations in shower Monte Carlo programs: the POWHEG BOX". In: *JHEP* 1006 (2010), p. 043. arXiv: 1002.2581 [hep-ph] (p. 59, 181).

[150] S. Alioli, P. Nason, C. Oleari, E. Re. "NLO single-top production matched with shower in POWHEG: s- and t-channel contributions". In: *JHEP* 0909 (2009), p. 111. arXiv: 0907.4076 [hep-ph] (p. 59, 181).

[151] E. Re. "Single-top Wt-channel production matched with parton showers using the POWHEG method". In: *Eur. Phys. J. C* 71 (2011), p. 1547. arXiv: 1009.2450 [hep-ph] (p. 59, 181).

[152] T. Melia, P. Nason, R. Röntsch, G. Zanderighi. "W+W-, WZ and ZZ production in the POWHEG BOX". In: *JHEP* 1111 (2011), p. 078. arXiv: 1107.5051 [hep-ph] (p. 59, 100).

[153] M.L. Mangano, M. Moretti, F. Piccinini, R. Pittau and A. Polosa. "ALPGEN, a generator for hard multiparton processes in hadronic collisions". In: *JHEP* 0307 (2003), p. 001. arXiv: hep-ph/0206293 (p. 59, 73, 100).

[154] B.P. Kersevan and E. Richter-Was. “The Monte Carlo Event Generator AcerMC 1.0 with Interfaces to PYTHIA 6.2 and HERWIG 6.3”. In: *Comput. Phys. Comm.* 149 (2003), pp. 142–194. arXiv: hep-ph/0201302 (p. 59, 73, 101).

[155] B.P. Kersevan and E. Richter-Was. “The Monte Carlo Event Generator AcerMC 2.0 with Interfaces to PYTHIA 6.2 and HERWIG 6.5”. In: *Comput. Phys. Comm.* 184 (2013), pp. 919–985. arXiv: hep-ph/0405247 (p. 59, 73, 101).

[156] S. Frixione and B.R. Webber. “Matching NLO QCD computations and parton shower simulations”. In: *JHEP* 0206 (2002), p. 029. arXiv: hep-ph/0204244 (p. 59, 73, 101, 212).

[157] S. Frixione, F. Stoeckli, P. Torrielli, B. R. Webber, C. D. White. ”The MCaNLO 4.0 Event Generator”. 2010. arXiv: 1010.0819 [hep-ph] (p. 59, 101).

[158] G. Corcella *et al*. “HERWIG 6.5: an event generator for Hadron Emission Reactions With Interfering Gluons (including supersymmetric processes)”. In: *JHEP* 0101 (2001), p. 010. arXiv: hep-ph/0011363 (p. 59, 101).

[159] J. M. Butterworth, J. R. Forshaw, and M. H. Seymour. “Multiparton interactions in photoproduction at HERA”. In: *Z. Phys. C* 72 (1996), 637–646. arXiv: hep-ph/9601371 (p. 59, 73, 101).

[160] T. Binoth, M. Ciccolini, N. Kauer, M. Krämer. “Gluon-induced W-boson pair production at the LHC”. In: *JHEP* 0612 (2006), p. 046. arXiv: hep-ph/0611170 (p. 59, 100).

[161] P. Golonka, Z. Was. “PHOTOS Monte Carlo: a precision tool for QED corrections in Z and W decays”. In: *Eur. Phys. J. C* 45 (2006), pp. 97–107. arXiv: hep-ph/0506026 (p. 59, 101).

[162] N. Davidson, T. Przedzinski, Z. Was. ”PHOTOS Interface in C++; Technical and Physics Documentation”. 2010. arXiv: 1011.0937 [hep-ph] (p. 59, 101, 102).

[163] Z. Was. “TAUOLA the library for tau lepton decay, and KKMC/KORALB/ KORALZ/... status report”. In: *Nucl. Phys. Proc. Suppl.* 98 (2001), pp. 96–102. arXiv: hep-ph/0011305 (p. 59, 74, 101, 102).

[164] J.D. Chapman *et. al.* “The ATLAS detector digitization project for 2009 data taking”. In: *J. Phys. Conf. Ser.* 219 (2010), p. 032031 (p. 59).

[165] The GEANT4 Collaboration. “GEANT4 — a simulation toolkit”. In: *Nucl. Instrum. Meth. A* 506 (2003), pp. 250–303 (p. 59, 73, 100).

[166] W. Lukas. “Fast Simulation for ATLAS: Atlfast-II and ISF”. In: *J. Phys. Conf. Ser.* 396 (2012), p. 022031 (p. 59, 100).

[167] P.J. Laycock, N. Ozturk, M. Beckingham, R. Henderson and L. Zhou. “Derived Physics Data Production in ATLAS: Experience with Run 1 and Looking Ahead”. In: *J. Phys. Conf. Ser.* 513 (2014), p. 032052 (p. 59).

[168] W. Lampl *et. al.* ”Calorimeter Clustering Algorithms: Description and Performance”. eprint: ATL-LARG-PUB-2008-002. 2008 (p. 60).

[169] The ATLAS Collaboration. “Electron performance measurements with the ATLAS detector using the 2010 LHC proton-proton collision data”. In: *Eur. Phys. J. C* 72 (2012), p. 001. arXiv: 1110.3174v2 [hep-ph] (p. 60).

[170] The ATLAS Collaboration. ”Electron efficiency measurements with the ATLAS detector using the 2012 LHC proton-proton collision data”. eprint: ATLAS-CONF-2014-032. 2014 (p. 60, 123).

[171] The ATLAS Collaboration. ”Electron efficiency measurements with the ATLAS detector using the 2015 LHC proton-proton collision data”. eprint: ATLAS-CONF-2016-024. 2016 (p. 60, 194).

[172] The ATLAS Collaboration. ”Electron identification measurements in ATLAS using $\sqrt{s}$ = 13 TeV data with 50 ns bunch spacing”. eprint: ATL-PHYS-PUB-2015-041. 2015 (p. 60).

[173] The ATLAS Collaboration. “Electron and photon energy calibration with the ATLAS detector using LHC Run 1 data”. In: *Eur. Phys. J. C* 74.10 (2014), p. 3071. arXiv: 1407.5063 [hep-ex] (p. 61, 123).

[174] S. Hassani, L. Chevalier, E. Lancon, J.F. Laporte, R. Nicolaidou, A. Ouraou. “A muon identification and combined reconstruction procedure for the ATLAS detector at the LHC using the (MUONBOY, STACO, MuTag) reconstruction packages”. In: *Nucl. Instrum. Meth. A* 572 (2007), pp. 77–79 (p. 61).

[175] The ATLAS Collaboration. “Muon reconstruction performance of the ATLAS detector in proton-proton collision data at $\sqrt{s}$ = 13 TeV”. In: *Eur. Phys. J. C* 76 (2016), p. 292. arXiv: 1603.05598 [hep-ex] (p. 61, 193).

[176] The ATLAS Collaboration. “Measurement of the muon reconstruction performance of the ATLAS detector using 2011 and 2012 LHC proton-proton collision data”. In: *Eur. Phys. J. C* 74 (2014), p. 3130. arXiv: 1407.3935 [hep-ex] (p. 61, 89, 123).

[177] T. Barillari *et. al.* "Local hadronic calibration". eprint: ATL-LARG-PUB-2009-001-2. 2009 (p. 62).

[178] M. Cacciari, G.P. Salam, and G. Soyez. "The Anti-k(t) jet clustering algorithm". In: *JHEP* 04 (2008), p. 063. arXiv: 0802.1189 [hep-ph] (p. 63).

[179] Y.L. Dokshitzer, G.D. Leder, S. Moretti, and B.R. Webber. "Better jet clustering algorithms". In: *JHEP* 08 (1997), p. 001. arXiv: hep-ph/9707323 [hep-ph] (p. 63).

[180] S. Catani, Y.L. Dokshitzer, M.H. Seymour, B.R. Webber. "Longitudinally-invariant $k_\perp$-clustering algorithms for hadron-hadron collisions". In: *Nucl. Phys. B* 406 (1993), p. 187 (p. 63, 186).

[181] The ATLAS Collaboration. "Jet energy measurement and its systematic uncertainty in proton-proton collisions at $\sqrt{s}$ = 7 TeV with the ATLAS detector". In: *Eur. Phys. J. C* 75 (2015), p. 17. arXiv: 1406.0076 [hep-ex] (p. 63, 191).

[182] The ATLAS Collaboration. "Determination of the jet energy scale and resolution at ATLAS using Z/γ-jet events in data at $\sqrt{s}$=8 TeV". eprint: ATLAS-CONF-2015-057. 2015 (p. 63).

[183] The ATLAS Collaboration. "Monte Carlo Calibration and Combination of In-situ Measurements of Jet Energy Scale, Jet Energy Resolution and Jet Mass in ATLAS". eprint: ATL-CONF-2015-037. 2015 (p. 63).

[184] The ATLAS Collaboration. "Data-driven determination of the energy scale and resolution of jets reconstructed in the ATLAS calorimeters using dijet and multijet events at $\sqrt{s}$ = 8 TeV". eprint: ATLAS-CONF-2015-017. 2015 (p. 63, 67, 191).

[185] The ATLAS Collaboration. "Jet Calibration and Systematic Uncertainties for Jets Reconstructed in the ATLAS Detector at $\sqrt{s}$ = 13 TeV". eprint: ATL-PHYS-PUB-2015-015. 2015 (p. 63, 191).

[186] The ATLAS Collaboration. "Identification of boosted, hadronically decaying W bosons and comparisons with ATLAS data taken at $\sqrt{s}$ = 8 TeV". In: *Eur. Phys. J. C* 76 (2016), pp. 1–47. arXiv: 1510.05821 [hep-ex] (p. 64, 186).

[187] D. Krohn, J. Thaler, L.-T. Wang. "Jet Trimming". In: *JHEP* 1002 (2010), p. 084. arXiv: 0912.1342 [hep-ph] (p. 64, 186).

[188] S.D. Ellis, C.K. Vermilion, J.R. Walsh. "Recombination Algorithms and Jet Substructure: Pruning as a Tool for Heavy Particle Searches". In: *Phys. Rev. D* 094023 (2010), p. 81. arXiv: 0912.0033 [hep-ph] (p. 64, 188).

[189] S.D. Ellis, C.K. Vermilion, J.R. Walsh. "Techniques for improved heavy particle searches with jet substructure". In: *Phys. Rev. D* 80 (2009), p. 051501. arXiv: 0903.5081 [hep-ph] (p. 64, 188).

[190] J.M. Butterworth, A.R. Davison, M. Rubin, G.P. Salam. "Jet substructure as a new Higgs search channel at the LHC". In: *Phys. Rev. Lett.* 100 (2008), p. 242001. arXiv: 0802.2470 [hep-ph] (p. 64, 188).

[191] The ATLAS Collaboration. "Calibration of the performance of b-tagging for c and light-flavour jets in the 2012 ATLAS data". eprint: ATLAS-CONF-2014-046. 2014 (p. 65).

[192] The ATLAS Collaboration. "Calibration of b-tagging using dileptonic top pair events in a combinatorial likelihood approach with the ATLAS experiment". eprint: ATLAS-CONF-2014-004. 2014 (p. 65).

[193] The ATLAS Collaboration. "Commissioning of the ATLAS b-tagging algorithms using $t\bar{t}$ events in early Run-2 data". eprint: ATL-PHYS-PUB-2015-039. 2015 (p. 65).

[194] The ATLAS Collaboration. "The Optimization of ATLAS Track Reconstruction in Dense Environments". eprint: ATL-PHYS-PUB-2015-006. 2015 (p. 65).

[195] The ATLAS Collaboration. "A neural network clustering algorithm for the ATLAS silicon pixel detector". In: *JINST* 9 (2014), P09009. arXiv: 1406.7690 [hep-ex] (p. 65).

[196] The ATLAS Collaboration. "Performance of missing transverse momentum reconstruction in proton-proton collisions at 7 TeV with ATLAS". In: *Eur. Phys. J. C* 72 (2012), p. 1844. arXiv: 1108.5602 [hep-ex] (p. 66, 67, 194).

[197] The ATLAS Collaboration. "Performance of Missing Transverse Momentum Reconstruction in ATLAS studied in Proton-Proton Collisions recorded in 2012 at 8 TeV". eprint: ATLAS-CONF-2013-082. 2013 (p. 66, 124).

[198] The ATLAS Collaboration. "Performance of missing transverse momentum reconstruction for the ATLAS detector in the first proton-proton collisions at $\sqrt{s}$ = 13 TeV". eprint: ATL-PHYS-PUB-2015-027. 2015 (p. 66, 67, 194).

[199] M. Cacciari, G.P. Salam. "Pileup subtraction using jet areas". In: *Phys. Lett. B* 659 (2008), pp. 119–126. arXiv: 0707.1378 [hep-ph] (p. 67, 192).

[200] M. Cacciari, G.P. Salam, G. Soyez. "The Catchment Area of Jets". In: *JHEP* 0804 (2008), p. 005. arXiv: 0802.1188 [hep-ph] (p. 67, 192).

[201] The ATLAS Collaboration. "Measurement of the ttbar production cross section in the tau+jets channel using the ATLAS detector". In: *Eur. Phys. J. C* 73 (2013), p. 2328. arXiv: 1211.7205 [hep-ex] (p. 69).

[202] The ATLAS Collaboration. "Measurement of the top quark pair cross section with ATLAS in pp collisions at $\sqrt{s}$ = 7 TeV using final states with an electron or a muon and a hadronically decaying tau lepton". In: *Phys. Lett. B* 717 (2012), pp. 89–108. arXiv: 1205.2067 [hep-ex] (p. 69).

[203] The ATLAS Collaboration. "Measurement of tau polarization in $W \to \tau\nu$ decays with the ATLAS detector in pp collisions at $\sqrt{s}$ = 7 TeV". In: *Eur. Phys. J. C* 72 (2012), p. 2062. arXiv: 1204.6720 [hep-ex] (p. 69).

[204] The ATLAS Collaboration. "Measurement of the $W \to \tau\nu_\tau$ Cross Section in pp Collisions at $\sqrt{s}$ = 7 TeV with the ATLAS experiment". In: *Phys. Lett. B* 706 (2012), pp. 276–294. arXiv: 1108.4101 [hep-ex] (p. 69).

[205] The ATLAS Collaboration. "Measurement of the $Z \to \tau\tau$ Cross Section with the ATLAS Detector". In: *Phys. Rev. D* 84 (2011), p. 112006. arXiv: 1108.2016 [hep-ex] (p. 69).

[206] The ATLAS Collaboration. "Search for the Standard Model Higgs boson in the $H \to \tau^+\tau^-$ decay mode in $\sqrt{s}$ = 7 TeV pp collisions with ATLAS". In: *JHEP* 09 (2012), p. 070. arXiv: 1206.5971 [hep-ex] (p. 69).

[207] The ATLAS Collaboration. "Search for a heavy narrow resonance decaying to $e\mu$, $e\tau$, or $\mu\tau$ with the ATLAS detector in $\sqrt{s}$ = 7 TeV pp collisions at the LHC". In: *Phys. Lett. B* 723 (2013), pp. 15–32. arXiv: 1212.1272 [hep-ex] (p. 69).

[208] The ATLAS Collaboration. "Search for supersymmetry in events with large missing transverse momentum, jets, and at least one tau lepton in 20 fb^{-1} of $\sqrt{s}$ = 8 TeV proton-proton collision data with the ATLAS detector". In: *JHEP* 09 (2014), p. 103. arXiv: 1407.0603 [hep-ex] (p. 69).

[209] The ATLAS Collaboration. "Search for the direct production of charginos, neutralinos and staus in final states with at least two hadronically decaying taus and missing transverse momentum in pp collisions at $\sqrt{s}$ = 8 TeV with the ATLAS detector". In: *JHEP* 10 (2014), p. 096. arXiv: 1407.0350 [hep-ex] (p. 69).

[210] The ATLAS Collaboration. "Search for charged Higgs bosons through the violation of lepton universality in $t\bar{t}$ events using pp collision data at $\sqrt{s}$ = 7 TeV with the ATLAS experiment". In: *JHEP* 03 (2013), p. 076. arXiv: 1212.3572 [hep-ex] (p. 69).

[211] The ATLAS Collaboration. "Search for charged Higgs bosons decaying via $H^{\pm} \to \tau\nu$ in $t\bar{t}$ events using pp collision data at $\sqrt{s}$ = 7 TeV with the ATLAS detector". In: *JHEP* 06 (2012), p. 039. arXiv: 1204.2760 [hep-ex] (p. 69).

[212] The ATLAS Collaboration. "Search for the neutral Higgs bosons of the Minimal Supersymmetric Standard Model in pp collisions at $\sqrt{s}$ = 7 TeV with the ATLAS detector". In: *JHEP* 02 (2013), p. 095. arXiv: 1211.6956 [hep-ex] (p. 69).

[213] The ATLAS Collaboration. "A search for high-mass resonances decaying to $\tau^+\tau^-$ in pp collisions at $\sqrt{s}$ = 7 TeV with the ATLAS detector". In: *Phys. Lett. B* 719 (2013), pp. 242–260. arXiv: 1210.6604 [hep-ex] (p. 69).

[214] The ATLAS Collaboration. "Search for third generation scalar leptoquarks in pp collisions at $\sqrt{s}$ = 7 TeV with the ATLAS detector". In: *JHEP* 06 (2013), p. 033. arXiv: 1303.0526 [hep-ex] (p. 69).

[215] The ATLAS Collaboration. "Jet energy measurement with the ATLAS detector in proton-proton collisions at $\sqrt{s}$ = 7 TeV". In: *Eur. Phys. J. C* 73 (2013), p. 2304. arXiv: 1112.6426 [hep-ex] (p. 72).

[216] J. Bellm *et. al.* "Herwig 7.0 / Herwig++ 3.0 Release Note". 2015. arXiv: 1512.01178 [hep-ph] (p. 73).

[217] M. Bahr *et. al.* "Herwig++ Physics and Manual". In: *Eur. Phys. J. C* 58 (2008), pp. 639–707. arXiv: 0803.0883 [hep-ph] (p. 73).

[218] P. Skands. "Tuning Monte Carlo Generators: The Perugia Tunes". In: *Phys. Rev. D* 82 (2010), p. 074018. arXiv: 1005.3457 [hep-ph] (p. 74).

[219] The ATLAS Collaboration. "New ATLAS event generator tunes to 2010 data". eprint: ATL-PHYS-PUB-2011-008. 2011 (p. 74, 100).

[220] Z. Was and P. Golonka. "TAUOLA as tau Monte Carlo for future applications". In: *Nucl. Phys. Proc. Suppl.* 144 (2005), pp. 88–94. arXiv: hep-ph/0411377 (p. 74).

[221] E. Barberio, B. van Eijk and Z. Was. "PHOTOS: A Universal Monte Carlo for QED radiative corrections in decays". In: *Comput. Phys. Commun.* 66 (1991), 115–128 (p. 74).

[222] T. Sjöstrand et al. "An Introduction to PYTHIA 8.2". In: *Comput. Phys. Comm.* 191 (2015), pp. 159–177. arXiv: 1410.3012 (p. 74, 100, 155).

[223] The ATLAS Collaboration. "Modelling $Z \to \tau\tau$ processes in ATLAS with τ-embedded $Z \to \mu\mu$ data". In: *JINST* 10 (2015), P09018. arXiv: 1506.05623 [hep-ex] (p. 74).

[224] The ATLAS Collaboration. "Performance of the ATLAS muon trigger in pp collisions at $\sqrt{s}$ = 8 TeV". In: *Eur. Phys. J. C* 75 (2015), p. 120. arXiv: 1408.3179 [hep-ex] (p. 74).

[225] M.J. Woudstra on behalf of the ATLAS Collaboration. "Performance of the ATLAS muon trigger in pp collisions at $\sqrt{s}$ = 8 TeV". In: *J. Phys.: Conf. Ser.* 513 (2014), p. 012040 (p. 74).

[226] The ATLAS Collaboration. "Data-Quality Requirements and Event Cleaning for Jets and Missing Transverse Energy Reconstruction with the ATLAS Detector in Proton-Proton Collisions at a Center-of-Mass Energy of $\sqrt{s}$ = 7 TeV". eprint: ATLAS-CONF-2010-038. 2010 (p. 76).

[227] W. Verkerke, D. Kirkby. "The RooFit toolkit for data modeling". 2003. arXiv: physics/0306116 (p. 82).

[228] M. Goblirsch-Kolb, on behalf of the ATLAS Collaboration. "Muon Reconstruction Efficiency, Momentum Scale and Resolution in pp Collisions at 8 TeV with ATLAS". 2014. arXiv: 1408.7086 [hep-ex] (p. 89).

[229] The ATLAS Collaboration. "Summary of ATLAS Pythia8 tunes". eprint: ATL-PHYS-PUB-2012-003. 2012 (p. 100, 155, 157).

[230] The ATLAS Collaboration. "Search for invisible decays of a Standard Model Higgs boson produced in association with a Z boson". eprint: ATL-COM-PHYS-2013-654. 2013 (p. 101).

[231] The ATLAS Collaboration. "Search for New Physics in the Dijet Mass Distribution using 1 fb^{-1} of pp Collision Data at $\sqrt{s}$ = 7 TeV collected by the ATLAS Detector". In: *Phys. Lett. B* 708 (2012), pp. 37–54. arXiv: 1108.6311 [hep-ex] (p. 116).

[232] The ATLAS Collaboration. "Pile-up subtraction and suppression for jets in ATLAS". eprint: ATLAS-CONF-2013-083. 2013 (p. 124).

[233] The ATLAS Collaboration. "Improved luminosity determination in pp collisions at $\sqrt{s}$ = 7 TeV using the ATLAS detector at the LHC". In: *Eur. Phys. J.* 73 (2013), p. 2518. arXiv: 1302.4393 [hep-ex] (p. 125, 211).

[234] THE LHC Higgs Cross Section Working Group. "Handbook of LHC Higgs Cross Sections: 2. Differential Distributions". 2012. arXiv: 1201.3084 [hep-ph] (p. 127).

[235] J. Beringer, *et. al.* "The review of particle physics". In: *Phys. Rev. D* 86 (2012), p. 010001 (p. 128).

[236] M. Baak *et. al.* "HistFitter software framework for statistical data analysis". In: *Eur. Phys. J. C* 75 (2015), p. 153. arXiv: 1410.1280 [hep-ex] (p. 128, 162).

[237] G. J. Feldman, R. D. Cousins. "A Unified Approach to the Classical Statistical Analysis of Small Signals". In: *Phys. Rev. D* 57 (1998), pp. 3873–3889. arXiv: physics/9711021 (p. 128).

[238] The ATLAS Collaboration. "Search for dark matter in events with a hadronically decaying W or Z boson and missing transverse momentum in pp collisions at $\sqrt{s}$ = 8 TeV with the ATLAS detector". In: *Phys. Rev. Lett.* 112 (2014), p. 041802. arXiv: 1309.4017 [hep-ex] (p. 134, 135, 155, 164, 165).

[239] The CoGeNT Collaboration. "Results from a Search for Light-Mass Dark Matter with a p-type Point Contact Germanium Detector". In: *Phys. Rev. Lett.* 106 (2011), p. 131301. arXiv: 1002.4703 [astro-ph] (p. 134, 135).

[240] The SuperCDMS Collaboration. "Search for Low-Mass Weakly Interacting Massive Particles Using Voltage-Assisted Calorimetric Ionization Detection in the SuperCDMS Experiment". In: *Phys. Rev. Lett.* 112 (2014), p. 041302. arXiv: 1309.3259 [physics.ins-det] (p. 134, 135).

[241] The COUPP Collaboration. "First Dark Matter Search Results from a 4-kg CF_3I Bubble Chamber Operated in a Deep Underground Site". In: *Phys. Rev. D* 86 (2012). [Erratum: *Phys. Rev. D* 90, no.7, 079902 (2014)], p. 052001. arXiv: 1204.3094 [astro-ph] (p. 134, 135).

[242] The SIMPLE Collaboration. "Final Analysis and Results of the Phase II SIMPLE Dark Matter Search". In: *Phys. Rev. Lett.* 108 (2012), p. 201302. arXiv: 1106.3014 [astro-ph] (p. 134, 135).

[243] The PICASSO Collaboration. "Constraints on Low-Mass WIMP Interactions on ^{19}F from PICASSO". In: *Phys. Lett. B* 711 (2012), pp. 153–161. arXiv: 1202.1240 [hep-ex] (p. 134, 135).

[244] P. Gondolo, G. B. Gelmini. "Cosmic Abundances Of Stable Particles: Improved Analysis". In: *Nucl. Phys. B* 360 (1991), pp. 145–179 (p. 145).

[245] The ATLAS Collaboration. “Search for new phenomena with the monojet and missing transverse momentum signature using the ATLAS detector in $\sqrt{s} = 7$ TeV proton-proton collisions”. In: *Phys. Lett. B* 705 (2011), pp. 294–312. arXiv: 1106.5327 (p. 149).

[246] M. R. Buckley. “Using Effective Operators to Understand CoGeNT and CDMS-Si”. In: *Phys. Rev. D* 88 (2013), p. 055028. arXiv: 1308.4146 (p. 149).

[247] J. Alwall *et. al.* “The automated computation of tree-level and next-to-leading order differential cross sections, and their matching to parton shower simulations”. In: *JHEP* 07 (2014), p. 079. arXiv: 1405.0301 (p. 155).

[248] M. Cacciari, G. P. Salam and G. Soyez. “FastJet user manual”. In: *Eur. Phys. J. C* 72 (2012), p. 1896. arXiv: 1111.6097 (p. 155).

[249] M. L. Mangano *et. al.* “Matching matrix elements and shower evolution for top-quark production in hadronic collisions”. In: *JHEP* 0701 (2007), p. 013. arXiv: hep-ph/0611129 (p. 156).

[250] The NNPDF Collaboration. “Unbiased global determination of parton distributions and their uncertainties at NNLO and at LO”. In: *Nucl. Phys. B* 855 (2012), pp. 153–221. arXiv: 1107.2652 [hep-ph] (p. 157).

[251] P. Skands, S. Carrazza, J. Rojo. “Tuning PYTHIA 8.1: the Monash 2013 Tune”. In: *Eur. Phys. J. C* 3024 (2014), p. 74. arXiv: 1404.5630 [hep-ph] (p. 157).

[252] N. F. Bell *et. al.* “Dark matter at the LHC: EFTs and gauge invariance”. In: *Phys. Rev. D* 92 (2015), p. 053008. arXiv: 1503.07874 (p. 164).

[253] The CMS Collaboration. “Search for narrow resonances using the dijet mass spectrum in pp collisions at $\sqrt{s}$ = 8TeV”. In: *Phys. Rev. D* 87 (2013), p. 114015. arXiv: 1302.4794 (p. 166).

[254] The CDF Collaboration. “Search for new particles decaying into dijets in proton-antiproton collisions at $\sqrt{s}$ = 1.96 TeV”. In: *Phys. Rev. D* 79 (2009), p. 112002. arXiv: 0812.4036 (p. 166).

[255] The CMS Collaboration. “Search for resonances and quantum black holes using dijet mass spectra in proton-proton collisions at $\sqrt{s} = 8$ TeV”. In: *Phys. Rev. D* 91 (2015), p. 052009. arXiv: 1501.04198 (p. 166).

[256] The Planck Collaboration. “Planck 2013 results. XVI. Cosmological parameters”. In: *Astron. Astrophys.* 571 (2014), A16. arXiv: 1303.5076 (p. 169).

[257] G. Bélanger, F. Boudjema, A. Pukhov and A. Semenov. "micrOMEGAs4.1: two dark matter candidates". In: *Comput. Phys. Commun.* 192 (2015), p. 322. arXiv: 1407.6129 (p. 169).

[258] G. Busoni, A. De Simone, T. Jacques, E. Morgante and A. Riotto. "Making the Most of the Relic Density for Dark Matter Searches at the LHC 14 TeV Run". In: *JCAP* 03 (2015), p. 022. arXiv: 1410.7409 (p. 169).

[259] M. Cirelli, E. Del Nobile and P. Panci. "Tools for model-independent bounds in direct dark matter searches". In: *JCAP* 1310 (2013), p. 019. arXiv: 1307.5955 (p. 170).

[260] The ATLAS Collaboration. "Search for new particles in events with one lepton and missing transverse momentum in pp collisions at $\sqrt{s}$ = 8 TeV with the ATLAS detector". In: *JHEP* 09 (2014), p. 037. arXiv: 1407.7494 [hep-ex] (p. 177).

[261] G. Cowan, K. Cranmer, E. Gross, O. Vitells. "Asymptotic formulae for likelihood-based tests of new physics". In: *Eur. Phys. J. C* 71 (2011), p. 1554. arXiv: 1007.1727 [physics.data-an] (p. 179, 215, 219).

[262] The NNPDF Collaboration. "Parton distributions for the LHC Run II". In: *JHEP* 04 (2015), p. 040. arXiv: 1410.8849 [hep-ph] (p. 180).

[263] A. Nelson. *MonoWZH: validation twiki*. 2015. URL: https://twiki.cern.ch/twiki/bin/viewauth/AtlasProtected/MonoWZHad (p. 185, 186).

[264] M. Czakon, P. Fiedler, A. Mitov. "The total top quark pair production cross-section at hadron colliders through $\mathcal{O}(\alpha_S^4)$". In: *Phys. Rev. Lett.* 110 (2013), p. 252004. arXiv: 1303.6254 [hep-ph] (p. 181).

[265] The NNPDF Collaboration. "Parton distributions with LHC data". In: *Nucl. Phys. B* 867 (2013), pp. 244–289. arXiv: 1207.1303 [hep-ph] (p. 181).

[266] The ATLAS Collaboration. "Identification of boosted, hadronically-decaying W and Z bosons in $\sqrt{s}$ = 13 TeV Monte Carlo Simulations for ATLAS". eprint: ATL-PHYS-PUB-2015-033. 2015 (p. 186–188, 190, 210).

[267] The ATLAS Collaboration. "Performance of jet substructure techniques in early $\sqrt{s}$ = 13 TeV pp collisions with the ATLAS detector". eprint: ATLAS-CONF-2015-035. 2015 (p. 187).

[268] A.J. Larkoski, I. Moult, D. Neill. “Power Counting to Better Jet Observables”. In: *JHEP* 12 (2014), p. 009. arXiv: 1409.6298 [hep-ph] (p. 188, 189).

[269] A.J. Larkoski, I. Moult, D. Neill. “Analytic Boosted Boson Discrimination”. In: *JHEP* 1605 (2016), p. 117. arXiv: 1507.03018 [hep-ph] (p. 188).

[270] A.J. Larkoski, G.P. Salam, J. Thaler. “Energy Correlation Functions for Jet Substructure”. In: *JHEP* 06 (2013), p. 108. arXiv: 1305.0007 [hep-ph] (p. 189).

[271] The CMS Collaboration. “Identification techniques for highly boosted W bosons that decay into hadrons”. In: *JHEP* 12 (2014), p. 017. arXiv: 1410.4227 [hep-ph] (p. 189).

[272] J. Thaler, K. Van Tilburg. “Identifying Boosted Objects with N-subjettiness”. In: *JHEP* 03 (2011), p. 015. arXiv: 1011.2268 [hep-ph] (p. 190).

[273] J. Thaler, K. Van Tilburg. “Maximizing Boosted Top Identification by Minimizing N-subjettiness”. In: *JHEP* 02 (2012), p. 093. arXiv: 1108.2701 [hep-ph] (p. 190).

[274] The ATLAS Collaboration. ”Tagging and suppression of pileup jets with the ATLAS detector”. eprint: ATLAS-CONF-2014-018. 2015 (p. 191).

[275] The ATLAS Collaboration. ”Expected Performance of Boosted Higgs ($\rightarrow b\bar{b}$) Boson Identification with the ATLAS Detector at $\sqrt{s}$ = 13 TeV”. eprint: ATL-PHYS-PUB-2015-035. 2015 (p. 191).

[276] The ATLAS Collaboration. ”Expected performance of the ATLAS b-tagging algorithms in Run-2”. eprint: ATL-PHYS-PUB-2015-022. 2015 (p. 192).

[277] The ATLAS Collaboration. “Performance of jet substructure techniques for large-R jets in proton-proton collisions at $\sqrt{s}$ = 7 TeV using the ATLAS detector”. In: *JHEP* 09 (2013), p. 076. arXiv: 1306.4945 (p. 192).

[278] The ATLAS Collaboration. ”Expected performance of missing transverse momentum reconstruction for the ATLAS detector at $\sqrt{s}$ = 13 TeV”. eprint: ATL-PHYS-PUB-2015-023. 2015 (p. 194).

[279] The ATLAS Collaboration. ”Selection of jets produced in 13TeV proton-proton collisions with the ATLAS detector”. eprint: ATLAS-CONF-2015-029. 2015 (p. 195).

[280] The ATLAS Collaboration. "Search for Dark Matter in association with a Higgs boson decaying to b-quarks in pp collisions at $\sqrt{s}$ = 13 TeV with the ATLAS detector". eprint: ATL-COM-PHYS-2015-1399. 2015 (p. 203, 212).

[281] The ATLAS Collaboration. "Search for diboson resonances in the $\mu\mu qq$ final state in pp collisions at $\sqrt{s}$ = 13 TeV with the ATLAS detector". eprint: ATL-COM-PHYS-2015-1223. 2015 (p. 203).

[282] The ATLAS Collaboration. "Jet energy scale and resolution measurements and their systematic uncertainties in proton-proton collisions at $\sqrt{s}$ = 13 TeV with the ATLAS detector". eprint: ATL-COM-PHYS-2016-213. 2016 (p. 210).

[283] The ATLAS Collaboration. "Jet Mass Reconstruction with the ATLAS Detector in Run 2". eprint: ATL-COM-CONF-2016-029. 2016 (p. 210).

[284] S. Dulat *et. al.* "New parton distribution functions from a global analysis of quantum chromodynamics". In: *Phys. Rev. D* 93 (2016), p. 033006. arXiv: 1506.07443 [hep-ph] (p. 212).

[285] L.A. Harland-Lang, A.D. Martin, P. Motylinski, R.S. Thorne. "Parton distributions in the LHC era: MMHT 2014 PDFs". In: *Eur. Phys. J. C* 75 (2015), p. 204. arXiv: 1412.3989 [hep-ph] (p. 212).

[286] A.L. Read. "Modified frequentist analysis of search results (The CL_s method)". eprint: CERN-OPEN-2000-205. 2000 (p. 219).

[287] A.L. Read. "Presentation of search results: The CL_s technique". In: *J. Phys. G.* 28 (2002), pp. 2693–2704 (p. 219).

[288] M. Baak, S. Gadatsch, R. Harrington, W. Verkerke. "Interpolation between multi-dimensional histograms using a new non-linear moment morphing method". In: *Nucl. Instrum. Meth. A* 39-48 (2015), p. 771. arXiv: 1410.7388 [physics.data-an] (p. 221).